



**HAL**  
open science

# A multimodal two-photon fluorescence endomicroscope and its associated tissue database to discriminate brain tumors intraoperatively

Hussein Mehidine

► **To cite this version:**

Hussein Mehidine. A multimodal two-photon fluorescence endomicroscope and its associated tissue database to discriminate brain tumors intraoperatively. Physics [physics]. Université Paris Cité, 2020. English. NNT : 2020UNIP7194 . tel-03917131

**HAL Id: tel-03917131**

**<https://theses.hal.science/tel-03917131>**

Submitted on 1 Jan 2023

**HAL** is a multi-disciplinary open access archive for the deposit and dissemination of scientific research documents, whether they are published or not. The documents may come from teaching and research institutions in France or abroad, or from public or private research centers.

L'archive ouverte pluridisciplinaire **HAL**, est destinée au dépôt et à la diffusion de documents scientifiques de niveau recherche, publiés ou non, émanant des établissements d'enseignement et de recherche français ou étrangers, des laboratoires publics ou privés.



Université  
de Paris

Université de Paris

Ecole doctorale Physique en Île-de-France, ED 564

Laboratoire de Physique des 2 Infinis Irène Joliot-Curie

**A multimodal two-photon  
fluorescence endomicroscope  
and its associated tissue  
database to discriminate  
brain tumors intraoperatively**

Par Hussein Mehidine

Thèse de doctorat de Physique/Optique biomédicale

Dirigée par Darine Abi Haidar

Présentée et soutenue publiquement le 29 Octobre 2020

Devant un jury composé de :

**Sophie BERNARD**, Professeur, Université de Paris, présidente.

**Walter BLONDEL**, Professeur, Université de Lorraine, rapporteur.

**Bruno MONTCEL**, Maître de conférence, HDR, Université Claude Bernard Lyon 1, rapporteur.

**Alain BOSSEBOEUF**, Directeur de recherche CNRS, Université Paris-Saclay, examinateur.

**Giorgio SEANO**, chercheur, Institut Curie, examinateur.

**Matthieu REFREGIERS**, chef de ligne de lumière, Synchrotron Soleil, membre Invité.

**Darine ABI HAIDAR**, Maître de conférence, HDR, Université de Paris, directrice de thèse.

**Titre :** Endomicroscope de fluorescence multimodale sous excitation biphotonique et sa banque de données tissulaire associée pour la discrimination per-opératoire des tumeurs cérébrales.

**Résumé :**

La procédure standard dans le traitement des tumeurs cérébrales consiste à réaliser une résection maximale des zones cancéreuses tout en préservant les régions éloquentes saines adjacentes du cerveau. Par conséquent, l'identification précise des berges de la tumeur ainsi que les zones infiltrées entourant, constitue un défi majeur pour le neurochirurgien. À ce jour, les techniques proposées ne sont pas capables de délimiter, avec une haute précision, les berges de la tumeur ni l'infiltration des cellules cancéreuses dans le tissu sain. La méthode de diagnostic utilisée pour discriminer précisément les tissus sains des tissus cancéreux avec une grande fiabilité est l'analyse histologique des biopsies. Cette analyse post-chirurgicale ex-vivo requiert plusieurs jours avant de fournir une réponse définitive. Un délai qui peut s'avérer fatal pour le patient. Pour répondre à cette problématique, un outil d'imagerie peropératoire qui comble les lacunes des techniques utilisées actuellement a été proposé. Cet outil, un endomicroscope multimodal fibré, fournira une information de diagnostic précise et instantanée sur les tissus sans excision, en per opératoire, et sera une vraie assistance pour le neurochirurgien pendant l'exérèse tumorale. Le développement de cet endomicroscope de fluorescence sous excitation biphotonique est présenté dans cette thèse. Cet endomicroscope permettra la détection de la fluorescence endogène des tissus cérébraux ainsi que la génération de la seconde harmonique. Ces signaux seront analysés par des méthodes quantitatives tel que l'analyse spectroscopique et l'analyse de la durée de vie de la fluorescence et des méthodes qualitative d'imagerie, donnant ainsi des informations sur la structure et l'état métabolique du tissu observé. Dans le cadre du développement instrumental de cet outil, visant une utilisation peropératoire, une sonde d'imagerie miniature a été développé et présentée dans cette thèse. Parallèlement au développement instrumental de cet endomicroscope, la construction d'une banque de données tissulaire basée sur le signal de fluorescence endogène des tissus cérébraux a été établi. Dans le cadre de la construction de cette banque tissulaire, dans cette thèse, différents types de tissus cérébraux, sains et tumorales, ont été analysé afin d'établir une signature optique spécifique à chaque nature tissulaire. Grâce à cette banque, l'endomicroscope sera capable d'établir une réponse diagnostic sur le tissu examiné en temps réel et d'une façon fiable, guidant ainsi le chirurgien dans son geste opératoire.

**Mots clefs :** Endomicroscope, fluorescence endogène, imagerie de la fluorescence, génération de la seconde harmonique, fluorescence sous excitation non linéaire, temps de vie de la fluorescence, MEMS, tumeurs cérébrales, Banque de données tissulaire.

**Title :** A multimodal two-photon fluorescence endomicroscope and its associated tissue database to discriminate brain tumors intraoperatively.

**Abstract :**

Standard of care in brain tumors management primarily consists of achieving a maximal safe resection, by removing all cancerous zones while preserving healthy eloquent adjacent brain areas. Consequently, the accurate delimitation of the tumor margins as well as the infiltrated areas that surrounds the tumor mass is a major challenge for the neurosurgeon. To date, the techniques that have been proposed are not able to delineate, with high accuracy, the tumor margins nor the infiltrating areas. The gold standard used method that discriminates normal from cancerous tissues with high reliability is the histopathological analysis of biopsied samples. This ex-vivo post-surgical analysis requires several days to provide a definite diagnosis response, a time delay that could be fatal for the patient. To address this problem, an intraoperative imaging tool that fill in the gaps of the actually used techniques has been proposed. This tool, a multimodal fibered endomicroscope, will be able to provide a real-time and precise diagnosis information intraoperatively on the tissues nature without excision, and will offer a strong assistance to the neurosurgeon. The development of this two-photon fluorescence endomicroscope is presented in this thesis. This endomicroscope is able to acquire the endogenous fluorescence signal of brain tissues as well as the second harmonic generation signal. These two signals will be analyzed through quantitative methods, such as spectroscopic analysis and fluorescence lifetime analysis, and through qualitative methods that derives from the two imaging contrasts, which will provide an information on the structure and the metabolic state of the imaged tissue. As a part of the instrumental development of this tool, dedicated to intraoperative use, a miniature imaging probe head has been developed and presented in this thesis. In parallel with the endomicroscope instrumental development, the construction of a tissue database based on the endogenous fluorescence signal of brain tissues has been established. As a part of the tissue database construction, in this thesis, different types of brain tissues, healthy and tumors, were analyzed in order to establish a specific multimodal optical signature to each tissue type. Relying on this database the endomicroscope will be able to establish a real time and a reliable diagnosis response, and thus, to guide the neurosurgeon during the surgical procedure.

**Keywords :** Endomicroscope, endogenous fluorescence, Fluorescence imaging, second harmonic generation (SHG), two-photon fluorescence, MEMS, Brain tumors, Tissue Database.

A ceux qui m'ont soutenu, à mes parents ...

C'est la volonté qui fait le chemin

# Table of contents

ACKNOWLEDGMENTS .....	10
FRENCH SUMMARY .....	12
LIST OF ACRONYMS .....	17
LIST OF FIGURES .....	20
LIST OF TABLES .....	29
CHAPTER 1.....	32
INTRODUCTION .....	32
<b>1.1 BRAIN AND CENTRAL NERVOUS SYSTEM TUMORS .....</b>	<b>34</b>
1.1.1 Preamble: cancer.....	34
1.1.2 Brain tumors.....	36
1.1.3 Meningioma .....	38
1.1.4 Glioma.....	39
1.1.5 Metastasis.....	42
<b>1.2 BRAIN TUMORS MANAGEMENT .....</b>	<b>43</b>
1.2.1 Diagnosis.....	43
1.2.2 Therapy .....	48
<b>1.3 INTRAOPERATIVE OPTICAL IMAGING MODALITIES.....</b>	<b>52</b>
1.3.1 Optical coherence tomography .....	53
1.3.2 Raman spectroscopy.....	56
<b>1.4 FLUORESCENCE IMAGING .....</b>	<b>58</b>
1.4.1 Fluorescence .....	58
1.4.2 Fluorescence microscopy.....	60
<b>1.5 FLUORESCENCE IMAGING FOR INTRAOPERATIVE USE.....</b>	<b>72</b>
1.5.1 Fluorescence guided surgery using 5-Aminolevulinic Acid .....	73
1.5.2 Intraoperative widefield microscopy .....	75
1.5.3 Intraoperative confocal endomicroscopy .....	75
1.5.4 Two-photon fluorescence endomicroscopy.....	77
<b>1.6 THESIS PROJECT.....</b>	<b>89</b>
CHAPTER 2.....	95
<b>WHAT IS THE UTILITY BEHIND USING ULTRASHORT DURATION AND HIGH POWER EXCITATION LASER PULSES IN AN ENDOMICROSCOPE AND WHAT IS THE EFFECT OF THESE PULSES ON BRAIN TISSUES AUTOFLUORESCENCE ? .....</b>	<b>95</b>
<b>2.1 CONTEXT OF THE STUDY .....</b>	<b>95</b>
<b>2.2 PAPER: THE IMPACT OF COMPRESSED FEMTOSECOND LASER PULSE DURATIONS ON NEURONAL TISSUE USED FOR TWO- PHOTON EXCITATION THROUGH AN ENDOSCOPE.....</b>	<b>98</b>
2.2.1 Introduction.....	99
2.2.2 Materials and methods .....	101
2.2.3 Results .....	105
2.2.4 Discussion .....	112
2.2.5 Conclusion.....	117



<b>CHAPTER 3</b> .....	118
<b>DOES THE AUTOFLUORESCENCE PROPERTIES EXTRACTED THROUGH A FIBRED-ENDOMICROSCOPE HAVE THE ABILITY TO DISCRIMINATE DIFFERENT BRAIN TISSUE TYPES, AND THEREFORE RELIABLE TO BE USED FOR INTRAOPERATIVE DIAGNOSIS ESTABLISHMENT ?</b> .....	118
<b>3.1</b> <b>CONTEXT OF THE STUDY</b> .....	118
<b>3.2</b> <b>PAPER: A TWO-PHOTON FLUORESCENCE BIMODAL ENDOMICROSCOPE DEDICATED FOR INTRAOPERATIVE BRAIN TUMOR DIAGNOSIS: A COMPARISON WITH BENCHTOP MICROSCOPY</b> ....	121
3.2.1 Introduction.....	121
3.2.2 Materials and methods.....	123
3.2.3 Results .....	126
3.2.4 Discussion .....	133
3.2.5 Conclusion.....	135
<b>CHAPTER 4</b> .....	136
<b>TOWARD MULTIMODALITY: DESIGN AND CHARACTERIZATION OF A MINIATURE 2D SCANNING PROBE HEAD BASED ON AN ELECTROTHERMAL ACTUATION MEMS MIRROR.</b> .....	136
<b>4.1</b> <b>CONTEXT OF THE STUDY</b> .....	136
<b>4.2</b> <b>PAPER: A CUSTOMIZED TWO PHOTON FLUORESCENCE IMAGING PROBE BASED ON 2D SCANNING MEMS MIRROR INCLUDING ELECTROTHERMAL TWO-LEVEL-LADDER DUAL S-SHAPED ACTUATORS</b> .....	140
4.2.1 Introduction.....	141
4.2.2 Materials and methods.....	143
4.2.3 Results .....	147
4.2.4 Discussion .....	151
4.2.5 Conclusion.....	153
<b>CHAPTER 5</b> .....	155
<b>WHAT IS THE MAXIMAL POST-OPERATION TIME WHICH PERMITS TO MEASURE CORRECTLY THE AUTOFLUORESCENCE SIGNAL ? SHOULD A TISSUE DATABASE BE ACQUIRED USING ONLY FRESH SAMPLES ?</b> .....	155
<b>5.1</b> <b>CONTEXT OF THE STUDY</b> .....	155
<b>5.2</b> <b>PAPER: MULTIMODAL IMAGING TO EXPLORE ENDOGENOUS FLUORESCENCE OF FRESH AND FIXED HUMAN HEALTHY AND TUMOR BRAIN TISSUES</b> .....	157
5.2.1 Introduction.....	158
5.2.2 Materials and methods.....	160
5.2.3 Results .....	162
5.2.4 Discussion and conclusion .....	166
<b>CHAPTER 6</b> .....	169
<b>DOES THE MULTIMODALITY OF CONTRAST IN NIR WINDOW PERMITS TO DEFINE RELIABLE DISCRIMINATION PARAMETERS BETWEEN HEALTHY AND TUMORS TISSUES? INVESTIGATION OF SCATTERING, ABSORPTION, AND ANISOTROPY PROPERTIES OF HUMAN BRAIN TUMORAL TISSUES IN THE NIR WAVELENGTH RANGE.</b> .....	169

6.1	CONTEXT OF THE STUDY.....	169
6.2	PAPER: COMPARISON OF OPTICALLY-DERIVED BIOMARKERS IN HEALTHY AND BRAIN TUMOR TISSUE UNDER ONE- AND TWO-PHOTON EXCITATION .....	172
6.2.1	Introduction.....	173
6.2.2	Materials and methods .....	174
6.2.3	Results .....	177
6.2.4	Discussion and conclusion.....	182
<b>CHAPTER 7.....</b>		<b>186</b>
<b>TOWARDS A MORE SPECIFIC TISSUE DATABASE: COULD QUANTITATIVE MULTIMODAL AND MULTISCALE OPTICAL ANALYSIS DISCRIMINATE LOW GRADE AND HIGH GRADE GLIOMA FROM HEALTHY BRAIN TISSUES ? .....</b>		<b>186</b>
7.1	CONTEXT OF THE STUDY .....	186
7.2	PAPER: OPTICAL SIGNATURES DERIVED FROM DEEP UV TO NIR EXCITATION DISCRIMINATES HEALTHY SAMPLES FROM LOW AND HIGH GRADES GLIOMA .....	189
7.2.1	Introduction.....	190
7.2.2	Materials and methods .....	192
7.2.3	Results .....	198
7.2.4	Discussion and conclusion .....	205
<b>CHAPTER 8.....</b>		<b>210</b>
<b>COULD QUANTITATIVE MULTIMODAL AND MULTISCALE OPTICAL ANALYSIS DISCRIMINATE GRADE I AND GRADE II MENINGIOMA FROM HEALTHY BRAIN TISSUES .....</b>		<b>210</b>
8.1	CONTEXT OF THE STUDY .....	210
8.2	PAPER: MOLECULAR CHANGES TRACKING THROUGH MULTISCALE FLUORESCENCE MICROSCOPY DIFFERENTIATE MENINGIOMA GRADES FROM HEALTHY BRAIN TUMOR TISSUE .....	213
8.2.1	Introduction.....	213
8.2.2	Materials and methods .....	215
8.2.3	Results .....	221
8.2.4	Discussion and conclusion .....	230
<b>CHAPTER 9.....</b>		<b>236</b>
<b>DISCUSSION AND CONCLUSION .....</b>		<b>236</b>
9.1	A TPF ENDOMICROSCOPE WITH A HIGH POTENTIAL FOR QUANTITATIVE DIAGNOSIS ESTABLISHMENT .....	236
9.2	TOWARD A MULTIMODAL TPF ENDOMICROSCOPE .....	238
9.3	A MORE ROBUST AND SPECIFIC TISSUE DATABASE .....	240
9.3.1	Spectral analysis for tissue discrimination .....	241
9.3.2	Fluorescence lifetime analysis for tissue discrimination .....	243
<b>BIBLIOGRAPHY .....</b>		<b>247</b>

# Acknowledgments

This PhD was a delightful journey of 3 years that changed my life on the personal and professional level. It has been my greatest learning and growing experience in all of my academic track: lots of articles to read, many courses to learn, and hundreds of hours of experimentation. Nevertheless, as any other achievement, it was not possible to pursue this degree and success alone. I am grateful to every colleague, professor, and person I have met during these three years at Paris-Saclay and Paris University. I appreciate every piece of information, knowledge, and experience you have shared with me.

The first person that I would like to thank is my PhD director Dr. Darine Abi Haidar. Since our first meeting, when I came to you for my master internship, you gave me the opportunity to prove myself, you trusted me and you believed in me and in my ability to work in this project. I am thankful and grateful for the opportunity you gave me, I was able to get my first experience in the research field because of you. During the three years of my PhD, you were always beside me, answering all of my questions, helping on the psychological level, guiding and supporting me. Your statement “it’s the will that makes the way” was always in my head to motivate me. I will be always gratified by you and by all what you have offered to me. Thank you from the bottom of my heart.

Furthermore, I would like to thank every colleague that have been working closely with me on this project. Ali Ibrahim who was the first person that shared with me his experience and knowledge during my master’s internship. Thank you for all your help and for every advice you gave me. Fanny Poulon, my friend and my colleague that helped me a lot during my internship as well during my first year of my thesis. We shared every single moment and every single detail in this project. You listened to all my problems and you always had the best solution. We worked, laughed and even cried together. Thank you.

Last but not least, my colleague Mira Sibai. One of the greatest people that I have ever met and that I learned a lot from. Thank you for every advice you gave me, for your endless support and the great vibes present when you are around. It was a big pleasure for me to work with you during my PhD, and for sure, you were the best conferences’ partner.

I want to thank also all the interns that I worked with and who left an unforgettable touch in this project: Eliot, Elise, Audrey, Emile and Jean-Francois. You made all of the work easier, appealing and even funnier, while with you the “salle de vie” was transferred to my desk. You were great and every one of you was a part of this success.

I would like also to thank Julien Selles, my PhD tutor, with who I had the opportunity to work during the first month of my PhD. Despite this short duration, I have learned very much from you and especially the most important basics of optical instrumentation and pulse compression process. Marie Alix Duval, my great PhD mentor, who was, with Julien Selles, a member of my PhD monitoring committee.

In addition, I cannot finish without mentioning the staff from our laboratory that I worked with: Marjorie, Laurent Pinot, Cédric and Françoise. Your contribution in our project was more than important. Thank you for you all your help in the biological, electronic and data processing aspect of my work.

I would like also to thank all of our collaborators who has been part of this project. In Sainte-Anne Hospital professor Bertrand Devaux, chief head of the neurosurgery department, and Professor Pascale Varlet, head chief of the neuropathology laboratory, who gave me the possibility to work so close to the clinic and with whom I had great

discussions. Indeed, a special big thanks for Matthieu Refregiers, chief head of DISCO beamline at synchrotron SOLEIL, for welcoming me to their platforms during my night shifts. It was a great opportunity to work with you within the same project and to have constructive and helpful discussions which gave me the opportunity to learn more.

A special thanks to Professor Huikai Xie and Dr Min Li, our collaborators from the University of Florida, for collaborating with us in the MEMS imaging probe head development.

Outside the lab, there was another type of support and the most important one. My friends who accompanied throughout my journey in France, who supported me, listened to me and who stayed beside me during shine and rain. Hussein Chokor, Hasan Obeid, Ali Saad and Mehzen Sindiane. You were the real friends that I will count on forever. Thank you for being a part of my life.

The “Kley” team, with whom I shared great moments and that I had big support, especially during the first confinement period when I was writing my PhD manuscript: Abdallah, Mary, Rawad, Tony, Marie-José, Hala, Yara, Ghady, Ali Hamdan, Nadim, Peter, Charbel, Tristan, Kamel. I love you all.

Finally, I would like to express my deepest gratitude to my family, especially my parents. Mom and Dad, you have always supported me in all of my choices, and made it so much easier for me to reach my goals, all these achievements are yours as much as they are mine. Thank you so much for being such giving, caring, loving, and supporting parents. You will always be the first and most important school in life. Without the lessons I received from you first, I would have never ever held the title “doctor”.

# French summary

Tout au long de son histoire, le cancer a été considéré comme un synonyme de la mort dans la société. Au fil des siècles, les médecins et les chercheurs ont amélioré leurs capacités à comprendre tout ce qui est lié au cancer, son origine, ses causes, ses symptômes et ses conséquences. De nouvelles techniques et méthodes de diagnostic et de thérapie ont été inventées, développées et appliquées. Ces progrès ont permis la guérison presque complète de divers types de cancer comme celui du testicule et les premiers stades du cancer du sein. Par contre, il existe toujours tant d'autres qui restent plus mortels et moins guérissables comme le cancer des poumons, du pancréas et du cerveau. Ce dernier se retrouve dans la catégorie des cancers de mauvais pronostic. Les tumeurs cérébrales sont considérées parmi les plus mortels bien qu'ils ne font pas partie des tumeurs les plus incidents. Il existe plusieurs types de tumeurs cérébrales qui se diffèrent selon leur origine de développement et selon l'endroit où il se développent dans le cerveau. Ces tumeurs sont réparties dans deux catégories majeures : La première concerne les tumeurs cérébrales primaires, qui naissent dans le cerveau. Cette catégorie englobe plusieurs types de tumeurs, et dont chaque type comprend plusieurs sous-types qui varient selon leur grade, nature histologique et leur agressivité. On peut distinguer les deux types les plus fréquents de cette catégorie, les méningiomes qui se développent à partir de la méninge et les gliomes qui se développent à partir des cellules gliales. Les gliomes se présentent sous différents grades et sous-types. Le plus malin et les plus agressive est le glioblastome, un gliome de grade IV qui représente lui seule 20% des tumeurs cérébrales primaires en terme d'incidence. La deuxième catégorie concerne les tumeurs cérébrales secondaires. Ce sont des métastases d'un cancer préexistant qui est né dans un autre organe du corps et dont ces cellules cancéreuses parviennent à migrer, via la circulation sanguine, vers le tissu cérébral pour développer de nouvelles tumeurs. Ces tumeurs sont dix fois plus fréquents que les tumeurs primaires. Pendant les dernières décennies, le diagnostic et le traitement des tumeurs cérébrales présentaient des grands défis pour la recherche scientifique dans le monde de l'oncologie. Malgré tous les développements et les avancements réalisés en terme de diagnostic et de traitement, l'évolution du taux de survie pendant ces trente dernières années n'a pas enregistré une augmentation notable.

Le problème réside essentiellement dans la bonne délimitation des berges tumorales pendant l'opération d'exérèse de la tumeur. Au cours de cette opération, le chirurgien vise à résecter toute les zones tumorales, bien visible à l'œil nu et détectable par l'IRM, en maximisant autant que possible les limites de cette résection. Mais la délimitation exacte de l'infiltration tumorale et des berges de la tumeur est très compliqué en per-opératoire à cause de la même apparence visuelle entre tissu sain et infiltré. Pour cela, des échantillons de biopsie sont souvent prélevés de ces zones afin d'être analysé histologiquement après l'opération. Ce processus permet d'avoir la confirmation si l'extraction est presque complète de la tumeur plusieurs jours après l'opération. Ce délai pourra être fatal pour le patient, car ces cellules sont la cause principale de la récurrence de la tumeur. Le vrai enjeu est donc la bonne définition de la limite de l'exérèse, ce qui influe directement sur la durée d'apparition des récurrences et par conséquence sur la durée de vie et le confort des patients.

Pour adresser ce défi, plusieurs techniques et approches ont été considérées et sont en cours d'utilisation en per-opératoire. La première approche c'est l'implémentation de l'analyse histologique en per-opératoire. Par contre, et en per-opératoire cette technique allonge le

temps de l'opération, nécessite une grande expertise et présente un taux élevé de fausses résultats car le processus de préparation des tissus n'est pas le même qui est utilisé au laboratoire.

Une autre approche chirurgicale a été proposée, consistant à utiliser des techniques spécifiques à la chirurgie, comme la chirurgie électro-stimulé et la chirurgie éveillée, qui visent le repérage des zones fonctionnels sains du cerveau afin de les protéger. Ces techniques ont montré une amélioration de la qualité de vie du patient ainsi que son taux de survie. Par contre ils sont très fatigants pour le patient et fournissent aucune information sur la nature tissulaire et peuvent parfois aboutir à des limites de résection très large.

Une autre approche chirurgicale en cours d'utilisation, c'est la chirurgie guidée par la fluorescence de l'acide 5-aminolévulinique (5-ALA). C'est un marqueur fluorescent exogène qui possède une spécificité de s'accumuler dans les zones cancéreuses, ce qui améliore la visualisation des zones. Mais cette technique aboutit parfois à un taux important de résultats faux négatives surtout dans le cas des gliomes bas grades, ce qui rend limitée, sa capacité à repérer l'infiltration tumorale.

Autres méthodes proposées consistent à utiliser les techniques d'imagerie pré-chirurgicales mais pendant l'opération, comme l'IRM per-opératoire ou l'échographie per-opératoire. Ces techniques permettent d'avoir un guidage en temps-réel et fournissent à la fois des informations structurelles et fonctionnelles des tissus. Cependant, ces techniques d'imagerie n'ont pas la précision, résolution et fiabilité de l'analyse histologique post-chirurgicale standard.

Si ces différents techniques proposés en per-opératoire ont permis de réaliser des gestes chirurgicaux plus précis et moins invasifs, les limites des systèmes d'imagerie externes ont été rapidement atteintes tant au niveau des performances que de l'ergonomie pour les applications nécessitant de localiser de petits tumeurs, notamment lorsque celles-ci sont diffuses. Le déplacement des tissus au cours de l'intervention chirurgicale, très marqué pour certains organes comme le cerveau, rend d'autre part souvent obsolète la localisation des lésions réalisée avant l'opération. Un intérêt croissant est donc apparu pour des outils d'imagerie capable de fonctionner au bloc opératoire et de suppléer ainsi les imageurs externes. Ces outils vont pouvoir aider le chirurgien à définir plus précisément et en temps réel les limites et les berges de la lésion tumorale, spécialement parce que le tissu sain et la marge tumorale peuvent avoir la même apparence lors de l'opération.

La concurrence internationale pour le développement de tels instruments est forte. Des endoscopes cliniques à champ large existent déjà et sont fréquemment utilisés en clinique. Malheureusement, ils souffrent d'une très faible résolution spatiale limitant l'étude à une inspection globale du tissu. Quant à l'endomicroscopie à la résolution cellulaire ou même subcellulaire, plusieurs techniques ont été proposées, incluant la microscopie confocale (Cellvizio et Five2 commercialisé par MaunaKea et OptiScan) ou multiphotonique (des prototypes de laboratoire) pour l'image fonctionnelle et la tomographie de cohérence optique (OCT) principalement pour l'image morphologique. En fin de compte, des endoscopes cliniques devraient combiner des modalités contrastées fonctionnelles et morphologiques avec un large champ de vue pour examiner une large zone tissulaire à une résolution cellulaire. Malheureusement, ces trois conditions ne sont pas encore disponibles, à nos jours, dans un même endomicroscope.

Dans ce contexte, le groupe de recherche du Dr Darine Abi Haidar, au sein du laboratoire IJCLab (Laboratoire de Physique des 2 Infinis Irène Joliot-Curie, Orsay, France), avait une perspective différente pour faire face à ce défi médical. Il propose le développement d'un endomicroscope à excitation non-linéaire multimodale qui permet au neurochirurgien

d'établir un diagnostic immédiat et précis sur les berges des tumeurs infiltrant en temps réel pendant l'intervention chirurgicale. Cet instrument miniaturisé pourra être inséré facilement dans le cerveau de l'homme et du petit animal. Il permettra la collection de deux contrastes d'imagerie : la fluorescence générés sous excitation biphotonique de quatre fluorophores endogènes (Le Nicotinamide Adénine Dinucléotide (NADH), les flavines (FAD), les lipopigments et les porphyrines) et la génération de la seconde harmonique (SHG), en les combinant avec l'analyse spectrale et l'analyse du temps de vie de fluorescence des molécules excités. La multimodalité est cruciale pour une analyse fiable et complète des tissus. Outre le développement instrumental, une grande banque de données tissulaire de haute qualité qui vise à caractériser optiquement tous les types des tissus cérébraux, en appliquant la multimodalité d'imagerie, est en cours de construction. Grâce à cette banque, une signature optique spécifique discriminatoire de la cancérisation tissulaire pourra être définie.

Mon travail de thèse durant ces trois dernières années s'inscrit dans le cadre de ce projet de recherche où j'ai participé à développer ces deux aspects, instrumental et banque de données tissulaire. J'ai pu lever plusieurs défis scientifiques et techniques au niveau instrumentale. J'ai mis en place et optimisé un endomicroscope de fluorescence à excitation biphotonique bimodal dédié à réaliser des mesures résolues spectralement et temporellement de la fluorescence. Une unité de de pré-compensation et de compression de pulse basée sur une ligne GRISM a été implémentée et testée. Une fibre endoscopique spécifique à double cœur de cristal photonique à maintien de polarisation a été conçue et fabriqué spécialement pour ce projet. Cette fibre nous a permis d'améliorer l'excitation des structures moléculaires non-centro symétriques (fibres de collagène), source du signal SHG. Cette fibre a été mise en place et les propriétés optiques de l'impulsion ont été caractérisé à la sortie de cette fibre endoscopique unique. L'acheminement d'impulsions ultracourtes (environ 30 fs) à la sortie de cinq mètres de longueur de cette fibre endoscopique a été assuré.

Par la suite j'ai travaillé sur le développement d'un système de balayage miniature qui permet à notre prototype d'acquérir des images et par conséquence de rajouter les modalités d'imagerie à notre endoscope. Pour ceci, une collaboration a été établie entre notre équipe de recherche et l'équipe du Pr. Huikai Xie du Laboratoire de Biophotonique et Microsystèmes (BML) de l'Université de Floride. Grâce à cette collaboration, notre équipe a pu obtenir les composants d'un système de balayage 2D miniature basé sur un miroir MEMS (Micro Electro-Mechanical System) à actuation électrothermique.

Outre le développement instrumental, et parallèlement, j'ai également travaillé sur la construction de la banque de donnée tissulaire. Cette banque de données de la fluorescence tissulaire servira (i) d'une part pour la discrimination de type tissulaire et de la classification de grade des tumeurs et (ii) d'autre part pour calibrer l'endomicroscope non linéaire multimodal en cours de développement. Les objectifs secondaires sont de déterminer la sensibilité et la spécificité de l'analyse optique et de comparer les tissus frais et fixés. Le principal objectif de la construction de cette banque est de déterminer les caractéristiques et la signature optique des différents types d'échantillons cérébraux humains frais. La construction de cette banque de données est basée sur une multimodalité de détection de différents contrastes optiques, sous excitation mono et biphotonique. Pour cela, nous utilisons trois plateformes de mesures spectroscopique et d'imagerie qui couvrent un large domaine d'excitation allant de l'ultraviolet profond jusqu'au proche infra-rouge. La cohorte d'échantillons concerne tout patient adulte présentant une pathologie oncologique ou épileptique nouvellement diagnostiqué au Centre Hospitalier Sainte-Anne (CHSA).

Durant ma thèse, j'ai pu publier et valoriser mes travaux de recherche réalisés dans le cadre de cette thèse dans plusieurs articles scientifiques. Chaque article répond à une question que je me suis posé tout au long de mon travail de thèse. Dans ce manuscrit je présenterai les questions ainsi que les réponses que j'ai apporté et publié. Donc ce manuscrit sera composé d'un chapitre introductif et de sept chapitres de résultats où chaque chapitre présente un article scientifique répondant à une question spécifique. Je termine par une discussion en dressant un bilan scientifique et personnel. Tout cela sera suivi par une perspective à court et à long terme.

Le premier chapitre est introductif où sont présentés les différents types des tumeurs cérébrales, le protocole de prise en charge des patients et les techniques existantes et utilisées pour améliorer le geste chirurgical.

Dans le chapitre 2, nous avons cherché à inspecter l'impact des impulsions hautement énergétiques et de durée ultra-courte, qu'on est capable de générer avec notre endomicroscope, sur les tissus cérébraux. Cette étude a montré que ces très courtes impulsions (40 fs) provoquent une augmentation importante du signal de fluorescence endogène. Le suivi spectrale et l'analyse de la durée de vie de la fluorescence n'ont pas révélés de changement significatif de ce qui indique une photodégradation et une phototoxicité induite limitée. Grâce à cette étude nous sommes capable, avec ses courtes durée d'impulsions d'optimiser le signal de fluorescence collecté sans induire des dommages tissulaires.

Le chapitre 3 présente une comparaison entre notre système endoscopique et un microscope de table sur des biopsies cérébrales humaines. Différents paramètres non linéaires sont explorés et des méthodes de discriminations basés sur ces contrastes sont proposées comme la méthode de phasor ainsi que le calcul de plusieurs rapports métaboliques et autres basés sur les spectres d'autofluorescence.

Le chapitre 4 résume la conception et la caractérisation d'une sonde d'imagerie endoscopique miniature (4 mm de diamètre) basée sur un système de balayage miniature basé sur un miroir MEMS à actuation électrothermique et une configuration double-lentille. Une caractérisation détaillée des propriétés mécaniques du miroir MEMS (angle de balayage optique OSA, temps de passage des pixels PDT, réponses en temps et en fréquence) a été présentée. Le résultat de ce développement était une sonde d'imagerie capable de fournir deux images par seconde sur un champ de vue de 450x450  $\mu\text{m}$  et une possibilité d'atteindre les quatre images/s sur un champ de vue de 250x250  $\mu\text{m}$ .

Le chapitre 5 décrit l'effet du temps de mesure post-résection sur les propriétés de fluorescence des échantillons cérébraux. Le changement des propriétés spectrales et temporelle de la fluorescence des échantillons frais après leur fixation dans le formol est également présenté. Cette étude montre la nécessité de réduire au maximum, le temps entre la résection et la réalisation des mesures multimodales sur les tissus frais. Bien que la fixation au formol affecte les propriétés de fluorescence, la discrimination entre tissus sains et tumorales reste toujours possible.

Le chapitre 6 présente une étude de caractérisation des propriétés optiques d'absorption ( $\mu\text{a}$ ), de diffusion ( $\mu\text{s}$ ) et d'anisotropie ( $g$ ) des différents types de tissus cérébraux humaines fixés. Cette étude a été réalisée dans le domaine des longueurs d'onde du proche infra-rouge. Ces coefficients ont été déterminés parallèlement à une analyse spectrale et de temps de vie de fluorescence menées sous une excitation bi-photonique. L'idée consiste à corrélérer la variation de ces coefficients avec la variation des propriétés de fluorescence des tissus. Différents paramètres discriminatoires incluant plusieurs rapports métaboliques comme le redox ratio, la densité relative de collagène définie comme le rapport du signal SHG sur



celui de fluorescence ainsi que la contribution relative du FAD libre, ont été déterminés. Les résultats obtenus ont confirmé le potentiel d'utilisation de plusieurs paramètres optiques pour révéler des caractéristiques discriminantes entre tissus sains et cancéreuses. Les chapitres 7 et 8 présentent deux études quantitatives et multimodales couvrant trois domaines d'excitation (DUV, visible et proche infra-rouge). Ces études ont été menées sur les deux types des tumeurs cérébrales les plus incidents, les gliomes et les méningiomes, afin de pouvoir discriminer leurs grades. Les gliomes de grade I et II ont été classés dans la catégorie des gliomes de bas grade (LG), tandis que les grades III et IV (GBM) dans la catégorie des gliomes de haut grade. Cette approche a permis l'exploration d'une très large palette de biomarqueurs qui permettent d'atteindre une discrimination plus fiable entre les différents grades tissulaires étudiés. L'évolution, entre chaque grade, de l'émission spectrale et celle du temps de vie de fluorescence de chaque molécule excitée dans les trois domaines a été suivie par différentes approches d'analyse. Les rapports métaboliques liés à ces molécules ainsi que la fraction d'émission du FAD libre et du NADH protéine-liée ont permis de révéler les altérations du métabolisme tissulaire au niveau moléculaire. En outre, le pouvoir discriminatoire de ces paramètres a été évalué à l'aide d'un algorithme de discrimination qui permettait d'identifier leur sensibilité (Se) et spécificité (Sp) à discriminer les différents types tissulaires.

Finalement, ce manuscrit se termine par le chapitre 9 qui comprend une discussion des résultats obtenus sur les deux aspects, instrumental et celui de la banque de données tissulaire. Je dresse ensuite les perspectives futures du projet à moyen et à long terme. Je termine ce chapitre par un bilan personnel.

# List of acronyms

**1PEF:** one Photon Emission Fluorescence  
**2PEF:** two-Photon Excitation Fluorescence  
**5-ALA:** 5-AminoLevulinic Acid  
**AC:** Alternating-Current  
**ADC:** Apparent Diffusion Coefficient  
**Al:** Aluminum  
**BBB:** Blood Brain Barrier  
**BML:** Biophotonics and Microsystems Laboratory  
**CARS:** Coherent Anti-Stokes Raman scattering  
**CCD:** Charge-Coupled Device  
**CHSA:** Centre Hospitalier Sainte Anne  
**CMOS:** Complementary Metal-Oxide-Semiconductor  
**CNRS:** Centre National de la Recherche Scientifique  
**CNS:** Central nervous system  
**Coll:** collagen  
**CPP:** Comité de Protection des Personnes  
**CT-scan:** Computed Tomography scan  
**DCF:** double-clad fibers  
**DC-PCF:** Double-Clad Photonic Crystal Fiber  
**DISCO:** Dichroism, Imaging, mass Spectrometry for Chemistry and biology  
**DM:** Dichroic Mirror  
**DNA:** Deoxyribonucleic Acid  
**DUV:** Deep UltraViolet  
**DWI:** Diffusion Weighted Imaging  
**EBRT:** External Beam Radiation Therapy  
**EEM:** Excitation-Emission Matrix  
**fMRI:** Functional MRI  
**FAD:** Flavin Adenine Dinucleotide  
**FGR:** Fluorescence-Guided Resection  
**FLDC:** Fluorescence Lifetime Decay Curve  
**FLIM:** Fluorescence Lifetime Imaging  
**FOV:** Field Of View  
**fps:** frames per second  
**FRET:** Förster Resonance Energy Transfer  
**FWHM:** Full Width at Half Maximum  
**GBM:** Glioblastoma Multiforme  
**GRIN:** gradient-index  
**GRISM:** GRating+prISM:  
**GVD:** Group Velocity Dispersion  
**H&E:** Hematoxylin and Eosin  
**HG:** High Grade

**HGG:** High Grade Glioma  
**IARC:** International Agency for Research on Cancer.  
**IJCLab:** Laboratoire de Physique des 2 Infinis Irène Joliot-Curie.  
**iMRI:** intraoperative Magnetic Resonance Imaging  
**Int:** Integral proportion  
**IRF:** Instrument Response function  
**IRT:** Internal Radiation Therapy  
**LG:** Low Grade  
**LGG:** Low Grade Glioma  
**LLIF:** Long Lifetime Intensity Fraction  
**LP:** Lipopigments to Porphyrins  
**MEMS:** Micro-Electro-Mechanical System  
**Meta:** Metastasis  
**MRI:** Magnetic Resonance Imaging  
**MRS:** Magnetic Resonance Spectroscopy  
**MT3:** Masson's Trichrome  
**MTSO:** Micro-Tethered-Silicon-Oscillator  
**NA:** numerical aperture  
**NADH:** Nicotinamide Adenine Dinucleotide  
**NFI:** Normalized Fluorescence Intensity  
**NIR:** Near Infra-Red  
**OCT:** Optical Coherence Tomography  
**OD:** Optical Density  
**OI:** optical index  
**OSA:** Optical Scan Angle  
**PET:** Positron Emission Tomography  
**PC-DCF:** Photonic Crystal Double-Clad Fiber  
**PDT:** Pixel Dwell Time  
**PhLAM:** laboratoire de Physique des Lasers, Atomes et Molécules  
**PIMPA:** Plateforme d'Imagerie Multiphotonique du Petit Animal  
**PpIX:** Protoporphyrin IX  
**PZT:** Piezoelectric  
**RD:** Diffuse Reflectance  
**ROI:** Region Of Interest  
**RNA:** Ribonucleic Acid  
**Se:** Sensitivity  
**SEM:** Scanning Electron Microscopic  
**SERS:** Enhanced Raman Spectroscopy  
**SHG:** Second Harmonic Generation  
**SiO<sub>2</sub>:** silicon dioxide  
**SMF:** Single Mode Fibers  
**SNR:** Signal-to-Noise Ratio  
**SOD:** Second-Order Dispersion  
**SOLEIL:** Source Optimisée de Lumière d'Énergie Intermédiaire du LURE

**SORS:** Spatially Offset Raman Spectroscopy  
**Sp:** Specificity  
**SPM:** Self-Phase Modulation  
**SRS:** Stimulated Raman Scattering  
**SRT:** Stereotactic Radiation Therapy  
**TC:** Collimated Transmission  
**TCSPC:** Time Correlated Single Photon Counting  
**TOD:** Third-Order Dispersion  
**TPEF:** Two-Photon Emission Fluorescence  
**TPF:** Two-Photon Fluorescence  
**TPFM:** Two-Photon Fluorescence Microscopy  
**Trp:** Tryptophan  
**Tyr:** Tyrosine  
**UMR:** Unité Mixte de Recherche  
**VIS:** Visible  
**WHO:** World Health Organization

# List of figures

<b>Figure 1.1:</b> From a normal cell, to a malignant tumor. Development process of a cancer [8] .....	34
<b>Figure 1.2:</b> Estimated number of incident cases (blue histogram) and deaths (red histogram) worldwide for both sexes and for all ages according to the international agency for research on cancer [12].	35
<b>Figure 1.3:</b> 5-year survival evolution for selected cancers, between 1986–1990 and 2011–2015 Arrow positions indicate survival estimates and arrow lengths indicate the change in survival between the periods 1986–1990 and 2011–2015 [16].	36
<b>Figure 1.4:</b> Illustration of primary and secondary brain tumors [20], [21] .....	37
<b>Figure 1.5:</b> Incidence distribution of primary brain tumors as a percentage of the total [22] .....	38
<b>Figure 1.6:</b> (right) An illustration showing a meningioma tumor growing and displacing healthy brain tissues. (left) MRI scan image of a sphenoid wing meningioma [17].	39
<b>Figure 1.7:</b> (left) An illustration showing glioblastoma tumor developing inside the brain tissues. (right) MRI scan image of a glioblastoma tumor in the parietal lobe [17] .....	42
<b>Figure 1.8:</b> (right) Illustration of several metastatic brain tumors. (right MRI scan image of multiple metastatic brain tumors that have spread from a melanoma skin tumor [17].	43
<b>Figure 1.9:</b> Top on the left: An MRI image of a brain tumor. Top on the right: Image of an H&E stained tumor biopsy tissue sample. Bottom: Illustration of a needle biopsy operation [17].	48
<b>Figure 1.10:</b> (a) illustration on an EBRT where the beams are directed to the brain from numerous angles and intersect at the tumor to deliver their high dose. The red ring shows the maximum dose and each outer ring represents lower and lower doses. (b) illustration of a SRT showing low-dose beams of radiation that intersect at the tumor to produce a high dose while minimizing exposure to nearby healthy brain [17] .....	51
<b>Figure 1.11:</b> illustration of a basic OCT imaging system showing the interference signal as a function of the reference mirror displacement when a low-coherence light source is used .....	54
<b>Figure 1.12:</b> (a) An OCT integrated fiber-endoscope dedicated for neuroimaging developed by A. Giese team in Germany [69] which implements GRIN rod endoscope head and a scan ensured via a galvo scanner. (b) A spectra domain OCT imaging system combined with a neurosurgical operating microscope and integrated with a commercially available neuro-navigation system presented by A. Giese et al. [65].	55

<b>Figure 1.13:</b> (a) Intraoperative Raman spectroscopy handheld probe developed by F. Leblond and K. Petrecca team. (b) Illustration of the probe being used intraoperatively, with the attached neuro-navigation tracking system showing the location of the tip of the probe (cross hairs) on the pre-surgery MRI image [78].....	57
<b>Figure 1.14:</b> Jablonski diagram. After an electron absorbs a high-energy photon the system is excited electronically and vibrationally. The system relaxes vibrationally, and eventually fluoresces at a longer wavelength. ....	58
<b>Figure 1.15:</b> Spectroscopic characteristics of the main endogenous fluorophores presented in biological tissues where their excitation spectra (a) and their emission spectra (b) are showed [83] .....	59
<b>Figure 1.16:</b> Illustration of a widefield fluorescence microscope setup.....	61
<b>Figure 1.17:</b> Illustration of a laser-scanning confocal fluorescence microscope setup. ....	62
<b>Figure 1.18:</b> Fluorescence images of a mouse kidney tissue acquired via a 63x/1.4 NA oil immersion objective on a widefield fluorescence microscope setup (a) and a laser-scanning confocal microscope setup (b) [102].....	63
Figure 1.19: (a) Spatial difference in fluorescence generation using one-photon excitation and two-photon excitation process [54]. (b) Illustration of Jablonski diagram .....	64
Figure 1.20: Variation of the absorption of photons in function of the light wavelength. The Photo-therapeutic window wavelength range is marked in blue the spectral range of visible and NIR light (650–850 nm) [104].....	64
<b>Figure 1.21:</b> Two-photon fluorescence image (a) and SHG image (b) of an 840x840 $\mu$ m region of a meningioma freshly excised tissue specimen. (c) TPF+SHG merging of the previous images.....	66
<b>Figure 1.22:</b> (a) Intensity contrast image of a histological cat eye section acquired via standard fluorescence microscope. (b) Same section imaged via Fluorescence lifetime imaging microscope reveals contrast by lifetime [119].....	67
<b>Figure 1.23:</b> Illustration of the frequency-domain measurement method: Phase shift and modulation that occurs between the excitation light (blue wave) and the fluorescence emitted signal (green wave) are shown. $\varphi$ : phase shift; $A_{ex}$ : amplitude of the excitation light; $A_{em}$ : amplitude of the emitted fluorescence light; $I_{ex}$ and $I_{em}$ : respective average intensities of the excitation and the fluorescence light [118]. ....	68
Figure 1.24: (a) Illustration of time-gated measurement method: The excitation light pulse is shown in blue while the fluorescence decay in green with three detection time gates ( $t_1$ , $t_2$ and $t_3$ ). (b) Schematic diagram of the time-correlated single-photon counting (TCSPC) acquisition method [118]. ....	69

Figure 1.25: Graphical representation of a phasor in the phasor plot. $g$ corresponds the x-coordinate, $s$ to the y-coordinate of the phasor in the phasor plot, $M$ the module and $\varphi$ the phase. ....	71
Figure 1.26: Graphical representation of a phasor in the phasor plot with an explanation of LLIF determination method.....	72
<b>Figure 1.27:</b> (a) Microsurgical white-light visualization of glioblastoma resection cavity after maximal conventional resection. (b) Visualization of PpIX fluorescence at tumor margin after conventional microsurgical resection[142].....	74
Figure 1.28: Photo showing the intraoperative use of a hand-held confocal endomicroscopy probe co-registered with a Stealth Station neuro-navigation system during brain tumor surgery [135]. ....	76
<b>Figure 1.29:</b> Schematic of fiber-optic two-photon fluorescence endomicroscope: (a) Two-fiber configuration; (b) Single-fiber configuration. SMF : single-mode fiber ; MMF : multimode fiber; DCF: double-clad fiber; SM: single-mode; MM: multi-mode [163].....	77
<b>Figure 1.30:</b> (A) Scanning electron microscope image of the Photonic Crystal Double Clad Fiber used by A. Ibrahim et al [173]. a: Core region surrounded by an air-silica microstructured region; b: Collecting cladding; c: Low index air cladding; d: Maintaining cladding. (B) Details of core surrounding air-silica microstructured region [173].....	79
<b>Figure 1.31:</b> Illustration of a conventional grating-based pre-compensation unit (a) and a GRISM pre-compensation unit [179] .....	79
<b>Figure 1.32:</b> Illustration of the fiber scanning technique using a PZT tube [179] and the beam scanning technique using a MEMS mirror [192].....	81
<b>Figure 1.33:</b> Comparison of several characteristics between electrostatic, electromagnetic and electrothermal actuation mechanisms [197] .....	82
<b>Figure 1.34:</b> (a&b) $10 \times 15 \times 40$ mm MEMS-based probe reported by hoy et al [202] 1: Endoscopic fiber with a GRIN collimating lens; 2: 2D MEMS mirror; 3: miniature aspheric relay lenses; 4: mirror; 5: dichroic mirror; 6: GRIN objective lens; 7: plastic optical fiber. (c) MEMS scanning probe reported by Jung et al. [172]. (d) Illustration of a TPF endomicroscope coupled with MEMS-based imaging probe reported by Fu et al. [171] ...	83
<b>Figure 1.35:</b> Representative ray plots for excitation light (red rays) in the forward direction from the fiber (DCF) to the sample and for the TPF collected signal (blue rays) in the backward direction for two objective lens configuration based on a GRIN lens (a) and a compound lens (b) reported by Y. Wu et al. [167]. (c) Custom achromatic objective lens design composed from 6 lenses reported by M.R Kyrish et al [205] .....	84
<b>Figure 1.36:</b> Schematic of fibred endomicroscope architecture, coupled with a PZT-based scanning probe, reported by the team of Frédéric Louradour at Limoges university (France) [189].....	85

**Figure 1.37:** Schematic of the fibred endomicroscope architecture (a) and the PZT-based scanning probe (b) reported by the team of Ki-Hun Jeong at Korea Advanced Institute of Science and Technology [190]. ..... 86

**Figure 2.1:** (a) Schematic of the endoscopic setup. TCSPC: time-correlated single photon counting, FI: Faraday Isolator, DM: dichroic mirror, DC-PCF: double-clad photonic crystal fiber, GRIN: gradient-index lens, BS: beam splitter, PMA: photomultiplier analyzer, and spectro: spectrometer; (b) raw SHG spectrum of urea; (c) fluorescence lifetime of urea fit to a Lorentzian function and its corresponding residual values. All components of the figure are produced by the authors. ....103

**Figure 2.2:** Fluorescence spectra detected by the endomicroscope at 800 nm excitation and at different laser pulse durations for (a) Rhodamine B and (b) Fluorescein. Each spectrum is normalized to the fluorescence obtained at 40 fs; (c) the integrated fluorescence intensity normalized to that measured at 40 fs, while the dashed curve is the corresponding fit to a power function with exponent  $b$ . The exponent describing fluorescein’s decay function is 1.28, while that of Rhodamine B is 0.94; (d) the mean fluorescence lifetime values (ns) for each dye as a function of pulse duration (fs). Error bars correspond to the standard deviation from five measurements per pulse. .... 106

**Figure 2.3:** The effect of pulse duration on TPEF obtained from a GBM sample. (a) The total autofluorescence spectrum at eight different pulse durations; (b) the integrated fluorescence intensity normalized to that measured at 40 fs, while the dashed curve is the corresponding fit to a power function with exponent  $b$ ; (c) spectrally unmixed fluorescence at 180 fs, and (d) spectrally unmixed fluorescence at 40 fs. The model fit and measured total fluorescence are also shown for (c) and (d). .... 107

**Figure 2.4:** Bar plot showing the mean fluorescence lifetimes for each fluorophore extracted from endoscopic time-resolved fluorescence measurements at different pulse durations. The error bars correspond to the standard deviations pooled from five ROIs per GBM sample. .... 108

**Figure 2.5:** TPEF images from a healthy cortical tissue sample (first row), GBM (second row), metastatic tissue (third row) and meningioma (fourth row) following an excitation of 890 nm and obtained using a 120 (first column), 240 (second column) and 340 fs (third column) pulse durations. The scale bar for all images correspond to 50  $\mu\text{m}$ , and the gray-scale display range for all three images is shown below one of the TPEF images in brackets. The normalized mean intensity from each TPEF image is plotted in the fourth column as a function of the excitation pulse used. The exponent,  $b$ , of the fitted power function is also displayed. .... 109

**Figure 2.6:** FLIM analysis: (a,d,g,j) represent fluorescence lifetime images obtained at three excitation pulses for healthy (first row), GBM (second row), metastatic (third row) and meningioma tissue (fourth row), respectively. The scale bar of 50  $\mu\text{m}$  is displayed in the third column for each tissue type and a horizontal color bar representing the range of calculated fluorescence lifetimes is shown below the set of images. The corresponding mean fluorescence lifetimes are plotted against pulse duration in (b,e,h,k) where error bars



correspond to the standard deviations obtained from calculating the values from five ROIs. The root mean square error, RMSE, and p-values  $> 0.05$  indicate no significant difference between the data points based on regression analysis and a paired t-test, respectively. (c,f,I,l) represent the phasor distribution of the fluorescence lifetimes and their intersections with the universal circle at pulse durations ranging from 120 fs to 340 fs..... 111

**Figure 2.7:** The decay of the TPEF intensity as a function of exposure time at low (a) and high (b) laser irradiances corresponding to those used on the multi-modal microscope and with the endomicroscope respectively. The error bars correspond to the standard deviation between pixels across a selected ROI. The fluorescence lifetime as a function of time at low (c) and high (d) laser irradiances. The error bars correspond to the standard deviation in the lifetime values calculated for the selected ROI. The horizontal line corresponds to the overall mean lifetime, and the p-value indicates no significant difference in lifetime values when measured for different exposure times based on a paired t-test. .... 112

**Figure 3.1:** Illustration of the bimodal endomicroscopic setup.....125

**Figure 3.2:** Normalized Fluorescence spectra acquired from a meningioma sample using 800, 830, 860 and 890 nm as excitation wavelength. (b) Shape of the excitation laser beam at the output of the endoscopic fiber at 800, 830, 860 and 890 nm. (c) Fluorescence spectra acquired from a control sample using several excitation mean power. (d) Variation of the Maximum Fluorescence Emission (MFE) as a function of the mean excitation power. (e) Fluorescence spectra acquired using different pulse duration from a GBM sample. (f) Variation of the Maximum Fluorescence Emission (MFE) in function of the laser beam pulse duration.....128

**Figure 3.3:** Normalized Fluorescence Intensity (NFI) Spectra acquired from the endomicroscope and from the benchtop microscope using 800 nm excitation for meningioma (a), control (b), metastasis (c) and GBM samples (d). (e) Comparison of the fluorescence maximum emission of Rhodamine-B solution, using 800 nm with 13 mW as excitation power, acquired from the benchtop microscope and from the endomicroscope. (f) Comparison of the spectral shape of Rhodamine-B solution excited with the same power on the benchtop microscope and the endomicroscope..... 129

**Figure 3.4:** TPF&SHG images acquired using 890 nm as excitation wavelength through the multimodal microscope from GBM (i), Meningioma (ii), metastasis (iii) and control (iv) sample. (a) Mean emission spectra of control, meningioma, GBM and metastasis sample acquired at 800 nm excitation wavelength through the endomicroscopic setup. Comparison between redox ratio (a), PN ratio (b) and ratio LP (c) derived from spectral measurements at 800 nm excitation through the benchtop microscope and the endomicroscopic setup. Scale bar: 200  $\mu\text{m}$  ..... 130

**Figure 3.5:** (a) SHG emission from urea crystals solution excited using 800 nm as excitation wavelength. (b) Measured IRF (blue curve) via the SHG emission spectra of urea crystals; Fitted curve of the IRF (red curve) via lorentzian fit; an arbitrary measured Fluorescence Lifetime Decay (FLDC, black curve) from a fresh sample..... 131

<b>Figure 3.6:</b> Phasor lifetime histogram acquired from the benchtop microscope (a,c) and from the endomicroscopic setup (b,d) for FAD (a,b) and for NADH (c,d).....	132
<b>Figure 4.1:</b> (a) Zemax shaded model of the probe design. (b) Footprint diagram of the tracked beam at the exit of the focusing lens.....	144
<b>Figure 4.2:</b> (a) An optical image of the Micro-Electro-Mechanical System (MEMS) mirror showing one of its two-level-ladder, double S-shaped actuators (red square); (b) Scanning electron microscopic (SEM) image showing the four actuators with the mirror plate; (c) Assembled probe; (d) Probe mechanical components. ....	145
<b>Figure 4.3:</b> Schematic of the characterization setup of the mechanical properties of the MEMS actuators.....	147
<b>Figure 4.4:</b> Measured reflectivity of the MEMS mirror plate.....	147
<b>Figure 4.5:</b> Optical scan angle variation with the driving voltage for the four actuators with the curve fitting equation of each one (black curves). ....	148
<b>Figure 4.6:</b> Measured pixel dwell time along a Y-axis scan line (a) and along an X-axis scan line (b). ....	150
<b>Figure 4.7:</b> The dynamic responses of the MEMS mirror actuators. Step response of the MEMS mirror four actuators (a–d) in the rise phase (heating up). Frequency response of the four actuators (e) corresponding to the Normalized displacement of the beam (field of view, FOV) with the frequency variation at a fixed voltage of 1.5 V. ....	150
<b>Figure 4.8:</b> Autocorrelation trace at the output of the endoscopic double clad fiber (DCF) fiber (black curve) and at the output of the MEMS scanning system (blue curve).....	151
<b>Figure 5.1:</b> (a) Spectra from a fresh control sample acquired using 405-nm excitation wavelength at multiple time points. (b) The mean peak fluorescence intensity derived hourly from 10 control samples with their corresponding SDs.....	162
<b>Figure 5.2:</b> (a) Spectrally unmixed emission spectra upon 405-nm excitation from the fresh control sample of Figure 1A at $t = 0$ . (b) Spectrally unmixed emission spectra after 5 hours of resection. (c) Bar graph comparing fluorescence lifetime values for each fluorophore measured at $t = 0$ and at $t = 5$ hours post resection. The error bars indicate the SD from all fresh control samples, while the p-values indicate whether the individual lifetimes after 5 hours post resection are significantly different from those obtained at the time of biopsy. (d) Box plot comparing the Lipopigments/FAD ratio at $t = 0$ and $t = 5$ hours derived from all control samples. The box plot includes the upper, the upper quartile (upper portion of box), the median (horizontal line in box), the lower quartile (lower portion of box), and the lower extreme (whisker). NADH, nicotinamide adenine dinucleotide; FAD, flavin adenine dinucleotide .....	163
<b>Figure 5.3:</b> (a) Averaged two-photon spectra from fresh control samples ( $n = 12$ ), fresh glioblastoma (GBM) samples ( $n = 13$ ), and fresh Meta ( $n = 11$ ) samples after 890-nm	

excitation; (b) corresponding averaged two-photon spectra for the three sample groups after tissue fixation: two-photon image from (c) a fresh control sample, (d) the control sample after fixation, (e) a fresh GBM sample, (f) corresponding fixed GBM sample, (g) a fresh Meta sample, and (h) corresponding fixed Meta sample. Scale bar: 100  $\mu\text{m}$  ..... 164

**Figure 5.4:** Fluorescence lifetime imaging microscopy (FLIM) from fresh (a) control, (b) glioblastoma (GBM), and (c) Meta sample; (d-f) histogram of the average lifetime superimposed on a color scale bar for each FLIM image above; (G-I) FLIM after each sample was fixed; (j-l) corresponding histogram. Scale bars = 200  $\mu\text{m}$  ..... 165

**Figure 6.1:** (a) Mean absorption coefficient,  $\mu_a$  ( $\text{mm}^{-1}$ ), as a function of excitation wavelength derived from integrating sphere measurements of control, diffuse glioma, glioblastoma, metastasis, and meningioma samples. (b) Histogram comparing the scattering coefficient,  $\mu_s$ , across all tissue types for each wavelength. (c) Anisotropy coefficient,  $g$ , derived from collimated transmission measurements and averaged among each tissue category. The error bars are the corresponding standard deviations from all tissues within the same category in all three figures.....178

**Figure 6.2:** First row: Two-photon images representative of (a) control, (b) diffuse glioma, (c) glioblastoma, (d) metastasis and (e) meningioma samples following 890 nm excitation. Red and green colors correspond to the TPEF and SHG intensities, respectively. Second row: (f-j) H&E stained images obtained from the same patient; (k-o) the autofluorescence spectra following 405 nm one-photon excitation, and the TPEF spectra following 810 and 890 nm excitation ..... 180

**Figure 6.3:** Bar plots of the optical index (OI) ratio (a), the lipopigment to porphyrin (LP) ratio (b), the redox ratio (c) and the collagen density (d) for each tissue group. The error bars correspond to the standard error averaged across the samples within each tissue group and the asterisks indicate significant differences with a p-value of 0.05..... 181

**Figure 6.4:** (a) Phasor plot of FLIM data obtained from all tissue samples following 890 nm excitation and 520 nm detection. (b) Box plot comparing the long lifetime intensity fraction ( $\alpha$ ) determined for each category..... 182

**Figure 7.1:** Fitting examples of the spectral data collected during Deep-UV excitation (275 nm) (a), for Visible excitation (405 nm) (v) and for NIR excitation (890 nm) (c).....195

**Figure 7.2:** Analysis of the Deep-UV data. Boxplots of three molecular ratios acquired from spectral data under 275 nm excitation wavelength: (a) shows the Tryptophan/Collagen ratio, (b) shows the Tryptophan/NADH ratio and (c) shows the Tryptophan/Tyrosine ratio for control, LG, and HG glioma. The central mark in each box represents the median while the box edges represent the first and the third quartile, respectively. The tables recap the p-values corresponding to the t-test of a couple of values distribution (see statistical analysis). (d) represent the 3D-discrimination clouds of the three molecular ratios comparing control, LG, and HG glioma. .... 199

**Figure 7.3:** Analysis of Visible data. (a) shows the mean type spectrum of control, LG, and HG glioma under 405 nm excitation. (b) shows the Integral proportion of the five

endogenous fluorophores: NADH, FAD, Lipopigments, Porphyrins I and Porphyrins II. (c) shows the average lifetime of the five endogenous fluorophores excited in each tissue type at 405 nm and for NADH and FAD excited at 375 nm. .... 200

**Figure 7.4:** Boxplots of three molecular ratios acquired from spectral data at 405 nm excitation: (a) shows the redox ratio (FAD/(NADH+FAD)), (b) shows the optical index (Porphyrins/NADH) and (c) shows the ratio LP (Lipopigments/Porphyrins) for control, LG glioma and HG glioma. The central mark in each box represents the median while the box edges represent the first and the third quartile, respectively. The values outside the box (red “+”) are considered as outliers. The tables recap the p-values corresponding to the t-test of a couple of values distribution. (see statistical analysis) ..... 201

**Figure 7.5:** Image comparison through the NIR set-up showing a comparison between control (a,d,g), LG (b,e,h) and HG (c,f,i) glioma using different imaging techniques: Hematoxylin-Eosin staining Images (a,b,c) ; FLIM images acquired at 890 nm (d,e,f), color bar represents the lifetime value. 2PEF + SHG images at 890 nm showing 2PEF signal in red and SHG signal in green (g,h,i). Scale bar: 100  $\mu$ m. .... 202

**Figure 7.6:** Phasor FLIM Analysis of NIR data. Global histogram of FLIM phasor plot (a,b,c) and Long Lifetime Intensity Fraction distribution ( $\alpha$ ) for Control, LG and HG (d,e,f) at 810 nm (b,c,e,f) at 890 nm (a,d) excitation for FAD (a,b,d,e) and NADH (c,f) channels. .... 202

**Figure 7.7:** Spectral Phasor Analysis of NIR data at 810 nm excitation wavelength. Comparison of three spectral phasor histogram for: Control (a), LG glioma (b) and HG glioma (c). .... 203

**Figure 7.8:** Boxplots of the three molecular ratios acquired from spectral images data acquired at 810 nm: (a) shows the redox ratio (FAD/(NADH+FAD)), (b) shows the optical index (Porphyrins/NADH) and (c) shows the ratio LP (Lipopigments/Porphyrins) for control, LG glioma and HG glioma. The central mark in each box represents the median while the box edges represent the first and the third quartile, respectively. The values outside the box (red “+”) are considered as outliers. The tables recap the p-values corresponding to the t-test of a couple of values distribution. (see statistical analysis). 204

**Figure 7.9:** 3D scatter cloud of three molecular ratios : Tryp/collagen from UV as X axis (UV), redox ratio from NIR as Y axis (NIR) and redox ratio from Visible as Z axis (VIS). a) general view of the 3D scatter cloud of control, LG, and HG glioma. b) Right side view of the 3D scatter cloud showing the Control-tumor threshold plane ( $z=0.503$ ). c) Left side view of the 3D scatter cloud showing the HG-LG threshold plane ( $y=0.607$ ). .... 205

**Figure 8.1:** Examples of spectral fitting of DUV and NIR collected data. (a) Fitted spectrum acquired using 275 nm as excitation wavelength (a); (b) Fitted spectrum acquired using 810 nm as excitation wavelength; (c) Fitted spectrum acquired using 890 nm as excitation wavelength. .... 218

**Figure 8.2:** Spectral Analysis using Deep UV and NIR excitation range. (a) Normalized mean Fluorescence Intensity (NFI) spectra of 10 control, 7 grade I and 8 grade II

meningioma samples acquired at 275 nm excitation. (b) Normalized mean Fluorescence Intensity (NFI) spectra of 24 control, 14 grade I and 11 grade II meningioma samples acquired at 890 nm excitation. .... 221

**Figure 8.3:** (a) Excitation-Emission Matrix map in DUV excitation range for control (a), grade I (b) and grade II meningioma (b)..... 222

**Figure 8.4:** Image comparison through the NIR and DUV imaging set-up presenting a comparison between control (a,d,g), Grade I meningioma (b,e,h) and Grade II meningioma (c,f,i) through NIR confocal TPEF + SHG images (a, b and c) 890 nm as excitation wavelength, and through DUV Tryptophan + Collagen full field images (d,e,f) using 275 nm as excitation wavelength. MT3 virtual staining Images (g,h,i); scale bar: 100  $\mu\text{m}$ .. 223

**Figure 8.5:** Spectral Phasor histograms using 810 nm (a,b,c) and 890 nm (d,e,f) for: Control (a,d), Grade I meningioma (b,e) and Grade II meningioma (c,f). .... 224

**Figure 8.6:** Group boxplots of six molecular ratios acquired from spectral data at 275nm (DUV) and 810 nm excitation (NIR) for control, grade I and grade II meningioma. DUV part shows Tryptophan/Collagen (N°1), Tryptophan/NADH (N°2) and Tryptophan/Tyrosine (N°3) ratios. NIR part shows PN ratio (Porphyrins/NADH) (N°4), ratio LP (Porphyrins/Lipopigments+Porphyrins) (N°5) and redox ratio (FAD/(NADH+FAD)) (N°6) ratios..... 226

**Figure 8.7:** (a) Boxplot view of SHG integral proportion (SHG-int) in the total spectra at 890 nm excitation wavelength for control, grade I and grade II meningioma; (b) collagen maximum intensity peak (Coll-peak) using 275 nm as excitation wavelength for control, grade I and grade II meningioma; (c) Collagen integral proportion (Coll-int) in the total spectra acquired using 275 nm Control, Grade I and Grade II meningioma. (d) 3D-discrimination ellipsoids of control, grade I and grade II meningioma where SHG-int, Coll-peak and Coll-int were taken as 3D coordinates. (e) table gathering the sensitivity and specificity of discrimination test results realized for 10 control vs 15 tumor samples and for 7 grade I vs 8 grade II meningioma samples..... 227

**Figure 8.8:** Fluorescence lifetime analysis of FAD (a,b,c) and NADH (d). Phasor FLIM histogram of FAD using 810 nm as excitation wavelength for control (a), grade I meningioma (b) and grade II meningioma (c), free and protein-bound FAD lifetime values are drawn as green circles intersecting with the universal circle; mean lifetime histogram of protein-bound NADH at 810 nm for control, grade I and grade II meningioma..... 228

**Figure 8.9:** Long Lifetime Intensity Fraction (LLIF) histogram of NADH (a,c,e) and FAD (b,d,f) issued from phasor FLIM analysis at 810 nm for Control (a,b), grade I meningioma (c,d) and grade II meningioma (e,f). .... 229

**Figure 9.1:** Schematic of the actual architecture of the under-development endomicroscope. GT: Glan Taylor; SMF: single mode fiber; PCD; Photon Counting Detector; PC-DCF: Photonic Crystal Double Clad Fibre; TPF: Two-Photon Fluorescence; FLT: Fluorescence Lifetime. .... 237

# List of tables

<b>Table 1.1:</b> Summary of the imaging modalities used for brain tumors diagnosis as well as the clinical use for each modality .....	46
<b>Table 1.2:</b> comparative table which highlights the different characteristics of our developed TPF endomicroscope system as well those of the systems reported in literature .....	88
<b>Table 1.3:</b> For each specific need its corresponding proposed solution .....	89
<b>Table 1.4:</b> The three different platforms used in this thesis work and the measurements modalities implemented in each platform. ....	91
<b>Table 1.5:</b> Light absorption and emission characteristics of all endogenous fluorophores that their fluorescence was analyzed and highlighted in this thesis work. ....	92
<b>Table 2.1:</b> Summary of reported studies that investigated the effect of exiting of short duration excitation pulse on biological cells/tissues.....	96
<b>Table 2.2:</b> Fluorescence lifetime values for each fluorophore averaged across all excitation pulse durations and regions of interests.....	108
<b>Table 3.1:</b> Summary of the sample's cohort included in this study.....	123
<b>Table 4.1:</b> Comparison between three different lens configuration designs used for optical endoscopic imaging [276].....	137
<b>Table 4.2:</b> Comparison of the main mechanical properties between three MEMS mirrors deploying Al/SiO <sub>2</sub> dual S-shaped bimorph electrothermal actuators with a different actuators level architecture each. ....	146
<b>Table 4.3:</b> The operating frequencies for both scanning axes for each imaging FOV with the maximum frame rate that can be reached for each FOV.....	153
<b>Table 6.1:</b> Summary of the cohort brain specimens included in this study.....	175
<b>Table 7.1:</b> Summary of the median values of the investigated molecular ratios extracted from DUV, visible and NIR excitation domains.....	187
<b>Table 7.2:</b> Summary of the mean fluorescence lifetime values of NADH and FAD extracted through the visible one-photon endoscope following 375 nm.....	187
<b>Table 7.3:</b> Clinical Characteristics of our sample's cohort .....	193
<b>Table 7.4:</b> Gaussian Parameters considered to fit the fluorescence emission spectrum of each fluorophore excited with 275 nm .....	194
<b>Table 7.5:</b> Gaussian Parameters used to fit the fluorescence emission spectrum of each fluorophore excited with 405 nm. ....	195

<b>Table 7.6:</b> Overlap volume percentage between the different ellipsoids .....	199
<b>Table 8.1:</b> Summary of the significant quantitative discrimination thresholds obtained in this chapter to differentiate healthy, grade I and grade II meningioma.....	212
<b>Table 8.2:</b> Gaussian Parameters considered to fit the fluorescence emission spectrum of the endogenous fluorophores excited in DUV range (275 nm) and in NIR range (810 nm and 890 nm) .....	219
<b>Table 9.1:</b> Summary of all the discrimination indicators in this thesis work to differentiate the grades of glioma and meningioma tumors. FLT: Fluorescence lifetime. The used signs indicate the variation of each indicator comparing with its counterpart in healthy tissues. + : slight increase/ ++ : significant increase/ - : slight decrease/ -- : significant decrease/ ~ : similar/ ~\ : similar with a decrease trend. Specificity and sensitivity corresponds to the discrimination of tumor vs healthy.....	244





# Chapter 1

## Introduction

Throughout its 4000-year history, cancer has been considered as the synonym of death in the society. It has a horrible image stuck in the people's head where some societies even have a big fear to pronounce its name and call it "That disease". Some of the earliest known descriptions of cancer were found in several papyrus scripts from Ancient Egypt. These scripts were discovered and deciphered late in the 19th century. The most famous are known as the "George Ebers" and "Edwin Smith" papyri which contain descriptions of cancer written around 1600 B.C. This latter is a copy of a part of an ancient Egyptian book on trauma surgery which describes eight cases of "tumors" or ulcers of the breast. It mentioned that these tumors were treated by cauterization with a tool called the fire drill [1]. This description adds also that there is no treatment for this disease. Although, the "cancer" word was not used, the origin of this word is credited to Hippocrates (460-370 BC), a Greek physician considered as the "Father of Medicine" [1].

Through ages, cancer has left doctors, patients, and scientists with questions that the medical and research fields could not start to address it until recent decades. For centuries and until now, the question that puzzled scientists is: Will we reach a time when we will be able to control or even to cure this disease?

Over the centuries, the humanity has improved its ability to understand all what it is related to cancer, its origin, causes, symptoms and outcomes. Furthermore, new diagnosis and therapy methods were invented and developed starting from imaging techniques and ending by therapy ways. Today, in 2020, medical researchers and scientists have reached an advanced stage of understanding, on a cellular level, the origin of cancer, what actually it is and how it develops and spreads, they have invented also many successful and targeted methods to treat it, whether surgically or medically.

Despite all these discoveries and improvements, cancer still occupy the second rank as the deadliest disease in the world that affects humans after the cardiovascular diseases [2]. These numbers and statistics may address a confusing view on cancer danger considering it as non-curable disease. But in reality, the situation is more complex while not all cancers are deadly or non-curable. Since that exists several cancer types and subtypes, its dangerousness varies from a type to another and depends on several factors related to its state in the patient. Nowadays, and due to the medical development, it exists cancer types that are 99% curable like testicular cancer and the first stages of breast cancer, but it still exists so many other cancer types which remains to be more fatal and less curable like lung, pancreatic and brain cancer [3].

Adding to the medical field, scientists from other fields, such as chemists and physicists, were strongly involved in the war against cancer. The aim is to combine the medical knowledge with other science fields abilities in order to create and develop new diagnosis and therapy methods. These multidisciplinary efforts aim to reduce the mortality of the poor prognosis cancer types and to improve their survival rates.

During these past three years, my thesis work takes part in this multidisciplinary research field and arises from a clinical problematic that aims to help the surgeon improving the diagnosis quality of brain tumor areas during resection surgery using an optical imaging technique with multimodal analysis methods. I have conducted my research work, in the French IJCLab laboratory (Laboratoire de Physique des 2 Infinis Irène Joliot-Curie, Orsay, France) as a member of the health pole and the Multimodal Instrumentation and Tissue Imaging team, under the supervision of Dr. Darine Abi Haidar.

This team has been cooperating for many years with Sainte-Anne hospital center in Paris, within the context of an interdisciplinary research project to address the problem of the poor diagnosis accuracy of cancerous areas during resection surgery. This project is divided into two main parts that complete each other:

The first part consists to develop a novel surgical real time imaging endoscope, that will be able to provide a fast and an accurate diagnosis response on brain cancerous areas relying on endogenous fluorescence emission.

As a necessary complementarity to this tool, the second part consists to build a tissue database that collects specific optical signatures of brain tissues in order to be used by this tool for a real-time diagnosis establishment and therefore to guide the neurosurgeon during the operation.

This manuscript presents the research work that I have done, in cooperation with my team members, on these two parts, the instrumental one and the tissue database. The first chapter of this manuscript consist of an introduction where in its first section I will describe the different brain tumor types as well their different grades that have been highlighted in this research work. In the second section, I will describe the brain tumor management process, from diagnosis techniques to therapy methods, with focusing on the surgery act where the clinical problematic of my research work arises from.

In the third section I will describe the main intraoperative optical imaging techniques that were proposed in the literature and achieved an advanced stage in their work to respond the brain surgery clinical problematic.

In the fourth section, I will describe the fluorescence process and its related microscopy techniques, their advantages, and their limitations as well its use for brain tumor diagnosis. In the fifth section, I will present the intraoperative fluorescence imaging techniques that were developed for brain surgery guidance, with a detailed description of the challenges that need to be addressed to develop a two-photon fluorescence endomicroscope, which consist of our approved technique to address the brain surgery clinical problematic

In the last section of this introduction, I will explain the context of our research project as well the main objectives of my thesis that I have working on to be achieved.

The second part of this manuscript is oriented around seven scientific papers that have been published during the three years of my thesis works. This part consists of seven chapters where each one addresses the response to a specific problematic arising from the context of my thesis work.

The final part of this manuscript consists of a discussion and conclusion chapter where the main obtained results and the achieved goals are discussed, as well addressing the future directions and perspectives of our project.

## 1.1 Brain and central nervous system tumors

### 1.1.1 Preamble: cancer

Human body consists of trillions of cells grouped together to form tissues and organs. Inside the cell nucleus, genes play the role of the cell brain, they give it the orders when to grow, to work, to die or to divide [4]. The cell division is a complex process which is controlled by hundreds of genes. When the cell genes work properly, they transmit a signal to the cell in the correct time, to grow and divide [5]. In adults, cells normally grow and divide to increase the cell population only when the body needs, such as to replace aging or damaged cells. When cells divide, they proceed to make exact copies of themselves where each cell divide into two identical cells, then two cells divide into four, and so on [4].

During this dividing process, gene mutation can be occurred, it means that a gene has been damaged or lost or copied twice [6]. These mutations can happen by chance or when there is a change or a damage in the DNA due to an external factor such as tobacco consumption, alcohol consumption, unhealthy diet and physical inactivity which consist of the four major cancer risk external factors worldwide [7].

Due to the mixing of the instructions in their DNA, mutated genes don't work properly, leading to give birth to an abnormal cell [4]. The latter becomes cancerous after mutations accumulate in the several genes that control cell proliferation [5]. The development process of a tumor is illustrated in a graphical way in figure 1.1 below, which shows the main phases that an abnormal divided cell goes in before transforming to a malignant tumor.

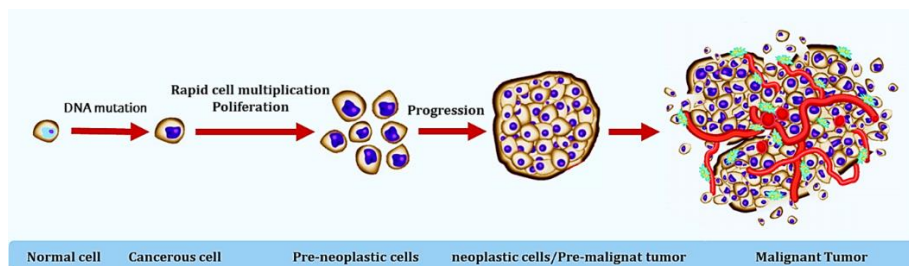


**Figure 1.1:** From a normal cell, to a malignant tumor. Development process of a cancer [8]

Over time, these abnormal cells become increasingly more resistant to the control that maintain normal tissue so the cells no longer understand the DNA instructions. It starts to grow in an out of control way, and as a result, it divides more rapidly than its progenitors and become less dependent to signals from other cells [5], [6]. Cancer cells differ from normal ones in several ways that allow them to grow in an uncontrollable process as well to become invasive. The major and the most important difference is that cancerous cells are less specialized than normal ones. Whereas normal cells mature into distinct cell types with specific functions, while cancer cells do not. This is one of the main reasons that, unlike normal cells, permits cancerous cells to continue dividing without stopping [9].

As cancer cells divide and their number increase, a tumor will develop and grow. Therefore, cancer cells have the same needs as normal cells. They need a blood supply to bring oxygen and nutrients to grow and survive [4]. During the early stages of cancer, the tumor is too small and can grow easily in order to get its supplies of oxygen and nutrients from nearby blood vessels. At this stage the tumor is considered as typically benign and remain confined

within the normal boundaries of a tissue [5]. As the tumor continues growing and becomes malignant, it needs more blood to bring more oxygen and necessary nutrients to the cancer cells development [4]. So cancer cells send signals for the tumor to develop its own blood vessels network in order to carry out its growth needs. This process is named angiogenesis and it is one of the reasons that keep the tumor grow and get bigger [4]. Moreover, the tumor gains the ability to break through the tissue boundaries and invade adjacent tissues. It also allows cancer cells to sneak into the blood vessels and to spread more easily to other organs of the body [5]. At this stage, which is considered as one of the terminal stages of cancer, cancer cells infiltrate the bloodstream or the lymphatic system and migrate to a new location in the body, where they start to divide and lay the foundation to develop secondary tumors named metastasis, literally meaning “new place” [5].

However, not all cancer cell types can metastasize, while in order to spread in the body, the migrated cells must have the ability to penetrate the normal barriers of the body so that they can both enter and exit the blood or lymphatic vessels [5]. Referring to the latest estimates released in 2018 by the International Agency for Research on Cancer (IARC), 18.1 million new cases of cancer were diagnosed worldwide [10]. Furthermore, it is the second leading cause of death in the world with an estimated 9.56 million deaths in 2017, where about 1 in 6 deaths is due to cancer [7]. The most common types occurring worldwide are lung, female breast, colorectal and prostate cancer, figure 1.2 shows the estimated number of incident and deaths cases recorded for the most incident cancer types worldwide. Indeed, estimations indicates that there will be 27.5 million new cases of cancer worldwide each year by 2040 [11].

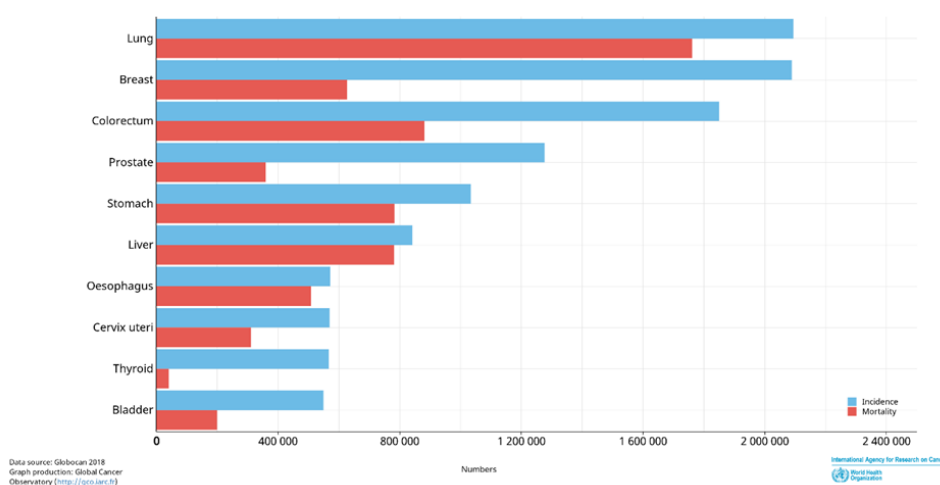


**Figure 1.2:** Estimated number of incident cases (blue histogram) and deaths (red histogram) worldwide for both sexes and for all ages according to the international agency for research on cancer [12]

In the positive side, a cancer is known also by its survival rate which indicates the proportion of patients that recovers after being diagnosed. However, this rate is not similar for all cancer types, it varies according to the tumor stage at diagnosis, treatment given and many other factors including country [13]. The survival rate of a cancer patient is currently measured often by the 5-year survival rate; it consists of the percentage of patients who lives at least five years after being diagnosed with cancer [14]. Several types of cancer

have nowadays high survival rates, including breast, thyroid, prostate, testicular and colon cancer. Pancreatic, liver, lungs and brain cancers have one of the worst survival rates of all cancer types. They are classified as poor prognostic cancer as their 5-year survival rates is less than 30% [13]. Indeed, the improvement of this rate in the last 30 years (period between 1986-2015) was not similar for all cancer types. Figure 1.3 show the evolution of the 5-year survival rate during the mentioned period, for the most incident and deadly cancer types. The worst improved rates were associated to mesothelioma, a rare, aggressive form of cancer that develops in the linings of the lungs, abdomen or heart [15], and to brain tumors [16].

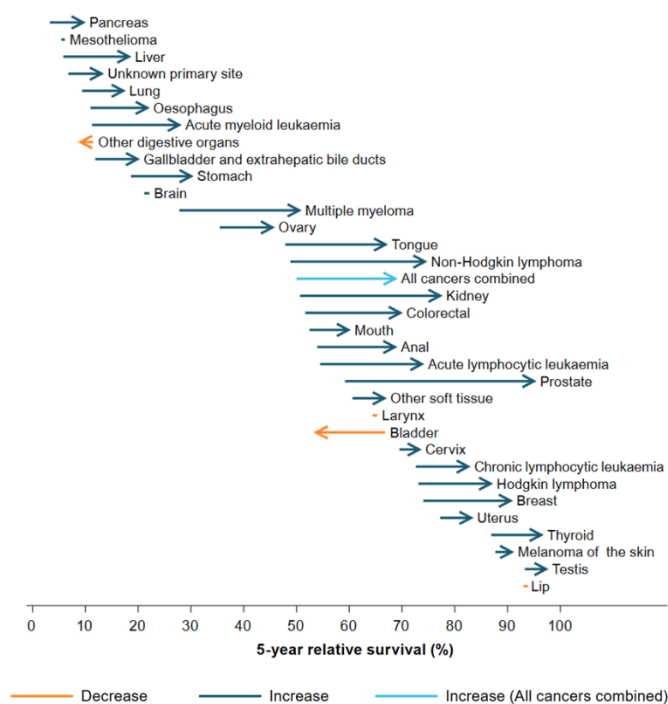


**Figure 1.3:** 5-year survival evolution for selected cancers, between 1986–1990 and 2011–2015. Arrow positions indicate survival estimates and arrow lengths indicate the change in survival between the periods 1986–1990 and 2011–2015 [16]

### 1.1.2 Brain tumors

The Brain is an amazing 1.3 kg organ that controls all body functions. It is considered as the head-chief of the human body which interprets the information from the outside world, and embodies the essence of the mind and soul. Intelligence, creativity, emotion, and memory are some of the many functions governed by the brain [17].

Similar to the other body organs, brain cells can develop tumors. However, brain and central nervous system (CNS) cancer occupy the 18<sup>th</sup> rank in term of incident cases (worldwide, 2018) and the 13<sup>th</sup> rank in term of deaths numbers [12]. Despite not being in the most common, brain and CNS tumors occupy a very high rank between the deadliest form of cancer, especially the malignant types [11].

Despite the improved understanding of the causes of this cancer and the development of the treatment methods (radiotherapy, chemotherapy...etc.) the 5-year survival rate of brain cancer has been barely increased (<2%) in the last 30 years [16]. Still today, the improvement of patient long-term survival rate of this cancer is one of the main concerns

of the neuro-oncology research society. Therapy methods and surgical aid tools has revealed significant advancement in the past decades. Despite these advancements, the survival time of patients with malignant and aggressive brain tumors remains too low (~8.1 months) [18]. In fact, the issue doesn't occur in the therapy stage, but in the process of cancerous regions diagnosis [18]. Nevertheless, at what stage does the identification of cancer areas lead to a poor diagnosis, thereby decreasing the patient's survival rate?

Several types of brain tumors exist, they may grow from nerves (neuroma, schwannoma), meninges (meningioma), pituitary gland (pituitary adenoma) or cerebellum (medulloblastoma, the most common pediatric tumor). They may also grow from the glial cells which form the internal brain tissue itself (glioma) [17]. Enclosed within the bony skull, brain tissues cannot expand to make space for a growing mass and as a result, the tumor compresses the normal brain tissues which cause symptoms. A classification and a grading system was considered by The World Health Organization (WHO) which standardize communication, treatment planning, and predict outcomes for brain tumors [19]. According to this system, brain tumors are classified by their location, cell type, referring to the cell of origin of the tumor, and their grade determined by their malignancy and the pathological evaluation of the tumor [19].

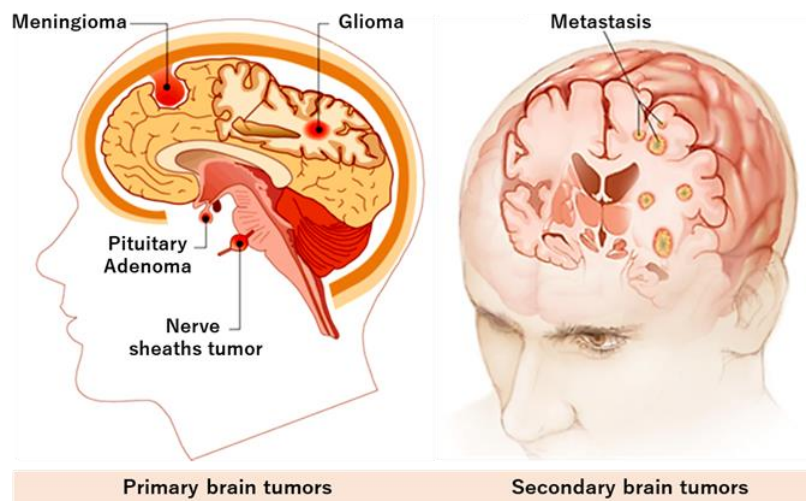


**Figure 1.4:** Illustration of primary and secondary brain tumors [20], [21]

As illustrated in figure 1.4, brain tumors are divided into two different categories, primary and secondary tumors. Primary brain tumors start in the brain and usually does not spread to other parts of the body [20]. It can be divided into different groups referring to where they are originating from or their tissue growth location.

However, the incidence distribution of primary brain tumors is not homogenous where Glioma and meningioma tumors are the most common types. Figure 1.5 shows the most incident brain tumors types as well the percentage of incidence of each one.

Secondary brain tumors, also known as metastatic tumors, occur when a cancer begin in another organ of the body and spread to the brain tissues due to the migrated cancer cells through the bloodstream or the lymph system [21]. The most common cancers that metastasize to the brain are lung (50%), breast (15-20%), skin melanoma (10%), kidney and colon (5%) [17].

Whether a brain tumor is benign, malignant, primary, or metastatic, all are potentially life-threatening.

In this research work, glioma (low and high grade), meningioma (grade I and II) and metastatic tumors have been studied. Each one of these three types will be described in the following subsections.

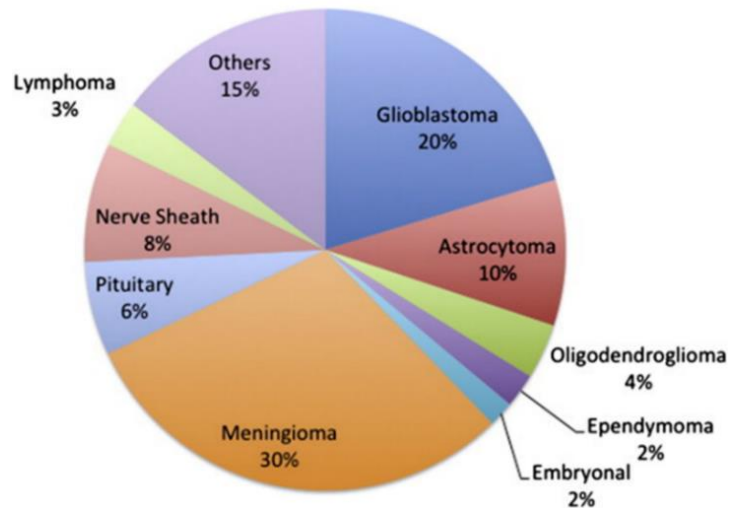


**Figure 1.5:** Incidence distribution of primary brain tumors as a percentage of the total [22]

### 1.1.3 Meningioma

Meningioma is a slow growing tumor that can arise at any location in the meninges, a membranous layer that covers the brain and the spinal cord and separate them from the skull, and to develop toward the inside of the skull [19]. This type is the most common extra-axial brain tumor representing around 30% of the diagnosed primary brain tumors [19]. According the last edition of WHO classification of CNS tumors (2016) [19], meningiomas are classified into three main categories which differ in grade and biological behavior.

The WHO Grade I meningioma is a benign tumor presenting the slowest growing process comparing the other grades [19]. It is the most incident grade and is recognized by the absence of anaplastic features [23]. Due to their slow growth, benign meningiomas may not cause symptoms for years after they start to develop and some people don't present any symptoms where the tumor is discovered accidentally after an MRI or a CT scan realized for a different reason [17].

The WHO Grade II meningioma is an atypical tumor that grows at a faster rate than a benign meningioma [24]. It is characterized by its high ability to invade the adjacent brain tissues, this invasion can reach also the surrounding dura matter and in some cases the skull bone [23], [24]. This grade has a higher risk of recurrence than grade I due do its higher malignancy.

The WHO Grade III meningioma is an anaplastic tumor which grows at a faster rate than benign and atypical meningiomas. Presenting less than 6% of the diagnosed meningiomas, grade III is a rare incident tumor [25]. It is considered as the most malignant grade and the most likely to invade the adjacent brain tissues [23].

In general, the deadliest meningioma tumors are the atypical and anaplastic ones due to their higher risk of recurrence and their aggressive behavior where the rate and the extent of their local spread are often greater than benign subtypes. Thus, and depending on the tumor location, even benign meningioma commonly invades adjacent anatomical structures and can become deadly, if they are not discovered and treated quickly, due to their progressive growth in the skull [25].

Symptoms of a meningioma tumor vary according to its grade, location, and size. They often first appear as headaches and seizures, caused by the increased pressure on the surrounding brain tissue due to the growing mass. Some patient may present also weakness in the arms or legs, or a loss of sensation may occur when a spinal cord meningioma is occurred [17].

When a meningioma is causing symptoms and is growing in size in a way that threat the patient brain, the total surgical removal of the tumor mass is often recommended [25]. Figure 1.6 shows an illustration of a meningioma tumor as well a corresponding MRI image.

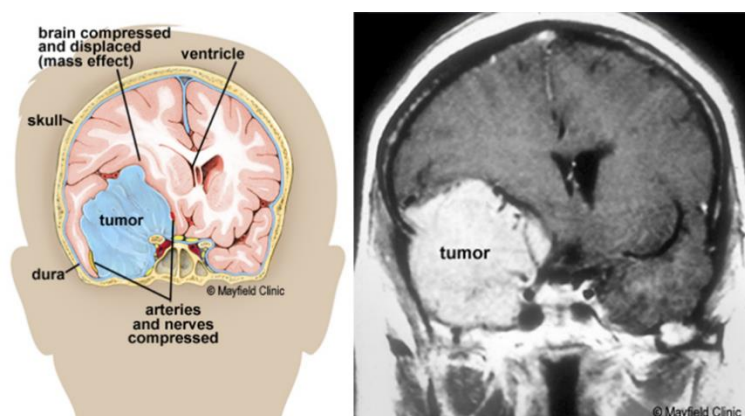


**Figure 1.6:** (right) An illustration showing a meningioma tumor growing and displacing healthy brain tissues. (left) MRI scan image of a sphenoid wing meningioma [17]

### 1.1.4 Glioma

The internal tissue structure of the brain is composed of neurons and glial cells, which provide the structural backbone of the brain and support the function of the neurons and hold them together. Classified as intra-axial brain tumors, glioma tumors arise from glial cells and can develop in any part inside the brain. Glioma is an umbrella term used to describe the different types of glial tumors: astrocytoma, oligodendroglioma, and glioblastoma [17]. Gliomas vary in their aggressiveness, their malignancy, and their histologic features. Some types are relatively benign and present a slow growth and are likely to be curable. Others are extremely malignant and present a fast growth and a very invasive character. These types are more difficult to be treated, and more likely to recur [17]. This group of tumors is the most incident primary brain tumors (>34%) and represents more than 80% of the malignant brain tumors [25].

According to the WHO grading system, Glioma tumors are classified into four different histopathologic grades (I, II, III and IV) depending on their location, their cell growth type, their malignancy and their pathological evaluation [19]. Furthermore, they are classified also into main categories according their grade, low grade, and high grade gliomas.



### 1.1.4.1 Low grade glioma

Low grade glioma is the term used to group grade I and grade II glioma. They include the slow growing tumor types which are considered as less aggressive than higher grades.

Grade I glioma known as pilocytic astrocytoma is a slow growing and relatively a benign tumor. It typically occurs in people who are younger than 25 years old and most commonly in children, where it begins in the cerebellum or brainstem [26].

Grade II glioma include several subtypes including oligodendroglioma and diffuse astrocytoma. This latter is the most common low grade glioma. It is a slow-growing tumor that arises from astrocytes. It typically occurs in young adults and tend to arise in the cerebral hemispheres of the brain [26]. Patients with grade II glioma present generally common symptoms including, seizures, headaches, weakness, speech, and language changes. As its name indicates, diffuse astrocytoma is a diffuse tumor with ill-defined boundaries where small clusters of tumors cell tend to grow and to infiltrate outside the tumor center toward the adjacent healthy tissues [26]. These infiltrated cells overlap with healthy cells which makes the complete removal of the tumor during surgery very difficult. Due to the infiltrative nature of these tumors, they have a very high risk of recurrences and most of the time they evolve into anaplastic tumors with more aggressiveness (grade III or IV). Furthermore, the timing of evolution into higher grades virtually determines the outcomes for the patients [27].

The second common low grade glioma is the oligodendroglioma, it is a relatively rare tumor with less than 4% incidence rate of all primary brain tumors. Arising from oligodendrocytes, it can grow anywhere in the brain, but it is more commonly found in the frontal and temporal lobes. It occurs mostly in adults, although they can occasionally occur in infants and children as well [19].

In a similar way as diffuse astrocytoma, oligodendroglioma grows slowly and tend to infiltrate the nearby healthy areas and often far from the tumor center. In some cases, it can grow rapidly and evolve over time to become more aggressive by transforming to an anaplastic tumor (grade III anaplastic oligodendroglioma) [19].

Usually, the first treatment option for low grade glioma patients is the maximal safe resection surgery. The main goal of such surgery is to remove as much as possible from the tumor mass, while preserving the healthy eloquent brain function areas especially that this tumor can occur adjacently to brain areas that control vision, language or body movement [26]. Safely identify these critical regions and protecting their functions was always a high priority goal for neurosurgeons. In addition to surgery, radiotherapy and chemotherapy may also be used depending on the tumor's size, location, and the extent of surgical removal. However, the response to treatment of a patient with low grade glioma depends on several factors including the tumor's genetic classification, extent rate of surgical resection, patient age, and his general health characteristics. Thus, and since that low grade glioma tumor present an important risk of recurrence, patients benefit from regularly monitoring after surgery for both tumor recurrence and progression to a higher grade tumor [19], [26]

### 1.1.4.2 High grade glioma

The high-grade glioma term or malignant glioma involves both grade III and IV gliomas, and reflect the fact that the management of these two grades is fairly similar. It includes the most aggressive and malignant tumor types characterized by their high mortality.

Grade III is a malignant glioma which includes mainly the anaplastic astrocytoma tumors and the anaplastic oligodendroglioma. This grade has a faster and higher growth index and it is more aggressive than grade I and II. It also invades the adjacent healthy tissues presenting a diffusely infiltrating neoplasm that demonstrates focal or dispersed anaplasia cells [17], [28]. This grade is relatively rare accounting less than 2% of all primary brain tumors [29].

Grade IV glioma, called glioblastoma multiforme and abbreviated as “GBM” is the highest grade of glioma tumors. It is also the most aggressive and malignant form of astrocytoma and considered as a common primary brain tumor accounting in more than 20% [22] and the most common malignant brain tumor accounting in more than 80% of all malignant brain tumors [29].

Several histologic features distinguish glioblastoma from all other grades such as the presence of necrosis (dead cells) zones in the tumor center and the increase of abnormal growth of blood vessels around the tumor mass. Glioblastoma is always a highly invasive and fast growing tumor that spreads quickly to invade the nearby healthy brain tissues. The recurrence of this grade is unavoidable due to its high ability to infiltrate far from the tumor site which make the entirely remove resection of the cancerous areas quite impossible [30]. However, glioblastoma is the deadliest brain tumor subtype having the worst survival rate. Its 5-year survival rate don't exceed 5% while the median survival time of a glioblastoma patient is around 8.1 months [3].

Patients with high grade glioma often present several symptoms related to the increased intracranial pressure, including confusion or change in mental status, seizures, neurologic deficits, headaches, vomiting, double vision [29].

As for treatment, the maximal safe resection surgery is the first line of treatment for both grades III and IV. They are treated by a multidisciplinary team which includes neurosurgeons, neuro-oncologists, and radiation oncologists.

However, the response to treatment of a patient with a high grade glioma is related to several factors and highly depends on the quality of the surgical act to remove as much as possible of the cancerous areas, while always protecting the critical brain function areas. Grade III glioma are likely to progress to grade IV, so patients are regularly monitored for both tumor recurrence and progression to a higher grade, with additional therapies recommended as needed [29].

The primary goal of the treatment process is not only to extend the survival time of the patient, but also to improve the life quality of the patient, by alleviating the neurological symptoms and preserving his cognitive functions [25], [29]. Figure 1.7 shows an illustration of a glioblastoma tumor as well a corresponding MRI image.

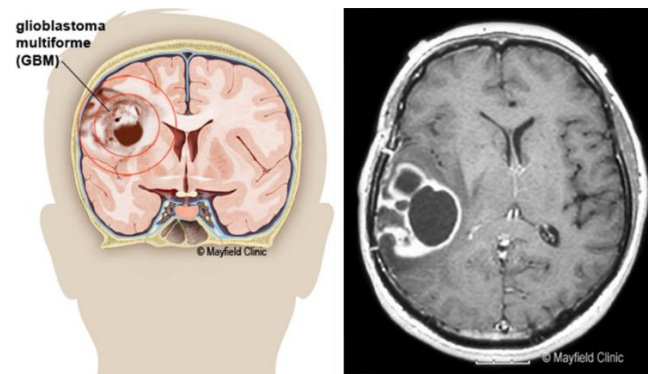


**Figure 1.7:** (left) An illustration showing glioblastoma tumor developing inside the brain tissues. (right) MRI scan image of a glioblastoma tumor in the parietal lobe [17]

### 1.1.5 Metastasis

Metastatic brain tumors develop from cancer cells which have been developed in another organ of the body and that spread to the brain through the blood stream. It can be found as one single tumor in the brain or as multiple tumors [17] throughout the brain and the spinal cord. The most common tumors that metastasize to the brain are lung cancer (50%), breast cancer (15-19%), and skin melanoma (10%) which account for 70–80% of brain metastases [31]. However, brain metastatic tumors are predominant outnumbering primary brain tumors by at least 10 to 1.2 [32] They have also a poor prognosis and high mortality rates, where only 8.1 % of patients survive after 2 years while the 5-year survival rate don't exceed 2.4 % [33].

Metastatic brain tumors are usually discovered when neurological symptoms like headaches, seizures cognitive changes or intracranial bleeding, start to appear in the patient. Some brain metastases may appear many years after the discovery the originating primary cancer while others metastasize and appear so quickly even before the discovery of the originating primary cancer [17].

Metastatic brain tumors patients are treated usually with a combination of surgery, radiation therapy, chemotherapy or immunotherapy if needed in order to treat both the metastatic tumor and the primary cancer. The options of treatment vary depending on the number of brain lesions along with their location, their size and the severity of the originating primary cancer [34]. For patients who presents one to five tumors of brain metastases, the surgery is performed to remove as much as possible of the tumors mass while radiation therapy may involve stereotactic radiosurgery which focuses a high dose of radiation specifically within smaller tumor sites [34].

For patients who presents more than five lesions, a whole brain radiation is added to the common treatment where the goal is not to treat only the visible metastases, but also the microscopic ones that remains too small to be detected. Together, this combination of therapies aims to increase the long-term survival time of the patient and to improve as much as possible his quality of life by addressing specific symptoms and preserving his brain cognitive functions [34].

Figure 1.8 shows an illustration of several metastatic brain tumors as well a corresponding MRI image.

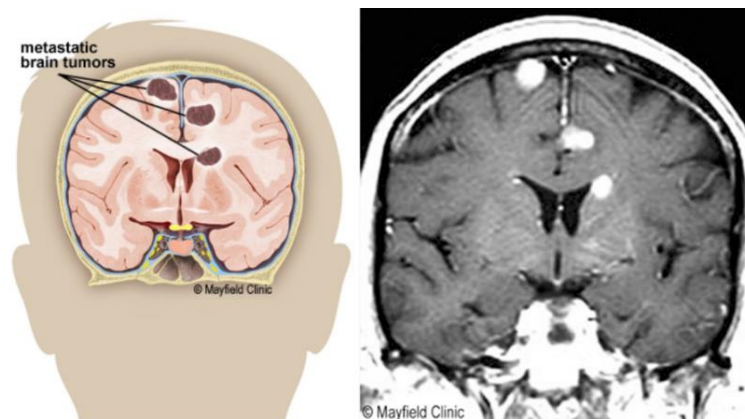


**Figure 1.8:** (left) Illustration of several metastatic brain tumors. (right) MRI scan image of multiple metastatic brain tumors that have spread from a melanoma skin tumor [17]

## 1.2 Brain Tumors management

The suffering journey of a patient with brain tumor starts with several warning signs. These signs appear as symptoms of an abnormal brain functionality. While so many of potential symptoms of brain tumors exists, it is very rare that one patient presents them all [35]. These symptoms vary depending on several facts: the location of the tumor where it develops and grow in the brain, which part of the body the affected zone of the brain controls and how big the tumor mass is [36]. The most two common symptoms of having a brain tumor includes:

- 1) Headaches: The growing process of a brain tumor mass increase the pressure on sensitive nerves and blood vessels, resulting in new headaches. Brain tumors headaches are characterized by a persistent pain, especially in the morning, and tend to persist for more than few days and they are usually accompanied by vomiting, nausea or new neurological symptoms [35], [36].
- 2) Seizures: During its growing, the brain tumor mass can push on nerve cells in the brain which may cause an interference with electrical signals and result in a seizure. Half of patient with brain tumors presents at least one seizure, and sometimes, the seizure is the first appearing symptom with a brain tumor patient [36].

In addition, other symptoms may also occur and could be a warning sign for developing a tumor mass in the brain such as personality or behavioral changes, vision problems, memory loss and confusion, fatigue, and depression.

### 1.2.1 Diagnosis

When several symptoms are combined and presented with the patient, many primary tests and procedures are recommended for him in order to check his general health. These tests include a neurological exam which aim to check mainly, among several functionalities, the mental status of the patient and his memory, the vision, balance capability, coordination, strength and reflexes [37]. In addition, additional tests may be performed such as audiometry, in order to detect hearing loss due to tumors near the cochlear nerve, or an endocrine evaluation test to detect abnormal levels of this hormone in the blood or urine caused by pituitary tumors. Abnormal performance or difficulty in one or more functional

area may provide information about the part of the brain that could be affected by a tumor [37].

### 1.2.1.1 Imaging

Depending on the results of the primary tests realized on the patient after symptoms appearing, and if a brain tumor is suspected, the first step toward a more precise diagnosis is the brain imaging. Imaging remains always as an efficient non-invasive method to positively impact the management of patients with brain tumor. This part of diagnosis is critical to the clinical management of brain tumor patients. Over time, brain imaging techniques were evolving, while nowadays, modern neuroimaging offers several non-invasive techniques and provide the ability to integrate functional, hemodynamic, metabolic, cellular, structural, and genetic information into the assessment process of patients with brain tumors [38]. Nowadays, these imaging techniques are used to diagnose and to identify the tumor grade pre-operatively, to plan and to guide the surgery intra-operatively, and to monitor and assess the treatment response and patient prognosis as well as to understand the effects of treatment on the brain post-operatively. Ongoing research in brain tumor imaging attempts to develop, validate, and implement clinically advanced neuroimaging techniques that can lead to have a more precise diagnosis process. These modern techniques are the major tool for neurosurgeon to establish and to select the most adapted treatment that targets the tumor of each individual patient [38].

The first imaging modality that may be recommended for a brain tumor patient is the Computed Tomography scan (CT-scan). A CT-scan is an imaging technique that uses X-rays beams to produce horizontal or axial images of the brain. It can provide more detailed information about brain tissue structures and spatial information related to injuries or other brain diseases [39]. It is largely used in the potential detection of hydrocephalus and mass effect of brain tumors as well calcification within some brain tumor types such as oligodendroglioma or meningioma [40].

CT-scan may be the first recommended imaging modality for brain tumor patient, but the primary one recommended is Magnetic Resonance Imaging (MRI), which remains as the standard of care imaging technique for neuro-oncologic practice [38]. MRI consists of using a powerful magnetic field, magnetic field gradients and radio waves to generate detailed images of the brain and other cranial structures that are clearer and more detailed than other imaging methods. This technique is a non-invasive technique and do not implement any use of ionizing radiation. Sometimes, it may require an injection of an external agent to enhance the contrast, called gadolinium, which is less likely to cause an allergic reaction than iodinated contrast material [37]. MRI have the advantage to offer a superior soft tissue contrast comparing with other cross-sectional imaging techniques allowing a better visualization of subtly infiltrated or disrupted parenchymal architecture. The primary use of conventional MRI in the initial brain tumor evaluation is to provide anatomical and structural information of the brain, including the localization of the tumor mass in the brain, the extent of tissue involvement and resultant mass effect upon the brain, ventricular system and large surrounding vasculature features visualization [38]. Through MRI, different image contrast approaches can be applied through different acquisition protocols in order to provide additional and complementary information to the diagnosis process. The most commonly used contrast approaches are: spin-echo T1-weighted image, T2-weighted

image, and proton density-weighted image. The intensity of the tumor zone appears different in each approach, while it is low in a T1-weighted image, it appears strong in T2-weighted image and shows an intermediate intensity when using proton-density weighted approach. Furthermore, some intravenous injected contrast agent, such as gadolinium which is the most widely used, have the ability to increase tissue contrast by accentuating the areas where contrast agents have leaked out of the blood brain barrier into the interstitial tissues which results in parenchymal enhancement [38].

However, relying on the conventional MRI enhanced contrast images is not sufficient to complete the necessary diagnosis report elements. Alone, it is not able to provide physiological information about the tumor or distinguish its different grades. Therefore, several advanced specialized MRI scan methods have been developed over time, including diffusion weighted MRI, perfusion MRI, functional MRI, and Magnetic Resonance Spectroscopy (MRS). Each one has its specific clinical use and provide additional information to the diagnosis process of a brain tumor.

Diffusion Weighted MRI Imaging (DWI) provides an overview on the diffusion of water molecules in brain tissues and offers a better differentiation of tumor borders than conventional MRI images. Through this technique, the apparent diffusion coefficient (ADC) could be calculated. The derived values from DWI images of this coefficient have been shown to be decreased in highly cellular tumors such as CNS lymphoma, medulloblastoma, and high-grade glioma [40]. This specialized technique has become a necessary routine sequence in the evaluation of brain vascular stroke but also offers additional value in the evaluation of brain tumors.

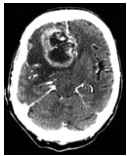
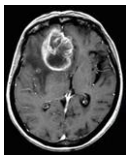
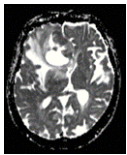
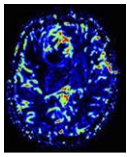
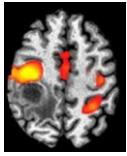
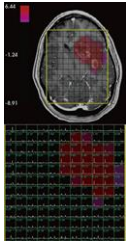
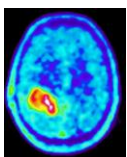
Perfusion MRI technique provides complementary information about the blood flow in brain tumors and its surrounding tissues and offers a better identification of microvasculature features than conventional MRI. It can be performed through two methods, with or without using an exogenous contrast agent. Contrast agent injection provides a better sensitivity and images with spatial resolution images, and therefore it is more widely used in clinical applications. However, arterial spin-labelling methods provide an ability to measure the cerebral blood flow without using an exogenous contrast agent [41].

Functional MRI (fMRI) relies on the relative alteration in the blood oxygenation level in order to evaluate and to investigate the brain activity change. It produces images of blood flow to certain areas of the brain and mainly used to determine and to locate which parts of the brain are handling critical functions. This technique is used before and after the surgery to identify these important parts of the brain such language, memory and movement control areas of patient being considered for brain surgery [37].

The MRS provides insight into the biochemical changes in the brain, especially in the tumor presence area. It compares the chemical composition of normal brain tissue with abnormal tumor tissue and analyses several different metabolites that can be measured to differentiate between tumor types such as amino acids, lipids, lactate and alanine [17]. MRS technique can be used to detect tissue changes in stroke, epilepsy, and seizure disorders areas and also to determine the tumor type and its aggressiveness, and to distinguish between tumor recurrence and radiation necrosis.

Sometimes other imaging tests are recommended to complement the diagnosis elements, such as Positron emission tomography (PET) imaging which highlight the high metabolic areas of the brain and commonly used to find cancer in other parts of the body if it's

suspected that the brain tumor may be a result of a metastasized cancer that has spread from another organ [37]. The combination of several imaging methods is necessary to help the neurosurgeon to better evaluate the tumor state and to adapt the suitable treatment plan following the diagnosis process. Table 1.1 present the described conventional imaging techniques used for brain tumor diagnosis and summarize the clinical use for each.

Imaging modality		Clinical use
	<b>CT scan</b>	Localizing the tumor and defining its dimensions; Provide information about calcifications, mass effect, hydrocephalus [42].
	<b>Conventional structural MRI</b>	Localizing the tumor and surrounding structures; diagnosis of supra- and subtentorial tumors; diagnosis of extra- and intra-axial tumors; pre-surgical planning with 3D imaging [42]
	<b>Diffusion MRI</b>	Assessing the progression and regression of white matter tracts caused by tumor growth or resection; Establishing spatial relationships between tumor border and white matter [42].
	<b>Perfusion MRI</b>	Obtaining information about the vascularity and the blood flow in the tumor region and the surrounding tissue [42]
	<b>Functional MRI</b>	Neurosurgical planning and neurologic risk assessment by localizing the cortical regions that control language, motor, and memory functions [42]
	<b>MRS</b>	Obtaining biochemical and metabolic information about the tumor, determining tumor type and grade by assessing the cellular contents, differentiating tumor from radiation necrosis [42]
	<b>PET</b>	Pre-operative functional mapping, assessing the highly metabolic areas within the tumor, differentiating between tumor recurrence and radiation necrosis, functional localization of cortical regions, predicting patient survival and prognosis [42]

**Table 1.1:** Summary of the imaging modalities used for brain tumors diagnosis as well as the clinical use for each modality

### 1.2.1.2 Biopsy

When the different imaging methods cannot provide and confirm the diagnosis, a biopsy may be recommended in order to determine the exact tumor type and its histologic features. Biopsy is a procedure that consists to remove a small number of cells from the tumor location determined through imaging modalities in order to be analyzed. There are generally two types of biopsies, the first one, called open biopsy, is realized when the tumor mass is close to the skull surface, where an incision is made in the skull and a small amount of tissue near the surface of the brain is removed [17]. The second one is called the needle biopsy and it is used when the tumor mass is deep in the brain. To reach this deep area, a small burr hole is drilled in the skull so that a hollow needle can be inserted in order to reach the tumor region and to extract a sample of tissue. During this biopsy method, a stereotactic frame is used to guide the needle into the brain and to reach precisely the abnormal lesion or tumor [39]. This method is illustrated in figure 1.9.

After the biopsy extraction, the tissue sample will be examined under a microscope, after a special staining, by an expert neuropathologist who performs a variety of tests to determine the tumor type and its grade and to establish a definite diagnosis. This examination is called the histopathological analysis; it consists of the study of the signs of the disease using microscopic examination of the sample after being treated through several chemical fixation processes. This examination permits to visualize the different tissue components after being stained with one or several dyes. The staining process allows to reveal cellular components and to provide contrast to the microscopic image of the extracted sample [43]. Several types of stains exist, each one is specific to highlight a different tissue structure. The most widely used stains is the combination of Hematoxylin and Eosin (H&E) staining, where the first one stains the cells nuclei in blue and the second stains the connective tissue and the cytoplasm in pink. It's also considered as the standard staining for histopathological analysis of human tissues due to its low cost and its ability to highlight a large panel of cytoplasmic, nuclear, and extracellular matrix structures [44]. However, the histopathological analysis process takes between 5 and 7 days before providing the final definite diagnosis results [17].



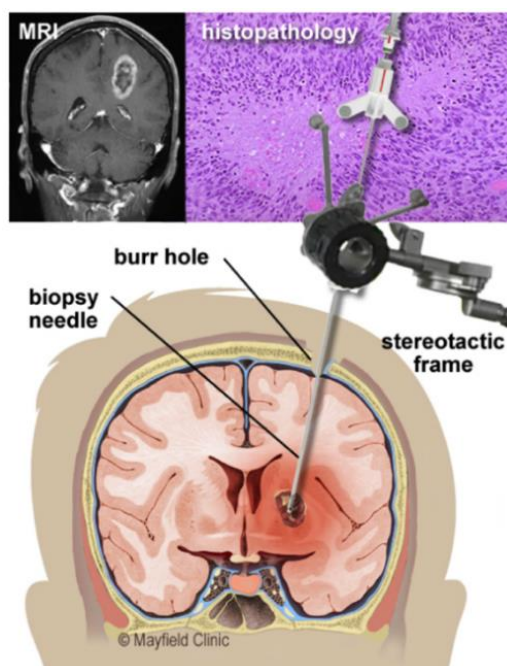


**Figure 1.9:** Top on the left: An MRI image of a brain tumor. Top on the right: Image of an H&E stained tumor biopsy tissue sample. Bottom: Illustration of a needle biopsy operation [17]

## 1.2.2 Therapy

Once all diagnosis elements are acquired, including primary neurological exams, imaging results and neuropathologist biopsy report, a multidisciplinary team consisting of neurosurgeons, neuro-oncologists and radiation oncologists discuss and establish the plan of action for the treatment.

Treatment process is individualized for each patient and depends on several factors such as tumor type, grade, malignancy, location as well as the overall health of the patient. The classical treatment process of a brain tumor is mainly based on a resection surgery to remove the tumor mass, followed at most of the time by post-surgery therapy methods such as radiotherapy and chemotherapy. For some tumor types, like brain stem glioma, just one method of treatment can be recommended, but for the majority of the other types a combination of several therapy methods is required [42].

### 1.2.2.1 Surgery

Surgery is considered as the primary treatment for brain tumors that can be removed without causing severe damage. The surgical operation has multiple goals which includes reducing the effects of the symptoms and improving the quality of life of the patient by eliminating the intracranial pressure caused by the tumor mass. It provides also the access for implantation of internal chemotherapy agents and to deliver intra-surgical treatments [45]. Thus, the primary and the most important goal of the surgical act is the removal of all or as much as possible of the tumor mass while preserving the critical functional brain areas without causing long-term neurological damage, which is called the maximal safe resection. However, depending on the size of the tumor mass, its location, malignancy and other factors, total removal may not always be possible. In some cases, where the tumor is benign or have a small size and easy to be separated from surrounding tissue, the complete

surgical removal remains possible. In other cases, when the tumor is located near sensitive functional areas or is malignant and presenting infiltrative features, such as high grade gliomas, it can't be separated from surrounding tissues and the surgery act remains risky [37]. Therefore, the success of the surgery reveals in the accurate delimitation of the tumor mass margins. However, tumor margins are not well defined as infiltrated cancerous cells diffuse outside the tumor center zone into adjacent healthy functional areas. This cell diffusion leads to the emergence of infiltrating zones, which overlap with the healthy zones with no visual distinguishing appearance during the surgery, thus making their removal very difficult [25]. This inability to fully visualize the tumor margins lead to a non-complete surgical cancerous zones removal which causes a faster recurrence of the tumor. Similarly, unnecessary removal of healthy functional brain tissues that does not contain cancer cells can lead to major neurological deficits that affects the quality of life of the patient. To this end, the challenge in malignant brain tumor surgery remains to reach a maximal safe removal of the cancerous zones while monitoring the oncological-functional balance to preserve brain functional areas.

To achieve a good balance, neurosurgeons use several techniques in order to evaluate tumor margins and functional areas before and during surgery. The generated functional MRI and Diffuse MRI pre-surgery diagnosis images provide important functional information and helps to show what are the functions of the near-tumor brain tissues that re responsible for [46]. However, these images do not always provide the needed precision to avoid these critical functional areas of the brain during surgery due the brain shift during the craniotomy. Therefore, intraoperative brain functional mapping became an important used technique to improve the safety and the effectiveness of surgery. It helps the neurosurgeon identifying the tumor margins and to differentiate between tumor, swelling (edema), and normal tissues, and to locate the precise areas of the eloquent brain functional areas. Over time, several intra-operative brain mapping techniques has been developed to assess and to guide the surgery, including direct cortical stimulation (electro-stimulated surgery), intra-operative MRI, intra-operative ultrasound imaging [45].

During a surgery that uses direct cortical stimulation, called electro-stimulated surgery, the surgeon uses a specific probe to deliver a weak electrical current into the brain and delicately stimulates a specific area. The result is a response from the body, such as a visible movement of the corresponding body part. This technique may be employed during surgery to help the neurosurgeon identifying the important functional areas. Direct cortical stimulation is used during surgery in order to map the cortical and subcortical function areas during and to adjust it in order to insure to successfully identify and preserve cortical areas responsible for language and minimize damage to motor function [47]. This technique has been shown to improve the complete tumor removal and to decrease the percentage of glioma patients which experience deficits in motor ability after surgery [47]. It has been shown to increase the percentage of patients who regained their baseline function within the first 90 days after surgery [48].

Despite its complexity and its highly cost, the intra-operative MRI technique is reliable, it helps the neurosurgeon to obtain anatomical and functional information, about tumor margins and distinguish between active, normal brain, and non-active tumor necrosis zones. It also helps him to adapt his surgical trajectory to reach the tumor region and to attend more efficient option by enhancing the contrast of intra-cranial lesions. Intra-operative

functional MRI can be an alternative to direct cortical stimulation where some studies has been shown that motor and sensory areas identified with intra-operative functional MRI are very similar to locations identified with direct cortical stimulation [49].

The intra-operative ultrasound imaging is used in to help the neurosurgeon determining the depth of the tumor in the brain and its diameter. It consists to send ultrasonic wave pulses into the brain, which then reflect back to the detector. The duration between sending and capturing the waves is measured through a computer measures, and thus deducting the depth of the reflective region. These ultrasound waves can also highlight motion features in the brain such as blood flow. This intra-operative imaging technique can make it easier for the surgeon to locate the margins of the tumor so that more extensive tumor removal can be achieved. It helps also to distinguish between tumor, necrosis, cysts, edema, and normal brain [50].

### 1.2.2.2 Radiation Therapy

As mentioned previously, brain tumor management consist in the most cases of a combination of therapy methods including surgical removal and two post-surgery methods: radiation therapy and chemotherapy.

Post-surgery radiation therapy consists of using ionizing radiation, such as X-rays or protons beams, to kill or to control the surgery residual tumor cells growth, which aid to prevent tumor recurrence after surgery. These radiation beam have the ability to raise direct damage to the DNA of cancerous cells, leading to cellular death [51]. Three primary techniques exist to deliver the radiation therapy beams into the patient head, external, internal, and stereotactic.

The External Beam Radiation Therapy (EBRT) is considered as the conventional radiation therapy method for brain tumors. Illustrated in figure 1.10 (a), this method involves radiation beams directing from outside the head into the tumor region. The high-energy radiation beams are produced through a linear accelerator, and have the ability to penetrate the skull and reach the internal tissues in order to deliver the radiation dose directly to the tumor region [52].

Illustrated in figure 1.10 (a), Stereotactic radiation therapy (SRT) involves the use if thin focused radiation beams to treat brain tumors. SRT uses imaging techniques, including CT scans or MRI and special computerized planning to precisely focus a high dose of radiation on the brain tumor, while preserving normal healthy surrounding tissues. The used focused beams allow radiation to be delivered in deep areas of the brain or spinal cord that might be considered inoperable, and can be delivered to tumors having one and one-half inches in diameter or smaller [52].

Internal Radiation Therapy (IRT), called brachytherapy, is the delivery of radiation therapy by putting radioactive material, called “implants” or “seeds.” directly into or near the brain tumor. While standard radiation ray beams irradiate the tumor from outside the body, IRT attacks the tumor from the inside.

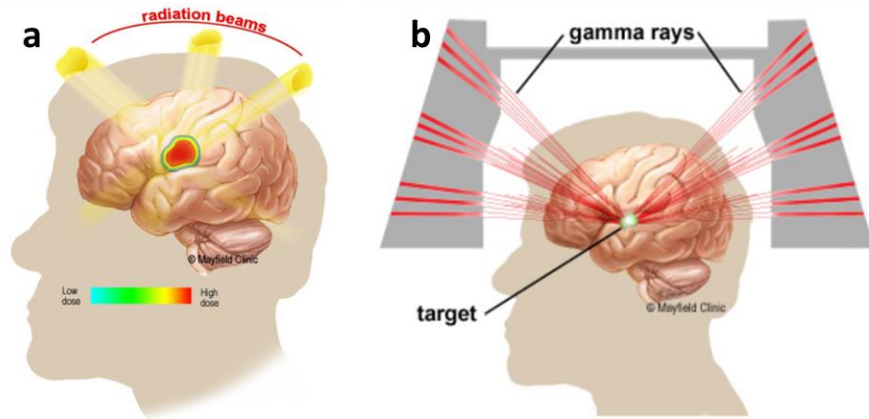


**Figure 1.10:** (a) illustration on an EBRT where the beams are directed to the brain from numerous angles and intersect at the tumor to deliver their high dose. The red ring shows the maximum dose and each outer ring represents lower and lower doses. (b) illustration of a SRT showing low-dose beams of radiation that intersect at the tumor to produce a high dose while minimizing exposure to nearby healthy brain [17]

### 1.2.2.3 Chemotherapy

Chemotherapy is a treatment method that consists of using toxic drugs to kill cancer cells in the patient body. These drugs have the ability to circulate in the blood toward the tumor location in order to kill cancer cells as well as the ability to eliminate cancerous cells in sites within big distances from the original cancer location. As a result, chemotherapy is considered as a systemic treatment [53].

Drugs used in chemotherapy treatment can be taken intravenously (injected through a vein) or orally in a pill form. Many types of chemotherapy drugs are available and may be used depending on the type of cancer but the most commonly used drug in brain tumors treatment is temozolomide (Temodar), which is taken orally as a pill [37]. Brain tumors treatment through chemotherapy is more complicated than treating tumors elsewhere in the body due the presence of a natural defense system called the blood-brain barrier (BBB) that protects the brain from external foreign substances. The BBB prevents these foreign substances, such as drugs, from passing from the blood into brain tissues. For this reason, a sufficient quantity of drug should be used in order to be effective in treating brain tumors, and to be able to surpass the BBB. However, even if the drug does penetrate the BBB, not all brain tumor types are sensitive to it or could respond to chemotherapy. Actively dividing cells are the most vulnerable to chemotherapy while most tumor cells and some normal cells fall into this category [53].

Chemotherapy can cause multiple side effects, depending on the type and the dose of the delivered drug, such as nausea, vomiting and hair loss. Determining the brain tumor cells type through the biopsy extraction can help the treatment team to decide if recommended chemotherapy will be helpful for the patient or if it will severe the side effects that affects his overall health [37].

### 1.3 Intraoperative optical imaging modalities

In the previous section, the different actually used conventional brain imaging modalities were presented as well as their advantages and their clinical use, before, during and after surgery.

These imaging modalities has become one of the most relied-upon tools in healthcare for diagnosis and treatment of patient with brain tumors. The evolution over time of these techniques, starting from the discovery of X-ray imaging to ultrasound imaging and toward magnetic resonance imaging and radio-isotopic imaging has led to revolutionary improvements in the quality of healthcare available today for patients. However, these presented techniques are largely focused on structural and anatomical imaging at the tissue or organ levels and their provided information did not reach yet the reliability and the precision of those provided by the standard histopathological post-surgery analysis. They have several limitations that prevents their attribution as sole standard techniques for brain tumor management. These techniques suffer from harmful effects of their imaging based elements such as ionizing radiations in the case of x-ray imaging and radioactivity in the case of radio-isotopic imaging and their unsuitability for young patients [54]. Furthermore, MRI modalities cannot provide specific chemical or dynamic information about the changes that occurs in real time (response to a treatment or a stimulus). Indeed, the intra-operative ultrasound imaging is not able to provide a resolution less than millimeters as well as the inability of these mentioned techniques to distinguish accurately and with high reliability between a benign and a malignant tumor.

To face these deficiencies, there was an insistent and a clear need to extend the imaging limits of intraoperative techniques toward cellular levels and to develop novel imaging tools for cancer detection at early stages, screening, diagnosis, and image-guided treatment of brain tumors.

Optical imaging overcomes many of these deficiencies, it is an emerging field that permits high-resolution and cross-sectional imaging of biological specimens. Optical imaging techniques are based on highlighting an optical property of a biological specimen when it is irradiated by light, whether a cell, a tissue, or an organ, to obtain a representative optical image. This light-matter interaction, responsible of the optical property variation, could be reflection, absorption, scattering or fluorescence. Therefore, the ability of laser beams, particularly in Near Infra-Red (NIR) wavelength range, to penetrate in biological specimens deeper than conventional light sources [54], have supported their use for optical imaging. Indeed, and by using a minimally invasive fiber-based endoscope system, the laser beam can reach many internal organs or tissue sites in order to be imaged optically [54].

Optical imaging techniques have superior advantages comparing to other conventional imaging techniques described in the previous section, they do not present any harmful side effects due the use of a non-ionizing light source. They are able to provide images with high resolution (less than 1  $\mu\text{m}$ ) which give it the ability to image objects from size scale of 100 nm to macroscopic objects [54]. Additionally, these techniques are particular to provide information on cellular processes, molecular changes, and tissue chemical composition by spectrally resolved and dynamic imaging. They are also suitable also to perform multidimensional imaging and to be combined to other imaging modalities such as ultrasound imaging. Indeed, optical imaging setups have the advantage of requiring a

minimal space in the operating room due to their relatively small size, as well as a high flexibility to be handheld.

The optical imaging domain is very large and rich, whether in term of the number of existed imaging modalities or in term of the large range of its application fields. It is also a domain with intense research worldwide to develop new methods of optical imaging, to improve the existing ones, and to miniaturize the used instruments, especially those used for clinical in-vivo imaging.

Several optical imaging techniques, dedicated to real time imaging, has been developed over time to respond to the brain surgery needs and to fill the lack of the currently used conventional imaging techniques. The three main developed methods to encompass this issue and that have been demonstrated and tested intraoperatively in brain surgery are the optical coherence tomography imaging, Raman spectroscopy imaging and fluorescence imaging.

### 1.3.1 Optical coherence tomography

Optical Coherence Tomography (OCT) is one of the most rapidly developed optical imaging technique in the last few decades and is rapidly growing in its applications. It has been massively successful in ophthalmology [54], [55] where it became a routine tool for retinal diagnostics, cornea and glaucoma surgery. Besides ophthalmology, several clinical applications have been demonstrated through the last decades and are actually widely applied in a diverse range of areas such as cardiology, dermatology and dentistry [55]–[57]. OCT is a reflection based imaging technique particularly suited for a highly scattering environment. It is analogous to ultrasound imaging, except that it relies on the detection of the back-reflected or back-scattered light by the tissue site. The scattered light, arising from a particular site in the tissue, is selected relying on the interference between the back-scattered detected signal and a reference beam. In fact, the interference between the propagating wavefronts of two light beams occurs when both wavefronts have a well-defined coherence (phase relation) within the overlapping site. This well-defined coherence of a wavefront from a source is maintained within a distance called coherence length. Therefore, if both, the reference beam and the back-scattered one, are derived from the same light source, a well-defined interference pattern will be occurred if their path length difference is within the coherence length [54]. This approach is illustrated in figure 1.11, where the displacement of the reference beam, ensured by an axial scan of a reference mirror, produce the path length difference between the reflected light from the reference mirror and the back-scattered light from the scattering site in the tissue.

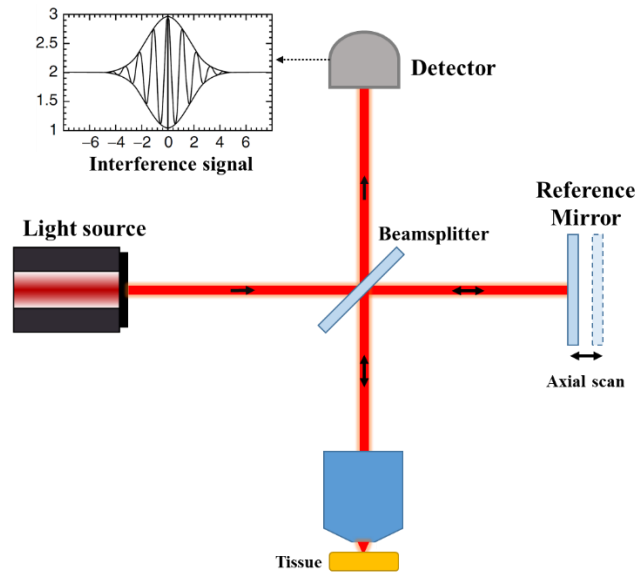


**Figure 1.11:** illustration of a basic OCT imaging system showing the interference signal as a function of the reference mirror displacement when a low-coherence light source is used

When a fully coherent light source is used, the interference between the reference beam and the back-scattered beam can be preserved over a large path-length difference induced by the reference mirror displacement. Therefore, the back-scattering light from a specific depth in the sample cannot be selected.

However, when a low-coherence light source is used, the interference pattern between the reference beam and the back-scattered beam is achieved when their path difference is within the coherence length. In a 3D scattering site, at any defined position of the reference mirror, only a given depth range of back-scattered light will interfere [54]. Therefore, by ensuring a scanning movement of the reference mirror, the depth discrimination could be achieved. The interference patterns hold the information about the refractive index variation of the tissue, which therefore provides the contrast of the optical image.

Through this low-coherence interferometry technique, OCT is able to perform cross sectional high-speed 3D imaging with micrometer-scale resolution [58]. Current OCT systems have generally resolutions of 2–20  $\mu\text{m}$  with a high depth penetration, compared to 110  $\mu\text{m}$  for high-frequency ultrasound imaging [54]. This technique is suitable to perform real-time imaging and can be integrated within a fiber-based endoscope. It is a fully non-invasive imaging technique with no need to use any external stains or dyes.

In the brain and other neural tissue imaging, and through the development of high speed and ultrahigh resolution OCT imaging systems [59]–[61], OCT has been demonstrated as a promising real-time neurosurgery guidance tool due to its ability to reveal fast dynamics and cellular features of the brain. Thus, OCT imaging is able to highlight fine structural details of brain tissues such as brain nuclei, lesion, fiber tracks, and brain blood vessels simultaneously in real-time and to detect important tissue landmarks for neurosurgery guidance [62]. In addition, novel functional OCT imaging approaches have been shown to reveal the cerebral microvasculature, to measure blood oxygenation, and to map the orientation of nerve fiber tracts [58].

OCT imaging technique has been successfully used in intraoperative guidance for brain tumor resection surgery, vascular neurosurgery, and spinal cord surgery and even in other neurosurgical interventions such as deep brain stimulation therapy [62]–[64].

The first intraoperative use of OCT in neurosurgery was reported by A. Giese team in 2006 [65]. Their system, presented in figure 1.12 b, was combined with a neurosurgical operating microscope and integrated with a commercially available neuro-navigation system which permits to track the field of view and trajectory of the microscope as well as the position of the incident laser beam relative to pre-surgery MRI images [65]. They demonstrated the application of OCT imaging to the intraoperative detection of residual tumor and surgery guidance during glioblastoma and other glioma tumors resection [66]. Later on, they demonstrated a potential application of OCT imaging in experimental neuro-endoscopy where they developed their system and integrate it into a fiber-based endoscope [67] (figure 1.12 a).

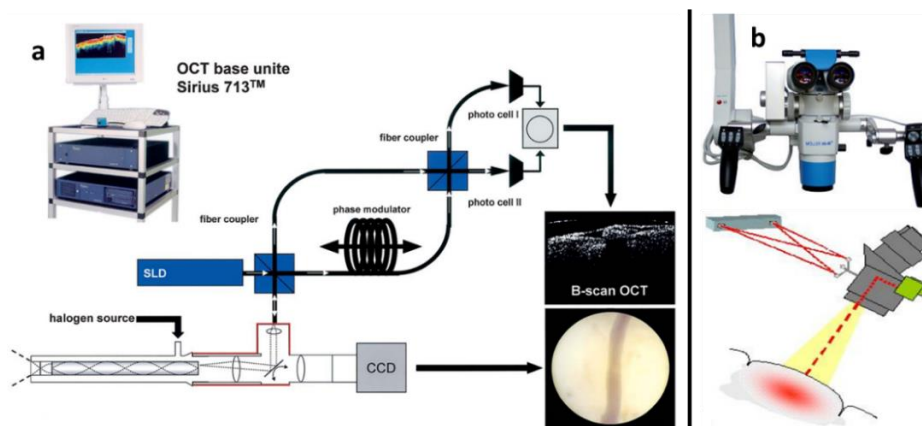


**Figure 1.12:** (a) An OCT integrated fiber-endoscope dedicated for neuroimaging developed by A. Giese team in Germany [69] which implements GRIN rod endoscope head and a scan ensured via a galvo scanner. (b) A spectra domain OCT imaging system combined with a neurosurgical operating microscope and integrated with a commercially available neuro-navigation system presented by A. Giese et al. [65]

Another team performed an intraoperative clinical diagnostic assessment of temporal chronic epileptic parenchyma, meningiomas, low and high-grade gliomas, and choroid plexus papilloma using a full field OCT imaging system [68]. Through this system, they managed to obtain a clear clinical identification of several tumoral and non-tumoral tissue features such as neurons subpopulation, myelin fibers, micro-calcification, microcysts and blood vessels [68]. Moreover, the combination of an OCT imaging system with other neurosurgery guidance tools such as intraoperative-MRI imaging, surgical microscope and automated neuro-navigation system allows a continuous analysis of the resection cavity and provides additional guidance information to the neurosurgeon [65], [66], [69].

Despite all the advantages of the OCT imaging technique, it still suffers from some important weakness factors, such as the low resolution that can be obtained and especially the depth resolution, comparing with other optical imaging modalities, which is considered as insufficient for tumor margin identification [70]. Another disadvantage is its low frame rate due to the slow scanning process used to acquire 3D images, while the respiratory and arterial cycle can induce movement of several millimeters which will result in image



distortion due to the displacement of the region of interest [71]. Adding to that OCT imaging cannot provide any chemical or metabolic information on the imaged tissue which reduces the reliability of establishing a precise diagnosis on the examined region.

### 1.3.2 Raman spectroscopy

Raman spectroscopy is a spectroscopic technique that is based on the inelastic scattering of photons, known as Raman scattering effect of light with matter, which was discovered and reported for the first time by C.V Raman in 1928. Since its discovery, Raman scattering has been widely adopted as a molecular probing tool in the fields of biology and chemistry [72]. When a sample is irradiated by a monochromatic light beam, this incident light undergoes scattering by interacting with molecules that constitute this sample. The majority of the scattered photons, called Rayleigh scattered photons, maintain the same energy as the incident ones. However, some fraction undergoes an energy shift resulting in a wavelength and amplitude change of the scattered photons which involves an energy transfer between the incident photons and the molecules [73]. The detected Raman scattered photons may undergo on a gain of energy (loss of wavelength), where the energy of the scattered photons is higher than the incident ones, called anti-Stokes line, or may undergo on a loss of energy (gain of wavelength), called Stokes line. In general, Stokes lines photons are the one used for the spectroscopic analysis. This energy shift is specific to molecular vibration of each molecule type where each type carries a specific Raman signature, which highly depends on its chemical structure [73]. These signatures provide information about the vibrational modes of the molecules presented in a material site. Thus, it is possible to analyze the molecular composition of a material by analyzing the Raman spectrum of the detected Raman scattered light [72].

Since that Raman scattered signal is too weak compared with the Rayleigh one, several complementary methods have been developed based on Raman effect, to improve the signal-to-noise ratio of the standard Raman spectroscopy, such as Surface Enhanced Raman Spectroscopy (SERS), Spatially Offset Raman Spectroscopy (SORS), Stimulated Raman Scattering (SRS) and Coherent Anti-Stokes Raman scattering (CARS) spectroscopy. Each method has a complementary advantage and improves the standard Raman spectroscopy technique, such as enhancing significantly the detected Raman signal (SERS and SRS), allowing to image deeper in the tissue within the area of interest (SORS) and reducing the background endogenous fluorescence signal (CARS) [74].

In brain tissue characterization, Raman spectroscopy have the ability to provide fast and non-destructive tissue molecular characterization *in vivo* or *in vitro* for biopsy, margin assessment, or for laboratory use. Through the spectroscopic information arising from several Raman active functional molecules in brain tissues, such as nucleic acids, proteins, lipids and carbohydrates, Raman spectroscopy is able to evaluate these molecules and to detect the chemical composition of brain tissues or to detect the changes in molecular structure between diseased and healthy tissues [74]. Although, most of reported Raman spectroscopy studies are exploratory, where *in vitro* experimental studies have shown that this technique can be useful and be relied on to discriminate healthy brain tissue from tissue with infiltrating cancer cells and solid cancerous masses. It has been demonstrated as a promising tool to realize real-time brain biopsy and an efficient tool to detect human dense cancer cells region *in situ* during surgery with a high sensitivity and specificity [75].

These abilities render Raman spectroscopy technique as a promising investigative and diagnostic tool for neurosurgery. Furthermore, this technique has the potential to be an important modality for intraoperative tissue evaluation during surgical resection and could be integrated or used in combination with other intraoperative imaging modalities such as MRI or ultrasonography to improve the in-depth intraoperative characterization of residual tumors [75].

In the published literature, the research group of F. Leblond and K. Petrecca has reported taking Raman spectroscopy into the neurosurgical site where they used a handheld contact Raman spectroscopy probe for intraoperative brain cancer margins identification. Through their studies, they managed to detect and to differentiate low grade from high grade glioma in vivo during surgery, and to detect distant diffused cancer cells within the surgical cavity and to distinguish brain tissues with diffused cancer cells from healthy ones with a high sensitivity and specificity [76], [77].

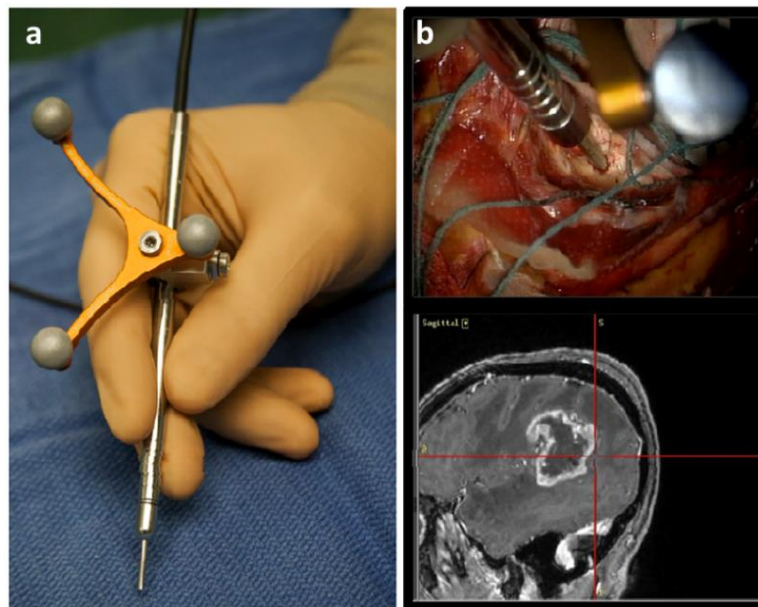


**Figure 1.13:** (a) Intraoperative Raman spectroscopy handheld probe developed by F. Leblond and K. Petrecca team. (b) Illustration of the probe being used intraoperatively, with the attached neuro-navigation tracking system showing the location of the tip of the probe (cross hairs) on the pre-surgery MRI image [78]

Shown in figure 1.13, their probe is coupled with a neuro-navigation system which allows the surgeon to navigate in the brain with the instrument, using the spatially-registered pre-surgery MRI images as a reference [78]. Their work revealed to the foundation of a medical device company (ODS medical) in order to push the limits of their system and to commercialize their reported developed probe [79].

The applicability of Raman spectroscopy to neurosurgery continues to evolve as its effectiveness in differentiation between the different cancerous brain tissue types. Despite the several advantages of this technique and its important complementary information that is able to provide, Raman spectroscopy suffers from several limitations. This imaging technique is only relevant for the surface close tissue regions and can't reach deep regions [80]. The very weak Raman signal and the low scattering efficiency leads to a long

acquisition time and makes the video rate imaging almost impossible. Furthermore, it suffers also from the interfered autofluorescence signal which is stronger than the Raman one which make its elimination challenging. Adding to, a sophisticated data analysis is often necessary [81].

For these reasons, much future improvement and development in both the imaging system and contrast agents will be needed before Raman spectroscopy imaging can become a reliable and powerful clinical reality.

## 1.4 Fluorescence imaging

### 1.4.1 Fluorescence

Fluorescence corresponds to the emission of light by a molecule that has absorbed light or other electromagnetic radiation. When the incident photon is absorbed by the molecule, its energy state passes from the ground state to another excitation state. Then, it undergoes into several non-radiative transitions before that it goes back to its ground state emitting a photon, within an interval of few nanoseconds, that have a lower energy (higher wavelength) than the incident one. This process of transition into an excited energy state of the molecule is described through the Jablonski diagram, illustrated in figure 1.14.

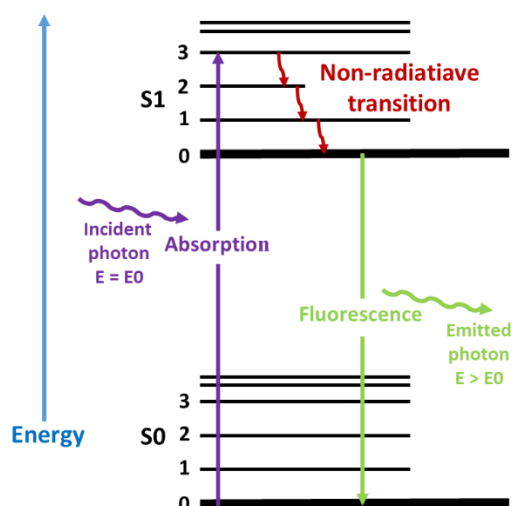


**Figure 1.14:** Jablonski diagram. After an electron absorbs a high-energy photon the system is excited electronically and vibrationally. The system relaxes vibrationally, and eventually fluoresces at a longer wavelength.

The fluorescent molecules, called "fluorophores" or "fluorochromes", are characterized by several specific parameters such as:

- 1) Wavelength of the excitation photon that are able to absorb and the emission wavelength of the photon that they emit.

- 2) Lifetime of their excitation state, called fluorescence lifetime which refers to the average time that the molecule spends in its excited state before emitting the fluorescent photon.
- 3) Efficiency of their fluorescence emission referring to the number of photons emitted relative to the number of photons absorbed.

In the last decades, fluorescence has been emerged as a new contrast for bioimaging. Therefore, the fluorescence emission will provide the image contrast of an imaged specimen that contains fluorescent molecules. However, two types of fluorophores have been explored to provide this contrast: exogenous fluorophores and endogenous fluorophores.

Exogenous fluorophores are fluorescent molecules that are added artificially to label specific structures in the specimen, where their distribution will become evident after light excitation. They can be excited generally in the visible or NIR wavelengths, where their emission spectra are perfectly identifiable and intense.

The second type is the Endogenous fluorescence also called auto-fluorescence, corresponds to the fluorescence emission of molecules that are naturally present in biological tissues. The majority of cellular autofluorescence molecules are mainly located in mitochondria, lysosomes, extracellular matrix as well as a variety of amino acids, where a large variety of endogenous fluorophores are known [82], [83]. Presented in figure 1.15, each fluorophore is specified by its absorption spectra, corresponding to the most efficient wavelength to excite this fluorophore, and by its emission spectra, corresponding to the wavelengths of its emitted fluorescence light [83].

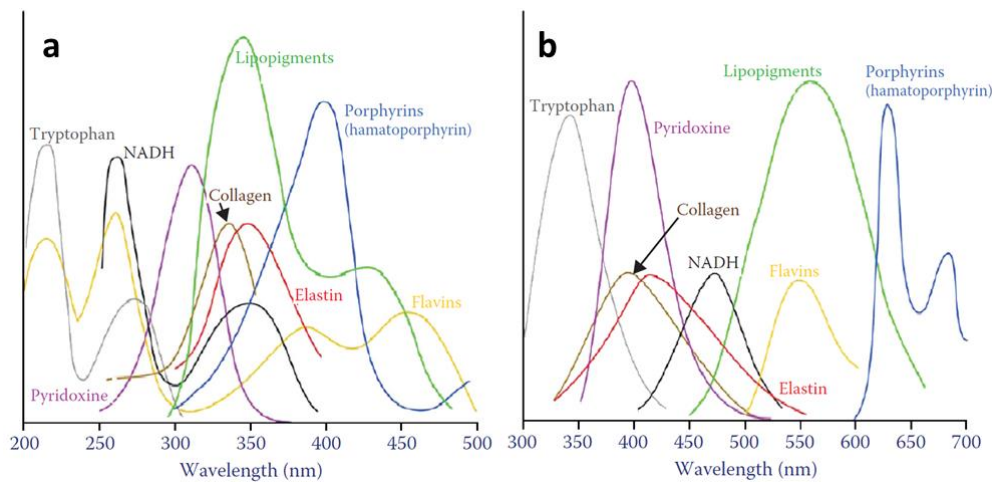


**Figure 1.15:** Spectroscopic characteristics of the main endogenous fluorophores presented in biological tissues where their excitation spectra (a) and their emission spectra (b) are showed [83]

Therefore, endogenous fluorescence imaging has been emerged as a non-invasive imaging technique that could be used *in vivo* without the introduction of any markers or staining agents, nor the prior preparation of samples.

Through time, the use of the endogenous fluorescence has increased to investigate brain tissues [82], [84] in order to discriminate between tumoral, infiltrating and healthy tissues [85]. It is considered as one of the main indicators and parameters to monitor the metabolism changes in cancerous tissues. In fact, most tumors promote a more glycolytic than oxidative metabolism, which is often accompanied by higher aggressiveness of these

tumors. Indeed, it has long been suspected that a deficit in mitochondrial function may be the cause of this metabolic orientation, an effect which is already known as the Warburg effect [86]. A theory explaining that the tumor cell orients its metabolism according to its needs, in response to its energy needs [87]. It is therefore interesting to highlight this metabolic variation based on a spectroscopic study as well as on the measurements of the fluorescence properties of certain metabolites. In agreement with other studies which have already been performed on this subject, endogenous fluorescence could provide a metabolic information and a specific signature on the tissue type, a signature which make possible the differentiation between cancerous and healthy tissue [88], [89], [89].

The spectroscopic study of brain tissue autofluorescence, applied for glioma tumor identification has proven its worth. With this technique it was possible to discriminate the grades of gliomas (high grade and low grade glioma) [90]. According to another spectroscopic study based on endogenous fluorescence, carried out in patients suffering from colon cancer, a large increase in the porphyrin spectrum was observed against a significant alteration in Flavins (FAD) and Nicotinamide adenine dinucleotide (NADH) levels in cancer areas [88]. Furthermore, measuring the fluorescence ratio variation of NADH over FAD could translate the different alterations in the metabolic process within the tissue [91]. Due to the Warburg effect, an increase of glucose consumption is occurred which leads to a change in the energy production and therefore to a change in the ratio between NADH and FAD. This ratio, known as the redox ratio has shown through several reported studies its ability to be a powerful tool to monitor changes in tissue metabolic state [92]–[94]. Therefore, different reported studies proposed an experimental definition of this ratio as an indicator of tissue malignancy. This ratio was observed varying in dysplastic cervical tissue samples which indicates increased metabolic activity [94]. Similarly, this ratio was observed also varying in cancerous epithelial tissues [95], cancerous bladder tissue [96], rat brain tumors [97] as well in glioblastoma human brain tissues [98].

## 1.4.2 Fluorescence microscopy

Fluorescence microscopy has emerged as one of the most important developments and major breakthroughs introduced in optical microscopy field [54]. Since its discovery, it has become the standard method of choice for multiple life-science applications including biological tissues and cell imaging. It has the advantage of providing a high Signal-to-Noise Ratio (SNR), which enables distinguishing spatial distributions of very low concentration of fluorophores in a medium. It was also the foundation of many later developed fluorescence-microscopy-based modalities used in bioimaging field. Fluorescence microscopy is used for the detection of specific structures, molecules, or proteins within a cell or a tissue. Using this technique, almost any component of living/fixed cells or tissues that can be stained, can be visualized and thereby specifically imaged [54].

### 1.4.2.1 Widefield fluorescence microscopy

Nowadays, the widely used fluorescence microscope setup follows the basic epifluorescence excitation setup. Illustrated in figure 1.16, its design consists of illuminating the specimen with the excitation light and collecting the emitted fluorescence signal via the same objective lens. A dichroic filter, which transmits or reflects the light depending on its wavelength, is used to select and to separate the excitation light from the fluorescence signal

which will be directed to the detector (camera, spectrometer, photon counting module ... etc.).

Widefield microscopy is one of the most basic microscopy techniques which consists of illuminating with light the whole specimen (figure 1.16). In widefield fluorescence microscopy, the emitted fluorescence light can be observed either through eye pieces, via the ocular, or captured by a camera to visualize the resulting image. Widefield fluorescence microscopy is an excellent technique to acquire 2D images of biological specimens with a rapid frame rate as the entire imaging field can be captured at once. The amount and the localization of specific fluorescent fluorophores can be visualized with fast temporal resolution which permits the following and the real time observation of several Processes in live cells [99]. However, due to entire sample illumination, several factors can reduce the spatial resolution of the acquired image. Fluorescence signal is generated from all focal planes of the sample, which leads to obtain a low contrast when imaging thick samples like spheroids and tissues. Therefore, it's difficult to determine the imaging depth in the sample, especially in thick samples as the emission light is incorporated all along the sample [100]. Indeed, the emitted fluorescence photons can undergo scattering inside the samples which make the image appear blurry, and consequently the wide field microscopy unsuitable sometimes to acquire 3D images. These blurry artifacts can be resolved through Fluorescence deconvolution microscopy and structured illumination microscopy, consisting of a computational technique that improves the resolution of the acquired images by removing the out-of-focus light and re-assigning blurred light to source points [99]. For these reasons, widefield fluorescence microscopy is mostly used to image thin specimens.

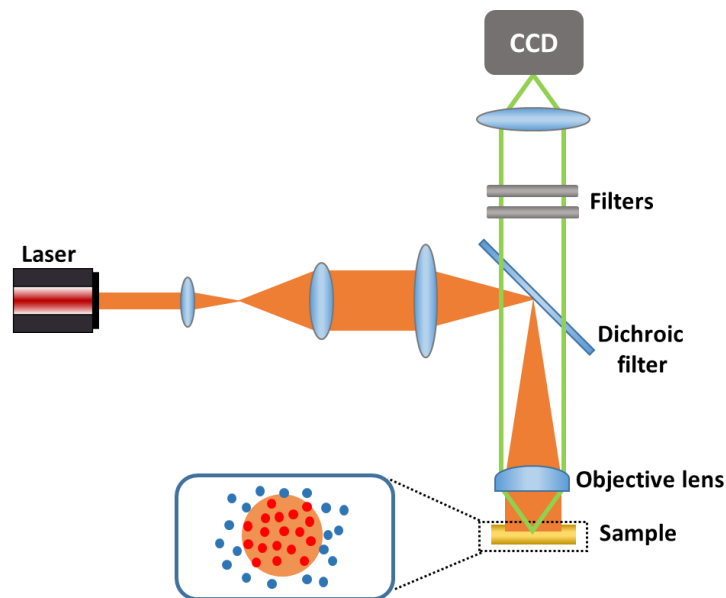


**Figure 1.16:** Illustration of a widefield fluorescence microscope setup

### 1.4.2.2 Confocal fluorescence microscopy

Contrary to the widefield microscopy, and instead of illuminating the entire sample at once, the excitation light in confocal microscopy is focused into a defined volume at a specific depth within the specimen (figure 1.17). This focusing leads to the emission of fluorescent light in a reduced volume (one point) in the focal plane. The most important improvement

that confocal microscopy techniques provides the ability to use spatial filtering to remove the out-of-focus blur light that occurs in the image when acquired with widefield microscopy [101]. For that, a pinhole is placed in the optical detection pathway (figure 1.17) to cut off the fluorescence photons that are emitted outside the focal spot, thus allowing only the fluorescence photons generated from the illuminated focus spot to enter the detector, and consequently to perform optical sectioning in thick specimens.

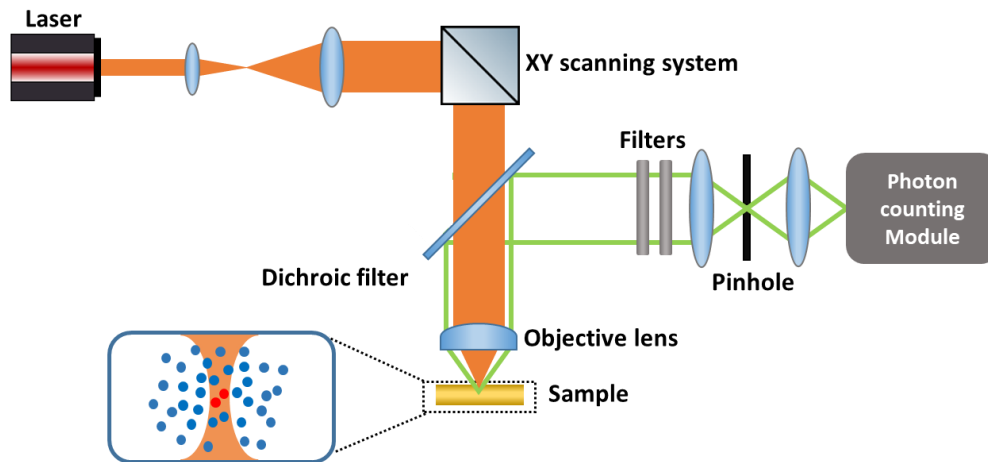


**Figure 1.17:** Illustration of a laser-scanning confocal fluorescence microscope setup.

Therefore, and by performing a beam-scanning process on the specimen in a raster pattern, the image of a single optical plane could be obtained, where does the appointment of laser-scanning (when the excitation used light is a laser beam) confocal microscopy come from. Thus, 3D structures within thick specimens could be imaged and be visualized by scanning several optical planes and stacking their images (called Z-stack imaging) in order to obtain a 3D image of the specimen. It is also possible, through confocal fluorescence microscopy, to analyze multicolor fluorescence staining by using a polychromatic light source or using several laser sources with several specific optical filters [101].

Confocal fluorescence microscopy is widely used to resolve and to visualize the detailed structure of specific components within the cell. Similar to the widefield fluorescence microscopy technique, different components of living and fixed cells or tissue sections can be specifically labelled using exogenous fluorophores and then visualized in high resolution. This technique offers several advantages over widefield fluorescence microscopy, including the higher resolution, the ability to control the excited depth of the imaging field, removing or reduction of background light that occurs away from the focal plane, and the ability to acquire images of multiple optical sections from thick samples [100].

In recent years, there has been a big explosion in the popularity and the use of confocal microscopy, due in part to the ease of obtaining high quality images from biological specimens, and due to the growing number of life science applications, especially in cell biology that need to acquire high resolution imaging for both fixed and living cells [100]. Therefore, confocal microscopy technique has been proved to be one of the most important advances ever achieved in optical microscopy.

In Figure 1.18, two fluorescence images of a mouse kidney tissue are presented, where the first one is acquired through wide field microscopy technique and the second one through

confocal microscopy technique [102]. It shows the improvement in term of spatial resolution that confocal microscopy offers to the acquired image.

However, the image acquisition speed is much slower in confocal imaging than in widefield imaging, due to the necessity of scanning the FOV point by point, which therefore decrease the frame rate. Indeed, and comparing to other optical microscopy techniques, the penetration depth in the sample is limited when using confocal microscopy. Thick specimens, like large spheroids, organoids, tissues, and small animal organs, should instead be optimally imaged using Two-Photon Fluorescence (TPF) microscopy technique.

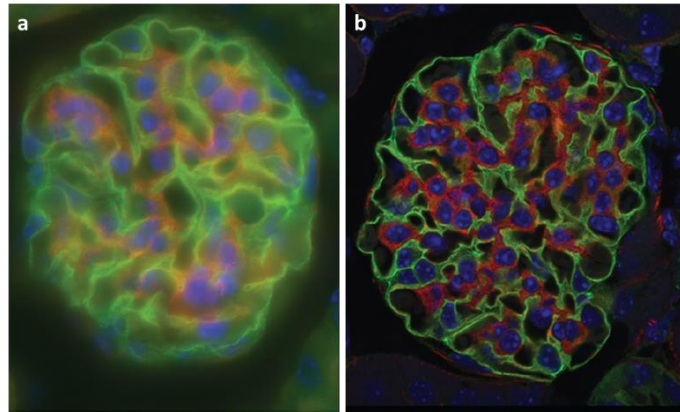


**Figure 1.18:** Fluorescence images of a mouse kidney tissue acquired via a 63x/1.4 NA oil immersion objective on a widefield fluorescence microscope setup (a) and a laser-scanning confocal microscope setup (b) [102].

### 1.4.2.3 Two-Photon Fluorescence Microscopy

In classic fluorescence microscopy methods (widefield and confocal), a fluorophore is excited by absorbing one single photon of a specific excitation wavelength. But in two-photon fluorescence microscopy, and instead of absorbing one photon, the fluorophore absorbs simultaneously two photons with a wavelength approximately twice the wavelength (half of the energy) needed for one photon absorption. This process is called two-photon excitation. When these two photons hit the fluorophore at exactly the same time (within several femtoseconds), the two absorbed photons combine their energy, resulting in fluorophore excitation and then the emission of one fluorescence photon. Figure 1.19 shows the difference in fluorescence generation between one photon and two-photon excitation (figure 1.19 a) and show an illustration of Jablonski diagram describing the two-photon absorption process (figure 1.19 b).



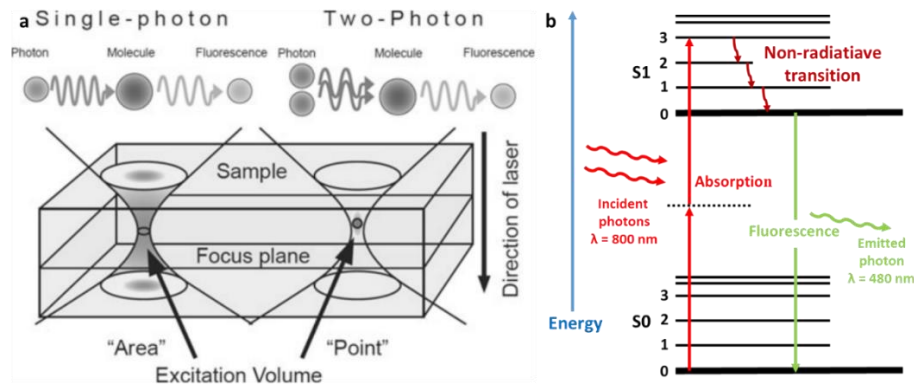


Figure 1.19: (a) Spatial difference in fluorescence generation using one-photon excitation and two-photon excitation process [54]. (b) Illustration of Jablonski diagram

Similarly, in three-photon excitation, the fluorophores absorb simultaneously three photons having three times the wavelength (one third of the energy) needed for one photon absorption. These processes are collectively called multi-photon excitation, which the nomination of multiphoton fluorescence microscopy come from [54].

Two-photon excitation has the advantage of being able to excite the same fluorophores as the one-photon excitation is able to. However, this excitation method allows the use of low energy infrared photons instead of using visible photons, like in one photon excitation, to generate fluorescence signal having the same wavelength [103]. In fact, infrared excitation light, used in two-photon fluorescence microscopy, have the ability to penetrate in the tissue more deeply than the visible excitation light. This wavelength range is called phototherapeutic window (also known as optical window or NIR window) and defines the range of wavelengths from 650 to 850 nm [104]. Within this window, the light has its maximum penetration depth in biological tissues, where their main components, such as water and blood (hemoglobin), have their lowest absorption values [102]. Figure 1.20 shows the phototherapeutic window wavelength range and also shows the variation of the absorption coefficient of several main tissue components as a function of the wavelength.

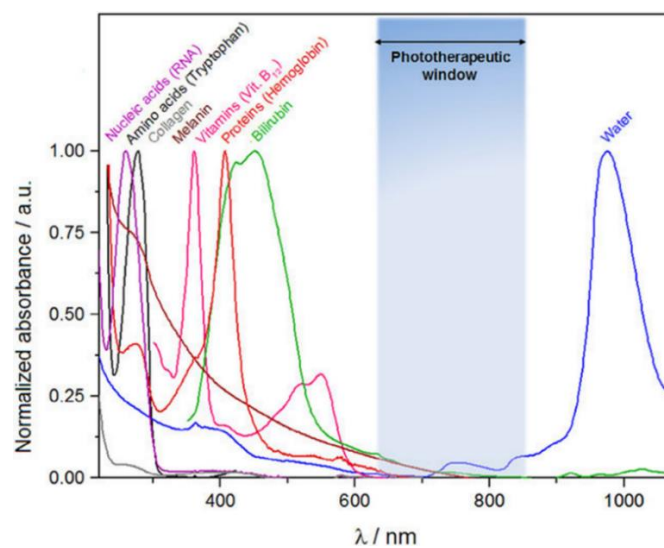


Figure 1.20: Variation of the absorption of photons in function of the light wavelength. The Photo-therapeutic window wavelength range is marked in blue the spectral range of visible and NIR light (650–850 nm) [104]

Within the photo-therapeutic window, the most dominant light-tissue interaction is the scattering. Since scattering increases the distance travelled by photons in the tissue, making the propagating excitation diffused rapidly, the probability of photon absorption also increases and therefore the increase of fluorescence emission [105]. Therefore, and due to its low energy level, infrared light is less damaging, and therefore especially useful when working with living samples.

Indeed, even when exciting within the phototherapeutic window, the probability that two-photon absorption occurs is much lower than one-photon absorption. In order to increase this probability, two main conditions are strongly needed:

- 1) Exciting the focal point with the highest possible number of photons.
- 2) Exciting during the smallest possible duration.

Thus, the use of a pulsed laser beams with high intensity and very short pulse duration (femtosecond duration order) is necessary. The use of such laser beam leads to fluorophores excitation only within the objective focus, because only in this area, the critical number of photons per time and space is reached. Therefore, all emitted fluorescence light is generated from one focal point in the imaged specimen, which strongly reduce the background noise with no need to use spatial filtering like one-photon confocal microscopy. Indeed, the ability to control and to determine accurately the position of the focal point allows obtaining optical sections of the under-surface regions of biological specimens with high resolution. The image is acquired in a similar way than in laser-scanning confocal microscopy: The excitation laser beam scans the specimen with a raster pattern in a 2D plane with recording the image intensity point by point. Therefore, a full 3D image is composed by serially scanning the specimen at several sequential Z positions (Z-stack).

Two-photon fluorescence microscopy is a powerful imaging tool that combines the advanced optical techniques of laser-scanning confocal microscopy with long wavelength multiphoton fluorescence excitation to perform 3D high-resolution imaging of biological tissues. The use of NIR light allow to image deeper in thick biological tissues. Furthermore, the localized energy during excitation leads to minimizing the photobleaching of fluorophores in the specimen and reducing their photodamage. It is particularly useful for cell biologists who seeks to study dynamic processes in living cells and tissues without producing significant damage to the specimen [100]. These advantages enable researchers to conduct experiments on thick tissue samples, such as brain slices and developing embryos that would be complicated to image with other microscopy techniques.

#### 1.4.2.4 SHG microscopy

Second Harmonic Generation (SHG, also called frequency doubling) is a non-linear (second order) optical coherent process that occurs when two incident photons that have the same frequency interacts simultaneously with a non-linear material, generating a single photon with exactly the double of energy of the incident photons (half of the excitation wavelength [106]).

In biological specimens, only non-centro symmetrical structures, such as collagen fibers structures and muscle myosin are capable of emitting SHG light [107]. SHG microscopic imaging offers many advantages that make it ideal for live cell and tissue imaging. Unlike the standard fluorescence imaging, SHG does not involve absorption process leading to the excitation of fluorescent molecules. Therefore, the imaged specimen does not suffer from

photo-toxicity effects or photo-bleaching [106], [108]. Using SHG imaging, fine structural details of tissues could be directly visualized without use of external staining dyes, due to that the contrast is produced purely from endogenous species. Similar to two-photon fluorescence microscopy, and due to the use of the NIR light in the phototherapeutic window, SHG microscopy can achieve high resolved images to depths of several hundreds of microns [109].

SHG signal can be generated using the same two-photon excitation process to generate fluorescence signal. Therefore, and using the same excitation beam and the same setup, it is possible to visualize the auto-fluorescence signal of the tissue as well as its SHG signal, resulting in two image modalities. Figure 1.21 shows a TPF (a) and a SHG image (a) from a meningioma fresh tissue acquired by our team via a Leica SP8 two-photo fluorescence microscope.

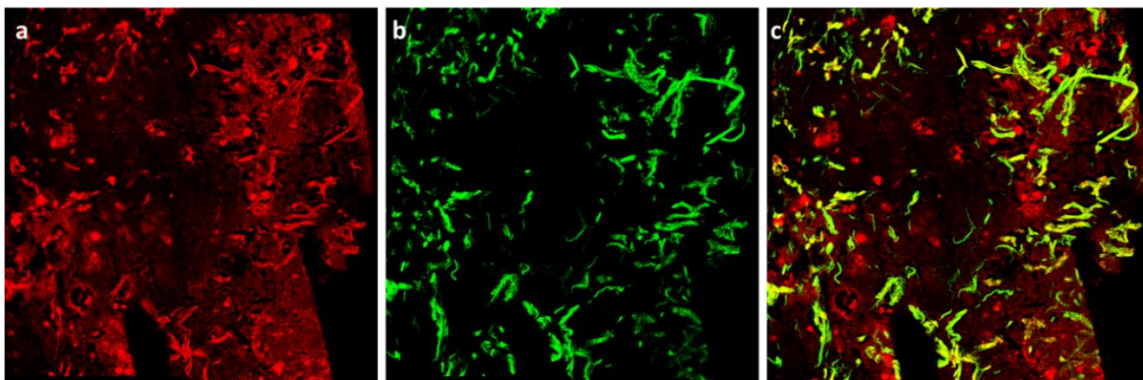


**Figure 1.21:** Two-photon fluorescence image (a) and SHG image (b) of an 840x840 $\mu$ m region of a meningioma freshly excised tissue specimen. (c) TPF+SHG merging of the previous images.

In 1986, Freund et al. [110] reported the first biological SHG images where they investigated the polarity of collagen fibers in rat tail tendon. Most of the recent reports on SHG imaging focus on visualizing collagen fibers structures in a variety of connective tissues and internal organs [111]–[114].

In cancerous tissues, the abnormal metabolism may lead to an alteration in the structure of proteins, which affects the level of SHG, making it a useful tool for diagnosis [107]. During angiogenesis, where the tumors develop new blood vessels around their mass to support infiltration, and during tumor cell invasion, collagen levels will increase in cancerous zones [115]. Therefore, high SHG signal were observed in glioblastoma tumor boundaries where invasive collagen was intercalated with tumor cells [116]. These observations make the SHG, especially when combined with two-photon fluorescence signal, a good indicator for tumor boundaries delimitation as well for cell infiltration

#### 1.4.2.5 Fluorescence Lifetime Imaging

Contrary to the standard fluorescence microscopy imaging, where the fluorescence intensity is used as contrast to create the image, Fluorescence Lifetime Imaging (FLIM) uses the fluorescence lifetime of the fluorophores as contrast to create the image.

The fluorescence lifetime is defined as the average amount of time that an excited molecule spends in its excited state before returning to the ground state and emitting a photon. Physically, it's defined as the time that the fluorescence intensity decays exponentially

(1/e) of its maximum [117]. For a given fluorophore, this process can be described following the equation (1.1) below:

$$I(t)=I_0.e^{-t/\tau} \quad (1.1)$$

where  $\tau$  is the fluorescence lifetime,  $t$  the time and  $I_0$  the intensity at  $t=0$ .

In the excited state, each type of fluorophore has its own lifetime. Therefore, the detection of the differences in fluorescence lifetime, allows to distinguish fluorophores that have the same emission spectrum and therefore to obtain a spatial information or to establish a spatial lifetime map of a fluorophore within a cell or a tissue. A FLIM image is constructed using the fluorescence lifetime value determined at each pixel to provide the image contrast, and displayed through a false-color scale between the different fluorophores within the specimen that have different fluorescence lifetime values [118]. Figure 1.22 highlight this differentiation and compares two images acquired from the same sections using standard fluorescence imaging and fluorescence lifetime imaging.

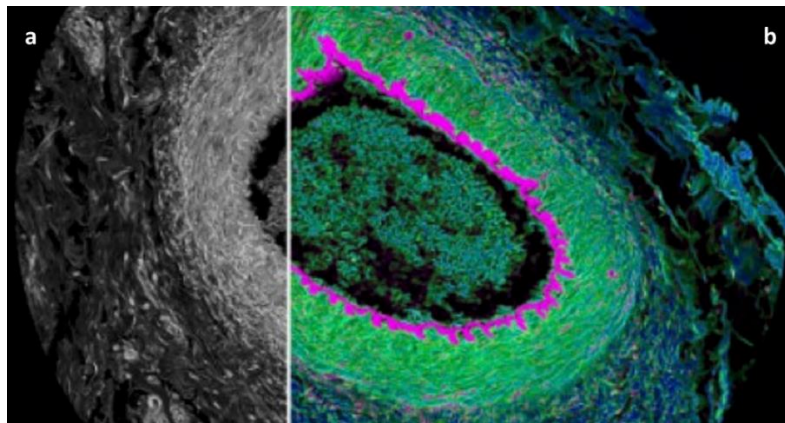


**Figure 1.22:** (a) Intensity contrast image of a histological cat eye section acquired via standard fluorescence microscope. (b) Same section imaged via Fluorescence lifetime imaging microscope reveals contrast by lifetime [119]

Fluorescence lifetime is affected by any energy transfer process between the excited fluorophore and its local environment such as molecular interaction or ion concentration [118]. However, it is not affected by the concentration of the fluorophore, or the intensity of the excitation laser beam.

When two-photon excitation process is used, the resulting image contrasts the fluorescence lifetime of the fluorophores within only the focal point, which can then be used to define and interpret the environmental factors of the molecules of interest and to be correlated with the fluorescence image.

However, measuring the fluorescence lifetime of a fluorophore is not simple as measuring its emission intensity. Several detection techniques have been developed to measure the fluorescence lifetime of a fluorophore [117]. These techniques are divided into two main categories: time-domain and frequency-domain methods.

The frequency domain method is based on the use of a sinusoidally modulated light to excite the specimen. The resultant detected fluorescence signal is then also sinusoidally

modulated with a decrease in the modulation depth and average intensity and is phase shifted comparing with the excitation light [118].

Therefore, both the modulation and the phase shift between these two signals can be used to determine the fluorescence lifetime. Figure 1.23 illustrates the wave form of the excitation light and the detected fluorescence signal as well as the phase shift ( $\varphi$ ) and the modulation that arise between these two signals

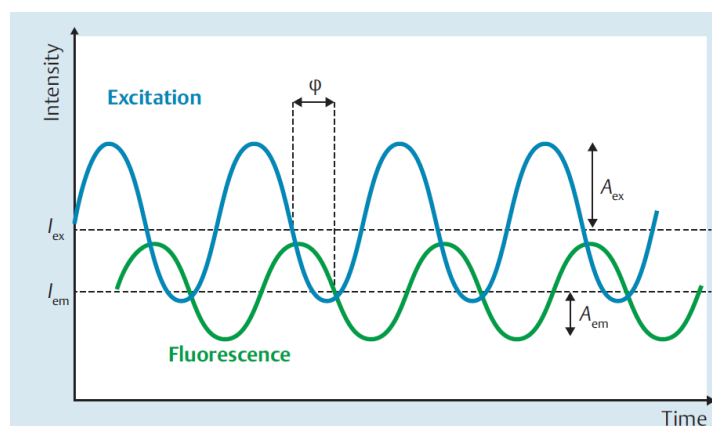


**Figure 1.23:** Illustration of the frequency-domain measurement method: Phase shift and modulation that occurs between the excitation light (blue wave) and the fluorescence emitted signal (green wave) are shown.  $\varphi$ : phase shift;  $A_{ex}$ : amplitude of the excitation light;  $A_{em}$ : amplitude of the emitted fluorescence light;  $I_{ex}$  and  $I_{em}$ : respective average intensities of the excitation and the fluorescence light [118].

The time domain methods consist of recording the fluorescence intensity decay of a fluorophore, after being excited with a pulsed laser beam, as a function of time. It can be performed either by time gating technique, as in wide-field microscopy, or by using the photon counting technique as in confocal microscopy and two photon fluorescence microscopy [118]. More precisely, time-domain method consists in measuring the time of emission delay of a single photon relative to the excitation pulse of the laser.

The time-gating technique consider the fluorescence signal as a continuous wave. The fluorescence decay curve can be recorded by sequentially shifting a narrow time gate on the signal wave and by measuring the amplitude of the signal in each time gate (figure 1.24 a). This method can avoid the photon pile-up effect when the detected fluorescence signal is high. Therefore, it is useful to be used in configurations with higher photon fluxes that needs high imaging rates. However, this technique have never reached the same precision as the photon counting technique and it's favored in situations where the imaging speed prevails over the resolution [120].

The photon-counting technique, known as Time Correlated Single Photon Counting (TCSPC) regard the fluorescence signal as a random sequence of single photon pulses. When a fluorescence photon is detected by a sensitive photomultiplier detector, an electronic signal (Start) is sent to the acquisition electronic system which enables the start of counting, which will be stopped by another signal (Stop) sent by the laser when it emits the next pulse.

This process is then repeated several times, so as to maintain the measurement conditions where a single fluorescence photon is detected at each pulse, and by counting the number

of photon pulses arriving at a series of time sequences, a photon counting histogram as a function of the fluorescence decay time, can be acquired (figure 1.24 b).

The main advantages of TCSPC technique is its high precision and its higher sensitivity which make it the best technique to deal with very low signal. One weakness point of this technique is the relatively low acquisition time which impose its use with low intensity signals [121].

The choice of either frequency or time-domain measurement methods to perform FLIM measurements will depends on the investigated fluorophores. Frequency-domain method is more suitable to investigate fluorophores with short-lifetimes while time-domain method is more flexible and can be applied to investigate long-lifetime fluorophores, which is better suitable for tissue measurements where a wide variety of molecules can be evaluated and allows in addition the treatment of multi-exponential decays [120].

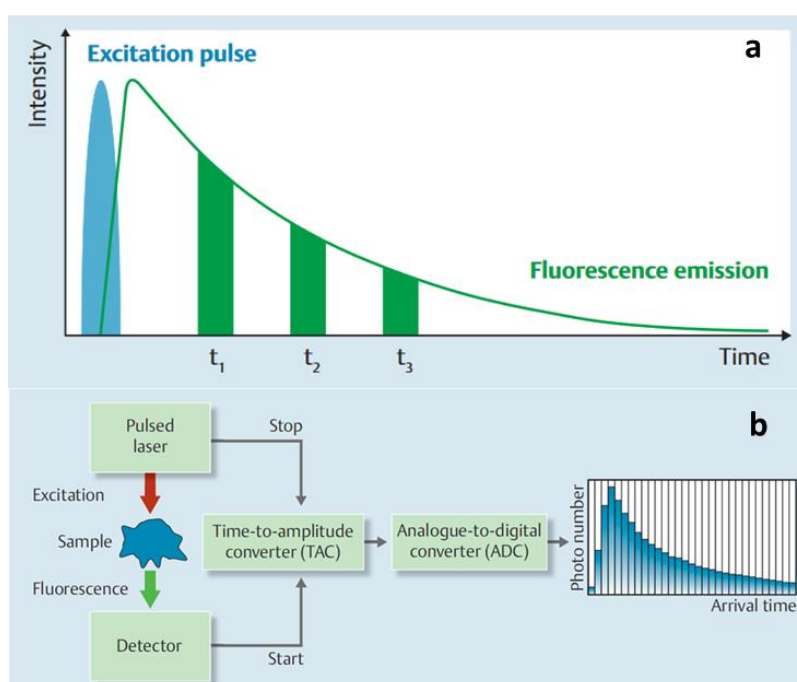


Figure 1.24: (a) Illustration of time-gated measurement method: The excitation light pulse is shown in blue while the fluorescence decay in green with three detection time gates ( $t_1$ ,  $t_2$  and  $t_3$ ). (b) Schematic diagram of the time-correlated single-photon counting (TCSPC) acquisition method [118].

FLIM is used to analyze the spatial distribution of specific cellular components within the cell or the tissue, such as proteins or nucleic acids. Through this imaging technique, it is possible to detect and to identify single fluorophores as well as to acquire several information about the local fluorophore environment in living cells [122]. It helps also to measure several factors within the cell such as pH, oxygen concentration, calcium ion amount and molecular binding. FLIM could also be used to monitor molecular interactions, such as Förster Resonance Energy Transfer (FRET) that permits reporting of the distance between a donor and acceptor molecule [122].

FLIM was used by several research teams in the world in order to investigate fluorescence lifetime alteration in brain tumors. Kantelhardt et al. performed an ex-vivo study using two-photon fluorescence imaging and FLIM using mouse models and freshly resected human

brain tumor samples. They found that the fluorescence lifetime of tumor adjacent brain tissues was consistently higher than that of healthy white matter [123]. More ex vivo studies were performed by L. Marcu group who showed that the average fluorescence lifetime was higher in cancerous zones than in healthy white matter and cortex regions [124]. They performed also in vivo FLIM measurements on different glioma grades tumors showing an ability to differentiate low grade from high grade glioma as well from normal cortex and white matter with a high specificity and sensitivity [125], [126]. Their group managed to implement FLIM detection in a fiber probe design for image-guiding brain tumor surgery [127]. They were able to perform a first exploratory clinical trial, on three patients undergoing tumor resection surgery, and showed that GBM had a significantly more irregular excitation lifetime distribution when compared to normal cortex [127]. Their Intraoperative experiments demonstrated also that FLIM-derived parameters allow for delineation of tumor areas from normal cortex where GBM samples presented a weaker fluorescence intensity (35% less) and a longer lifetime NADH than normal cortex [127]. These results demonstrate the potential of FLIM use as a powerful tool for image-guided surgery of brain tumors and its ability to offer a reliable complementary information to establish an accurate diagnosis.

**Analysis methods** Fluorescence lifetime acquired data could be analyzed through several methods in order to extract the lifetime value of the excited molecule from its fluorescence decay curve. The most known methods are the mono/multi-exponential curve fitting, Laguerre polynomial fitting and a non-fitting method called phasor plot analysis [122]. In this research work, exponential fitting as well as phasor plot analysis were applied. However, and during a fluorescence decay measurement, the detected signal does not depend only on the analyzed sample but also on the response time of the used setup, called Instrument Response function (IRF). This parameter should be considered when fitting methods are applied to extract the lifetime value. The used method to measure the IRF depends on the used measurement setup. To measure this parameter, we need a fluorophore with a very short lifetime like erythrosin B or dapi [118]. Indeed, when two-photon excitation is applied, the IRF could be measured more precisely by measuring the time response of a non-linear crystal (SHG emitter). Thus, the measured fluorescence lifetime in a region of interest from tissue is the convolution of the IRF and the intrinsic fluorescence decay.

Due to its simplicity, the exponential fitting of the fluorescence decay curve is the most widely used method to analyze FLIM data. Therefore, the fluorescence lifetime of a single component is an exponential fluorescence decay which corresponds to a mono-exponential fit and therefore the provided output is a single lifetime value with goodness of fit parameters, such as  $\chi^2$  close to 1. However, large deviation of  $\chi^2$  values (superior to 1) designates multi-exponential decay and therefore the presence of multiple fluorescence components within the excited area where the recorded response is a linear combination of the exponential decay of each component. [128] Thus, two lifetime extraction approaches could be applied in multi-exponential fitting: a deconvolution of the response by the measured IRF and several exponentials, or a tail fit where only the portion of the decay curve that excludes the IRF impact is fitted.

The second method is the phasor plot analysis method. The phasor approach has the potential of simplifying the analysis of FLIM data and permits to avoid the problems of the exponential fitting analysis and offers as well a graphical global view of the processes that affects the fluorescence decay occurring within each pixel [129]. It was first developed to analyse FLIM data acquired using frequency domain method, but it is applicable also for analyzing FLIM data acquired using time domain methods as well. With the phasor approach, each decay component or molecular species is identified by a single vector in the "phasor plot". This vector is called phasor and its location in the phasor plot is unique, regardless of the number of exponentials needed to describe the fluorescence intensity decay [130]. When the phasor falls on the universal circle, it can be associated with a single lifetime value of a mono-exponential decay. However, if it doesn't fall or if it isn't located on the universal circle, the corresponding highlighted molecular species must have a complex or a multiexponential decay [129].

When frequency domain method is used, the phasor is described by a module  $M$  and a phase  $\varphi$  that are transformed according to the equation 1.2 in order to be graphically represented as a phasor vector in the phasor plot [130], [131]. As represented in figure 1.25 below, the x and y coordinates of a phasor in the phasor plot are respectively:

$$g = M \cdot \cos(\varphi) \quad ; \quad s = M \cdot \sin(\varphi) \quad (1.2)$$

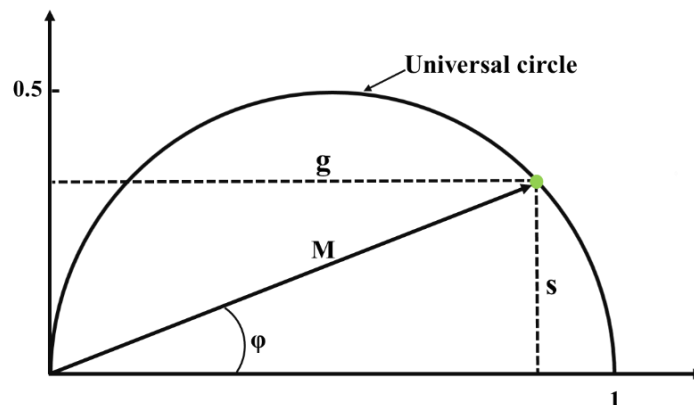


Figure 1.25: Graphical representation of a phasor in the phasor plot.  $g$  corresponds the x-coordinate,  $s$  to the y-coordinate of the phasor in the phasor plot,  $M$  the module and  $\varphi$  the phase.

However, the theoretical equations that transform the fluorescence intensity decay to a phasor in the phasor plot are different for time domain and frequency domain techniques [130]. When the fluorescence decay intensity  $I(t)$  is acquired via a time domain method, the  $G$  and  $S$  coordinates in the phasor plot, corresponding to the decay profile  $I(t)$ , can be obtained by the following equations (1.3) and (1.4):

$$S_{i,j}(\omega) = \int_0^{\infty} I(t) \cdot \cos(\omega t) \cdot dt / \int_0^{\infty} I(t) \cdot dt \quad (1.3)$$

$$G_{i,j}(\omega) = \int_0^{\infty} I(t) \cdot \sin(\omega t) \cdot dt / \int_0^{\infty} I(t) \cdot dt \quad (1.4)$$

Where  $\omega$  is the laser repetition angular frequency and the indices  $i$  and  $j$  identify a pixel in the acquired FLIM image. Therefore, the fluorescence lifetime decay of each pixel is represented in the phasor plot by a phasor. After being plotted, a phasor cloud is obtained



which corresponds to all phasors corresponding to the FLIM image pixels. This phasor cloud is then fitted into a polynomial fit line in order to extract the two-lifetime values of each component of the decay, where the intersection of this fitting line with the universal circle determine the long and the short lifetime of the investigated fluorophore components [132] (figure 1.26). Therefore, in this research work, this line pertains to the free and protein-bound component of FAD and NADH, as the fluorescence decay of these two fluorophores was analyzed using the phasor analysis method.

Afterwards, the Long Lifetime Intensity Fraction (LLIF) could be extracted through the plotted phasor for each plotted phasor. This parameter, designated sometimes by  $\alpha$ , corresponds to the fraction of fluorescence emitted by the fluorophore component with the longer lifetime. Graphically, the LLIF of each pixel is obtained by projecting its phasor to the fitting line that intersects the universal circle [129]. The distances between the projection position of each phasor count and the position of the short lifetime value on the universal circle is calculated (A in figure 1.26). In addition, the distance between the two intersection position of the fitting line with the universal circle is also calculated (B in figure 1.26). Consequently, the LLIF value is the ratio between the distance A over the distance B. Thus, it corresponds to the fractional contributions of free FAD or protein-bound NADH.

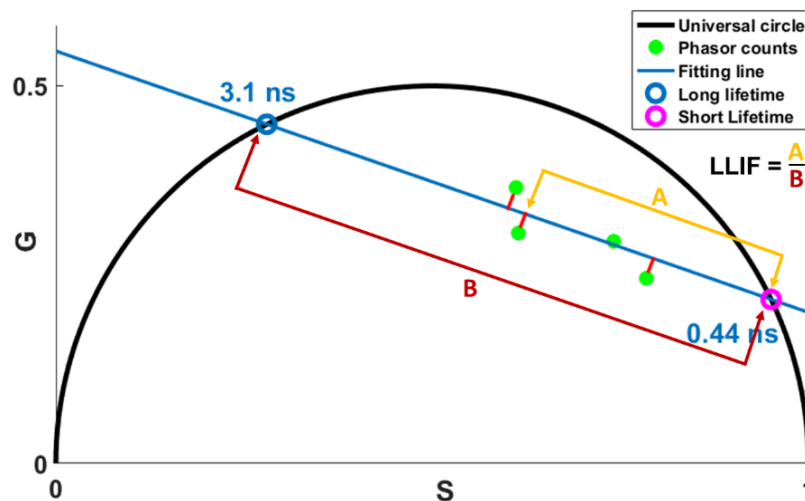


Figure 1.26: Graphical representation of a phasor in the phasor plot with an explanation of LLIF determination method.

## 1.5 Fluorescence imaging for Intraoperative use

Nowadays, fluorescence benchtop microscopes with their different techniques (widefield, confocal...) are widely used in all over the world for a large variety of applications. As described in the last section, fluorescence microscopes have the ability to image and to visualize almost any component within a cell or a tissue that can be stained. Moreover, even without staining, endogenous fluorescence imaging and spectroscopy has shown a great importance for cell/tissue imaging as well as monitoring tissue metabolism and therefore discriminating cancerous tissues.

Similar to OCT and Raman spectroscopy, several efforts have been exerted in the last decades to bring fluorescence microscopy technique into the surgical field.

However, transition from benchtop microscopy to intraoperative endomicroscopy is challenging. Benchtop microscopes, in particular two-photon fluorescence microscopes, are roomy and needs a large space to be installed. Further, the objectives that are used cannot be fitted into medical instruments or to be applied directly in the patient while delivering the excitation beam, using free-space optics, to internal organs in the body is too complicated. However, advances in optics, bioengineering, biotechnology, experimental oncology, and biochemistry have encouraged the transition of fluorescence microscopy into the preclinical area. Miniaturization of the optical components and the scanning methods in confocal methods was necessary in this transition process. Thus, optical fibers were the best adapted solution to guide the laser light to the internal tissues as well as the miniaturized developed scanning systems to fit into millimeters scale medicals endoscopes that are easy for surgeons to handle.

On the other hand, several biochemical agents were conceived or developed in order to be used for fluorescence guided surgery. These label agents are intended to improve the surgery guidance by enhancing the generated fluorescence signal and serves also to label specific structures or specific fluorophores within the cells/tissue in order to be monitored and studied quantitatively. The most famous exogenous marker that is widely used in fluorescence guided surgery studies is the 5-Aminolevulinic Acid.

### **1.5.1 Fluorescence guided surgery using 5-Aminolevulinic Acid**

5-AminoLevulinic Acid (5-ALA) is a metabolic targeting agent that is orally administered to the patient. It is known by its extraordinary ability to penetrate the BBB and the tumor interface in brain tumors [133], [134] . So far, no other known oral targeting agent is available for fluorescence guided surgery that can accumulate, like 5-ALA, within malignant brain tumors and their surrounding infiltrating zones outside of the tumor mass.

Once 5-ALA is caught by a cancerous cell, it is metabolized into protoporphyrin IX (PpIX), a fluorescent metabolite [133]. PpIX has an efficient excitation wavelength in the visible light range (405 nm). Under blue light excitation, normal brain tissue reflects the light, while tumor zones with accumulated PpIX emits a bright fluorescence light in the NIR range with a main large peak centered around 634 nm and second small one around 710 nm [135]. Figure 1.27 shows a micro-surgical cavity observed with white light (figure 1.27 a) and when excited with a visible light (figure 1.27 b). Healthy brain areas appeared in blue (reflected light) while infiltrating areas, where 5-ALA is accumulated, appears fluorescent in red (figure 1.27 b).

Large studies and clinical trials, performed by several groups in the world, showed the importance of 5-ALA use to guide brain tumor surgeries, and especially for glioma surgeries [136]–[140]. The diagnostic accuracy of 5-ALA-induced tissue fluorescence in malignant gliomas is a key benefit for 5-ALA fluorescence guided Surgery. Multiple studies have found a high sensitivity, specificity, and positive predictive value for tissue fluorescence and malignant glioma tumor tissue. Values close to 90% have been consistently described by most groups in both newly diagnosed tumors as well as recurrent malignant gliomas [133]. Furthermore, the use of 5-ALA fluorescence with surgical microscopes for high grade glioma resection guidance have shown an increase of 6 months in patient life expectancy [141].

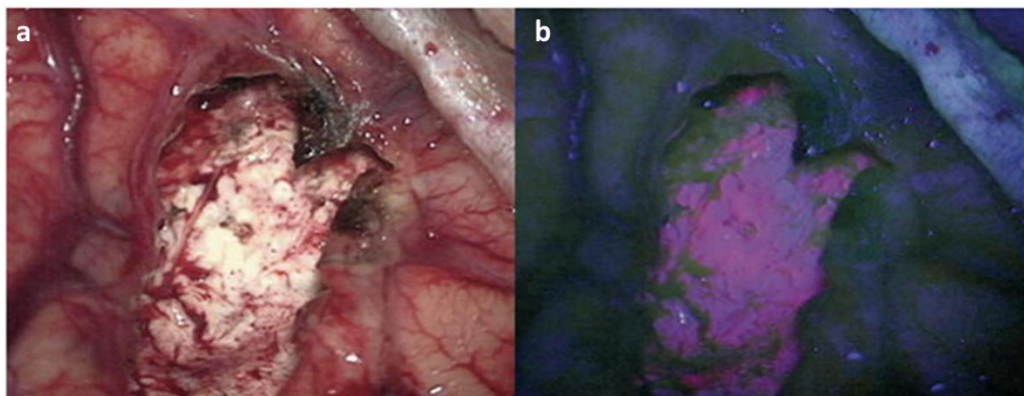


**Figure 1.27:** (a) Microsurgical white-light visualization of glioblastoma resection cavity after maximal conventional resection. (b) Visualization of PpIX fluorescence at tumor margin after conventional microsurgical resection[142]

Several quantitative approaches have been proposed to improve the 5-ALA ability in discriminating healthy from tumors margins during brain tumor surgery. One approach is to calculate the severity of the malignancy of a tumor relying on the induced fluorescence intensity by calculating the ratio between the induced fluorescence intensity over the reflected excitation one, known as fluorescence intensity ratio, which can be useful to predict the proliferative activity of the tumor [143].

Another approach consists of that two states of PpIX fluorescence contribute to the total emission of the main detected peak. Reported intraoperative spectroscopy studies raised the presence of these two states in low and high grade glioma, where the first one is the already known main peak centered at 634 nm while the second state peaks around 620 nm [144]. Taking into account the contribution of the second state have been shown to help improving the discrimination of glioma margins from healthy areas during 5-ALA fluorescence guided resection [140].

Other potential significant advancements involve the intraoperative use of high-magnification imaging optical technologies, such as confocal endomicroscopy instead of low resolution widefield endomicroscopy, which may improve the detection of fluorescence signal to the cellular level [145].

Similar to the other techniques, 5-ALA fluorescence guided surgery suffers from several limitations and drawbacks. Disruption of the BBB is necessary for fluorophore accumulation and in some low-grade gliomas cases, this may decrease or change the contrast accumulation [135].

Furthermore, it suffers from false positive fluorescence observation, where in many cases, 5-ALA-induced fluorescence not associated with malignant tumor tissue has been observed [133]. Several groups have reported the presence of fluorescence in tissue areas surrounding the resection cavity in regions very close to active tumor cells [133], [146], [147] but not in healthy brain regions distant from the gross tumor region. Indeed, the timing of 5-ALA administration is very important too and may account for the lack of tumor fluorescence in limited cases which leads to obtain false negative fluorescence results.

### 1.5.2 Intraoperative widefield microscopy

Widefield microscopy was the first fluorescence microscopy technique that have been implemented and used for endoscopic applications. Its low cost comparing with other techniques, the ability to observe the full surgical field, to have a real-time and a fast acquisition as well its simple use without interrupting the surgical workflow are the major advantages of the intraoperative use of technique. [148][140].

This technique refers to surgical microscopy, where the entire field of view is imaged and observed continuously through an eyepiece or a fast detection CCD camera coupled with a display screen. The use of custom operative microscopes with fluorescein [149] and PpIX fluorescence [150] measurements modules was reported for intraoperative imaging use. Several fluorescence detection modules are commercially available for use on operative microscopes for 5-ALA and fluorescein-guided tumor resection in brain surgeries [135] . These systems offer a magnification of 5x to 40x, and a spatial resolution from 10 to 100  $\mu\text{m}$  which is still higher than the cellular level [92], [135].

However, the major drawback of this technique is its low resolution. In addition, the uncertainty at the margins where fluorescence intensity decrease and the struggle of visualization on the sides of a resection cavity and shaded areas in the surgical cavity are some of the limitations [135]. Furthermore, the limitations of wide-field visualization technologies in fluorescein-guided surgery are common to those of 5-ALA studies [151]. For PpIX fluorescence visualization, the PpIX emission is quantitatively correlated and related to the increase of malignancy at a microscopic level in both low-grade and high-grade gliomas [152]. Such conclusions highlight the limitations of fluorescence detection using the current widefield imaging setups at low concentrations of this marker or when few number of cells are labelled. Additional limitations for this technique are fluorescence absorbance by blood and tissue layers where visible light is used for imaging, the low fluorescence intensity in most of low-grade gliomas [135], and absence of quantitative analysis of fluorescence generated signal.

### 1.5.3 Intraoperative confocal endomicroscopy

In 1988, the first fiber optic confocal microscopy was conceived and then commercialized in 1994 [135]. Later, the first results of confocal microscopy use in neurosurgery were reported [153]. As figure 1.28 shows, these endoscopes employ a miniature handheld probe associated with a movable workstation and a display screen. It offers an ability to perform non-invasive real-time imaging through optical sectioning at a well-known depth in the tissue. It showed also an interesting ability to deliver real-time images similar to those provided by histopathological analysis [154], although this development is still being validated.

Two commercial systems of confocal endoscopes are actually available and have been reviewed both for neurosurgical applications [155]. The first one is proposed by the Australian company OptiScan under the name of OptiScan FIVE [156]. Their latest version, FIVE 2, have a remarkable improved abilities comparing the ancient version FIVE 1. It uses 488 nm as excitation wavelength with an excitation power starting from 10  $\mu\text{W}$  to 1mW. It has a 475x475  $\mu\text{m}$  FOV with a focal plane that can reach a depth up to 400  $\mu\text{m}$  and a frame rate that can reach 3 frames per second. It offers a high resolution images with 0.55  $\mu\text{m}$  and 5.1  $\mu\text{m}$  as lateral and axial resolution respectively [156].

The second system is proposed by the French company Mauna Kea technologies under the name of Cellvizio [157]. Their system offers the choice to use two excitation wavelength 488 nm or 660 nm. It has nine objectives that cover FOV ranging from 300 to 600  $\mu\text{m}$  with a frame rate which can reach 12 frame per second [135], [157].

The first study that investigated the feasibility of intraoperative confocal fluorescence endoscopy in brain surgery was reported for a variety of brain tumor types using intravenous fluorescein injection for tumor visualization. Results of this study showed that intraoperative imaging allows the neuropathologist to establish a diagnosis, but this diagnosis was not as reliable and accurate as the standard histological staining [135], [158], [159].

Another study, performed on patients with gliomas, allowed the establishment of an accurate diagnosis with a specificity and sensitivity of 94% and 91% respectively, compared to the analysis of the frozen sections and permanent histologic diagnosis [160]. Ongoing studies using this technique aims to improve and to validate these values.

Confocal fluorescence endoscopy could also be used as a fast diagnostic tool for biopsy specimens in ex vivo tissue analysis in the operating room. The utility of using staining agents such as 5-ALA, fluorescein, acridine orange (stains DNA/RNA/lysosome) and sulforhodamine 101 (stains glial cell) for visualization of tumor cells was demonstrated with the OptiScan endoscopic system [153], [161].

The major limitations of the intraoperative confocal endoscope are the necessity of non-standard image analysis and interpretation that requires expertise and specific training, along with the use of a low power laser excitation. Furthermore, the acquired image quality and its diagnostic value, as well as the surgeon's knowledge in histopathology, are important factors in the practical application of intraoperative confocal endomicroscopy because the resulting images may sometimes differ from the stained histopathological slides and require additional training for interpretation and analysis [135]. Additionally, the probe should be in a stable position during image acquisition and similar to the wide field endoscopes, the quantitative analysis of the generated fluorescence signal is always absent.



Figure 1.28: Photo showing the intraoperative use of a hand-held confocal endomicroscopy probe co-registered with a Stealth Station neuro-navigation system during brain tumor surgery [135].

### 1.5.4 Two-photon fluorescence endomicroscopy

With the recent developments in optical microscopy techniques and their micro-mechanical components, TPF endomicroscopy became an attractive research tool for clinical applications. It shows a promising potential in exploiting the TPF imaging for in vivo studies and clinical applications. For instance, huge research efforts are employed for the development of small sized TPF endomicroscopes that can fit into a standard endoscope for in vivo and clinical studies while maintaining the TPF imaging ability similar to a standard TPF benchtop microscope. However, TPF endomicroscopy devices face major challenges to maintain the ability and the advantages of TPF excitation in tissue imaging. The major challenges include: the delivery of single-mode ultrashort pulses without alteration with high intensity to maintain the high probability of two-photon absorption, a wide efficient collection of the generated TPF signal, miniature and fast 2D or 3D scanning systems coupling miniature objective lens with good optical properties, and overall miniaturization of the probe assembly.

#### 1.5.4.1 Excitation laser delivery and TPF signal collection

The first challenge to overcome in the development of any TPF endomicroscope is ensuring an efficient delivery of single-mode femtosecond laser pulses as well ensuring a high ability of multimode TPF signal collection. Single Mode Fibers (SMF) are known for their ability to deliver and focus single-mode femtosecond laser pulses to a near diffraction limited spot. However, the small core diameter of a SMF weakens its ability of TPF signal collection in an efficient way. To overcome such drawbacks, some reported systems used a separate multimode fiber, in a two-fiber endoscope configuration (figure 1.29.a), to achieve an effective TPF signal collection [162]. The large core diameter (1-2 mm) of the collection multimode fiber and its high Numerical Aperture (NA, 0.4-0.8) widens the collection area and hence increases the collection efficiency [163]. In addition, it reduces the sensitivity of the collection efficiency to the spherical and chromatic aberrations of the objective lens.

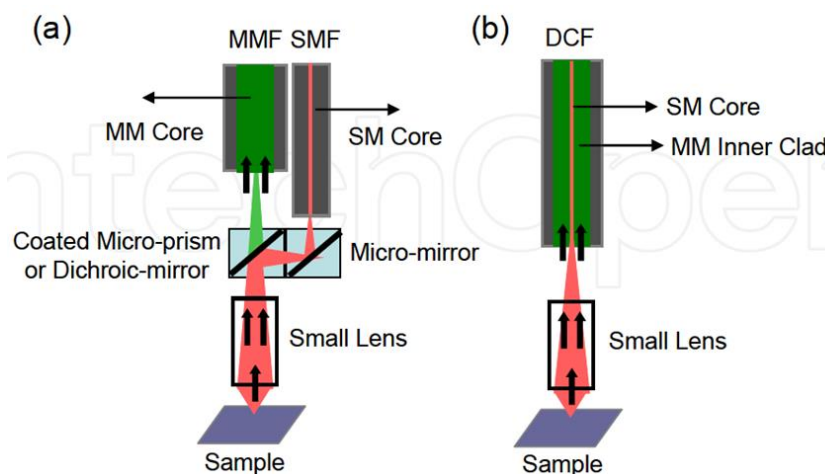


**Figure 1.29:** Schematic of fiber-optic two-photon fluorescence endomicroscope: (a) Two-fiber configuration; (b) Single-fiber configuration. SMF : single-mode fiber ; MMF : multimode fiber; DCF: double-clad fiber; SM: single-mode; MM: multi-mode [163].

However, minimizing the endomicroscope is considered difficult as the two-fiber configuration impose the use of a dichroic mirror with its associated optics to separate the excitation light from the collected one (figure 1.29 a). Thus, to achieve an endomicroscope with higher flexibility and more miniaturized, the two-fiber configuration was replaced by a one-fiber configuration with the use of double-clad fibers (DCF) in the developed TPF endomicroscopes [164]–[167] (figure 1.29 b). These DCFs are a step-index fiber composed of a single mode core that ensure the single-mode laser pulses delivery, a multimode inner cladding layer to ensure the TPF signal collection and an outer cladding layer. Furthermore, the advancements in the field of optical fibers fabrication have made it possible obtaining DCFs with high performance including large inner clad diameter and high NA and less nonlinear optical effects [163].

Typically, germanium-doped silica, pure silica, and fluorine-doped silica, are respectively the materials used for the fabrication of these three layers. The DCF, permitting single-mode delivery of the excitation light through the single-mode core and collection of multimode TPF signals via the inner clad, is commercially available (SMM900, Fibercore Ltd) [168] and has been successfully applied in a scanning fiber-optic TPF endomicroscope with an exceptional imaging ability [164], [166], [167], [169]. In comparison with a single-mode fiber, the DCF significantly improves the collection efficiency of TPF signals by 2-3 orders [163]. Photonic crystal double-clad fiber (PC-DCF) is another type of DCFs. This type involves a single-mode core with pure silica and inner and outer cladding layers with hybrid air-silica structures [170]. PC-DCF is also commercially available (DC-165-16 P, Crystal Fiber) [168] and has been used for developing TPF endomicroscopy technologies [165], [171]–[173]. The PC-DCF has a core/inner clad diameter of 16/165  $\mu\text{m}$  and NA of 0.04/0.6. Increasing the core diameter of the PC-DCF reduces the nonlinear optical effects while decreasing the core diameter will improve the resolution [163]. For that, to obtain a compact fiber-optic TPF endomicroscope, the core size of the fiber has to be chosen carefully with a compromise among the excitation/collection efficiency, the nonlinear effects, the overall diameter, and the probe's rigid length and the resolution.

A. Ibrahim et al. [173] from our research team, developed a TPF endomicroscope that involves a five-meter length customized micro-structured PC-DCF dedicated and approved for in vivo nonlinear imaging. Numerical and experimental studies showed that this customized fiber has a significantly better resolution than other micro-structured DCFs reported in literature for endoscopic imaging [168], [174], [175]. This customized fiber employs a 0.27 NA inner cladding and a small diameter (6.4  $\mu\text{m}$ , 0.097 NA) undoped core to prevent the risk of parasite auto-fluorescence, where they managed to deliver through this core very short pulses (33 fs) [173]. A scanning electron microscopy image of this fiber is shown in figure 1.30.

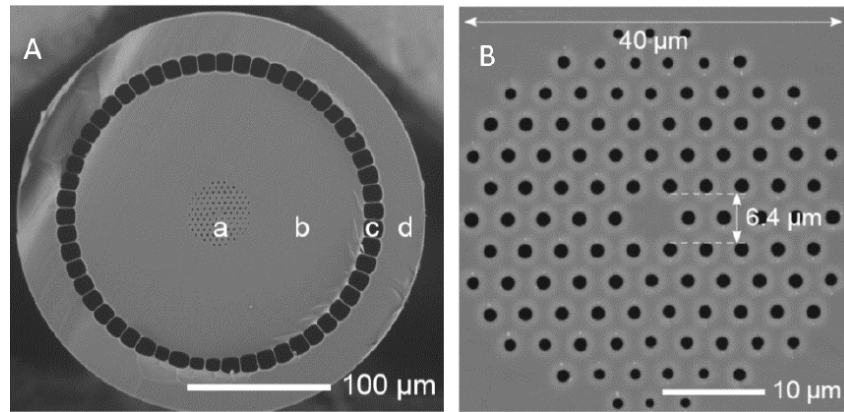


**Figure 1.30:** (A) Scanning electron microscope image of the Photonic Crystal Double Clad Fiber used by A. Ibrahim et al [173]. a: Core region surrounded by an air-silica microstructured region; b: Collecting cladding; c: Low index air cladding; d: Maintaining cladding. (B) Details of core surrounding air-silica microstructured region [173].

### 1.5.4.2 Pulse pre-compensation

Once the endoscopic fiber is chosen, the delivery of the ultrashort pulses to its exit with the same properties as the entry is also challenging. As the SMF, DCF and PC-DCF show normal dispersion, ultrashort pulses transmitted in these fibers will be temporally expanded due to Group Velocity Dispersion (GVD) and nonlinear effects such as self-phase modulation (SPM) [163], leading to increase the pulse duration and consequently reducing the excitation efficiency of the endoscopic fiber and even making it strongly low if the fiber length is long. Therefore, the use a pulse pre-compensation unit become necessary for fiber-optic TPF endomicroscopes with such fibers in order to keep a very short pulse at the exit of long length fibers. In the last decades, different configuration of pre-compensation units has been developed. A first approach was to conceive a system that compensate for second-order dispersion (SOD). Passive dispersive units such as diffraction grating based units and prism based units were reported [162], [169], [176]–[178]. The most used one is the diffraction grating based unit [163], [178]. Illustrated in figure 1.31 a, this unit includes two identical gratings arranged in parallel where the first one disperses the spectral components of the incident beam which are re-collimated by the second grating toward a mirror allowing the resulting beam to travel the opposite path, in order to reconstitute a beam without spatial dispersion.

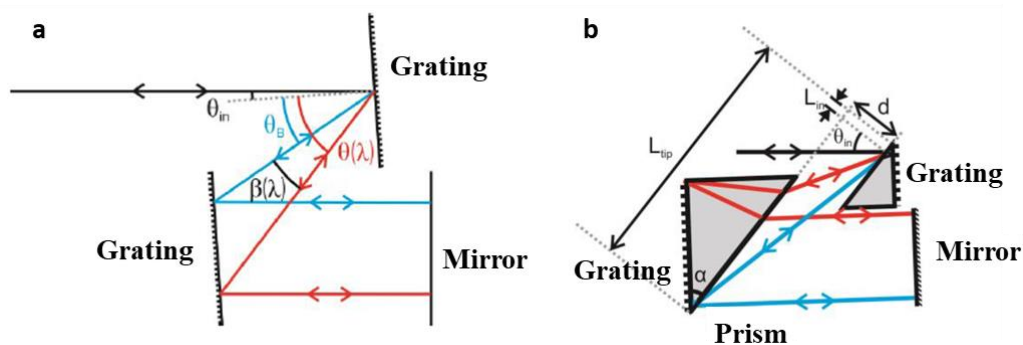


**Figure 1.31:** Illustration of a conventional grating-based pre-compensation unit (a) and a GRISM pre-compensation unit [179]



With this method, pulse duration within the range of 100 fs could be obtained at the exit of 1 or 2-meter length endoscopic fiber when using a laser beam with similar pulse duration. However, this method with its double-pass configuration is generally sensitive to optics alignment. In addition, the third-order of dispersion (TOD) was not compensated with it, resulting in pulses that are still temporally stretched through propagation along fibers that exceed 2-meters length.

To overcome this drawback, new approaches were proposed which consist of combining the reported passive systems to compensate for SOD and TOD simultaneously, such as combining chirp mirrors with a prism-based unit [177], or the association of diffraction gratings with prisms, called GRISM line (GRating+prISM) (figure 1.31 b) [180]. These configurations managed to provide pulse durations at the exit of the endoscopic fiber even shorter than those generated by the laser source making it the best pulse compensation method for two-photon endomicroscopes [168], [173], [175].

### 1.5.4.3 Miniature scanning system

Another challenge faced while developing a fiber-optic TPF endomicroscope is the scanning system at the distal end of the endoscopic fiber. Such system should be miniature enough in order to be suitable for in vivo clinical applications and to be coupled to medical instruments. It should also have enough performance and abilities to ensure a high resolution imaging with a fast frame rate.

Two main scanning techniques are used in the scanning systems of the reported TPF endomicroscopes: The fiber scanning technique and the beam scanning technique.

The fiber scanning technique (figure 1.32 a) consist of scanning the distal tip of the endoscopic fiber cantilever at its mechanical resonant frequency with a piezoelectric actuator in order to generate vibration movement at the fiber cantilever base. Most of resonant fiber-optic piezoelectric scanners implement a tubular piezoelectric (PZT) actuator (figure 1.32 a) where the fiber-optic cantilever is glued within the actuator tube [181]–[184]. This technique is widely used in the field of TPF endomicroscopy [164], [184]–[187] due to its low cost and to other several advantages. It permits the assembly of head probe that have the enough miniaturization required for in vivo clinical imaging ( $< 2$  mm in diameter and 25 mm rigid length) [188]. In addition, it didn't require high voltage signals ( $< 30$  V) to be driven, while its main advantage is the possibility to perform imaging with very high frame rates (up to 25 fps for a FOV of 50  $\mu\text{m}$ ) [189].

However, due to the existence of several mechanical constraints, the control of this type of device requires significant optimizations, which affects its linear displacement and its ability to perform homogenous and repetitive scanning patterns as well as limiting its imaging Field Of View (FOV) [181], [190], [191]. In addition, spiral and lissajous scanning patterns, that suffers from the non-uniform FOV illumination, are the most common adopted scanning patterns when using this scanning technique due the difficulty of generating the raster pattern. The use of these patterns (spiral and lissajous) makes the photon counting and the image reconstruction process too sophisticated, while avoiding the geometrical image distortions associated with these patterns become more difficult.

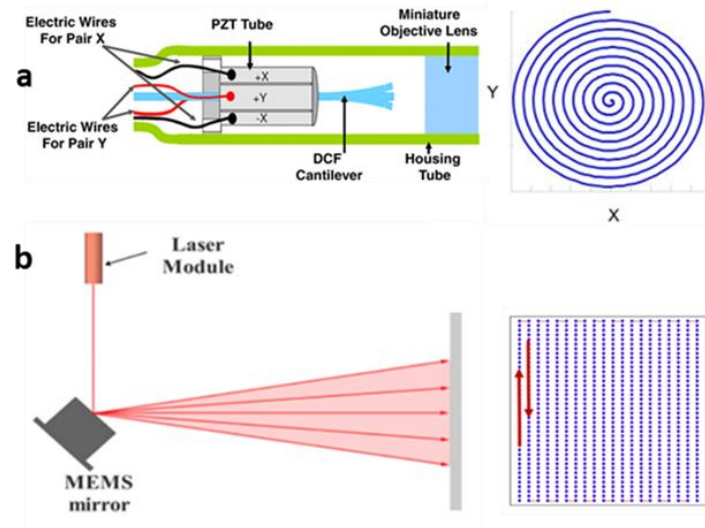


**Figure 1.32:** Illustration of the fiber scanning technique using a PZT tube [179] and the beam scanning technique using a MEMS mirror [192].

The second scanning technique is the beam scanning technique with a Micro-Electro-Mechanical System (MEMS) mirror (figure 1.32 b). It consists of implementing, at the exit of the endoscopic fiber, a micro-mirror plate attached to several actuators that allows the plate to rotate in two dimensions, ensuring therefore the scanning of the outgoing beam. The scanning mirror can be micro-fabricated and implemented within a silicon substrate bench that is tilted with  $45^\circ$  to the beam direction and attached to the control circuits on the same chip [193], [194] permitting though a side viewing imaging. Typical MEMS-based scanning systems includes micro-mirrors with a 0.5-2 mm aperture and can achieve a mechanical scanning angle up to  $\sim 30^\circ$  with driving voltages starting from 3V to 120 V depending on the actuation type [195]–[197]. Using MEMS scanning technique, a simple raster scanning pattern can be easily generated (fig 1.29 b). In addition, it has an easy scanning control and could achieve a large imaging FOV with high frame rates. In particular, using an electrostatic actuation provide a high actuation force with a very fast frame rate (up to 10 kHz as operating frequency) with an extremely low power consumption [197], [198].

Furthermore, several types of MEMS mirror, that differs in their actuation mechanism, exists as the figure 1.33 shows. Electrostatic, electromagnetic and electrothermal are the main actuation mechanisms used for MEMS mirror devices development. Each actuation type has different characteristics and advantages over the another one, e.g electrostatic actuation have a small scanning range and needs high driving voltage, but could achieve a high scanning speed with a very low power consumption, while electrothermal could achieve a large scanning fields with a low driving voltage but with a low frame rate [197] (figure 1.33). This heterogeneity of the characteristics offers a good flexibility of choice to the researchers in order to decide which type of actuation to use which corresponds to their specific needs.

	Electrostatic	Electromagnetic	Electrothermal
Driving Voltage	~100V	~3V	~5V
Scanning Range	$\pm 10^\circ$	$\pm 20^\circ$	$\pm 30^\circ$
Linear Control	Complex	Medium	Simple
Integration	Simple	Complex	Simple
Operation Speed	~10 kHz	~1 kHz	100's Hz
Power Consumption	Negligible	~150mW	~85mW
Current	Extremely small	50-100mA	~15mA
Fill Factor	~5%	~5%	25%

**Figure 1.33:** Comparison of several characteristics between electrostatic, electromagnetic and electrothermal actuation mechanisms [197]

Despite its advantages, this technique is less used in two-photon endomicroscopes development that the PZT-based technique due to its high cost or its high sensitivity to electrostatic shock. The major drawback that MEMS-based probes suffers from is their total outer diameter due the relatively large substrates and the drive circuits. Most of the reported MEMS-based probes have a diameter around 5-6 mm [199] which is larger than the diameter of the PZT-based probes ( $< 4$  mm). However, the team of Pr. Huikai Xie reported a new MEMS chips design in order to achieve more miniaturization of the probe head. A total outer diameter of 2.8 mm was further reached, yielding in an OCT imaging probe [199], [200].

Several multiphoton endomicroscopes based on a MEMS scanning mirrors were reported in the literature [165], [172], [201], [202]. In 2006, the first TPF endomicroscope probe head based on a 2-D MEMS mirror was reported by Piyawattanametha, et al. including a 0.75 mm x 0.75 mm electrostatic MEMS mirror, with a fast axis scanning frequency of 3.5 kHz in a raster scanning pattern [201]. Later, Fu et. al assembled a TPF endomicroscope that involves a 5 mm diameter probe head based on a single-lens configuration which includes and electrothermal 0.5 mm x 0.5 mm 2-D MEMS mirror that achieved  $\pm 30^\circ$  as optical scan range and a scanning speed of 7 lines of a raster pattern per second over an area of  $80 \times 130 \mu\text{m}^2$  [171]. Jung et al developed a scanning probe head with 1 cm diameter based on a two-lens configuration and that employs an electrostatic MEMS mirror (figure 1.34 c). They managed to obtain high resolution TPF images over a large imaging FOV [172]. Hoy and co-workers developed a MEMS-based scanning device that also employs an electrostatic MEMS mirror dedicated for TPF imaging. Scanning with a lissajous pattern, their device able to reach an imaging speed of 10 frames per second with a 310  $\mu\text{m}$  as FOV. However, the dimensions of their device were large  $10 \times 15 \times 40 \text{ mm}^3$  (figure 1.34 a&b) [202].

Overall, MEMS scanners have a big potential to be more widely used in TPF endomicroscopes development. Reducing the probe diameter and its components size is still representing a big engineering challenge for endomicroscopic applications.

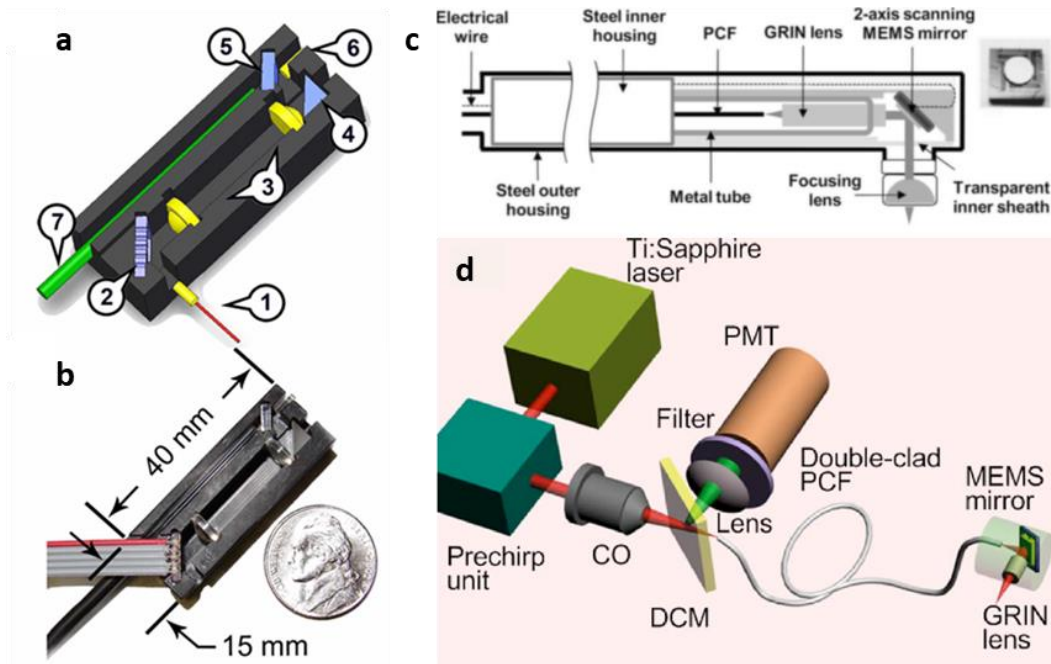


**Figure 1.34:** (a&b)  $10 \times 15 \times 40$  mm MEMS-based probe reported by hoy et al [202] 1: Endoscopic fiber with a GRIN collimating lens; 2: 2D MEMS mirror; 3: miniature aspheric relay lenses; 4: mirror; 5: dichroic mirror; 6: GRIN objective lens; 7: plastic optical fiber. (c) MEMS scanning probe reported by Jung et al. [172]. (d) Illustration of a TPF endomicroscope coupled with MEMS-based imaging probe reported by Fu et al. [171]

#### 1.5.4.4 Miniature objective lens

Moreover, choosing the high-quality miniature imaging optics of the scanning probe is considered too important for TPF endomicroscope development. The main optical component is the objective lens. It should be optimal to reach a small excitation focus with a high NA with a millimetric or sub-millimetric size in order to achieve high lateral and axial resolution as well as a high excitation and collection efficiency. It should have also a good optical performance over a broad spectral range, a compact size, and a high ability to reduce chromatic aberration. For instance, gradient-index (GRIN) lenses, have been widely employed as objective lenses in TPF endomicroscopes due to their cylindrical geometry and their small diameter [165], [166], [171], [182], [203]. Mostly, a GRIN objective lens with a diameter of  $0.35\sim 3$  mm and a NA of  $0.3\sim 0.6$ , can generate lateral and axial resolutions respectively within the order of  $1\sim 2$   $\mu\text{m}$  and  $5\sim 20$   $\mu\text{m}$ , [163].

Nevertheless, this lens type didn't succeed to overcome efficiently the chromatic aberration artifact that leads to a considerable focal shift between the NIR excitation beam and the visible TPF signals and therefore to reduce the TPF signal collection efficiency figure 1.35 (a) [167], [204].

Recent advances in the development of micro-optics led to develop other lens designs that have been employed to avoid the GRIN lenses drawbacks. Y. Wu et al. proposed a TPF endomicroscope that employs a miniature compound lens composed from pair of aspherical lenses with 2.2 mm as diameter (figure 1.35 b) as an objective instead of GRIN lens in order to improve the chromatic aberration correction and therefore the collection efficiency of TPF signal. They conducted a study to compare the performance of their compound lens objective configuration (figure 1.35 b) with a GRIN lens objective configuration (figure 1.35

a) at the same conditions of magnification and NA for both configuration [167]. As a result, they managed to improve the TPF signal collection efficiency by a factor of 9 and by a factor of 4 for SHG.

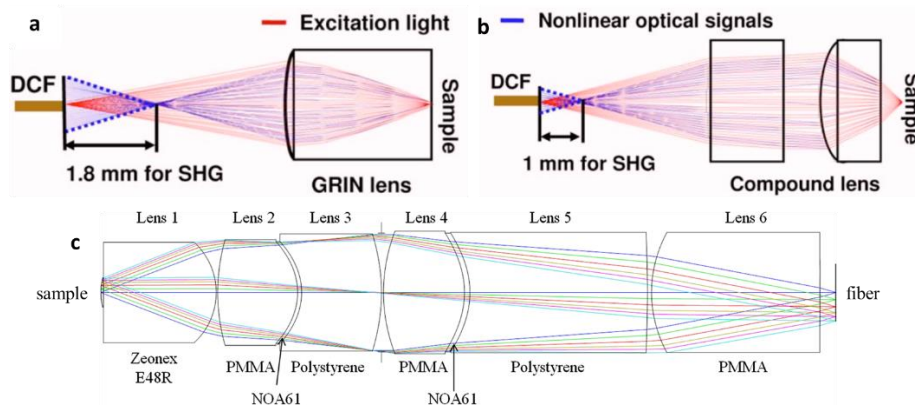


**Figure 1.35:** Representative ray plots for excitation light (red rays) in the forward direction from the fiber (DCF) to the sample and for the TPF collected signal (blue rays) in the backward direction for two objective lens configuration based on a GRIN lens (a) and a compound lens (b) reported by Y. Wu et al. [167]. (c) Custom achromatic objective lens design composed from 6 lenses reported by M.R Kyrish et al [205]

Other teams adopted the use of custom designed lens configuration that consist of combining four to six aspheric and achromatic lenses (figure 1.35 c) in order to reach an optimal collection efficiency for TPF an SHG signals [204]–[207].

However, these configurations suffer from the costly and complicated fabrication process of miniaturized achromatic and aspherical lenses as well as their accurate assembly. Furthermore, the use of several lenses leads to increase the length of the objective configuration (~10 mm) which reduces the flexibility needed to reach certain organs compared to GRIN objective lens [204].

#### 1.5.4.5 State of the art in Two-photon endomicroscopy

As mentioned previously, two-photon fluorescence imaging is widely used in several biomedical applications. Several research groups in the world have proposed developing miniaturized two-photon fluorescence setups for cell/tissue examination. However, due to the high development cost, few groups developed setups for endoscopic applications or for surgery guidance with a serious intent to achieve clinical trials stage. These setups generally differ in the choice of the main excitation wavelength, the detection modality, the endoscopic fiber design, and the miniaturized scanning systems technique with their associated micro-objective lenses.

Among the most successful setups reported are those developed by the team of Professor Min Gu of Swinburne University [164], [208], [209]. Their setup employs a 2.5 m length commercial DCF from Fibercore and an excitation wavelength of 800 nm. Two detection modalities consisting of TPF and SHG signal are included. Their scanning probe consist of a PZT-based scanner with a diameter of 3 mm.

Another setup was reported by the group of Professor Chris Xu of Cornell University [210], [211]. Their setup includes a commercial hollow core photonic band-gap fiber, where they excite using two excitation wavelength 800 nm for TPF imaging with a relative high

excitation power and 406 nm to perform reflectance imaging as well. Their imaging probe consist of a PZT-based scanner with a diameter of 5 mm and is able to perform imaging over a large FOV (1150x1150  $\mu\text{m}$ ). However, their system does not include a SHG detection module, while their endoscopic fiber has a relative short length (1m).

The team of Professor Frédéric Louradour of Limoges university has been working in the last years on the development of a TPF endomicroscope [184], [189], [212]. Their setup includes two excitation modules with two different laser sources where they used 760 and 850 nm in order to optimally excite NADH and FAD, respectively. They used two-pulse pre-compensation unit (one for each laser source) based on a GRISM line that includes transmission gratings. Indeed, their used endoscopic fiber is similar to the one used by our team which consist of customized PC-DCF but with a smaller core diameter (3.55  $\mu\text{m}$ ). Their imaging probe consist of a PZT-based scanner with a relatively small diameter (2.2 mm) and able to perform TPF imaging with high speed (25 images per second). Their detailed setup architecture is presented in figure 1.36. Recently, they added a TCSPC detection module to realize FLIM acquisitions [189], [212].

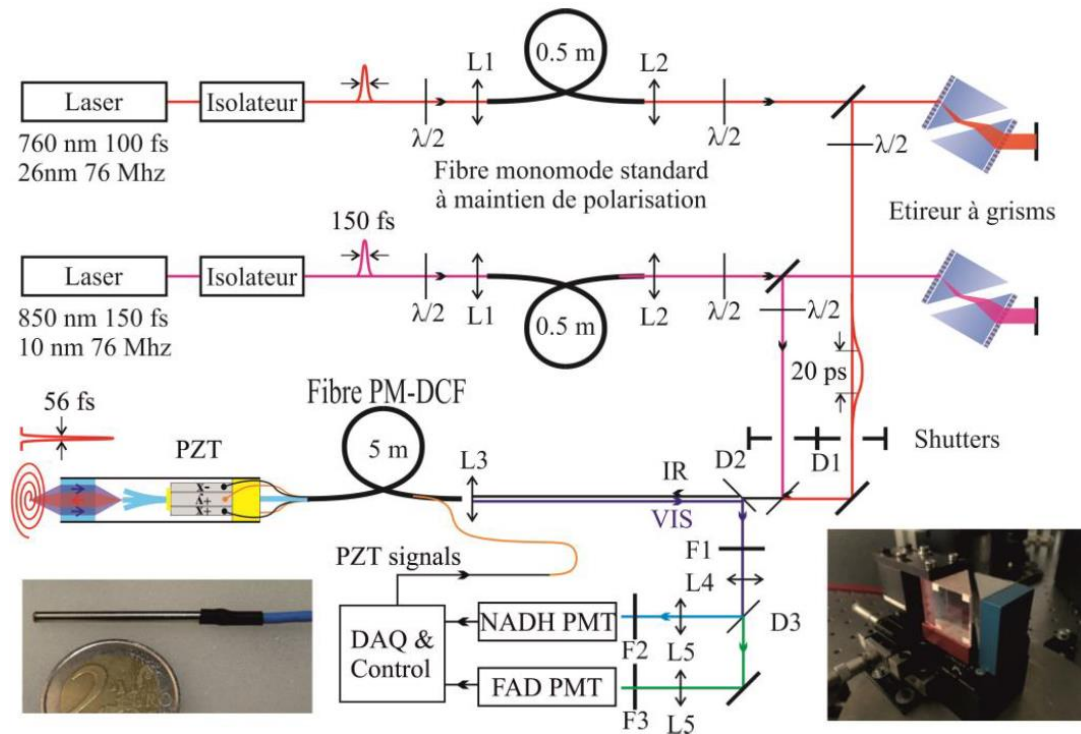


**Figure 1.36:** Schematic of fibred endomicroscope architecture, coupled with a PZT-based scanning probe, reported by the team of Frédéric Louradour at Limoges university (France) [189]

Recently, the team of professor Ki-Hun Jeong at KAIST (Korea Advanced Institute of Science and Technology) reported a TPF endomicroscope for in vivo imaging applications [190]. Their setup employs a commercial DCF from Fibercore with a possibility to excite with two wavelengths, 840 or 880 nm (figure 1.37 a). Their imaging probe consists of a PZT-based scanner that includes in addition a micro-tethered-silicon-oscillator (MTSO) (figure 1.37 b) in order to separate the biaxial resonant scanning frequencies. This technique allows them to ensure scanning following a lissajous pattern with 99% in scanning density

and imaging speed of 5 frames per second. However, their used endoscopic fiber length was too short (17 cm) which make it unsuitable for intraoperative imaging.

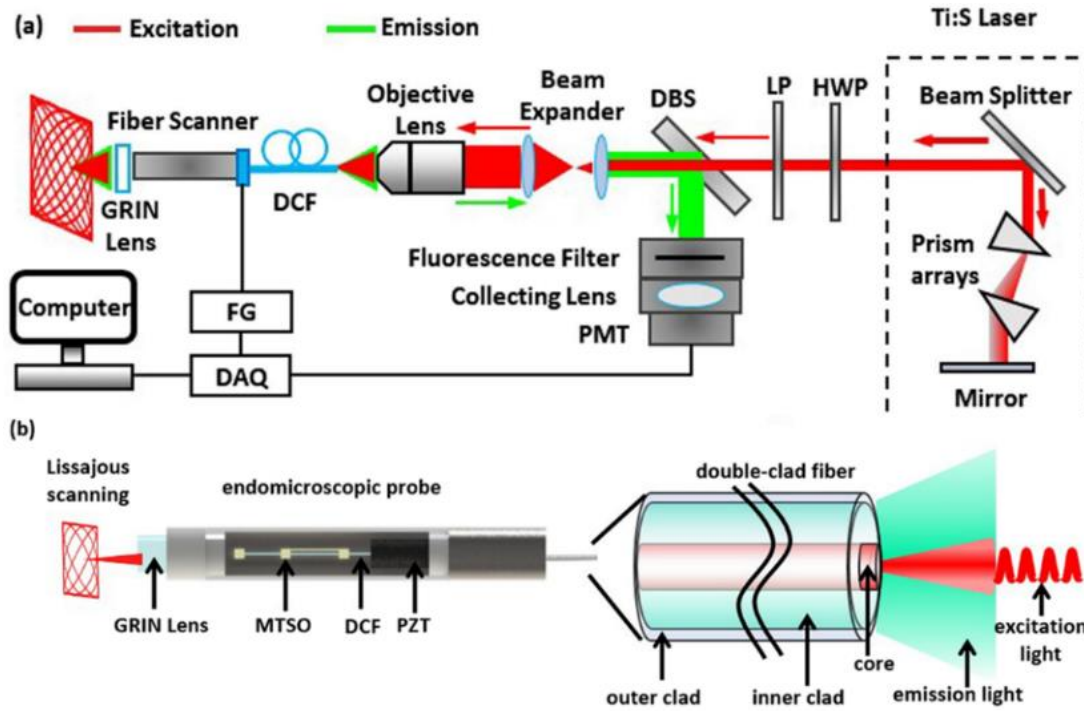


**Figure 1.37:** Schematic of the fibred endomicroscope architecture (a) and the PZT-based scanning probe (b) reported by the team of Ki-Hun Jeong at Korea Advanced Institute of Science and Technology [190].

However, all ex vivo/in vivo imaging tests performed by the mentioned groups were realized on a few rat/mice or fixed human samples in order to demonstrate the imaging abilities of their developed setups. In addition, the architecture of the reported setups was not built for clinical use and does not provide quantitative information necessary for a reliable diagnosis establishment. Indeed, no tissue database construction was reported by any of these groups, which indicates the non-capacity of these developed setups to be transferred in the surgical area.

Table 1.2 summarize the main characteristics of the TPF endomicroscope setups developed by the four mentioned groups and compare it the characteristics of our actual developed TPF endomicroscope.

	<b>Our system (University of Paris)</b>	<b>Min Gu (Swinburne University of Technology)</b>	<b>Chris Xu (Cornell University)</b>	<b>Frédéric Louradour (Limoges University)</b>	<b>Ki-Hun Jeong (Korea Advanced Institute of Science and Technology)</b>
<b>Fiber</b>	customized PC-DCF 5m length 6.4/185 $\mu\text{m}$ core/outer cladding diameter	Commercial DCF (SMM900, Fibercore) 2.9 m length 3.6/125 $\mu\text{m}$ core/outer cladding diameter	commercial hollow core photonic band-gap fiber (HC-800-2, NKT Photonics) 1 m length 7.5 $\mu\text{m}$ core diameter	customized PC-DCF 5m length 3.55/188 $\mu\text{m}$ core/outer cladding diameter	Commercial DCF (SMM900, Fibercore) 17 cm length 3.6/125 $\mu\text{m}$ core diameter
<b>Excitation wavelength</b>	800 nm	800 nm	800 nm 406 nm	760 nm 850 nm	840 or 880 nm
<b>Pulse duration</b>	57 fs	70 fs	110 fs	56 fs	100 fs
<b>Excitation power</b>	up to 70 mW (higher power could be achieved)	up to 30 mW	up to 60 mW	up to 120 mW	-
<b>Scanning system</b>	MEMS	PZT	PZT	PZT	PZT coupled with a MTSO
<b>Probe head diameter</b>	4 mm	3 mm	5 mm	2.2 mm	2.6 mm



<b>FOV</b>	450x450 $\mu\text{m}/4\text{ V}$	475x475 $\mu\text{m}$	1150x1150 $\mu\text{m}$	250x250 $\mu\text{m}/$ 30 V 450x450 $\mu\text{m}/60\text{ V}$	400x450 $\mu\text{m}$
<b>Frame rate</b>	2 fps/ 450x450 $\mu\text{m}$ FOV	1.7 fps/475x475 $\mu\text{m}$ FOV	4.1 fps/200 $\mu\text{m}$ FOV	4 fps/450x450 $\mu\text{m}$ FOV 8 fps/250x250 $\mu\text{m}$ FOV	5 fps/100 $\mu\text{m}$ FOV
<b>lateral resolution</b>	0.4 $\mu\text{m}$ (with GRIN lens)	1 $\mu\text{m}$	0.5 $\mu\text{m}$	0.8 $\mu\text{m}$	0.7 $\mu\text{m}$
<b>Detection modalities</b>	TPF SHG FLT Spectroscopy	TPF SHG	TPF Reflectance	TPF SHG FLIM	TPF SHG
<b>Target</b>	Fresh human brain tissues	mouse tail/rat kidney tissues	mouse lung tissues	rat/mouse/ human skin & lung tissues	mouse kidney/ear tissues
<b>Quantitative analysis</b>	YES	NO	NO	NO	NO
<b>Tissue data base</b>	YES	NO	NO	NO	NO

**Table 1.2:** comparative table which highlights the different characteristics of our developed TPF endomicroscope system as well those of the systems reported in literature

## 1.6 Thesis project

In the previous two sections, the different optical imaging techniques that were brought into the surgical field to respond the medical challenges of brain tumor resection were presented. A wide-ranging presentation of these techniques, their advantages and their limitations were enumerated as well as the most developed tools that are attracting interest. In the last few decades, a significant progress was noticed in developing intraoperative optical imaging tools with their corresponding commercialized systems. With the Raman spectroscopy Handheld probe [78] or the confocal fluorescence endoscopic probes [156], [157], these label-free tools gave an important add to the medical field. Combining these tools with other modalities that provide complementary tissue information can enhance their effectiveness and their diagnosis establishment reliability.

However, and despite this technological progress, medical challenges faced by neurosurgeons during brain tumor resection are still presented. The developed tools are still in proof of concept stage and they did not reach yet the mass clinical trials stage. In addition, their tissue differentiation ability did not reach the reliability that is strong enough to be applied for clinical standards. Consequently, they are not considered as a reliable standard tool that could be used or to be implemented in routine clinical protocols. One of the major technical missing elements in the development to this point is the lack of multimodal contrasts and analysis, as well as the rely on a high quality tissue database on the studied organ that support the diagnosis establishment.

In this context, the research group of Dr. Darine Abi Haidar, at IJCLab laboratory, had a different perspective to face this medical challenge. This research team carries multidisciplinary skills and strong expertise in microscopy techniques and non-linear optics as well as biology, biochemistry, and tissue characterization.

Looking to what have been developed, the advantages and the limitations of each imaging technique and to the various approaches described in the literature, and based on their expertise, they adopted a specific approach to develop an imaging tool that respond to all the medical and technical needs. This approach will offer a tool that is able to provide a high spatial resolution at the cellular scale, to be label-free and with no use of chemical agents or external markers, miniaturized and adapted to the surgical operating room as well as to be able to provide a fast, reliable and reproducible multimodal diagnosis response. For every specific need, they proposed its solution to overcome the presented issues. Table 1.3 show each need with its proposed solution.

<b>Needs</b>	<b>Proposed solution</b>
High resolution: cellular scale	Two-Photon microscopy
Non-toxic/label free	Endogenous fluorescence
Fast response	Intraoperative guidance
Reliable diagnosis	Multimodality of contrasts
In vivo Miniature Imaging system	Endomicroscope

**Table 1.3:** For each specific need its corresponding proposed solution

To this end, a research project was created to develop a multimodal two-photon fluorescence endomicroscope along with a big high quality optical tissue database that characterize optically all types of brain tissues.

As a member in this research project, I conducted my PhD thesis for three years at the IJCLab laboratory. This laboratory is a research mixed unit (UMR 9012) of the French National Center of Scientific Research (CNRS: Centre National de la Recherche Scientifique) and of the University of Paris-Saclay and University of Paris.

Before starting my thesis work, several scientific obstacles have already been raised to meet the challenges described. A first test prototype of a two-photon excitation endomicroscope has already been built up. Through this setup, a pre-compensation unit based on a GRISM line has been implemented and tested [173]. Different commercially available double clad fibers have been characterized in order to determine the best one to be suited to this application [168]. Maximal achievable resolution and collection efficiency that could be reached when combining these fibers with GRIN objective lenses was also investigated [175]. These preliminary studies reached conclusions about an available architecture for a two-photon endomicroscope, however the perfect suited fiber did not yet exist. So, they described the ideal fiber as a combination of some of the tested fibers, thus leading to the development of a custom made DC-PCF.

In collaboration with PhLAM laboratory (Laboratoire de physique des lasers, atomes et molécules, UMR 8523, Laboratory of laser physics, atoms, and molecules) in the city of Lille-France a specific microstructured double clad fiber, was custom made and specially designed for our endomicroscope. This specific fiber was set up and the optical characteristics of the pulse were analyzed at the output of this unique endoscopic fiber. The delivery of ultrashort pulses (around 30 fs) at the exit of 5 meters' length of this endoscopic fiber has been ensured.

Based on these conclusions and these technical achievements, the first objective of my thesis was improving the existing endomicroscope setup and its excitation efficiency by increasing the excitation power with preserving a short pulse duration. Indeed, it was necessary to improve the collection efficiency by optimizing the quantitative spectral and fluorescence lifetime detection in order to investigate our endomicroscope ability to excite and to collect the autofluorescence signal

The second objective was building a second prototype dedicated to large investigation of human brain fresh tissues autofluorescence generated through the endomicroscope. We aimed to determine the ability of our developed system to generate a high quality signal, to exploit the collected signal and to inspect its potential to provide the needed quantitative information necessary for tissue discrimination

The third objective was to overcome another technical challenge, the miniature scanning system development in order to achieve the stage of a multimodal endomicroscope. The goal was to design the best adaptable scanning probe head for TPF imaging that meets our technical needs and satisfy our clinical needs. Therefore, this scanning system is dedicated to performing qualitative imaging acquisitions through its integration, in the future, with the endomicroscope setup and to be coupled with the endoscopic fiber to ensure intraoperative imaging.

For this reason, a collaboration was established between our research team and the team of Pr. Huikai Xie from Biophotonics and Microsystems Laboratory (BML) of the University

of Florida. This laboratory is specialized in the micro/nanofabrication technology of innovative integrated microsystems, optical MEMS, micro-mirrors, micro-actuators, with affordability for medical, industrial, space and consumer electronics applications. Through this collaboration, our team was able to obtain the components of a customized miniature scanning system based on a 2D electrothermal MEMS mirror.

However, the interest of any instrumental development dedicated to a clinical purpose relies on its ability to analyze and interpret a biological signal as well as to establish a reliable diagnosis response. For that, supporting our endomicroscope with a high quality tissue database is necessary to ensure a real-time diagnosis establishment. The construction of our tissue database is oriented to establish for each brain tissue type (healthy and cancerous) its specific optical signature. Therefore, we used three different platforms to perform multimodal and multi-scale measurement, ranging from DUV to NIR, to image different staged brain samples. Table 1.4 summarize the three excitation ranges with the measurement modalities and platforms used in each range as well as the excitation wavelength that could be used.

<b>Range</b>	<b>DUV</b>	<b>VIS</b>	<b>NIR</b>
<b>Location</b>	Soleil Synchrotron	Sainte-Anne Hospital	IJCLab-Orsay
<b>Platform</b>	DISCO beamline	Bimodal one-photon endoscope	PIMPA platform
<b>Wavelength</b>	270-340 nm	375 & 405 nm	690-1040 nm
<b>Modalities</b>	Widefield imaging Fluorescence spectroscopy	Fluorescence spectroscopy Fluorescence lifetime	TPF imaging SHG imaging Spectral imaging FLIM

**Table 1.4:** The three different platforms used in this thesis work and the measurements modalities implemented in each platform.

First of all, a cooperation protocol was launched with the neurosurgery and the neuropathology department in Sainte-Anne hospital. This protocol allows our team receiving all types of fresh human brain tissue samples issued from resection operations. Furthermore, a spectroscopy setup based on visible one photon excitation fluorescence endoscopic probe is implemented close to the operating room. Through this endoscope, bimodal measurements including spectral and fluorescence time analysis could be acquired, using 375 nm and 405 nm as excitation wavelength.

After receiving the sample, and after being analyzed using the one photon endoscope, fresh samples are directed to our laboratory, located in Orsay-France, to complete the analysis. In IJCLab laboratory, we have an access into the “plateforme d’imagerie multiphotonique du petit animal” (PIMPA). This platform consists of a benchtop microscope, combining a confocal and a multiphoton fluorescence microscopic setup. Thus configured, this platform has the specificity of combining together different imaging modalities (spatial, temporal,

and spectral), multimodality of major importance for in-vivo experiments. Through this platform, we were able to perform TPF imaging, SHG imaging, FLIM and spectral imaging to analyze the auto-fluorescence in the NIR spectral range of the received samples.

The second Partner in our tissue database construction is SOLEIL synchrotron (Source Optimisée de Lumière d’Energie Intermédiaire du LURE). It’s a research center Located on the “Plateau de Saclay” in Saint Aubin-France, that consists of an electron accelerator that produces synchrotron radiation, with a spectral range from infrared to hard X-rays, an extremely powerful light that permits exploration of inert or living matter (<https://www.synchrotron-soleil.fr/en>). Working on DISCO beamline (Dichroism, Imaging, mass Spectrometry for Chemistry and biology), that delivers a radiation beam in the DUV range, gave us the access to two different setups optimized to work in spectral range. The first setup is a micro-spectrometer called POLYPHEME dedicated to performing spectroscopic measurements, while the second one consists of a widefield fluorescence microscope called TELEMOS. This collaboration gave our team the access to a wider range of excitation light as well as to study the autofluorescence of new fluorophores that cannot be excited in the visible or the NIR spectral range.

Through these different setups and this multiscale excitation, we were able to highlight and to analyze with multimodal contrasts the fluorescence emission of several endogenous fluorophores. These fluorophores are presented in table 1.5 with their specific spectroscopic excitation and emission properties.

<b>Fluorophore</b>	<b>Molecular type</b>	<b>Efficient excitation range</b>	<b>Maximum emission wavelength</b>
Tyrosine	Amino Acid	250-290 nm [83]	300 nm [83]
Tryptophan	Amino Acid	250-310 nm [83]	350 nm [83]
Collagen	Structural Protein	265-325 nm [83]	390 nm [83]
Nicotinamide Adenine Dinucleotide (NADH)	Co-enzyme	300-380 nm [83]	440 nm for protein-bound NADH 460 nm for free NADH [83]
Flavin Adenine Dinucleotide (FAD)	Co-enzyme derivative of riboflavin	370-450 nm [83]	530 nm [213]
Lipofuscin/Lipopigments	Lipids	400-500 nm [82]	580 nm [82]
Porphyryns	Protein prostatic group	400-450 nm [83]	630 & 690 nm [83]

**Table 1.5:** Light absorption and emission characteristics of all endogenous fluorophores that their fluorescence was analyzed and highlighted in this thesis work.

Similar to the instrumental development, and before my PhD start, this database has reached an advanced stage in term of data collection, analysis, and treatments of a big set of multimodal data.

The proof of concept of the qualitative aspect of our imaging technique, which consists of TPF+SHG imaging, was validated. “Blind” histological analysis was realized by expert neuropathologists in Sainte-Anne Hospital on our database TPF+SHG images, to discriminate healthy from tumor samples. Therefore, they were able to recognize the different tissue types with high sensitivity (88%) and a high specificity (71%) [98]. A large study using Multiscale excitation and multimodal measurement managed to establish several discrimination factors between healthy, primary and secondary brain tumors with an excellent sensitivity and specificity that exceeds 92% [214]. Furthermore, optical coefficients (scattering, absorption and anisotropy) of the main brain tumors types were investigated in the visible wavelength range [215], while another study managed to discriminate through qualitative factors grade I from grade II meningioma [216].

During my thesis, my work on the tissue database was a continuous work to that has been started since the creation of this project. The first objective was to complete the tissue database with the non-investigated tissue properties, such as optical coefficients in the phototherapeutic window. The second objective was to respond to several tissue-database related problematics such as the effect of the post-excision measurements time on the tissue fluorescence properties and the potential of the reliance on the formalin fixed sample instead of fresh one to build tissue database.

The third objective was to implement new treatment and analysis methods to improve the tissue discrimination reliability by searching for new discrimination parameters. Indeed, we aimed to render our tissue database more specific by trying to discriminate quantitatively and through multimodal contrasts, the different grades issued from the same brain tumor type.

To this end, several tasks were addressed in my thesis work on both, the instrumental development, and the tissue database construction. The different tasks and problematics that have been responded are enumerated below and each task will constitute a chapter in this manuscript, presented as a scientific paper:

- 1) What is the utility behind using ultrashort duration and high power excitation laser pulses in an endomicroscope and what is the effect of these pulses on brain tissues autofluorescence?
- 2) Does the autofluorescence properties extracted through a fibred-endomicroscope have the ability to discriminate different brain tissue types, and therefore reliable to be used for intraoperative diagnosis establishment?
- 3) Toward multimodality: design and characterization of a miniature 2D scanning probe head based on an electrothermal actuation MEMS mirror.
- 4) What is maximal post-operation time which permits to measure correctly the autofluorescence signal? Should a tissue database be acquired using only fresh samples?

- 5) Does the multimodality of contrast in NIR window permits to define reliable discrimination parameters between healthy and tumors tissues? Investigation of scattering, absorption, and anisotropy properties of human brain tumoral tissues in the NIR wavelength range.
- 6) Towards a more specific tissue database: Could quantitative multimodal and multiscale optical analysis discriminate low grade and high grade glioma from healthy brain tissues?
- 7) Could quantitative multimodal and multiscale optical analysis discriminate grade I and grade II meningioma from healthy brain tissues

## Chapter 2

# What is the utility behind using ultrashort duration and high power excitation laser pulses in an endomicroscope and what is the effect of these pulses on brain tissues autofluorescence?

### 2.1 Context of the study

As mentioned in the introduction, the motivation behind building a multimodal TPF endomicroscope arise from addressing the clinical need to detect infiltrative and diffuse brain tumor cells surrounding tumor borders, at a cellular scale, during surgery and without the use of exogenous contrast. Although it is well-known that these infiltrative tumor cells that have migrated beyond the solid tumor region are the main cause of tumor recurrence [30]. Intraoperative imaging modalities currently used to guide brain tumor resection such as intraoperative MRI or intraoperative ultrasound imaging, lack the spatial resolution and the sensitivity required to detect these cells.

Recently, confocal fluorescence endomicroscopy has been introduced into the operating room to provide high-resolution images in the sub-micron range [158]. However, the superior spatial resolution comes at the cost of a reduced imaging depth, the need for exogenous contrast and phototoxicity. On the other hand, TPF imaging, provide similar spatial resolutions and image contrasts to confocal fluorescence, but with the added benefit of imaging deeper into tissue and inducing less photobleaching [217]. For these reasons, exploiting the impact of two-photon excitation process generated via a TPF endomicroscope became a crucial step towards our goal of providing an accurate intraoperative diagnosis response.

Theoretically, shorter excitation pulses duration, under a constant mean power, increase the probability of two-photon absorption, thereby increasing the fluorescence emission intensity without being distorted from light scattering or absorption effects [218]. Before the start of this study, our team had already successfully designed and set up a pulse compression and pre-compensation unit based on a GRISM line so that excitation pulses of 300 fs down to 40 fs is possible at the exit of our customized PC-DCF endoscopic fiber [173]. However, shorter pulses increase the laser peak power, which could, in turn, increase the risk of photobleaching and tissue damage within the excited tissue volume. In literature,



and as summarized in the table 2.1 below, previous reported studies had similar conclusions while others reached opposing conclusions.

Reference	Experimental Setup	Biological Specimen	Effect of compressed excitation pulse duration
K. Konig et al. [219]	780 and 920 nm excitation (complete pulse durations and mean power)	In vitro Chinese hamster ovarian cells	Faster photobleaching and cell death
S.N. Arkhipov et al. [220]	800 nm excitation 19, 42 and 100 fs pulse duration 5 & 15 mW	In vivo Drosophila larvae	Faster photobleaching and cell damage
P. Xi et al. [221]	810 nm excitation 12 fs and 100 fs pulse duration 10 mW	Fixed mouse tissue and fresh rat tendon	Signal enhancement, no changes in photobleaching rates
Saytashev et al. [222]	37 fs and 100 fs pulse duration	Drosophila melanogaster	Signal enhancement, Reduced cell death
D. Pestov et al. [223]	14 fs and 280 fs	Human melanoma tissue and rat red blood cells	Signal enhancement, Photobleaching independent on pulse shape
H.J. Koester et al. [224]	75 fs to 3.2 ps	layer 5 neocortical neurons in rat brain slices	Signal enhancement, Photobleaching independent on pulse shape

**Table 2.1:** Summary of reported studies that investigated the effect of exciting of short duration excitation pulse on biological cells/tissues.

Therefore, before converting the bimodal endomicroscope to a miniaturized multimodal endomicroscope for intraoperative imaging, it was necessary to characterize the effect of compressed laser excitation pulse durations on neuronal tissues and to investigate the induced biological effect of exciting tissue with such pulses? In particular, the main question that this study aim to address is: What is the risk of inducing photodamage in brain tissue when exciting with ultra-short duration pulses (<100 fs)

**Methods** Eight human brain tissue samples were provided by our collaborators at Sainte Anne Hospital. These samples were resected and fixed in a formalin solution. They are originated from patients with different brain tumor types: GBM, metastatic tumors,

meningioma, and epilepsy control samples. Excitation pulse durations from 340 fs down to 40 fs were applied using the TPF endomicroscope and were validated by imaging samples on a benchtop multiphoton microscope.

Fluorescence lifetime changes was used to probe any induced molecular damage within the excited region of the tissue. These changes would suggest changes in the pH, local temperature, or protein binding that would happen in the case of cell distress or damage. Additionally, a photobleaching study was conducted using the benchtop multiphoton microscope setup. Tissue samples were continuously irradiated with short pulse durations (100 fs), simulating the highest incident irradiance expected for future imaging with the intraoperative TPF endomicroscope as well as the highest irradiance that is currently used with the multimodal multiphoton microscope, as part of the tissue database construction.

**Results and conclusion** Three endogenous fluorescence properties of ex vivo brain tissues were monitored to investigate the desired improvement of TPF fluorescence signal and to exploit if short laser pulse durations using 800 nm and 890 excitation wavelength caused any photo-induced tissue damage: 1) the overall TPF signal intensity, 2) the spectral shape of the detected spectra and 3) the fluorescence lifetime properties of several endogenous fluorophores (NADH, FAD, Lipopigments and porphyrins. A decrease in the fluorescence intensity would indicate photobleaching and possible photo-induced damage. In contrast, changes in the spectral shape would mean changes in the absorption coefficients of the excited fluorophores, which would occur if these fluorophores had undergone molecular changes.

The characteristic fluorescence spectral shapes and lifetime values did not change with pulse duration but had the desired effect of improving the TPF intensity. In both studies, the endoscopic and the imaging one, the TPF intensity decrease according to  $\tau_p^{-b}$ , where  $\tau_p$  is the pulse duration in femtosecond with an exponent value  $b=1.21\pm 0.17$ , which is close to the theoretical value of 1. The extracted fluorescence lifetime values did not change with elongated irradiation, indicating no significant photochemical changes in the microenvironment of fluorophores during irradiation. Finally, photobleaching will eventually occur at a rate that depends on the excitation irradiance, but rather independent on the excitation pulse duration. The results from this study suggest that pulse durations compressed to 40-120 fs is sufficient to generate efficient TPF and SHG signals without causing morphological or metabolic changes in neuronal tissues for a given mean laser power. Therefore, a pulse duration of 40 fs was implemented in our imaging protocol for the new developed TPF endomicroscope prototype, where a large cohort of fresh human brain samples was used to investigate the endomicroscope ability to generate a bimodal quantitative information that is reliable for tissue discrimination and though for diagnosis establishment, as described in the next chapter.

## 2.2 Paper: The Impact of Compressed Femtosecond Laser Pulse Durations on Neuronal Tissue Used for Two- Photon Excitation Through an Endoscope

www.nature.com/scientificreports

# SCIENTIFIC REPORTS

**OPEN** **The Impact of Compressed Femtosecond Laser Pulse Durations on Neuronal Tissue Used for Two-Photon Excitation Through an Endoscope**

Received: 6 June 2018  
Accepted: 11 July 2018  
Published online: 24 July 2018

Mira Sibai<sup>1</sup>, Hussein Mehidine<sup>1,7</sup>, Fanny Poulon<sup>1</sup>, Ali Ibrahim<sup>1</sup>, P. Varlet<sup>3,4</sup>, M. Juhaux<sup>1</sup>, J. Pallud<sup>2,4,6</sup>, B. Devaux<sup>2,6</sup>, A. Kudlinski<sup>5</sup> & Darine Abi Haidar<sup>1,7</sup>

Accurate intraoperative tumour margin assessment is a major challenge in neurooncology, where sparse tumours beyond the bulk tumour are left undetected under conventional resection. Non-linear optical imaging can diagnose tissue at the sub-micron level and provide functional label-free histopathology *in vivo*. For this reason, a non-linear endomicroscope is being developed to characterize brain tissue intraoperatively based on multiple endogenous optical contrasts such as spectrally- and temporally-resolved fluorescence. To produce highly sensitive optical signatures that are specific to a given tissue type, short femtosecond pulsed lasers are required for efficient two-photon excitation. Yet, the potential of causing bio-damage has not been studied on neuronal tissue. Therefore, as a prerequisite to clinically testing the non-linear endomicroscope *in vivo*, the effect of short laser pulse durations (40–340 fs) on *ex vivo* brain tissue was investigated by monitoring the intensity, the spectral, and the lifetime properties of endogenous fluorophores under 800 and 890 nm two-photon excitation using a bi-modal non-linear endoscope. These properties were also validated by imaging samples on a benchtop multiphoton microscope. Our results show that under a constant mean laser power, excitation pulses as short as 40 fs do not negatively alter the biochemical/ biophysical properties of tissue even for prolonged irradiation.

Maximal safe resection is the first line of defence against tumours of the central nervous system<sup>1</sup>. In fact, the extent of resection is a significant prognostic factor, whereby complete or near complete resection can prolong overall patient survival<sup>2</sup>, while also improving their quality of life<sup>3</sup> compared to patients with sub-optimal resection. A complete resection is typically assessed by comparing the tumour volume that is determined from contrast enhanced T1- and T2- weighted Magnetic Resonance Imaging (MRI) before and after surgery, whereby removing more than 90% of a tumour is considered a near complete resection<sup>4</sup>. The challenge in achieving complete resections is mostly attributed to the necessity of preserving functional tissue, the increased ineffectiveness of pre-MRI based neuronavigation as the surgery progresses due to the increased brain shift and deformations, as well as due to the inability of current intraoperative imaging to identify sparse infiltrating tumours that have migrated beyond the bulk tumour<sup>4</sup>. While the first two challenges are alleviated by functional and anatomical intraoperative imaging, such as tractography and intraoperative MRI where available, state of the art image-guidance cannot delineate diffuse tumours from normal tissue or identify sparse malignant foci that have infiltrated into adjacent tissue. These residuals are the main cause of high relapse rates among patients, where recurrence originates from within 2 cm of the resection cavity<sup>5</sup>. Intraoperative MRI, for example, has a spatial resolution of only 3 mm due

<sup>1</sup>IMNC Laboratory, UMR 8165-CNRS/IN2P3, Paris-Saclay University, 91405, Orsay, France. <sup>2</sup>Neurosurgery Department, Sainte-Anne Hospital, Paris, France. <sup>3</sup>Neuropathology Department, Sainte-Anne Hospital, Paris, France. <sup>4</sup>IMA BRAIN, INSERMU894, Centre de Psychiatrie et de Neurosciences, Paris, France. <sup>5</sup>Université Lille, CNRS, UMR 8523-PhLAM Laboratory, F-59000, Lille, France. <sup>6</sup>Paris Descartes University, Paris, France. <sup>7</sup>Paris Diderot University, Sorbonne Paris Cité, F-75013, Paris, France. Correspondence and requests for materials should be addressed to D.A.H. (email: abihaidar@imnc.in2p3.fr)

SCIENTIFIC REPORTS | (2018) 8:11124 | DOI:10.1038/s41598-018-29404-0

1

### 2.2.1 Introduction

Maximal safe resection is the first line of defense against tumors of the central nervous system [225]. In fact, the extent of resection is a significant prognostic factor, whereby complete or near complete resection can prolong overall patient survival [226], while also improving their quality of life [226] compared to patients with sub-optimal resection. A complete resection is typically assessed by comparing the tumor volume that is determined from contrast enhanced T1- and T2- weighted Magnetic Resonance Imaging (MRI) before and after surgery, whereby removing more than 90% of a tumor is considered a near complete resection [227]. The challenge in achieving complete resections is mostly attributed to the necessity of preserving functional tissue, the increased ineffectiveness of pre-MRI based neuro-navigation as the surgery progresses due to the increased brain shift and deformations, as well as due to the inability of current intraoperative imaging to identify sparse infiltrating tumors that have migrated beyond the bulk tumor [227]. While the first two challenges are alleviated by functional and anatomical intraoperative imaging, such as tractography and intraoperative MRI where available, state of the art image-guidance cannot delineate diffusive tumors from normal tissue or identify sparse malignant foci that have infiltrated into adjacent tissue. These residuals are the main cause of high relapse rates among patients, where recurrence originates from within 2 cm of the resection cavity [30]. Intraoperative MRI, for example, has a spatial resolution of only 3 mm due to the low magnetic field strength in the majority of the devices and thus has the potential for tumor cells of volumes less than 174 mm<sup>2</sup> to be left undetected [228].

Fluorescence-guided resection (FGR) on the other hand, in the form of 5-Aminolevulinic Acid (ALA) induced Protoporphyrin IX (PpIX), is the current standard of care in Europe [151]. It has been a valuable and practical adjunct in achieving safe, complete resection, even beyond the tumor margins defined by MRI [151], [228]. However, ALA-PpIX FGR, among other optical techniques [151], [229], presents sub-optimal sensitivities and specificities to efficiently identify low-grade tumors or even diffusive high-grade tumors at the time of resection. That is because available intraoperative optical imaging modalities utilize a broad excitation beam and diffuse remitted light from the tissue; and as a result, they will inherently have a limited spatial resolution in the sub-millimeter to millimeter range [151], [229]. Intraoperative confocal microscopy on the other hand, enables visualization of live tissue cyto-architecture with spatial resolutions from 0.4 to 1.2  $\mu\text{m}$ , yet at the expense of imaging depth and increased photobleaching and tissue damage [158]<sup>9</sup>. Moreover, endogenous structures do not provide sufficient contrasts for confocal fluorescence microscopy and hence exogenous contrast agents are required.

Nevertheless, it is still worthwhile to expand the clinical utility of light-based techniques because of its practicality as well as its unique biophysical properties when applied to the tissue. The unique advantage over other common intraoperative modalities is that the derived intrinsic optical signals can directly relate to the physiological and metabolic state of tissue [230]. Optical measurements should interrogate tissue preferably non-invasively at the sub-micron level and without exogenous contrast, to exploit these advantages optimally. Label-free high-spatial resolution optical imaging can provide the surgeon with a fast microscopic assessment of tumor margins at the surgical cavity as well as from the resected tissue, potentially alleviating the need for time-consuming standard histopathology, while better ensuring no tumor cells are left behind. This is possible using non-linear optical

excitation schemes to measure, for example, two-photon emission fluorescence (TPEF) and second harmonic generation (SHG) from endogenous fluorophores.

In non-linear optical imaging, because the distribution of the excitation light must be concentrated in space and time, the non-linear signal is only generated from within a confined tissue volume, and the detected signal is mostly attributed to ballistic photons rather than multiple scattering photons [217]. As a result, two-photon imaging exhibits superior imaging properties compared to conventional linear optical microscopy, where images have spatial resolutions and image contrasts reaching those obtained from confocal microscopy, but with the added benefit of imaging deeper into tissue and inducing significantly less photo-bleaching and tissue toxicity [217]. Although the theoretical advantages of two-photon excitation have been well established for decades, clinical use of two-photon microscopy has only recently gained momentum as pulsed laser systems and dispersion pre-compensation units are becoming more assessable.

As eluded above, shorter excitation pulses increase the probability of two-photon absorption, while maintaining the average power constant. In fact, an inverse relationship between the amplification in TPEF or SHG with pulse length has been proposed [218], [231], [232]. However, since shorter pulses increase the laser peak power, it is critical to prevent photobleaching or photo-induced tissue damage within the focal volume. To date, only a limited number of studies have evaluated the photochemical changes that may occur under these excitation conditions. The rate of photo-induced tissue damage *in vitro* was evaluated and compared to typically used longer pulses either by direct monitoring of the fluorescent images with time or by studying cell viability assays post-irradiation [219]–[224]. Published studies arrived at opposite conclusions; KÖnig et al. and Arkhipov et al. observed faster photobleaching rates and more cell damage using laser excitation pulses shorter than 100 fs [219], [220], while Xi et al., Saytashev et al., Pestov et al., and Koester et al., found that shorter pulses actually reduced cell lethality under the same radiance exposure [221]–[224]. Since the overall aim is to diagnose and analyze tissue during craniotomy and since ultrafast excitation pulses enhances the efficiency of two-photon fluorescence [218], [233], it is essential to test whether these ultrafast excitation pulses could induce photo-toxicity or tissue damage. Here, we evaluate the potential for neuronal tissue damage of *ex vivo* human brain under different excitation laser pulses by measuring the tissue's spectral and fluorescence lifetime properties. During these studies, we kept the mean laser power constant typically used in two-photon microscopy for optically thick tissue

Monitoring changes in the characteristic spectral shape and fluorescence lifetimes of common endogenous fluorophores allows one to detect biochemical and metabolic changes that occur in tissue at the sub-micron and cellular levels in real-time, prior to the tissue undergoing macroscopic structural transformations. Specifically, distortion in the fluorescence spectrum and reduction of the emitted fluorescence intensity can indicate photo-degradation and photobleaching as it is used to assess the efficacy of photodynamic therapy [234]. In the case of photobleaching, the initial fluorophore undergoes structural changes resulting in having altered spectral absorption and emission properties [234]. Therefore, under the same measurements conditions (NA of the objective, mean laser power, and pulse repetition frequency), any changes in the spectral shape (not intensity) should correspond to changes in the molar absorption coefficient which will only occur in turn if the fluorophore has been molecularly transformed. As the tissue scattering properties at the

excitation wavelength may to some degree still affect the generated TPEF signal [235], changes in the fluorescence lifetimes of these fluorophores are also measured to validate conclusions drawn from the spectral analysis. Since fluorescence lifetime measurements are self-referenced [236], the derived characteristic lifetime values are insensitive to many of the biophysical factors mentioned above. Changes in lifetime values correspond rather to alterations in the fluorophore's protein binding properties, its metabolic state, or even changes in the local temperature and pH [236], all of which occur before cell death. Therefore, the goal is to use the complementary capabilities of spectral and lifetime tissue analysis to 'sense' whether compressing the excitation pulse will result in early biochemical changes in the irradiated tissue's micro-environment as an indicator of photo-induced tissue damage, here as a function of the pulse peak power.

With the present nonlinear endomicroscopic setup built in-house, spectrally- and time-resolved point fluorescence measurements can be performed on ex vivo tissue with different short femtosecond excitation pulses at wavelengths ranging from 690–1040 nm. Our custom-built fiber-based endomicroscopic setup is capable of generating excitation pulses from 300 fs down to 25 fs delivered to the distal end of a 5 meter long microstructured double-clad photonic crystal fiber (DC-PCF) [173]. The size, the numerical aperture (NA) and the composition of the DC-PCF core and its inner cladding were optimally selected by numerically characterizing -spectrally and temporally- the laser pulse at the distal end of the DC-PCF after propagating through the compression and pre-compensation unit designed in-house [173]. For brain tissue characterization, the fluorophores nicotinamide adenine dinucleotide (NADH), Flavin adenine dinucleotide (FAD), Lipopigments, and Porphyrins are of interest. For this study, two non-linear optical properties of individual endogenous fluorophores are extracted with this setup, TPEF and the fluorescence lifetime, to evaluate whether the desired fluorescence signal enhancement upon irradiating tissue with ultrashort femtosecond laser pulses (<100 fs) would result in tissue toxicity. While a miniaturized MEMS scanning system is currently being integrated into the system for future in vivo studies, two-photon and FLIM imaging were performed on the same biopsied samples at the multiphoton imaging platform for small animals (PIMPA). The motivation behind using the benchtop multi-photon microscope is that FLIM, TPEF and SHG imaging will further validate possible changes detected by endoscopic measurements across a larger field of view, while also spatially assessing metabolic, morphological, and structural changes that may have been under sampled by point measurements.

## 2.2.2 Materials and methods

### 2.2.2.1 Samples

The study protocol was approved by the human research institutional review board of the Sainte-Anne Hospital – University Paris Descartes (CPP Ile de France 3, S.C.3227). All methods were carried out in accordance with the relevant guidelines and regulations. Eight brain tissue biopsy samples were obtained from Sainte Anne Hospital's neurosurgery department (Paris, France) with the informed consent of the patients and the hospital's review board. The excised samples were fixed and classified as either Glioblastoma Multiforme, Meningioma grade I or II, Metastases, or healthy cortical tissue. The one

healthy sample and three GBM samples were 150  $\mu\text{m}$  thick, while the three meningioma and one metastatic tissue samples were sliced into 3 to 5 mm thick sections.

### 2.2.2.2 Point spectral and lifetime fluorescence measurements with the endomicroscopic setup Instrumentation

The endomicroscopic setup built in-house is shown in Figure 2.1(a). A Titanium: Sapphire laser source (Mai Tai DeepSee, Spectra-Physics, Santa Clara, CA, USA) is pumped with an average power of 2.4 W and is tunable from 690–1040 nm. The Faraday isolator (FI) prevents back reflection reaching the laser cavity. The 0.5-meter-long single-mode fiber and the grating prism, GRISM, line together comprise the compression and pre-compensation unit, which corrects for second and third order dispersion effects, ensuring temporal confinement of the excitation beam and the generation of a Fourier-transform-limited pulse. The laser beam is then injected into the proximal end of a customized double-clad photonic crystal fiber (DC-PCF) characterized and described elsewhere [173]. Briefly, this DC-PCF has a central core diameter of 6.4  $\mu\text{m}$  and an NA of 0.097 (at 800 nm), while its surrounding region is comprised of an air/silica microstructured region with a diameter of 40  $\mu\text{m}$ . The outgoing beam is further focused by passing through a gradient-index (GRIN) lens, (GT-MO-080-018-AC-900-450, GRINTECH, Jena, Germany). The temporal pulse width can be modulated from 300 fs down to 25 fs at a repetition rate of 80 MHz by adjusting the distance between the two prisms of the GRISM line and the angle of the beam incident on the first prism. A dichroic mirror (DM) and a 660 nm low-pass filter separates the collected fluorescence signal from the incoming excitation beam. The beam splitter (BS) divides the fluorescence signal between spectrally (70%) and time-resolved detection arms (30%). A motorized filter wheel (450  $\pm$  10 nm, 520  $\pm$  10 nm, 550  $\pm$  30 nm, 620  $\pm$  10 nm and 680  $\pm$  10 nm) and a hybrid photomultiplier detector assembly (PMA Hybrid 40 PicoQuant, Germany) collects the time-resolved fluorescence, while the spectrometer (QE Pro, Ocean Optics, France) collects the spectrally-resolved fluorescence signal with a spectral resolution of 1.5 nm and across the spectral range of 200 to 1000 nm. The characteristic SHG spectrum of urea in Figure 2.1(b) (known to have negligible autofluorescence and a high SHG signal) obtained at the distal end of the endoscope signifies the fact that the DC-PCF does not generate background autofluorescence despite being 5 meters long. The instrument response function (IRF) of the system (Figure 2.1(c)) from the same urea sample was found to be 13.5 ps after applying a Lorentzian fit. This signifies the system's ability to resolve the fluorescence lifetimes of endogenous fluorophores from the IRF.

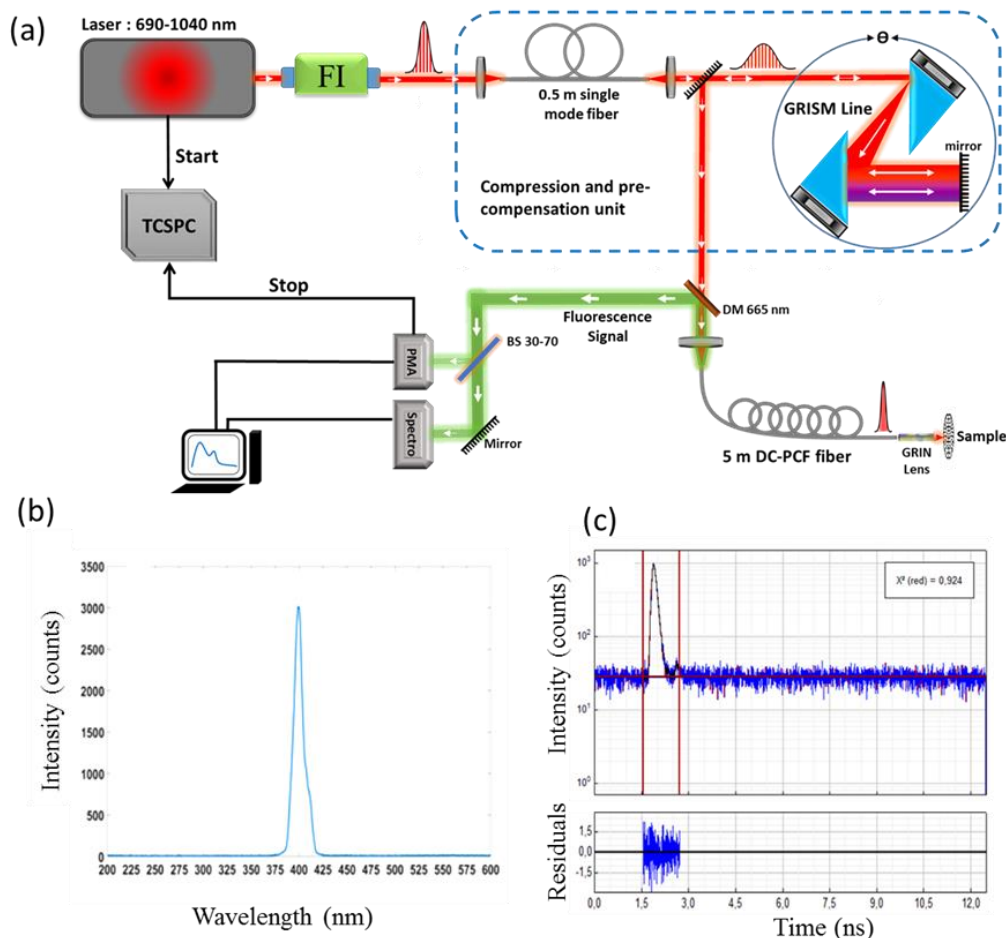


**Figure 2.1:** (a) Schematic of the endoscopic setup. TCSPC: time-correlated single photon counting, FI: Faraday Isolator, DM: dichroic mirror, DC-PCF: double-clad photonic crystal fiber, GRIN: gradient-index lens, BS: beam splitter, PMA: photomultiplier analyzer, and spectro: spectrometer; (b) raw SHG spectrum of urea; (c) fluorescence lifetime of urea fit to a Lorentzian function and its corresponding residual values. All components of the figure are produced by the authors.

### 2.2.2.3 Endomicroscopic measurements at different laser pulse durations

Two fluorescent dyes, Rhodamine B (Sigma-Aldrich) and Fluorescein (Sigma-Aldrich), both dissolved in water, were used as standards to validate their spectral shapes and lifetimes values with theory or data found in literature, prior to tissue measurements. For each standard, a drop of aqueous dye solution yielding a concentration of  $10^{-6}$  M was placed on a microscope slide and positioned as shown in Figure 2.1(a). For all measurements, the average laser power at the sample was 30 mW with a beam size of 0.1 mm and the excitation wavelength was 800 nm. Measurements were taken at pulse durations ranging from 40 fs to 150 fs. The lifetime decays were fitted to a mono-exponential decay function using the FluoFit software from PicoQuant and the characteristic lifetime value of each dye was extracted.

For the ex vivo fluorescence measurements, the fixed tissue samples were placed in the sample holder, and the same measurement variables as used for the fluorescent dyes were employed; the mean power of 30 mW with the range of pulse durations for the 800 nm excitation. For each pulse duration, and for each region of interest (ROI) of the sample, the



time-resolved fluorescence lifetime decay profiles were collected and analyzed using FluoFit software to extract the lifetimes of four endogenous fluorophores: NADH, FAD, Lipopigments, and Porphyrin I. The fluorescence spectra, on the other hand, were first smoothed and then spectrally decomposed using a custom MatLab script to recover fluorescence spectra of these individual fluorophores including Porphyrin II. Per measurement, five ROIs were selected. For statistical analysis, a t-test was performed to test whether the lifetimes for each fluorophore were different in the five ROIs when measured at the same pulse duration. If the lifetimes were statistically similar ( $p > 0.05$  and type II error,  $\beta$ ,  $< 0.1$ ), a one-way ANOVA test was performed on lifetimes from all ROIs as a function of pulse duration. If the five ROIs resulted in significantly different lifetime values for the same pulse duration, a paired t-test was performed for each ROI as a function of pulse duration. In either case, significant differences between the mean lifetime values were determined for a p-value  $< 0.05$ .

#### **2.2.2.4 Multi-modal imaging with the multiphoton microscope Instrumentation**

A multiphoton imaging platform for small animals (PIMPA) comprising the multi-modal multi-photon microscope (Leica TCS SP8 MP, Leica Microsystems, Wetzlar, Germany) and controlled through Leica's acquisition software is the key instrument. The same Mai Tai Ti:Sapphire tunable laser source (690–1040 nm) equipped with an automated dispersion compensation unit was used. The maximum available power varied from 1.8 to 2.4 W for the different wavelengths. The laser pulse can be tuned between 70 fs and 300 fs at a fixed repetition rate of 80 MHz at the output of the cavity. A water-immersion objective was used (HCX IRAPO L 25x NA 0.95), and the field of view at a fixed focal depth was 433  $\mu\text{m}$  by 433  $\mu\text{m}$  for a working distance of 1.5 mm. Two external non-descanning hybrid detectors (Leica Hyd-RLD 2, Leica Microsystems, Wetzlar, Germany) are added to the multiphoton microscope for enhanced two-photon detection, but spectrally-resolved two-photon fluorescence can be obtained as well. A  $448 \pm 20$  nm band-pass filter (Semrock, FF01-448/20-25) is placed in front of the first detector for SHG detection, and a  $520 \pm 30$  nm bandpass filter (Semrock FF01-520/35-25) is placed in front of the second detector for TPEF imaging. A time-correlated single-photon counting (PicoQuant TCSPC module, Berlin, Germany) is added to measure time-resolved fluorescence data. Lifetime images can be spectrally resolved by the two band-pass filters on the detection side.

#### **2.2.2.5 Two-photon imaging and FLIM at different laser pulse durations**

For all ex vivo tissue measurements, the average power at the focal plane was set to 1.85 mW and 1.96 mW when the excitation wavelength was 800 nm and 890 nm, respectively. The two wavelengths, 800 nm and 890 nm were chosen for optimal TPEF and SHG detection, respectively. The same wavelengths were used for FLIM as well. Prior to ex vivo measurements, the power at the objective for different pulse durations was measured. An acquisition of two-photon imaging of the samples required 500 ms, while FLIM required an acquisition time of 2–3 s per sample and the excitation pulse duration varied from 120 fs to 340 fs. TPEF and SHG images were analyzed on ImageJ, while fluorescence lifetime data collected at  $448 \pm 20$  nm and  $520 \pm 30$  nm were combined and

fitted to a two-exponential decay function using the Symptomie software provided by PicoQuant. For each tissue sample, five ROIs were chosen for fluorescence lifetime analysis at each pulse duration. Paired t-tests were performed for examining whether the recovered values differed significantly as a function of the excitation pulse duration. For the photobleaching study, TPEF and FLIM were acquired every minute for 20 minutes after 800 nm excitation at two irradiance conditions. In both cases, the pulse duration was set to 100 fs and the acquisition time was fixed at 20 seconds per image. In the first case, the average laser power was raised to 38 mW, and the TPEF images and FLIM were acquired after 800 nm excitation to emulate the maximum irradiance produced with the endomicroscope as suggested in our preliminary tests [237]; a mean laser power of 20–27 mW is needed to generate a minimal two-photon fluorescence signal in tissue at pulse durations of 40 fs-[237]. For the same irradiance but for 100 fs pulse durations, this maximum laser power corresponded to 38 mW. The second case involved simulating the maximum average laser power used by the multi-modal microscope, which was 8 mW. The same set of measurements were performed on a different region of the sample but at this maximum laser power. Based on ongoing ex vivo measurements, laser powers higher than 8 mW resulted in saturating the sensitive hybrid detectors. In both cases, TPEF was first collected for twenty minutes, then an adjacent ROI was selected for FLIM. The same fitting routine used for the endoscopic lifetime measurements was performed at each time point [215].

## 2.2.3 Results

### 2.2.3.1 Endomicroscopic measurements at different laser pulse durations

To determine if the fluorescence intensity is a function of the temporal excitation pulse width two standard fluorophores Rhodamine B and fluorescein in aqueous solutions were used. This establishes that the temporal excitation pulse width does not confound lifetime measurements for the different tissue metabolic states and microenvironments. Figure 2.2 (a, b) show the normalized fluorescence intensity spectra of Rhodamine B and fluorescein, respectively, following 800 nm excitation with different laser pulse durations. For both dyes, the spectral shape is not distorted as the pulse duration shortens, but the intensity is positively correlated with pulse duration. The fluorescence intensity is amplified five times when the pulse duration is set to 40 fs as opposed to the conventional pulse width of 150 fs for both dyes. Figure 2.2(c) plots the mean fluorescence intensity as a function of pulse duration for both dyes. In both cases, the fluorescence intensity decays with increasing pulse duration as a power function with an exponent  $b = 1.28$  and  $0.94$  for fluorescein and Rhodamine B, respectively. The goodness of fit,  $R^2$ , for each is  $0.985$  and  $0.921$ . Figure 2.2(d) on the other hand, shows that the derived fluorescence lifetime values for both dyes remain constant ( $p > 0.89$ ) at all pulse durations when maintaining the same average power measured at the focal plane.

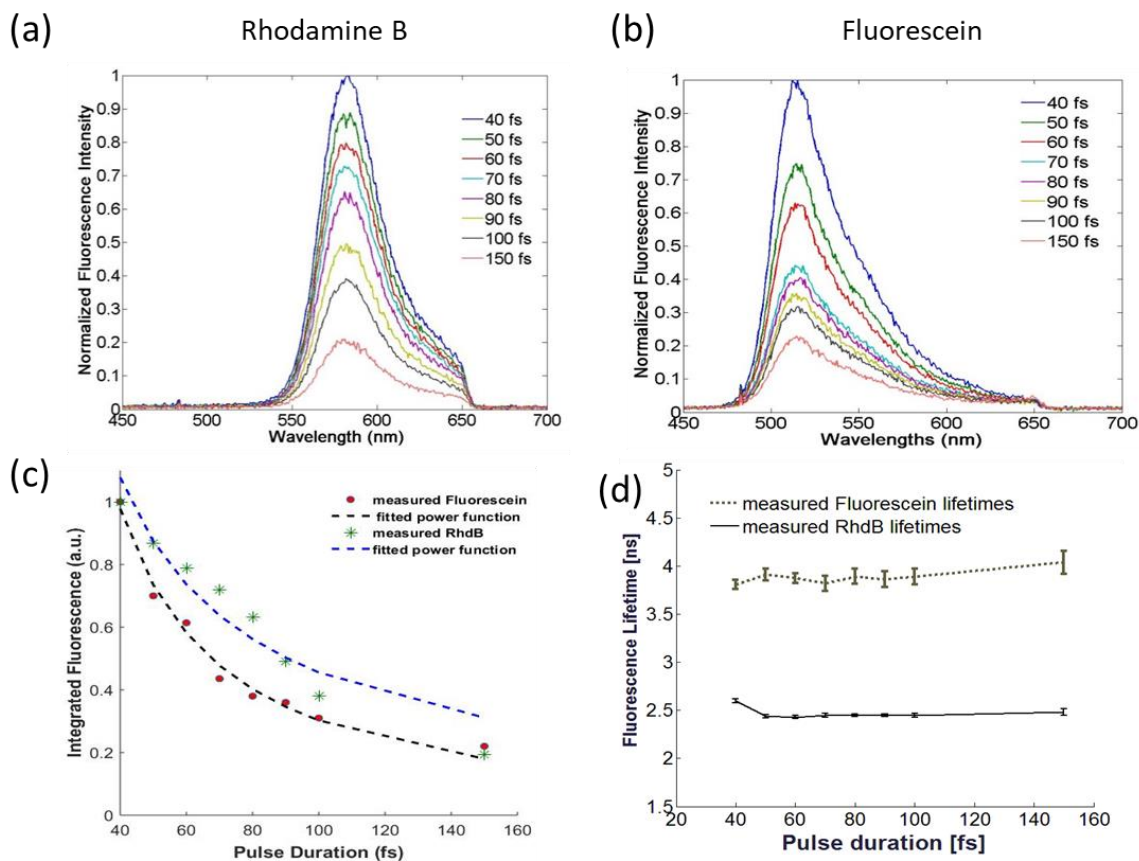


**Figure 2.2:** Fluorescence spectra detected by the endomicroscope at 800 nm excitation and at different laser pulse durations for (a) Rhodamine B and (b) Fluorescein. Each spectrum is normalized to the fluorescence obtained at 40 fs; (c) the integrated fluorescence intensity normalized to that measured at 40 fs, while the dashed curve is the corresponding fit to a power function with exponent  $b$ . The exponent describing fluorescein's decay function is 1.28, while that of Rhodamine B is 0.94; (d) the mean fluorescence lifetime values (ns) for each dye as a function of pulse duration (fs). Error bars correspond to the standard deviation from five measurements per pulse.

A similar effect of pulse duration on the autofluorescence intensities from ex vivo tissue is exemplified in Figure 2.3. The overall fluorescence intensity measured from a glioblastoma multiforme (GBM) sample increases by a factor of 4 when the 180 fs pulse is compressed to 40 fs, while the overall spectral shape is maintained (Figure 2.3(a)). The decay in the fluorescence intensity with longer excitation pulses was best fit to a power function with the exponent  $b = 0.85$ . Figure 2.3(c, d) depict the spectrally unmixed fluorescence at 180 fs and 40 fs, respectively, where spectra of individual fluorophore components can be compared. Previous in vivo spectral measurements in rats with brain tumors were used as a basis to fit NADH [97], and the FAD was adjusted to its basis emission spectrum found in the literature [238], while the remaining three fluorophores were fitted to Gaussian functions. The fluorescence intensity below 420 nm is unaccounted for in our model. However, it is attributed mostly to collagen crosslinks, having an absorption peak at 380 nm. Decomposing the fluorescence spectra into the individual fluorophores was necessary to validate whether different pulse durations altered the biochemical state of these five endogenous molecules used in diagnosing brain diseases. The relative contribution of each

fluorophore remained constant, indicating that no spectral distortion pertaining to any individual fluorophore investigated had occurred as a result of using shorter excitation pulses. In fact, when comparing the peak intensity of each fluorophore at 180 fs and 90 fs pulse duration, for example, the fluorescence signal amplification was found to be  $2.6 \pm 0.24$ . Although Figure 2.3 pertains to results from a GBM sample, similar conclusions were found for all available tissue types: healthy cortical tissue, meningioma, and metastatic tissue, where the exponent of the power function was found to be between 0.85 and 1.35

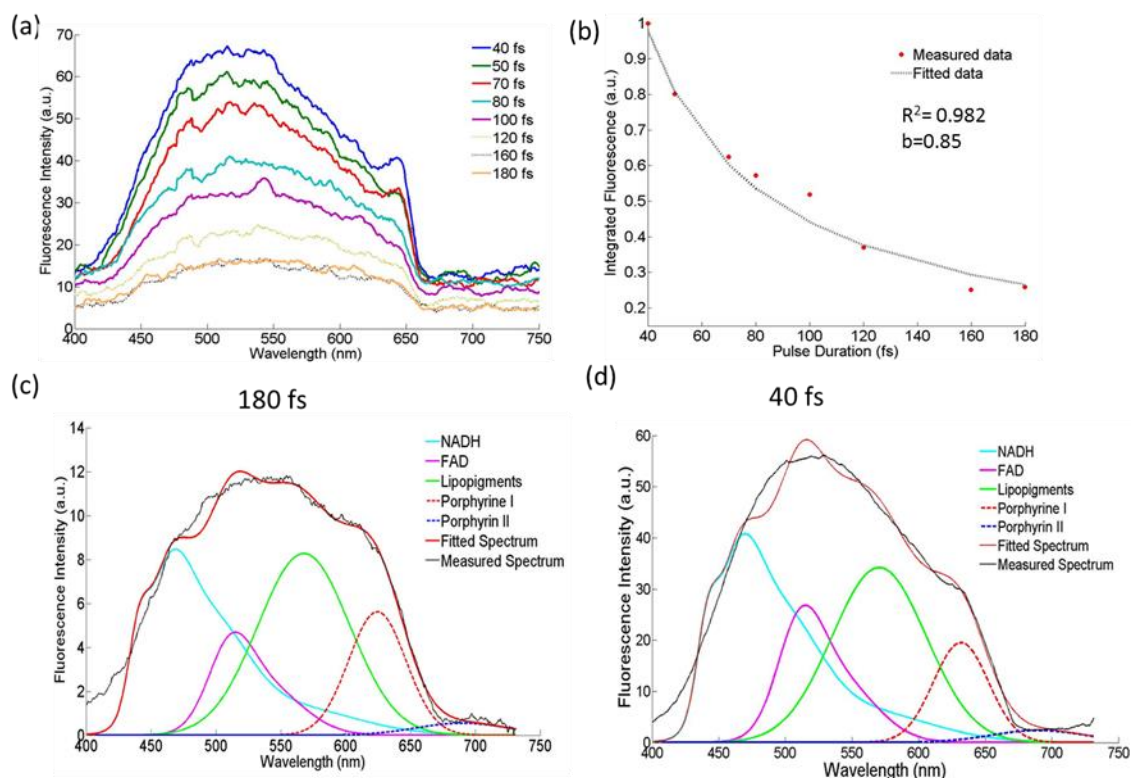


**Figure 2.3:** The effect of pulse duration on TPEF obtained from a GBM sample. (a) The total autofluorescence spectrum at eight different pulse durations; (b) the integrated fluorescence intensity normalized to that measured at 40 fs, while the dashed curve is the corresponding fit to a power function with exponent  $b$ ; (c) spectrally unmixed fluorescence at 180 fs, and (d) spectrally unmixed fluorescence at 40 fs. The model fit and measured total fluorescence are also shown for (c) and (d).

As a means to gauge possible changes in the metabolic and chemical binding state of the relevant fluorophores in tissue, time-resolved fluorescence was performed following 800 nm excitation. The band-pass filters allowed the extraction of the characteristic fluorescence lifetimes of NADH, FAD, Lipopigments, and Porphyrin I after fitting the decay profiles with a mono/bi-exponential decay fit [97], [215]. As an example, the mean lifetimes recovered for each fluorophore from GBM samples is depicted in the histogram of Figure 2.4, where the excitation pulse varied from 40 fs to 220 fs in steps of 20 fs. The error bars correspond to the standard deviations pooled from five different ROI measurements for each of the GBM samples. The deviation in the recovered lifetimes for each fluorophore across all GBM samples did not vary greatly across the region of interests, and more importantly, it did not vary according to the pulse duration applied.

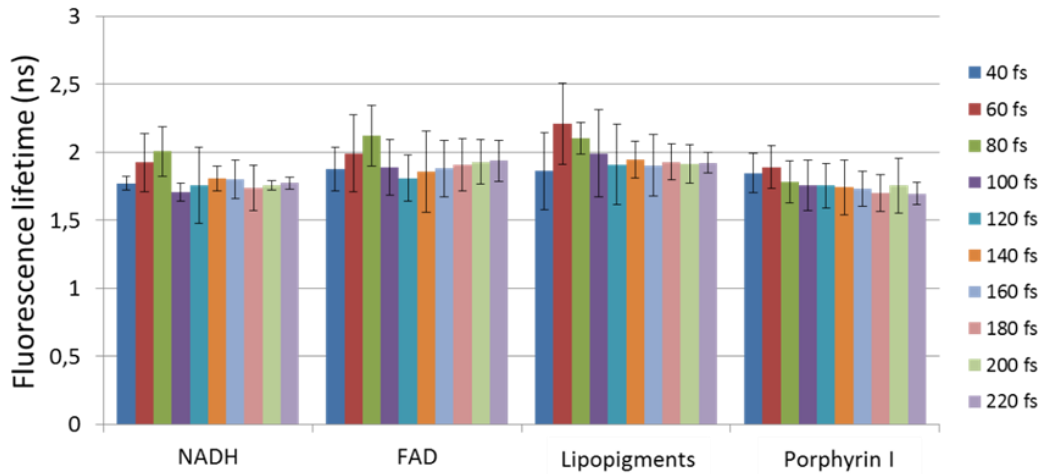


**Figure 2.4:** Bar plot showing the mean fluorescence lifetimes for each fluorophore extracted from endoscopic time-resolved fluorescence measurements at different pulse durations. The error bars correspond to the standard deviations pooled from five ROIs per GBM sample.

The mean fluorescence lifetimes recovered from all pulse duration measurements for each tissue type is summarized in Table 2.2. The minimum p-value calculated from each fluorophore per sample is provided in the last column, indicating there was no significant difference in the lifetime values recovered at different excitation pulses ( $p \gg 0.05$ ) for all four tissue types. As mentioned in the methods section, if under the same excitation pulse, five ROIs resulted in statistically different lifetime values for a given fluorophore, a paired t-test was performed for each ROI instead of an ANOVA test pooled from all five ROIs treated with ten pulse durations. This was the case for the lifetime values of FAD and Lipopigments from healthy cortical tissue, as well as the FAD lifetimes from Meningioma and Metastatic samples. Nevertheless, the minimum p-value among all four fluorophores per tissue type was always larger than 0.29, indicating that short and long excitation pulses resulted in recovering similar fluorescence lifetime values at the 95% significance level and a power of 98%.

Tissue Type	NADH (ns)	FAD (ns)	Lipopigments (ns)	Porphyrin I (ns)	p-value
Healthy Cortex	1.40 ± 0.13	1.53 ± 0.13	1.60 ± 0.15	1.57 ± 0.095	0.81
GBM	1.92 ± 0.13	2.0 ± 0.06	2.0 ± 0.17	1.90 ± 0.079	0.97
Metastatic	1.89 ± 0.14	1.84 ± 0.230	2.02 ± 0.27	3.47 ± 0.012	0.29
Meningioma	1.63 ± 0.095	1.78 ± 0.095	1.92 ± 0.18	3.19 ± 0.67	0.50

**Table 2.2:** Fluorescence lifetime values for each fluorophore averaged across all excitation pulse durations and regions of interests.

### 2.2.3.2 Two-photon imaging at different laser pulse durations

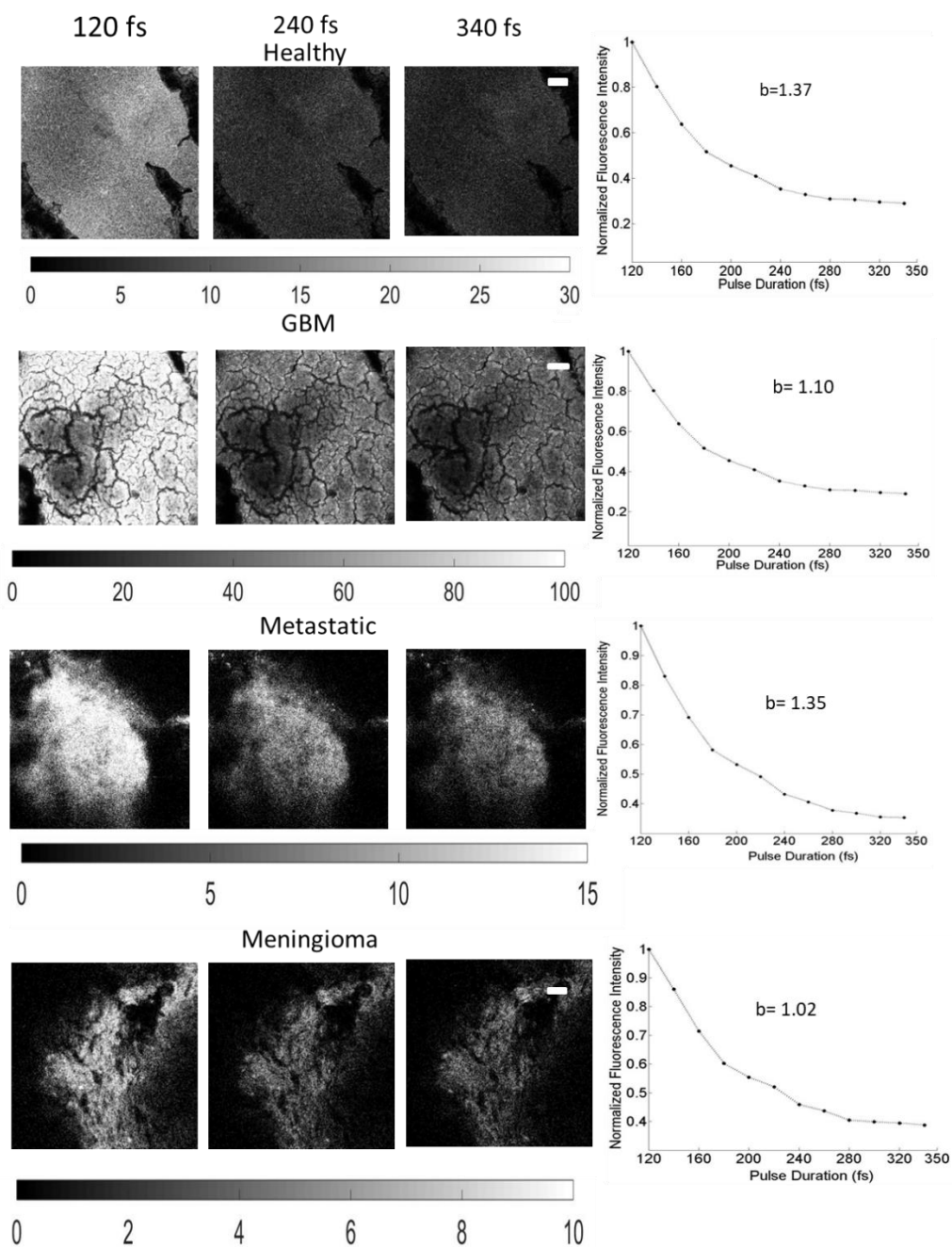


**Figure 2.5:** TPEF images from a healthy cortical tissue sample (first row), GBM (second row), metastatic tissue (third row) and meningioma (fourth row) following an excitation of 890 nm and obtained using a 120 (first column), 240 (second column) and 340 fs (third column) pulse durations. The scale bar for all images correspond to 50  $\mu\text{m}$ , and the gray-scale display range for all three images is shown below one of the TPEF images in brackets. The normalized mean intensity from each TPEF image is plotted in the fourth column as a function of the excitation pulse used. The exponent,  $b$ , of the fitted power function is also displayed.

Figure 2.5 illustrates the quality impact of compressing the excitation pulse duration of two-photon images from healthy cortical tissue (first row), GBM (second row), metastatic

(third row) and meningioma (fourth row) biopsied samples, respectively. The first three columns correspond to TPEF images taken at 120, 240 and 340 fs following 890 nm excitation  $520 \pm 30$  nm detection. The gray scale color bar range was kept constant for all three pulse durations per sample as displayed under each image set, so the superior image quality at the shortest pulse is prominent. Two-photon images from GBM and Metastatic samples also showed significant SHG signal (not shown here). The fourth column of each row shows the fluorescence intensity as a function of excitation pulse averaged across each image and normalized to the mean intensity obtained at 120 fs. All curves were best fitted to a power function with an exponent power,  $b$ , displayed on the plots. For each sample, the TPEF signal decayed with similar values of  $b$  (1.02–1.37). Shortening the excitation pulse by a factor of 2 (from 240 to 120 fs) resulted in an intensity enhancement of at least 2.6 in the TPEF images. TPEF and SHG signals at 800 nm (not shown here) resulted in similar intensity decay profiles to those obtained at 890 nm excitation with the exponent  $b$  ranging from 1.1 to 1.4.

After examining the benefit of shortening the excitation pulse durations towards improved image quality of two-photon imaging with no visual photo-degradation, it was necessary to test whether shorter pulses, induced any changes in the biochemical state of the endogenous fluorophores, mainly NADH and FAD based on the available detection filters. This was first assessed by FLIM as shown in Figure 2.6. Examples of fluorescence lifetime images at the three excitation pulses are shown (Figure 2.6 (a, d, g, i)) for each tissue type. Images are displayed with a common fluorescence lifetime color code since FLIM produced the same extent of lifetime values for all three excitation pulse durations. The distribution of the fluorescence lifetime was extracted by fitting the fluorescence decay profile of a given ROI to a double exponential tail function. The mean lifetimes and corresponding standard deviations were obtained from averaging the values of five ROIs per image and are plotted in Figure 2.6 (b, e, h, k). The dashed lines in each plot correspond to the mean fluorescence lifetimes recovered at all excitation pulse durations. The data points were fitted to this horizontal line, and the resulting root mean square error, RMSE, is shown on the top right corner of each plot, indicating that no linear increase/decrease in the recovered values was observed as a function of pulse duration. Furthermore, a paired t-test was performed to show that there was no significant difference between the recovered values ( $p$ -value = 0.99 and type II error = 0.99). A previously established phasor approach [129], [239] was also applied to the FLIM data to better visualize the consistency in the recovered lifetime values when the excitation pulse duration varied from 120 fs to 340 fs. The phasor plots in Figure 2.6 (c, f, i, l) show that the shape of the 95% confidence ellipse is small and corresponds to almost the same two lifetime values on the universal circle for all pulse durations per tissue type.

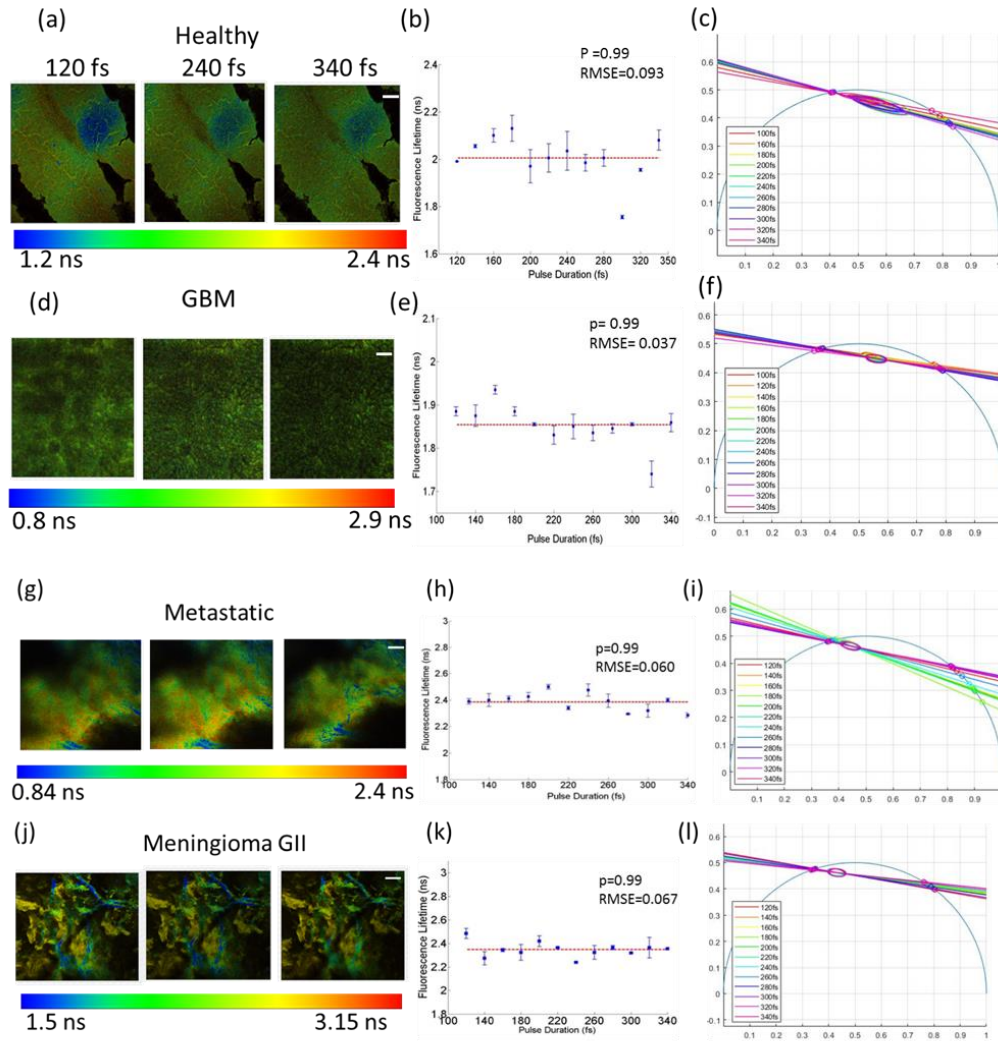


**Figure 2.6:** FLIM analysis: (a,d,g,j) represent fluorescence lifetime images obtained at three excitation pulses for healthy (first row), GBM (second row), metastatic (third row) and meningioma tissue (fourth row), respectively. The scale bar of  $50\ \mu\text{m}$  is displayed in the third column for each tissue type and a horizontal color bar representing the range of calculated fluorescence lifetimes is shown below the set of images. The corresponding mean fluorescence lifetimes are plotted against pulse duration in (b,e,h,k) where error bars correspond to the standard deviations obtained from calculating the values from five ROIs. The root mean square error, RMSE, and p-values  $> 0.05$  indicate no significant difference between the data points based on regression analysis and a paired t-test, respectively. (c,f,i,l) represent the phasor distribution of the fluorescence lifetimes and their intersections with the universal circle at pulse durations ranging from 120 fs to 340 fs.

Since higher laser fluence rates can cause photobleaching, the laser power was tuned to produce the maximum fluence rates used for imaging tissue at PIMPA and the maximum fluence rate that will be used in vivo with the endomicroscope. This was found to be  $22 \times 10^8\ \text{W}/\text{cm}^2$  and  $1.0 \times 10^9\ \text{W}/\text{cm}^2$  for the multi-modal microscope (at 8 mW with 100 fs excitation pulses) and the endomicroscope prototype (at 38 mW with 100 fs excitation pulses) respectively. The corresponding TPEF decay profiles as a function of exposure time are shown in Figure 2.7 (a, b). The photobleaching decay rate is observed to be significantly



slower at the high irradiance case, where the fluorescence intensity only decreased by 11% after 20 min of imaging (Figure 2.7 (b)). In both low and high irradiance conditions, a double exponential best fitted the decay curves ( $R^2 > 0.98$ ) incorporating a fast and slow photobleaching decay constant. At  $2.2 \times 10^8 \text{ W/cm}^2$ , the photobleaching half-life period was 18 min and the photobleaching decay constants were 0.78 and  $0.024 \text{ min}^{-1}$ . The photobleaching half-life period on the other hand of the same sample irradiated at  $1.0 \times 10^9 \text{ W/cm}^2$  was estimated to be 200 min and the photobleaching decay constants were 0.8 and  $0.004 \text{ min}^{-1}$ . The mean fluorescence lifetime for each FLIM acquired every minute is also shown in Figure 2.7 (c, d) after irradiating at  $2.2 \times 10^8 \text{ W/cm}^2$  and  $1.0 \times 10^9 \text{ W/cm}^2$ , respectively. The p-values indicate no significant changes in the lifetime values as a function of exposure time for both cases. Additionally, the mean lifetimes of  $1.55 \pm 0.39 \text{ ns}$  and  $1.51 \pm 0.47 \text{ ns}$  at low and high irradiances are similar, as indicated by the horizontal dashed lines.

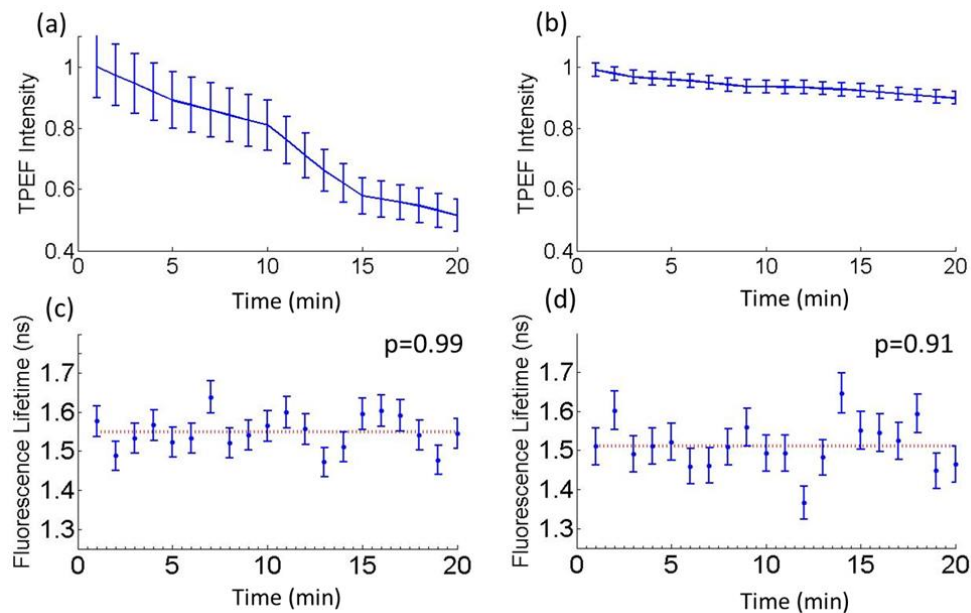


**Figure 2.7:** The decay of the TPEF intensity as a function of exposure time at low (a) and high (b) laser irradiances corresponding to those used on the multi-modal microscope and with the endomicroscope respectively. The error bars correspond to the standard deviation between pixels across a selected ROI. The fluorescence lifetime as a function of time at low (c) and high (d) laser irradiances. The error bars correspond to the standard deviation in the lifetime values calculated for the selected ROI. The horizontal line corresponds to the overall mean lifetime, and the p-value indicates no significant difference in lifetime values when measured for different exposure times based on a paired t-test.

## 2.2.4 Discussion

Maximal surgical resection of solid tumors can be a curative treatment for most cancer patients without local or distal metastasis. Because of the potential for metastasis, surgery is followed by adjuvant chemotherapy and radiation therapy [226]. However, current intraoperative imaging modalities lack the sensitivity and spatial resolution to detect sparse or diffusive tumors [230]. This is more so the case for brain tumors, as their margins can be indiscernible from normal brain tissue, hence increasing the risk of relapse due to the limited

efficacy of chemotherapy in the brain. Accurate tumor margin assessment requires microscopic tissue characterization *in vivo*, in near real-time on the one hand, while also having the ability to analyze the entire resection bed on the other hand. To date, no imaging technology can effectively examine tissue *in vivo* over a large field of view at a cellular level [230], which is the motivation behind developing a varifocal non-linear endomicroscope. It was shown that multiple optically accessible tissue properties could be measured and quantitatively correlated to disease biomarkers [215], [236]; multi-modal optical measurements will provide quantitative histopathological information *in vivo* and for freshly resected tissues during the course of the surgery, stain-free. To generate sufficient non-linear signals such as two-photon fluorescence and SHG, Fourier-transform limited femtosecond pulsed lasers and a high NA at the objective are required to temporally and spatially focus the beam [217]. The excitation pulse duration is inversely proportional to the molecules' two-photon absorption cross section and thus shorter excitation pulses are desired for superior image quality, enhanced imaging depth and for faster acquisition times [218], [231]. Compressing the pulse duration, however, results in quadratically amplifying the peak laser power at the sample, potentially causing photo-induced damage to the tissue [219], [220], [231]. Therefore, as a prerequisite to future *in vivo* studies, it was necessary to study the effect of shortening the excitation pulse duration on tissue microenvironment. The study involved evaluating the spectral and lifetime fluorescence properties of relevant endogenous fluorophores in the brain from fixed tissue samples pathologically classified as healthy cortical tissue, GBM, metastases, or meningioma (grade I or II) as a function of pulse width. Although the endogenous fluorescence properties *in vivo* may differ from that of fixed tissue [215], measurements were performed on Formalin fixed tissue to separate changes in tissue morphology/structure due to autolysis and putrefaction from that induced by altering the laser pulse width for two-photon excitation. Formalin-based tissue fixation has been shown to minimally alter tissue optical properties as well as the characteristic autofluorescence spectra compared to when tissue is frozen prior to optical measurements [240]. Moreover, tissue fixation did not affect the lifetime of fluorescent proteins produced in HeLa cells [241]. Direct monitoring of cell death at its early stage using intensity and lifetime autofluorescence is not new. Wang and colleagues monitored the NADH fluorescence lifetime in cultured Hela cells as well as in 143B osteosarcoma after inducing apoptosis [242]. NADH lifetimes were found to increase for the first 15 minutes of imaging and gradually decrease thereafter [242]. For intensity-based measurements, individual NADH and FAD fluorescence spectra did not seem to change greatly upon apoptosis or necrosis, but rather the redox ratio,  $\text{NADH}/\text{NADH}+\text{FAD}$

, tended to increase systematically after treatments. The difference in the response of NADH fluorescence intensity and NADH lifetimes to metabolic perturbations is probably due to the difference in NADH binding, where the former measurement is sensitive to Complex I binding, while time-resolved NADH fluorescence arise from multiple protein bindings [242]. The shape of the autofluorescence spectra is also known to shift or distort under conformational or environmental changes [242]. Therefore, to identify any initial metabolic transformations that occur at the onset of disease, changes in the TPEF/SHG intensity (Figure 2.5), spectral shape (Figures 2.2 and 2.3), and the fluorescence lifetimes (Figure 2.6) were all used to investigate the influence of compressing the laser's pulse width on tissue.

Endoscopic measurements on fluorescent standards were first performed to test the effect of pulse duration on the photophysical properties of fluorophores removed from the confounding effects of light attenuation in tissue. The characteristic fluorescence spectral shapes (Figure 2.2 (a, b)) and lifetime values (Figure 2.2 (c)) did not change with pulse duration but had the desired effect of amplifying the two-photon fluorescence intensity. Moreover, the non-linear endoscopic measurements resulted in mean fluorescence lifetimes of  $2.46 \pm 0.019$  ns and  $3.89 \pm 0.075$  ns for Rhodamine B and fluorescein respectively, which are consistent with that reported in the literature (2.28–2.34 ns for Rhodamine B and 3.6–4.2 ns for fluorescein) under two-photon excitation [243], [244]. Similarly, shortening the duration of the laser pulses did not alter the photophysical, metabolic and protein-binding states of endogenous fluorophores in *ex vivo* tissue (Figures 2.3 and 2.4 and Table 2.1). Despite tissue being a diffusive medium, the spectral shapes and the relative contribution of each fluorophore to the total fluorescence spectrum remained similar across all pulse durations (Figure 2.3 (c, d)). This is consistent with the study by Dunn et al., where the lateral resolution and the two-photon fluorescence intensity in tissue simulating phantoms were found to be largely independent on tissue optical properties (at both the excitation and emission wavelengths) up to a sampling depth of 250  $\mu\text{m}$  [234], and thus, the same conclusion is expected for excised fresh tissue. In *vivo*, tissue absorption and scattering will be accounted for by measuring the spectrally-resolved diffuse reflectance, which will be incorporated into the endomicroscope and is the subject of future studies. From this study, unmixing the fluorescence spectra and fitting the spectra to that of the five endogenous fluorophores indicate that there may be a peak unaccounted for in our fitting model around or below 400 nm (Figure 2.3 (c, d)). This may be attributed to autofluorescence or SHG from collagen crosslinks as the peak was even more prominent for meningioma and metastatic samples, but not evident in healthy tissue. In the meningioma and metastatic samples, modelling the additional SHG/autofluorescence signal as a Gaussian curve yielded better goodness of fit values and reduced the corresponding overall RMSE. Fitting the SHG/autofluorescence signal for GBM samples, on the other hand, resulted in poor fitting accuracy and was thus not included in the spectral fitting at 800 nm excitation. At 890 nm excitation, on the other hand, the SHG peak of collagen at 445 nm is well characterized in the total fluorescence signal, which was convolved in the TPEF images of Figure 2.5 for GBM and metastatic tissue. The relatively high SHG signals due to increased collagen in meningioma and metastatic brain tissue are described extensively in the literature [216], [244]. In both the endoscopic and imaging study, the two-photon intensities decrease according to  $\tau_p^{-b}$ , where  $\tau_p$  is the pulse duration in femtoseconds and  $b = 1.21 \pm 0.17$ , which is close to the theoretical value of 1 [231]. Deviations from the theoretical trend has been attributed to the spectral broadening of the excitation beam as a result of shortening pulse width, where at ultrashort pulse durations, the spectral bandwidth can surpass the fluorophore's spectral absorption bandwidth, significantly reducing the efficiency of two-photon absorption and in turn its emission [231], [232]. This lower limit in pulse duration therefore depends on the fluorophore's non-linear excitation spectrum [231], [232]. In any case, the close to 1 exponent,  $b$ , suggests that the decays in the two-photon signals from all sampled tissue were not caused by photobleaching, but by the increase in the signal to noise ratio as predicted theoretically.

Pulse durations shorter than 100 fs at the focal plane were not always possible using the microscope setup due to the limited capabilities of the standard automated pre-compensation unit, but, the consistency in the fluorescence lifetime values for all four tissue types suggests that no photo-induced local heating, or changes in the pH or protein-binding states of the relevant biomolecules occurred as a result of compressing the pulses (Figures 2.4 and 2.6 and Table 2.1) for both point-based and microscopic imaging techniques. It is difficult to relate the fluorescence lifetime values recovered from the endoscope with those extracted from imaging for two reasons. First, FLIM data were collected at broader spectral bandwidths (see materials and methods section) where the lifetime values are derived from FAD (free) and from NADH (bound), while the point-based measurements were spectrally filtered to yield lifetime values of NADH, FAD, Lipopigments, and Porphyrin I. Second, the excitation wavelengths were different and thus the relative contribution of NADH and FAD to the overall FLIM signal at 890 nm will differ from that obtained with the endoscope at 800 nm. There is limited data on the fluorescence lifetimes of endogenous molecules in the neuronal tissue under two-photon excitation. The average fluorescence lifetimes in fixed meningioma tissue measured here agree with those found by Zanello and colleagues under two-photon excitation at 810 nm [216]. In the same study, the NADH lifetimes under one-photon excitation (at 405 nm) differed from that under two-photon excitation (810 nm). The only other study involving two-photon FLIM of human brain samples was that by Kantelhardt and colleagues who recovered average fluorescence lifetimes of 1.4 ns in parenchymal tissue and lifetimes of 2.1 ns in GBM [245], under 750 nm, generally matching the values obtained here (Table 1). Incidentally, the relatively wide range of fluorescence lifetime values depicted on FLIM of healthy, metastatic, and meningioma tissue (Figure 2.6) corroborated the need to perform a t-test on the endoscopic lifetime data for a single ROI rather than an ANOVA pooled from several ROIs, highlighting the benefit of wide-field quantitative imaging compared to point detection. Additionally, the small standard deviations relative to the mean values demonstrate that time-resolved fluorescence measurements are reproducible and can potentially be used as a quantitative biomarker (Table 2.1 and Figure 2.6).

The photodamage induced by prolonged two-photon irradiation as a function of excitation power has been studied *in vitro* [223], [232], [246], *ex vivo* [223], [245], [246] and *in vivo* [220], [222], [246], where tissue damage was assessed using different parameters. These mostly included evaluating the rate of photobleaching [223], [232], [246], the rate of temporary photo-enhancement followed by bleaching [220], [223], and the fraction of noticeable morphological damage observed on TPEF intensity images [223], [246]. At first, the literature seems divided whether phototoxicity manifests itself as an overall decay in the fluorescence signal with a photobleaching rate having a 3<sup>rd</sup> to 4<sup>th</sup> order dependence on the mean laser power [247]–[249], or whether phototoxicity is manifested as a sudden increase in the TPEF intensity followed by gradual photobleaching. More so, some studies report both phenomena within different regions of the same sample [222]. However, the confounding results can be explained by the different experimental conditions used, which can be stratified based on the irradiance at the site of measurement. Vogel et al., estimated a theoretical irradiance threshold for cell death at a repetition rate of 80 MHz to be  $8 \times 10^{10} \text{ W/cm}^2$  [250]. At such incident irradiance, plasma formation and cell blebbing from myelin sheath were simultaneously observed in fresh and frozen spinal tissue [250], due to

multi-photon absorption events. Photo-enhancement was the main indicator of photodamage in Gali et. al's in vivo and ex vivo mouse brain study [246], where the threshold for photo-induced molecular damage ranged from  $7 \times 10^{10}$  to  $13 \times 10^{10}$  W/cm<sup>2</sup> for poor and lipid-rich regions respectively. The aforementioned irradiances are at least two orders of magnitude higher than what is used in our project. Nevertheless, the fact that the same manifestations of photodamage was evident for samples collected in vivo, in live cultured cells, as well as in frozen and fixed tissue at these high irradiances [246], regardless of excitation pulse width, suggests that two-photon excitation induced damage is a photochemical effect rather than a physiological effect [223], [246], justifying as well, the use of fixed tissue in this study. Accordingly, if photo-induced damage had occurred, fluorescence lifetime measurements would have indicated so.

The photobleaching study presented here involved irradiating tissue samples at two irradiances simulating the highest incident irradiance expected for future in vivo imaging with the endomicroscope as well as the highest irradiance currently used ex vivo with the multi-modal two-photon microscope at relatively short excitation pulse widths (100 fs). Since the TPEF signal decayed as a bi-exponential function (Figure 2.7(a, b)), both oxygen mediated photobleaching and oxygen independent photobleaching pathways were implicated, which are the same pathways induced under one-photon excitation [251]–[254]. The faster photobleaching decay component has been attributed to the reaction of the fluorophore to molecular oxygen, while the oxygen independent pathway has been characterized with slower photobleaching rates [251]. Our samples were exposed to oxygen for at least 15 minutes prior to tissue fixation and another 15 minutes before acquiring two-photon images. Interestingly, the oxygen-mediated exponential decay caused 30% in the overall reduction of the TPEF signal under  $2.2 \times 10^8$  W/cm<sup>2</sup>, the maximum irradiation used on the multi-modal microscope, while it resulted in only 3% in the overall fluorescence decay under  $1.0 \times 10^9$  W/cm<sup>2</sup>, the maximum irradiation expected on the endomicroscope. This explains the faster photobleaching kinetics at  $2.2 \times 10^8$  W/cm<sup>2</sup>, where imaging of the same region of interest needs to be completed within the first few minutes. The rate of photobleaching does not only depend on the irradiance and the presence of oxygen, but on the local distribution of chromophores as well as the concentration of fluorophores [253]. The variation in the fluorophore concentration for different ROIs could further explain the difference in photobleaching kinetics at  $2.2 \times 10^8$  W/cm<sup>2</sup> vs.  $1.0 \times 10^9$  W/cm<sup>2</sup>. Similar photobleaching kinetics was observed by Samkoe et al. where faster photobleaching occurred when live CV-1 kidney cells were irradiated with  $3 \times 10^7$  W/cm<sup>2</sup> compared to when the cultured cells were irradiated with  $6 \times 10^7$  W/cm<sup>2</sup> [251]. This was explained by the fact that oxygen consumption is slower under lower irradiance conditions and thus, the oxygen dependent regime lasts longer [251]. Additionally, in the same study by Samkoe et al., the oxygen-mediated photobleaching decay constant did not vary between the low and high irradiance conditions, but rather the relative contribution of each photobleaching pathway depended on irradiance; this is also observed here (0.78 vs. 0.80 min<sup>-1</sup>).

Time-resolved fluorescence measurements did not change with prolonged irradiation (Figure 2.7 (c, d)), indicating no significant photochemical changes in the microenvironment during irradiation. The difference in the response of autofluorescence intensity and lifetime after prolonged two-photon excitation has also been observed in several photodamage studies [241], [255], [256] and was attributed to the difference in each method's sensitivity to the

fluorophore's biochemical state and microenvironment. In fact, Blinova et al., found that time-lapsed NADH fluorescence lifetime measurements under similar excitation and emission wavelengths used here, were sensitive to NADH binding to dehydrogenases, while fluorescence intensity based measurements were sensitive only to NADH associated with Complex I, providing another explanation for the observed differences [255]. A limitation of the photobleaching study is that TPEF and FLIM were detected across a broad spectral range (428–555 nm) and thus assessing individual endogenous fluorophores and their binding states was not possible. Therefore, under these conditions, one can conclude that the decay in the fluorescence intensity (Figure 2.7 (a, b)) is due to the reduction in the overall amount of endogenous NADH and FAD as a result of continued two-photon excitation, while the constant fluorescence lifetime values (Figure 2.7 (c, d)), corresponding only to bound NADH and free FAD, indicate that their local microenvironment, metabolic state, and their protein binding states did not change following prolonged two-photon excitation. Nevertheless, it could be possible that the origins of photobleaching and formation of oxidative species may not be detected with spectral range of the current detectors ( $\sim 420\text{--}550\text{ nm}$ ) and will be addressed in a pre-clinical brain tumor model prior to clinical intra-operative imaging.

It is important to reiterate that in the work presented here, compressing the excitation pulse duration did not result in photobleaching or any changes in the fluorophores' properties when the mean laser power (1–2 mW), pixel dwell time (1.2  $\mu\text{s}$ ), and repetition rate (80 MHz) was maintained for 800 and 890 nm excitation wavelengths. Therefore, the precise effect of shortening excitation pulses will not only depend on pulse length but also on the very fluorophore, tissue volume, pixel dwell time, laser wavelength, the repetition rate and whether the excitation pulse is transforming limited or chirped.

### 2.2.5 Conclusion

The benefit of employing shorter laser pulses is well documented and further validated here on ex vivo brain tissue samples of different pathologies; The laser-induced tissue toxicity possible at these pulse durations due to thermal or photophysical effects have however, not been investigated despite the recent developments of compact ultrashort two-photon imaging modalities. This work studied the relationship between endogenous autofluorescence when tissue is two-photon excited at different pulse widths. Higher TPEF and SHG signals are achieved at shorter pulses without causing distortion in the spectral shape of individual fluorophores, nor any deviations from the expected inverse relationship between TPEF/SHG intensity and pulse duration. Similarly, the characteristic endogenous fluorescence lifetimes did not vary with decreasing pulse duration and with prolonged irradiation. Over time, photobleaching will eventually occur at a rate dependent on the excitation irradiance, but rather independent on the excitation pulse width. At the irradiances used here, the photobleaching curves demonstrate similar photobleaching pathways as described in conventional one-photon excitation and thus the same precautions in conventional pulsed laser-based imaging should be applied here at thresholds specifically defined for each two-photon imaging system and tissue type. Overall, these findings suggest that pulse durations compressed to 40–120 fs is sufficient to generate efficient TPEF and SHG signals without causing conformational, morphological, or metabolic changes in neuronal tissue for a given mean laser power.

## Chapter 3

# Does the autofluorescence properties extracted through a fibred-endomicroscope have the ability to discriminate different brain tissue types, and therefore reliable to be used for intraoperative diagnosis establishment?

### 3.1 Context of the study

In the previous chapter, the two-photon excitation efficiency of our developed TPF endomicroscope was investigated. Indeed, the effect of the generated ultrashort laser pulses were on neuronal tissues as well as their effect to the autofluorescence signal of the excited endogenous fluorophores was studied.

In this chapter, we are investigating the collection and the detection efficiency of our endomicroscope as well its ability to generate an exploitable autofluorescence signal. Consequently, an important question, that have never been addressed before, arise from conducting this study: Does the autofluorescence signal detected through this endomicroscope could reveal the main discrimination tissue related parameters and therefore to be reliable for a diagnosis establishment use?

In addition, the motivation behind this study is to determine how much we can quantitatively benefit from the detected autofluorescence signal and to exploit in order to determine quantitative discrimination parameters.

To respond this question, we conducted a comparison study, through a large cohort of fresh human brain samples, between the autofluorescence response of this cohort generated via the endomicroscope setup and its counterpart generated via a multiphoton benchtop microscope. This benchtop microscope is considered as our tissue database standard reference setup, since that all tissue characterization studies were conducted and published on this setup [89], [98], [214], [216], [257]. Indeed, all tissue NIR discriminative parameters that were concluded in our previous works, were extracted through this microscope. Furthermore, the detection and collection capabilities of our developed endomicroscope, compared with the benchtop microscope setup, were also investigated.

**Methods** A samples cohort of forty-nine fresh human samples consisting of 17 healthy control, 11 meningioma, 11 metastatic tumors and 10 glioma samples was used in this study.

Spectral and fluorescence lifetime measurements were performed on this cohort using two different setups:

- 1) Our home-made developed bimodal TPF endomicroscope to acquire TPF +SHG spectra as well the fluorescence lifetime of NADH and FAD
- 2) A multiphoton benchtop microscope to perform TPF+SHG imaging, FLIM and spectral acquisitions.

A urea crystal solution, SHG signal emitter, was used to determine the instrument response function of our endomicroscope. Indeed, a rhodamine B fluorescent solution was used to compare the detection and collection efficiency of the two used setups.

**Results and conclusion** The first analyzed endomicroscope included modality is the spatially resolved fluorescence signal detection. The detected spectra showed that a 40 mW mean excitation power with 40 fs pulse width is sufficient to collect an exploitable spectrum without tissue damaging. Indeed, higher mean excitation power, up to 70 mW could be used, in order to detect higher exploitable spectral intensities while preserving a 40 fs pulse duration and without distorting the spectral shape of the detected signal as well as the tissue characteristics or viability. However, higher excitation mean power could be achieved since that only 25% of our laser source maximal mean power (4 W) is used.

The detected TPF+SHG spectra through a meningioma sample presenting a dense collagen structure, following 800, 830, 860 and 890 nm showed an SHG peak centered properly at 402 nm, 414 nm, 432 nm, and 442 nm, respectively. Hence, with a shift that does not exceed 4 nm for all acquired spectra, the excellent tunable excitation and collection efficiency following several wavelength was demonstrated.

The spectral shape of the detected spectra from the different interrogated brain tissue types showed an excellent detection efficiency of the endomicroscope. The comparison between the benchtop microscope and the endomicroscope showed also that the porphyrins emission range is more efficiently detected in the endomicroscope. Indeed, the acquired fluorescence signal of rhodamine B solution was higher when using the endomicroscope.

The mean TPF+SHG spectra of all examined tissue types have shown a significant difference between healthy and tumor tissues following the same trend observed in our previous studies of tissue characterization when using the benchtop microscope [89], [215], [216].

Furthermore, results of three acquired molecular ratios (redox ratio, Porphyrins-NADH ratio and Lipopigments-Porphyrins ratio) via the two compared setups showed an excellent similarity between their distribution ( $p$ -value > 0.65). This similarity allows the use of these extracted ratios to collect a discriminative information related to the metabolic activity and to the vascularization aspect of the imaged tissues.

The second investigated endomicroscope detection modality was the time-resolved fluorescence detection. Firstly, the instrument response function (IRF) of fluorescence lifetime detection module was measured. Fitted to a lorentzian profile, the IRF decay curve had a lifetime of 88.2 ps (FWHM of the fit curve) which is considered as negligible compared to a nanosecond order fluorescence lifetime value of an endogenous fluorescence measured by the endomicroscope. This small value indicates a high precision of the endomicroscope measured lifetime values and confirms our high system's ability to resolve the fluorescence lifetimes of endogenous fluorophores from the IRF.



Finally, and through a phasor analysis plot, the extracted free and protein bound NADH and FAD lifetime values via the two setups were quite close despite the low number of phasor counts obtained via the endomicroscope comparing with the microscope.

To this end, these obtained results permits us to validate our endomicroscope ability to generate a highly exploited quantitative response through bimodal spectral and fluorescence lifetime measurements. The validation of this quantitative bimodality to exploit the autofluorescence signal of fresh human brain samples is the final step before heading toward the multimodality, which will be tackled in the next chapter.

## **3.2 Paper: A Two-Photon Fluorescence Bimodal Endomicroscope Dedicated for Intraoperative Brain Tumor diagnosis: a comparison with benchtop microscopy**

Paper submitted to Journal of Biomedical Optics journal.

Submission ID: JBO 200333

### **3.2.1 Introduction**

Despite being among the least frequently diagnosed cancer in the world[11], brain and Central Nervous System (CNS) tumors occupy a high rank between the deadliest forms of cancer, especially the malignant types[258]. The incidence of brain tumors has increased sharply in the last 20 years among different ages[259], their survival rates have barely increased in the last 30 years[260] despite the improved understanding of the causes of this cancer and the development of the treatment methods (radiotherapy, chemotherapy...etc.). Till today, total resection of the tumor mass is the main therapy method to treat most brain tumor types, especially the malignant and the infiltrating ones. The surgical operation is considered as the most critical and crucial step in brain tumor management. The main goal of such surgery is to remove as much as possible from the tumor mass, where the main challenge encountered by the surgeon is the ability to identify accurately the tumor margins, which allows him to enhance the operation quality and reduce the recurrence outcomes[28]. Infiltrating tumor margins, which contains active cancerous cells, present often similar appearances to the adjacent healthy tissues. However, the maximal safe removal of all tumor borders, including these margins, is mandatory as well as preserving the healthy functional adjacent zones. Leaving tumor cells in the resection cavity will highly increase the recurrence rate of the tumor and its mortality after the operation[261]. To ensure reaching an optimal safe resection limit, and to confirm the success of the surgery, biopsy samples are extracted from the resection cavity for post-surgery histological analysis purposes. This analysis relies on a Hematoxylin & Eosin (H&E) staining of the extracted samples in order to obtain precise information on the nature of the sample tissue. Nevertheless, this analysis takes several days after the surgery to establish the final diagnosis. Relying on the human judgment and the expertise of the anatomopathologist, this analysis is still the gold standard method to provide such information.

To address these issues, and to improve the surgical gesture, numerous imaging techniques were proposed to guide the surgeon intraoperatively (i.e. intraoperative MRI[262], intraoperative ultrasound imaging[263]). Neurosurgical virtual reality and simulation have improved also the pre-operative visualization and planning[264]. These techniques have brought several improvements to the quality of the surgical gesture and have demonstrated their usefulness. However, intraoperative retraction and tumor resection often result in brain shifts, making it challenging to assess the extent of resection in real time. In addition, the mentioned techniques lack reliability and high resolution, and do not manage to lead to a total resection of cancerous sites or at least reach the same precision of the post-surgery H&E diagnosis.

In the last two decades, several spectroscopy-handheld tools have been developed as an auxiliary to the intraoperative total resection[265] such as Raman spectroscopy probes[77],

[266] and under the premise that real-time use and the adjustment of the instrument angle could facilitate the detection of remaining tumor cells [265].

Fluorescence-guided surgery using 5-aminolevulinic acid (5-ALA) has been considered as an important addition to the neurosurgeon's toolkit[140]. This technique allows direct fluorescence visualization and increases the rate and extent of high-grade glioma tumors, but it has shown limited efficiency in identifying diffuse low-grade gliomas and micro-infiltration cases[267]. In addition, this technique didn't show a high specificity towards tumor cells regions, where a fluorescence signal was detected in inflammatory cells in adjacent regions within the resection cavity [139], [267].

On the other hand, label free optical imaging techniques have emerged as novel tools which allow high-resolution and cross-sectional imaging methods such as Optical Coherence Tomography (OCT)[268], [269] and Two-Photon Fluorescence (TPF) imaging probes[98]. These tools can be used endoscopically to realize intraoperative high speed imaging without introducing any external markers. TPF Microscopy has shown a better ability to discriminate multimodally the healthy brain tissues from tumor ones at a cellular scale, and most importantly reaches a step that allows it to compete H&E staining images[98], [270]. Comparing to OCT, its superior spatial resolution makes it more efficient as a non-invasive imaging technique for tumor sites diagnosis.

In previous works, we have demonstrated the reliability of this technique and the proof of concept was validated on fresh human tissues[98]. Using a TPF multimodal benchtop microscope, the building of an optical tissue data base was launched few years ago. The aim of this data base is to specify each type and grade of brain tumor with its specific optical signature in order to establish different discriminative parameters between these types. Through this data base, we managed to discriminate healthy control tissues, with a high sensitivity and specificity, and by using several parameters and molecular analysis, we could categorize the tissue from: 1) high grade and low grade glioma [270], 2) grade I and grade II meningioma[216] and 3) secondary and primary brain tumor [214]. Thus, we decided to invest in this technique and to develop a TPF fibred endomicroscope able to excite efficiently four endogenous fluorophores: Nicotinamide adenine dinucleotide (NADH), Flavins (FAD), Lipopigments and Porphyrins, as well as the detection of Second Harmonic Generation (SHG) issued from collagen structures. Relying on multimodality of analysis (TPF & SHG imaging, fluorescence lifetime, and spectral analysis) our tool will be able to provide a fast, reliable, and accurate real-time diagnosis.

Concerning the instrumental development of the endomicroscope, a detailed characterization of a five meter length specific microstructured endoscopic fiber has already approved its usage for in vivo non-linear imaging[173], [271]. Numerical and experimental studies have been performed to characterize the pulse compression and its delivery through the endoscopic fiber as well as all optical related technical parameters[168], [173].

Once the instrumental requirements and technical challenges were addressed, the next step is to investigate the ability of this endomicroscope to provide a reliable biological response and to validate its biological aspect. This aspect covers the endomicroscope's capacity to extract, from human tissues, reliable information that can be employed for a tumor-healthy discrimination. Therefore, a comparison between the response of our endomicroscope with the response of a TPF benchtop microscope platform was launched. This benchtop multimodal platform constitutes the standard reference for in-vitro tumor diagnosis,

especially as it is the same platform used for our tissue data base building[98], [214], [216], [270]. Still, this platform is not adapted to clinical use and could not be implemented in the hospital workflow.

The purpose of this paper is to investigate the capability of our endomicroscope to provide the same characteristics of spectrally and time resolved fluorescence signal provided by the benchtop TPF microscope, which the diagnosis information is based on. We are investigating spectral shape, molecular ratios, and fluorescence lifetime values extracted from our endomicroscope with the same parameters extracted from the TPF multimodal microscope, using a large cohort of fresh human brain samples.

### 3.2.2 Materials and methods

#### 3.2.2.1 Samples

According to the approval with Sainte-Anne Hospital – University Paris Descartes Review Board (CPP Ile de France 3, S.C.3227), sample tissues were collected during surgery times from the Department of Neurosurgery and Neuropathology at the Sainte-Anne Hospital. All methods and measurements were performed accordingly with the relevant guidelines and regulations of this approval, and informed consents were obtained from all patients. Forty-nine fresh samples were extracted from thirty-nine patients and directly sent to our laboratory to perform the measurements. The different tissue types as well as the relative number of each type are shown in table 3.1 below.

<b>Tissue Type</b>	<b>Description</b>	<b>Number</b>
Control	Healthy cortical tissue, epileptic tissue	17
Meningioma	Grade I and II	11
Metastasis	Thyroid and lung carcinoma	11
Glioma	Anaplastic oligo-astrocytoma, astrocytoma (grades II and III), Glioblastoma (GBM)	10

**Table 3.1:** Summary of the sample’s cohort included in this study.

#### 3.2.2.2 Benchtop microscope

This platform consists of a Leica TCS SP8 multimodal multiphoton fluorescence benchtop microscope (Leica Microsystems, Wetzlar, Germany) controlled via Leica’s acquisition software. This microscope is coupled with a Ti:Sapphire tunable laser source from 690nm to 1040 nm (Mai Tai, spectra Physics). This laser source can provide a maximum power of 2.4 W at 800 nm and at a repetition rate of 80 MHz with a 70 fs as minimum pulse duration due to its integrated automated dispersion compensation unit. The objective that was used is a 25 X water-immersion objective (HCX IRAPO L 25X NA 0.95, Leica). For spectral acquisition, a hybrid internal detector (HyD, Leica, Germany) placed in the confocal head of the microscope was used. It covers a detection range from 380nm to 780 nm. For two-photon fluorescence, SHG and FLIM imaging, two external non-descanned hybrid detectors

(HyD-RLD, Leica Microsystems, Wetzlar, Germany) added to the microscope detection channel, were used. The first detector was dedicated to capture the NADH fluorescence signal when using 800 nm as excitation wavelength and SHG signal when using 890 nm by putting a  $448 \pm 20$  nm band-pass filter (Semrock, FF01-448/20-25) in front of its detection port. The second one was dedicated to capture the FAD fluorescence signal by putting a  $520 \pm 30$  nm band-pass filter (Semrock FF01-520/35-25) in front of its detection port. For fluorescence lifetime imaging acquisition, a time-correlated single-photon counting module (PicoQuant TCSPC module, Berlin, Germany) was coupled with the two external hybrid detectors, which permits us to perform NADH and FAD lifetime imaging at 800 nm.

### 3.2.2.3 Two-photon endomicroscopic setup

As presented in figure 3.1, the bi-modal endomicroscopic setup consist of a Ti: Sapphire laser source (Chameleon Ultra II, Coherent) tunable with an emission band of 680 nm-1080 nm. This source is capable to generate pulses with a duration of 140 fs with a repetition rate of 80 MHz and an average power of 4W over 800 nm. At the exit of the laser source, a Faraday Isolator (ISO-05-800-BB, Newport) was installed to protect the laser source from destabilizing feedback or actual damage from back-reflected photons. To compensate the dispersion (second and third order) and the non-linear effects occurring inside the endoscopic fiber<sup>22,24</sup>, a pre-compensation unit was used. This unit comprise two main components:

- 1- A 50 cm single mode fiber (SMF) to stretch the spectrum in order to be able to reach a shorter pulse duration at the exit of the endoscopic fiber.
- 2- A GRISM (GRating+prISM) line stretcher, which consist of two diffraction gratings joined to two prisms. The pulse duration at the output of the endoscopic fiber is then controlled and adjusted due to two geometric parameters in this line: the incidence angle of the beam on the first prism and the distance separating the two prisms.

Outgoing from the GRISM line, the laser beam is then coupled to a customized specific micro-structured Double Clad Fiber (DCF). This fiber was characterized and described in previous work<sup>22</sup>. It has a single mode central core to ensure the excitation with a diameter of a  $6.4 \mu\text{m}$  and a numerical aperture of 0.097 (at 800 nm). It is surrounded by an air/silica micro-structured region with a diameter of  $40 \mu\text{m}$  to separate the central core from the collecting inner cladding. The role of this latter is to collect the fluorescence signal with a numerical aperture of 0.27. The beam outgoing from the fiber is further focused using a 40X objective (HC PL APO 40X/1.1 W CORR CS2, Leica). At the exit of the fiber, the pulse duration width can be adjusted from 140 fs at the output of the laser cavity down to 40 fs. The captured fluorescence signal is then separated from the injected laser beam using a dichroic filter, and then filtered through a short pass filter. A 70-30 beam splitter is also used to divide the signal to two parts: 70% directed toward a spectrometer (QE Pro, ocean insight) to analyze the spectra with a spectral resolution of 0.76 nm and across a detection range from 200 nm to 1000 nm. The remaining 30% are directed toward a PMT (PMA 182, PicoQuant, Germany) to analyze the fluorescence lifetime. This latter, and before entering to the PMT, passes through a motorized filter wheel which comprises five band-pass filters dedicated to select the fluorescence signal of each molecule separately ( $488 \pm 10$  nm for NADH,  $520 \pm 10$  nm for FAD,  $580 \pm 23$  nm for Lipopigments,  $620 \pm 13$  nm for Porphyrins I and  $660 \pm 13$  nm for Porphyrins II).

The spectral and lifetime measurements were conducted using 800 nm as excitation wavelength. The setup was optimized to deliver the maximum beam mean power at the output of the objective at the shortest pulse duration. The objective that was used is the same used with the benchtop microscope setup (HCX IRAPO L 25X NA 0.95, Leica) in order to achieve the best possible comparison conditions. With a 1 W (25% of the maximum mean power delivered by our laser source) as mean power injected in the SMF fiber of the pulse compression, we managed to obtain 70 mW as excitation mean power with 40 fs as pulse duration.

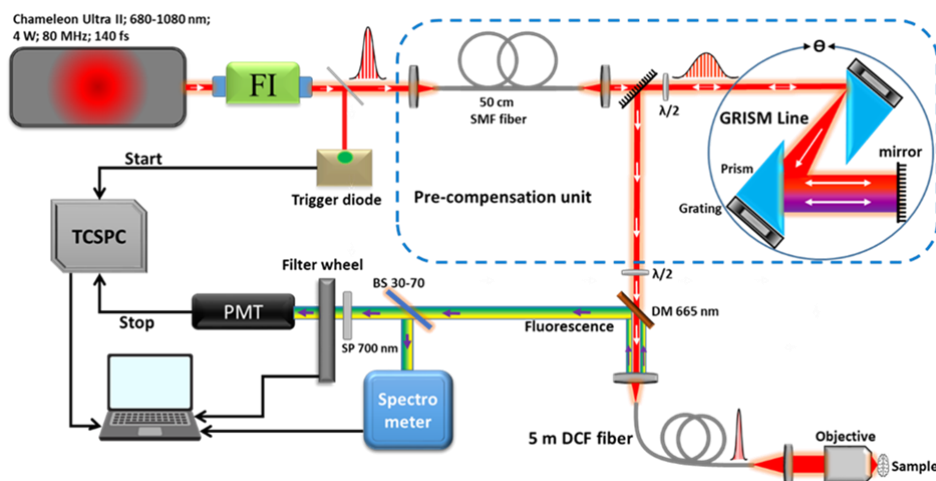


Figure 3.1: Illustration of the bimodal endomicroscopic setup

### 3.2.2.4 Data analysis

#### Spectrally resolved data

Issued from the benchtop microscope using 800 nm excitation, spectral data were extracted via FIJI software then it was plotted using a homemade developed Matlab software used in previous work by our team<sup>19</sup>. Using 800 nm as excitation wavelength, we are able to highlight the fluorescence emission of four endogenous fluorophores: NADH, FAD, Lipopigments and Porphyrins. The same software was used to process the spectral data issued from the endomicroscopic setup. Through this software, the fluorescence emission of each fluorophore was represented by a Gaussian fit whose maximum wavelength and bandwidth follows the given values as shown in Table 3.2.

Fluorophores	Spectral bandwidth [nm]	Maximum emission range [nm]
NADH bound	40-48	443-445
NADH free	45-50	460-470
FAD	30-50	520-530
Lipopigments	0-180	570-600
Porphyryns I	0-10	615-630
Porphyryns II	0-10	675-690

Table 3.2: Gaussian parameters used to fit the emission fluorescence spectra

Therefore, the integral proportion of each fluorophore was then calculated. It is defined by the ratio of the integral under the fitted fluorophore emission curve on the integral under the total fitted spectrum. Thus, we were able to extract and calculate three different molecular ratios following the equations 3.1, 3.2 and 3.3 below:

$$\text{Redox ratio: FAD}/(\text{NADH}+\text{FAD}) \quad (3.1)$$

$$\text{Optical index: Porphyrins}/\text{NADH} \quad (3.2)$$

$$\text{Ratio LP: Lipopigments}/\text{Porphyrins} \quad (3.3)$$

### Time-resolved data

Acquired fluorescence lifetime data was treated using the phasor approach. Contrary to the exponential fitting, this approach is a non-fitting technique. It consists of representing the Fluorescence Lifetime Decay Curve (FLDC) in a graphical view<sup>38</sup> where each FLDC is represented by a vector called “phasor” having its unique location in the phasor histogram. For the benchtop microscope FLIM data, the size of each image was reduced from 512x512 pixel to 16x16 pixel, adding each 32x32 pixel together to form a reduced pixel. Afterwards, each FLD of each reduced pixel was converted into two coordinates,  $S_i(\omega)$  and  $G_i(\omega)$  in a Cartesian plot following the equations 3.4 and 3.5:

$$S_i(\omega) = \int_0^{\infty} I(t) \cdot \cos(\omega t) \cdot dt / \int_0^{\infty} I(t) \cdot dt \quad (3.4)$$

$$G_i(\omega) = \int_0^{\infty} I(t) \cdot \sin(\omega t) \cdot dt / \int_0^{\infty} I(t) \cdot dt \quad (3.5)$$

$S_i(\omega)$  and  $G_i(\omega)$  are respectively to the x and y coordinates of the phasor corresponding to a reduced pixel “i” in the image, while  $\omega$  is the laser repetition angular frequency related to the sampling period ( $T_s$ ) and to the signal length (L) in the equation 3.6 below:

$$\omega = 2\pi / (L \cdot T_s) \quad (3.6)$$

Afterwards, the global phasor histogram grouping all phasor counts of all FLIM images of all samples, is plotted. To calculate the fluorescence lifetime values corresponding to each molecule, the local maxima of the global phasor histogram is identified to draw a fitting line. The position of the two intersections of this fitting line with the universal circle are linked to the two fluorescence lifetimes values<sup>[132]</sup>.

## 3.2.3 Results

### 3.2.3.1 Spatially resolved fluorescence results

Starting with the excitation and detection capabilities of the endomicroscopic setup, the spectral shape of the laser beam at the exit of the endoscopic fiber was recorded using four different wavelengths: 800, 830, 860 and 890 nm. These spectra were plotted and shown in figure 3.2(b). The spectral shape of the excitation laser beam did not change sharply with the wavelength, while each spectra was centered on its proper adjusted wavelength. To

confirm the efficiency of the excitation efficiency, we acquired the fluorescence spectra using the excitation wavelengths cited above from a meningioma sample presenting a high SHG emission. The four fluorescence spectra acquired under 800, 830, 860 and 890 nm excitation wavelength, are shown in figure 3.2(a). The maximum emission wavelength of the SHG peak on these four spectra confirm the excellent excitation efficiency with the wavelength tuning. Respectively to 800, 830, 860 and 890 nm, the SHG peak was centered at 402 nm, 414 nm, 432 nm, and 442 nm. The measured shift was less than 4 nm for all spectra, which confirm the excellent tunable excitation efficiency of our endomicroscopic system.

Once the collection efficiency through multiple excitation wavelengths is validated, the excitation power efficiency of the endomicroscopic setup is demonstrated. Using 800 nm as wavelength, a 70 mW as excitation mean power can be reached at the exit of the endoscopic fiber. This mean power is more than enough to excite a biological tissue. Several spectral measurements, on an arbitrary control sample to figure out the minimum excitation power that we should use to get an exploitable spectrum, were performed. Furthermore, a minimum threshold of 100 recorded counts through the spectrometer at 1 s of acquisition time for an exploitable spectrum was fixed by our team. The spectra acquired using several excitations mean power were plotted and are shown in figure 3.2(c). Beyond 41 mW, the acquired fluorescence spectra exceed our fixed threshold, while using 70 mW the recorded spectra was strong enough to be used in the imaging acquisition. In addition, the variation of the maximum emission intensity in function of the excitation power was determined. The fluorescence emission increased nearly 10 times from 16 mW to 70 mW. Plotted in figure 3.2(d), a fit power function was used to fit the variation of the fluorescence emission maximum in function of the excitation power, where an exponent value  $b=2.69$  was found. Next, the pulse duration compression and its impact on the fluorescence emission was validated. From an arbitrary GBM sample, and using 800 nm as excitation wavelength, the fluorescence spectra was acquired using several pulse durations. Starting from 40 fs, which is the minimal pulse duration reached by our system, up to 140 fs which is the pulse duration of the beam at the input of the SMF fiber of the compression unit. Figure 3.2(e) shows the acquired spectra, where we can notice that the spectral shape is not distorted as the pulse duration increases, while the variation of the intensity is positively correlated with the pulse duration variation. This variation is shown in figure 3.2(f), where the maximum of the fluorescence intensity was plotted in function of the pulse duration. The fluorescence intensity is amplified four times when the pulse duration is compressed from 140 fs to 40 fs; this variation was fitted into a power function where an exponent value  $b = -0.93$  was found.



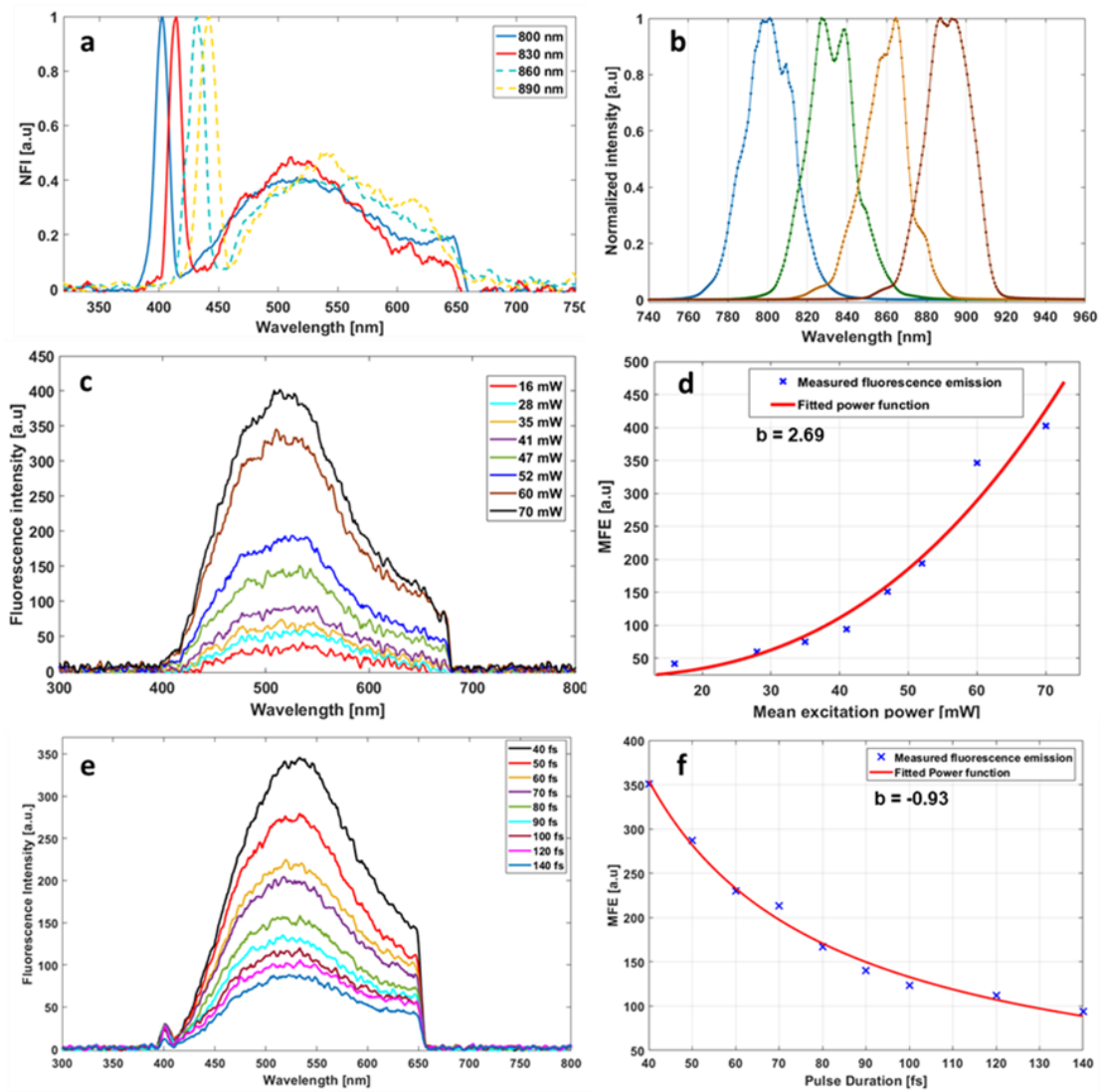


**Figure 3.2 :** Normalized Fluorescence spectra acquired from a meningioma sample using 800, 830, 860 and 890 nm as excitation wavelength. (b) Shape of the excitation laser beam at the output of the endoscopic fiber at 800, 830, 860 and 890 nm. (c) Fluorescence spectra acquired from a control sample using several excitation mean power. (d) Variation of the Maximum Fluorescence Emission (MFE) as a function of the mean excitation power. (e) Fluorescence spectra acquired using different pulse duration from a GBM sample. (f) Variation of the Maximum Fluorescence Emission (MFE) in function of the laser beam pulse duration.

Once the tunability, excitation power, and temporal pulse compression properties were validated, we conducted spectral measurements on all the cohort of fresh samples. For each sample, we selected 3-4 Region of Interest (ROI) depending on the sample size to perform local spectral acquisition using 800 nm as excitation wavelength. Afterwards, we compared the spectra acquired from four different samples via the endomicroscope to those acquired via the benchtop microscope in order to confirm the correct spectral shape of the fluorescence signal detected by our setup. Shown in figure 3.3, fluorescence spectra were recorded from a meningioma (a), control (b), metastasis (c) and GBM (d) fresh samples. Looking to the spectral shape, we can notice that the same shape obtained through the benchtop microscope is also obtained via the endomicroscope, even better through this

latter. Firstly, and using 800 nm, the benchtop microscope is not able to detect SHG signal, due to the presence of the 448+20 nm bandpass filter in front of the detector, contrary to the endomicroscope which is able to detect SHG signal with a high sensitivity. We noticed also that the spectra acquired via the endomicroscope were slightly wider in the right side corresponding to the porphyrin's emission peak (650-680 nm), which is more noticeable in metastasis and GBM spectra. This shift is due to the higher quantum efficiency (90%) of the spectrometer used in the endomicroscopic setup than the hybrid internal detector of the benchtop microscope.

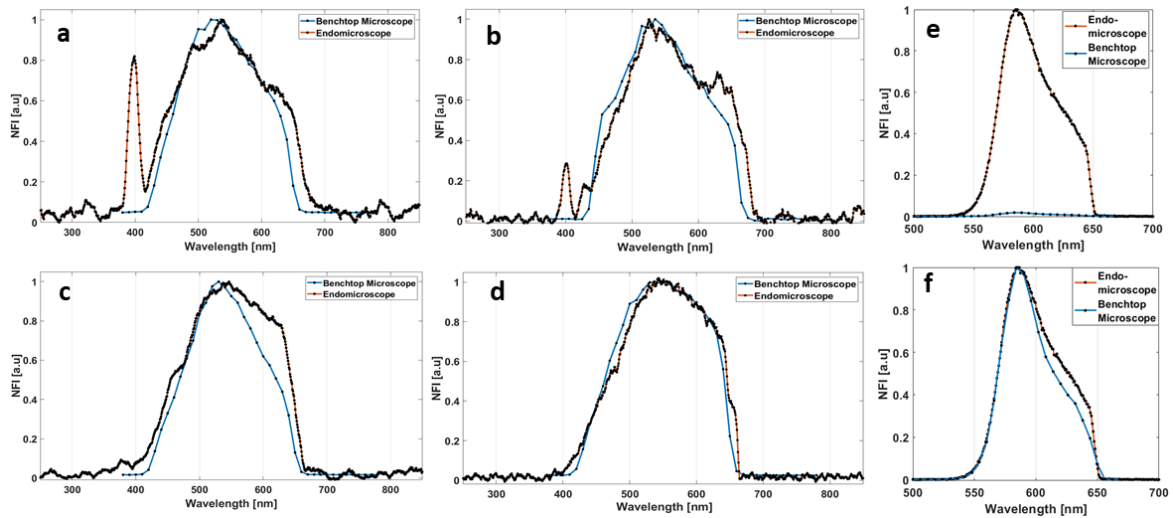


**Figure 3.3:** Normalized Fluorescence Intensity (NFI) Spectra acquired from the endomicroscope and from the benchtop microscope using 800 nm excitation for meningioma (a), control (b), metastasis (c) and GBM samples (d). (e) Comparison of the fluorescence maximum emission of Rhodamine-B solution, using 800 nm with 13 mW as excitation power, acquired from the benchtop microscope and from the endomicroscope. (f) Comparison of the spectral shape of Rhodamine-B solution excited with the same power on the benchtop microscope and the endomicroscope

Adding to this, when using the benchtop microscope, a higher excitation mean power than the one used in the endomicroscope is needed to be used. This hypothesis is confirmed through figure 3.3(e), where the fluorescence spectra of 10  $\mu$ l of Rhodamine-B solution (Rhodamine B, 83689, Sigma Aldrich) was recorded from the benchtop microscope and from the endomicroscope. Under the same conditions (800 nm as excitation wavelength, 13 mW as mean excitation power and 70 fs as pulse duration), the acquired signal from endomicroscope was strongly higher than the signal acquired from the benchtop microscope. In addition, when normalizing each spectrum to its maximum, we can observe the same spectral shift around 630 nm (figure 3.3(f)) observed in tissues spectra.

In term of spectral discrimination ability between tumor and healthy tissues, mean spectra acquired through the endomicroscope from all tissue's types were plotted in figure 3.4(a). All spectra were acquired at the same pulse duration and the same excitation power. Noting that the error bars were divided by 3 for all types. Control tissues present higher fluorescence emission than other tumor types with a negligible SHG emission comparing with the other tumor types.

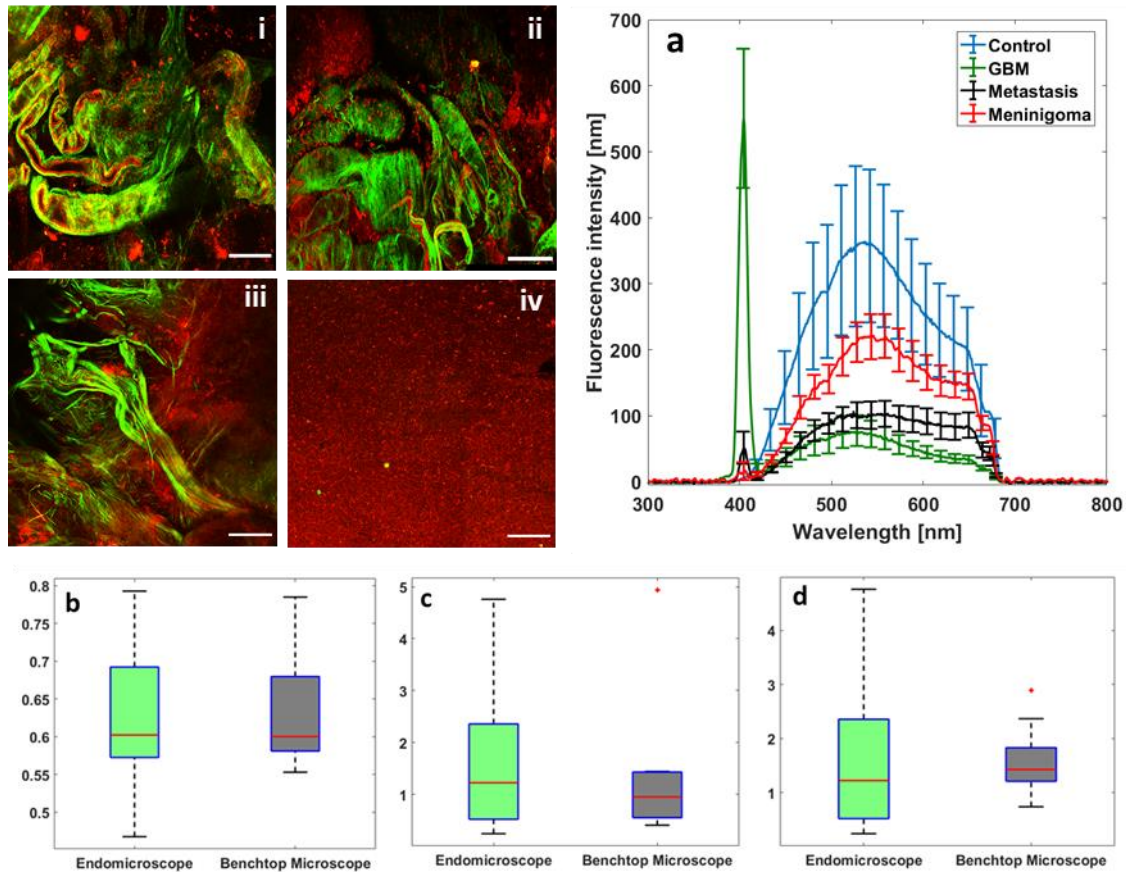


**Figure 3.4:** TPF&SHG images acquired using 890 nm as excitation wavelength through the multimodal microscope from GBM (i), Meningioma (ii), metastasis (iii) and control (iv) sample. (a) Mean emission spectra of control, meningioma, GBM and metastasis sample acquired at 800 nm excitation wavelength through the endomicroscopic setup. Comparison between redox ratio (a), PN ratio (b) and ratio LP (c) derived from spectral measurements at 800 nm excitation through the benchtop microscope and the endomicroscopic setup. Scale bar: 200  $\mu$ m

Meningioma samples present the lower fluorescence emission but the higher SHG emission. These spectral characteristics were confirmed regarding the TPF + SHG images acquired from the benchtop microscope using 890 nm excitation wavelength. This wavelength was used because the first hybrid external detector of the benchtop microscope cannot detect the SHG emission issued from 800 nm excitation due to the presence of the  $448 \pm 20$  nm band-pass filter in front of its detection port. Looking to these images, we can see a clear TPF fluorescence image acquired from a control sample (figure 3.4 iv), while the meningioma image (figure 3.4 ii) is dominated by SHG signal resulting from the dense collagen fibrous structures. The same trend was observed in metastasis samples (figure 3.4.iii) with less SHG signal and higher fluorescence signal. In GBM sample (figure 3.4 i) we can see both signal, fluorescence and SHG signal derived from the borders of large vessels. The last spectral characteristic was the molecular ratios extraction from the spectral fitting process. Using the fitting parameters shown in table 3.2, all spectra acquired through the benchtop microscope and the endomicroscopic setup from all control samples were fitted in order to extract the emission contribution in the total spectrum of each excited molecule NADH, FAD, Lipopigments and porphyrins. A comparison of the three molecular ratios extracted from both setups is shown in figure: 3.4(b) for redox ratio, 3.4(c) for PN ratio

and 3.d for LP ratio. Similar values distribution was obtained for all three ratios with a respectively p-values of 0.77, 0.67, 0.95. These values confirm the similarity of molecular ratios extraction via the endomicroscope and validate its ability to obtain valuable discrimination between tumor and healthy tissues.

### 3.2.3.2 Time resolved fluorescence results

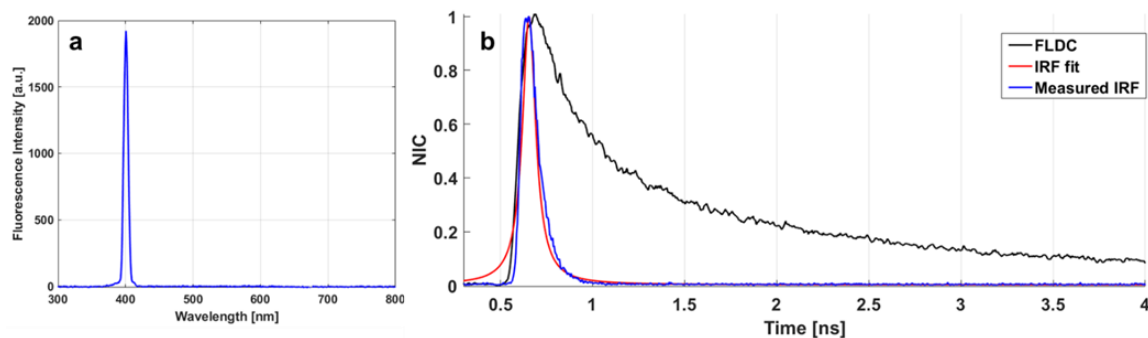


**Figure 3.5:** (a) SHG emission from urea crystals solution excited using 800 nm as excitation wavelength. (b) Measured IRF (blue curve) via the SHG emission spectra of urea crystals; Fitted curve of the IRF (red curve) via Lorentzian fit; an arbitrary measured Fluorescence Lifetime Decay (FLDC, black curve) from a fresh sample.

Moving to the second modality of measurements, fluorescence lifetime. The first extracted parameter is the instrument response function (IRF) of the TCSPC module used in the endomicroscopic setup. The IRF is measured by recording the lifetime decay curve of the SHG signal of a urea crystal solution using 800 nm as excitation wavelength (Urea, U5128, Sigma Aldrich). The recorded spectrum was plotted in figure 3.5 (a), it shows a unique peak centered at 402 nm (same shift recorded for the SHG peak issued from meningioma samples shown in figure 3.2(a)) which means an exact signal through which to measure the IRF. The measured lifetime decay of this SHG signal is shown in figure 3.5(b) (blue curve). It was compared to an arbitrary Fluorescence Lifetime Decay Curve (FLDC) issued from a fresh sample (black curve). The IRF decay curve was fitted via a Lorentzian fit (red curve, figure 3.5(b) where a Full Width at Half Maximum (FWHM) value of 88.2 ps was found. This value is negligible compared to a nanosecond order fluorescence lifetime value measured by the endomicroscopic setup.

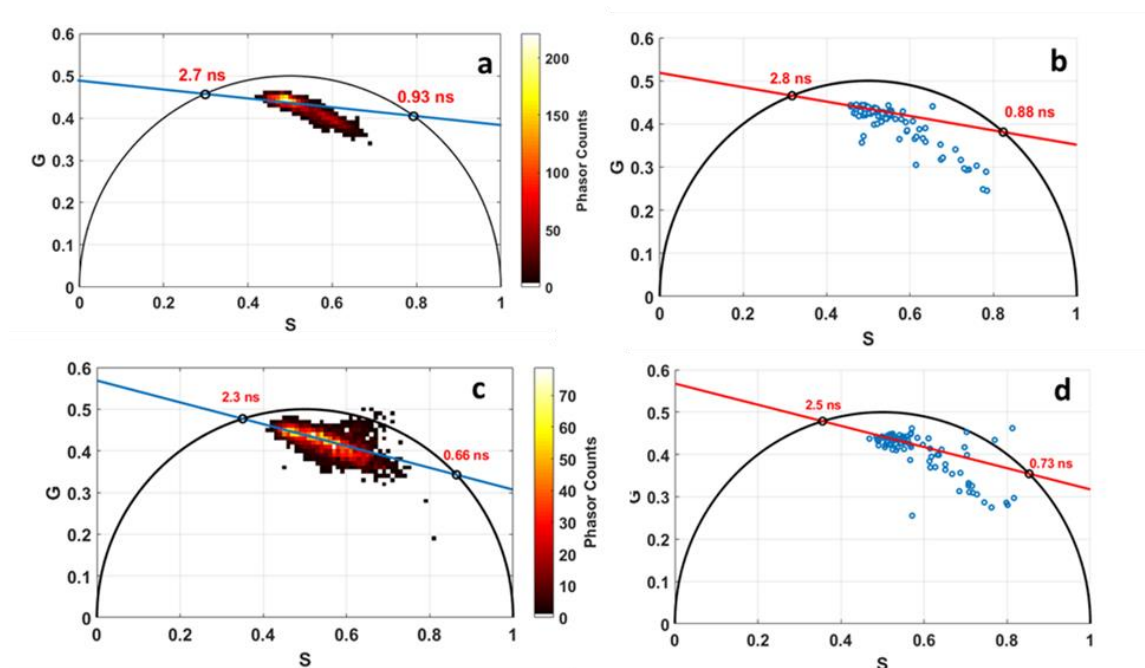


**Figure 3.6:** Phasor lifetime histogram acquired from the benchtop microscope (a,c) and from the endomicroscopic setup (b,d) for FAD (a,b) and for NADH (c,d).

This negligible value validates the precision of the lifetime values acquired through this setup and confirms the high system's ability to resolve the fluorescence lifetimes of endogenous fluorophores from the IRF. Once the IRF is measured, we conducted lifetime measurements for all control samples (17 samples) on several ROIs for each sample (same ROI of spectral measurements). All collected curves were treated through the phasor lifetime method. The obtained phasor histogram was plotted to compare it with the histogram plotted through the benchtop microscope FLIM measurements on the same samples using 800 nm as excitation wavelength.

In figure 3.6, lifetime phasor histogram of FAD issued from the benchtop microscope (a, c) and the endomicroscopic setup (b, d) are shown. The lifetime values obtained through the two setups were close to each other (2.7 ns and 2.8 ns for free FAD; 0.93 ns and 0.88 ns for protein-bound FAD). Likewise, NADH phasor histogram issued from the benchtop microscope and the endomicroscope were compared and shown respectively in figure 3.6(c&d). The lifetime values obtained were close to each other but less than FAD lifetime values (2.3 ns and 2.5 ns for protein bound NADH; 0.66 ns and 0.73 ns for free NADH). The obtained difference was 0.1 ns for FAD and 0.2 ns for NADH. This difference is still accepted regarding the fact that the number of the phasor counts in the benchtop microscope FLIM images is much higher than phasor counts acquired through the endomicroscope. Looking to the phasor cloud shape in both compared histograms, we can notice a similar shape. In NADH histogram, we can find several phasors count outside the universal circle for both the benchtop microscope and the endomicroscope in the same zone.

### 3.2.4 Discussion

In this work, we have presented a bimodal TPF endomicroscope dedicated for intraoperative imaging during a brain tumor surgery. This tool aims to improve the surgical act by delimitating the tumor infiltrating boundaries and providing the surgeon with multimodal quantitative and qualitative information on the tissue's nature. We compared the endomicroscope generated bimodal response with that generated by our standard reference, a multiphoton multimodal TPF benchtop microscope. Therefore, we showed that our developed setup can deliver a high-quality signal, similar to that delivered by the standard reference, validating its efficiency and its capability to provide useful information for clinical intraoperative use.

Nevertheless, the development of this type of instruments is not considered novel. In fact, several works in the state of the art have managed to acquire high quality in vivo TPF&SHG images from rats and mice tissues[106], [166], [186], [190], [210], [272]. The team of F. Louradour discussed the addition of a FLIM modality to the TPF&SHG imaging capabilities[184], [273]; this added modality allowed collecting additional information on the cellular energy metabolism during in vivo testing. However, most of the mentioned works performed their imaging tests on animal samples and their studies were directed toward developing high quality instrumental abilities. Moreover, most of the reported developed setups are not intended, at least in the short term, for clinical applications in the operating room since that no specific human tissue data base was established. To our knowledge, the application of TPF imaging on a large number of human fresh samples was never reported before; reported in vivo imaging measurements were only performed on rat samples without offering any multimodality perspective of analysis that could be applied later on human organs.

Years ago, we successfully elaborated a protocol with Sainte-Anne hospital in Paris, to receive fresh human brain tissues issued from surgical resection. Indeed, our research group is building a multimodal specific optical tissue database that is oriented to characterize the optical signature of all types of human brain tumor tissues and thus to define the specific multimodal optical signature for each type[98], [214]–[216], [270], [274], [275]. Such tissue database is of significant importance for clinical use by neurosurgeons, where advanced instrumental and technical abilities are required. Chiefly, this database will be associated to our endomicroscope and will combine multimodal analysis (fluorescence and SHG detection correlated with fluorescence lifetime and metabolic ratio analysis) in order to establish, via fast discriminative algorithms, a fast and efficient diagnosis of cancerous activity in the examined regions.

In this comparative study, we performed several spectral and fluorescence lifetime measurements on a large cohort of fresh human brain samples using different excitation wavelength, excitation mean power and pulse duration in order to investigate the differences between the response of the endomicroscope with the response of the benchtop microscope. The efficiency of exciting using several wavelength was approved in figure 3.2(a). The shifted SHG peak between the different wavelengths showed that our excitation is suitable for a multiscale excitation. This tunability gives our endomicroscope a large panel of spectral since that our four excited molecules do not have a maximum absorption cross section at the same wavelength. While NADH have a higher absorption cross section at

800nm, this cross section remains very weak at 890 nm where the porphyrins have a better cross section than at 800 nm[231].

In addition to the tunability, we examined the collection efficiency of our endomicroscope and its ability to excite with a high excitation power. We found that exciting with 40 mW as mean power, corresponding to 0.5 nJ as pulse energy at 80 MHz repetition rate, is sufficient to detect an exploitable spectrum which exceeds our fixed minimum threshold of detected counts during 1 s of acquisition time. We also managed also to easily reach 70 mW as excitation mean power at the exit of the endoscopic fiber using 25% of the laser mean power delivered by our laser source, which means that we can also obtain higher excitation mean power than 70 mW. The obtained spectra using this mean excitation power (figure 3.2(c)) are strongly enough to be analyzed and to be used for image reconstruction. This high emission will allow us to obtain high quality TPF&SHG images and to obtain a higher signal to background noise ratio. The ability to deliver high excitation power will give us the capacity to better deal with solid tumors and to perform high quality images on all types of brain tumor samples.

The last examined property of the excitation process is the sub-fs pulse duration delivery. Spectral measurements, conducted on a GBM sample with different pulse duration (figure 3.2(e)), quantified the improvement of the fluorescence signal with the decrease of the pulse duration. A 4 times higher signal was obtained when compressing the laser pulse duration from 140 fs down to 40 fs. While the pulse duration is inversely proportional to the fluorophore's absorption cross section; shorter excitation pulses are requested for superior image quality, to enhance the imaging depth and to increase the number of recorded images per second[218].

Once the excitation wavelength, mean power and pulse duration were adjusted, we conducted a spectral and fluorescence lifetime measurements campaign on all samples cohort through two different setups: 1) the benchtop microscope platform which allows us to perform multimodality of measurements and 2) the bimodal endomicroscopic setup which is able to acquire spectral and lifetime local measurements.

Firstly, the spectral shape of the signal acquired via these two setups was compared where similar efficiency of fluorophore emission detection was noticed for both instruments, except for porphyrins. The spectrometer used in the endomicroscopic setup is more sensitive and have a higher quantum efficiency than the detector of the benchtop microscope. It provides our endomicroscope a higher efficiency to collect low fluorescence signals and more precision to detect signal of low cross section fluorophores at 800 nm, such as porphyrins. In addition, we proved that our endomicroscopic setup have a higher collection efficiency than the benchtop microscope platform (figure 3.3(e)). This excellent efficiency allows us to use less mean power to excite our tissues, leading to deliver less pulse energy so less localized photo-damage. The fact that we use less optical elements in the detection path in the endomicroscope, a high sensitivity and resolution spectrometer and exciting with a shorter pulse duration, give our endomicroscope the ability to run faster acquisitions and to reach, in the future, a higher imaging frame rate.

In term of discrimination ability between tumor and healthy tissues, the mean acquired spectra of all samples plotted in figure 3.4(a), have shown a remarkable difference of fluorescence & SHG emission between the different types of tissues, in harmony with what was reported in our past studies using the benchtop microscope[215], [270], [275]. This

variation of spectral characteristics and signal emission constitute an important confirmation of the discrimination ability of our endomicroscopic setup which was confirmed through the TPF&SHG images acquired via the benchtop microscope. Furthermore, the same distribution of three molecular ratios was obtained from the benchtop microscope and from the endomicroscope. This similarity permits us to rely on these ratios extracted from the endomicroscope to establish a discriminative information connected to the metabolic activity of the tissue. These ratios were tested in our past studies via 3D discriminative algorithms and proved their power to diagnose with a high specificity and sensitivity different grades of tumor from healthy samples[98], [270].

Moving to the second modality of analysis, fluorescence lifetime measurements were performed. We used the phasor technique to extract lifetime values from both FLIM extracted benchtop microscope images and the decay curves obtained from the endomicroscope. As a non-fitting technique, this method has the potential to simplify the analysis of FLIM images and to avoid the fitting errors associated with mono-exponential or bi-exponential fitting technique[132]. This method of analysis was used in our past studies and managed to detect changes in glioma tumor at the level of molecular contribution and repartition of free and protein-bound state of FAD and NADH[270]. Comparing the histograms acquired from the benchtop microscope and from the endomicroscope, and despite the low number of phasor counts obtained via this latter, the two lifetime values of each molecule were close to each other. This similarity permits us also to integrate this analysis technique in the endomicroscope future data processing fast discriminative algorithms in order to complete our multimodality of acquired contrasts.

### 3.2.5 Conclusion

The bimodality is the first step on the track of reaching a multimodality. In this work, the ability of a TPF bimodal endomicroscope, tested on a large cohort of fresh human brain samples, to discriminate different types of human brain tissues was discussed. The endomicroscope revealed a low photo-damage and successfully provide a reliable and reproducible response through fast acquisition measurements. Furthermore, the reliability of the biological response was ensured, in addition to overpassing typically reported technical and instrumental requirements.

Concerning future perspectives, a biocompatible and serializable endoscopic handheld probe, dedicated to intraoperative use by the surgeon, is under development. This probe consists of a miniature scanning system based on an electrothermally actuated Micro Electro Mechanical System (MEMS) mirror and has already been characterized to be utilized for in vivo imaging essay. This system is under development to reduce its total outer diameter and electronic control station. Indeed, a fast acquisition processing software, which includes our developed advanced analysis and discriminative methods and based on artificial intelligence, is needed to exploit the technical and biological abilities of our tool.

In short, after demonstrating the instrumental and biological capabilities of our endomicroscope, obtaining a commercial multimodal Two-Photon Fluorescence endomicroscope dedicated for intraoperative brain imaging is more achievable.



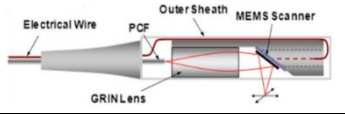
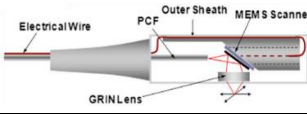
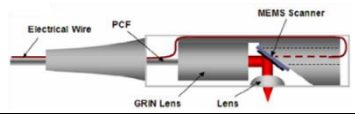
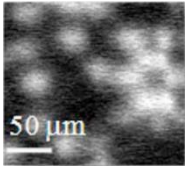
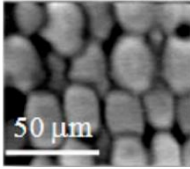
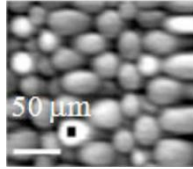
## Chapter 4

# Toward multimodality: design and characterization of a miniature 2D scanning probe head based on an electrothermal actuation MEMS mirror.

### 4.1 Context of the study

In the previous two chapters, the quantitative aspect of the endomicroscope has been investigated and its ability to generate a reliable and discriminative information was validated. The next step in the instrumental development of our endomicroscope is to implement the qualitative aspect in order to reach the multimodality. Qualitative ability of the endomicroscope is traduced by its ability to perform endoscopic imaging acquisition with high performance. As mentioned in the introduction, a miniature high performance scanning system that permits high resolution imaging is required for TPF + SHG endoscopic imaging. To reach this goal, we headed toward the MEMS-based scanning systems in order to build a miniature endoscopic probe head that meet our needs. Using this scanning technique, we can easily perform raster scanning pattern with high density as well with a relatively simple drive and control process. Within MEMS-based scanners, several types of actuation mechanism exist that differs in their characteristics (figure 1.30). Choosing the actuation mechanism depends on the desired factors and its field of application. Electrothermal actuation was chosen by our team to be employed in our customized scanning probe. It permits scanning with a large FOV and requires a very low driving voltage ( $\sim 4V$ ) [197]. Furthermore, an architecture consisting of double level of dual S-shape was accorded to the MEMS mirror bimorph actuators in order to obtain a high stability and scanning control with a relative low step response.

However, choosing the proper lens configuration is also necessary in order to achieve the maximal resolution and the highest possible collection efficiency. Table 4.1 presents three different lens configurations that are widely used for optical endoscopic imaging where a study that compares these three configurations, in term of resolution, FOV size and packaging flexibility, was reported by S. Tang et al. [276]

	Design I	Design II	Design III
			
<b>20 <math>\mu\text{m}</math> fluorescent beads image</b>			
<b>Image resolution</b>	Low	High	High
<b>Packaging flexibility</b>	Easy	Complex	Easy
<b>Field Of View</b>	Large	Small	Large
<b>Working distance</b>	Long	Short	Short

**Table 4.1:** Comparison between three different lens configuration designs used for optical endoscopic imaging [276].

The two-lens configuration was employed for our probe design since that offers the best combination between high resolution and short working distance for high TP signal collection efficiency. Once the actuation mechanism and the lens configuration and the micro-lenses are chosen, a customized probe head was customized and fabricated in collaboration with the team of Prof. Huikai Xie from university of Florida. The first lens used in this probe is an achromatic doublet lens (NT65-564, Edmund Optics) with 1 mm as diameter and 1.5 mm as focal length, which is used as collimation lens and placed at the distal end of the fiber to collimate the laser beam before it hit the mirror plate. Reflected through the mirror plate, the laser beam will be focused with an aspheric lens with a large diameter (2.4 mm), a high Numerical Aperture (NA= 0.58) and a short working distance (0.9 mm) (354140-B, Thorlabs).

Characterizing the MEMS mirror and its mechanical properties is necessary in order to investigate the imaging capabilities of our probe and to reveal any technical problem or deficit within the actuator's architecture. This study represents the first step to reach our final goal. Mirror plate reflectivity, optical Scan Angle (OSA), Pixel Dwell Time (PDT), step response, frequency response and the impact of the probe optical components on the delivered excitation pulse were investigated in this study.

**Methods** Two different setups were used in this study. The first one was used to measure the mirror plate reflectivity, it employs a polychromatic light source with a monochromator, an objective to focus the light toward the mirror plate that reflect in into a photodiode sensor to measure its mean power. The second setup was dedicated for OSA, PDT, step, and frequency response measurements. It consists of a laser diode that emits a 430 nm laser beam toward the MEMS mirror, driven with an AC voltage generator, which reflect it

toward a high speed CCD camera. The MEMS mirror have a 0.52x0.52 mm aperture and a footprint of 1.3x1.5 mm. It employs four identical Al/SiO<sub>2</sub> electrothermal two-level ladder dual S-shaped bimorph actuators.

**Results and conclusion** The aluminum coated mirror plate showed a reflectivity higher than 80% over a range starting from 470 nm to 800 nm which covers the generated fluorescence signal when exciting at 810 nm. This parameter was found around 74% at 405 nm which corresponds to the SHG wavelength. Measuring the reflectivity of the mirror plate, over this wide wavelength range, permits to quantify its light transmission. This quantification is necessary to correct the detected spectral response and consequently to optimize the derived metabolic ratios. These ratios as well the collagen density related parameters are extracted through fitting the detected spectra, following the emission wavelength of each fluorophore.

OSA variation was measured for each actuator with a drive voltage up to 4 V. This variation was quasi linear for the four actuators and achieved  $\sim \pm 24^\circ$  scanning range at 4 V within the vertical scanning axis, while the horizontal axis has a lower scan range ( $\sim \pm 14^\circ$ ). This difference is attributed to the non-uniformity of the thickness of the deposited Al/SiO<sub>2</sub> layers in each scanning axis actuators which led to a difference in the thermal resistance of the actuators [277]

However, this quasi-linearity of OSA variation led to a constant PDT variation over both scanning axes. With a standard deviation less than 10% for both axes. Therefore, the mirror actuators permit a stable scanning with a uniform speed along a raster pattern. Therefore, it avoids image distortion and improve the quality of the acquired images.

Further, dynamic responses including step response and frequency response of each actuator has been investigated. Rise time for all actuators was around  $\sim 4.1$ - $4.5$  ms while the fall time was little bit higher ( $\sim 4.8$ - $5.4$  ms) which is caused by the heat stored in the mirror plate and that flows back into the actuators during the cooling phase During the cooling phase [278].

These values are important to be measured in order to be integrated to the drive and control system of the MEMS scanner to achieve an accurate trigger between the MEMS actuators and the photon counting module. Therefore, temporal phase shift between scan process and photon counting can be avoided and consequently the spatial shift between the pixel rows of the acquired image. Frequency response of each actuator showed resonance peaks around 1400 and 1800 Hz corresponding respectively to the actuators tip-tilt modes and piston mode. However, the imaging FOV decrease sharply when the scanning frequency increases. At high frequencies, only 10 % of the initial FOV can be achieved. This decrease limits the ability to change the scanning speed without a FOV change but it can be overcome by adjusting the drive voltage for each scanning frequency in order to preserve a stable imaging FOV.

Lastly, the effect of the optical components on the pulse duration was identified, were the pulse duration increased from 45 fs at the distal end of the endoscopic fiber to 57 fs at the exit of the focusing lens.

To this end, our probe head has a 4 mm as outer diameter and is able acquire TPF images with a scanning speed of 2 images per second that could be achieved over an imaging FOV of 450x450  $\mu\text{m}$  with an excitation beam of 57 fs pulse duration.

The next step, which is already ongoing and under tests, is the development of the drive and control acquisition software. Such software will drive the MEMS scanner and synchronize its scan movement with the photon counting detector as well as to transfer to convert the analogical data to numerical values in order to process into image reconstruction.

## 4.2 Paper: A Customized Two Photon Fluorescence Imaging Probe Based on 2D scanning MEMS Mirror Including Electrothermal Two-Level-Ladder Dual S-Shaped Actuators



Article

### A Customized Two Photon Fluorescence Imaging Probe Based on 2D scanning MEMS Mirror Including Electrothermal Two-Level-Ladder Dual S-Shaped Actuators

Hussein Mehdine <sup>1,2</sup>, Min Li <sup>3</sup>, Jean-Francois Lendresse <sup>1</sup>, Françoise Bouvet <sup>1</sup>, Huikai Xie <sup>4</sup> and Darine Abi Haidar <sup>1,2,\*</sup>

<sup>1</sup> Université Paris-Saclay, CNRS/IN2P3, IJCLab, 91405 Orsay, France; mehdine@imnc.in2p3.fr (H.M.); jf.lendresse@hotmail.fr (J.-F.L.); francoise.bouvet@ijclab.in2p3.fr (F.B.)

<sup>2</sup> Université de Paris, IJCLab, 91405 Orsay, France

<sup>3</sup> Suzhou Institute of Biomedical Engineering and Technology (SIBET) Chinese Academy of Sciences (CAS), Suzhou 215163, China; limin@sibet.ac.cn

<sup>4</sup> School of Information and Electronics Technology, Beijing Institute of Technology, Beijing 100081, China; hk.xie@ieee.org

\* Correspondence: darine.abihaidar@ijclab.in2p3.fr

Received: 1 June 2020; Accepted: 20 July 2020; Published: 21 July 2020



**Abstract:** We report the design and characterization of a two-photon fluorescence imaging miniature probe. This customized two-axis scanning probe is dedicated for intraoperative two-photon fluorescence imaging endoscopic use and is based on a micro-electro-mechanical system (MEMS) mirror with a high reflectivity plate and two-level-ladder double S-shaped electrothermal bimorph actuators. The fully assembled probe has a total outer diameter of 4 mm including all elements. With a two-lens configuration and a small aperture MEMS mirror, this probe can generate a large optical scan angle of 24° with 4 V drive voltage and can achieve a 450 μm FOV with a 2-fps frame rate. A uniform Pixel Dwell Time and a stable scanning speed along a raster pattern were demonstrated while a 57-fs pulse duration of the excitation beam was measured at the exit of the probe head. This miniature imaging probe will be coupled to a two-photon fluorescence endoscope oriented towards clinical use.

**Keywords:** micro-electro-mechanical system (MEMS) mirror; two-photon imaging; electrothermal actuators; 2D scanning probe

#### 1. Introduction

Today, total resection is still the main therapy to deal with brain tumors. Surgery is considered critical for brain tumor management, where the main challenge is to accurately identify tumor margins to improve its resection outcomes [1]. Tumors boundaries often have similar visual appearance with the surrounding healthy areas, which makes the surgeon unable to delineate these margins correctly and thus results in subtotal removal and tumor recurrence [1]. To obtain more information about these margins and to confirm the success of the surgery, biopsy samples are extracted for histological analysis, which involves Hematoxylin and Eosin (H&E) staining. The results from this post-surgery analysis are only provided several days after to form the absolute diagnosis. This is apart from the fact that if the results show that tumor cells were not well extracted and a second intervention is needed, the final diagnosis relies on human judgment based on expertise and experience of the pathologist. Several methods have been transferred to the operating room to resolve the inherent

### 4.2.1 Introduction

Today, total resection is still the main therapy to deal with brain tumors. Surgery is considered critical for brain tumor management, where the main challenge is to accurately identify tumor margins to improve its resection outcomes [28]. Tumors boundaries often have similar visual appearance with the surrounding healthy areas, which makes the surgeon unable to delineate these margins correctly and thus results in subtotal removal and tumor recurrence [28]. To obtain more information about these margins and to confirm the success of the surgery, biopsy samples are extracted for histological analysis, which involves Hematoxylin and Eosin (H&E) staining. The results from this post-surgery analysis are only provided several days after to form the absolute diagnosis. This is apart from the fact that if the results show that tumor cells were not well extracted and a second intervention is needed, the final diagnosis relies on human judgement based on expertise and experience of the pathologist. Several methods have been transferred to the operating room to resolve the inherent limitation of biopsy-based histology such as functional brain mapping [279] and intra-MRI [280]. However, these intraoperative modalities have not yet reached the reliability and the precision of the standard H&E post-surgery analysis. However, optical imaging is an emerging field that permits high-resolution and cross-sectional imaging of biological tissues such as Optical Coherence Tomography (OCT) imaging [268] and Two-Photon Fluorescence Microscopy (TPFM) [98]. Both OCT and TPFM can be used endoscopically to perform intraoperative imaging for cancer detection without the use of exogenous dyes. TPFM has been shown to quantitatively and qualitatively discriminate healthy brain tissues from tumoral ones at the subcellular level, therefore competing with H&E stained images [98], [270]. The label free and superior spatial resolution of TPFM renders it very useful as a non-invasive diagnosis technique for biomedical imaging applications.

To this end and to address these issues, our team is developing a Two-Photon Fluorescence (TPF) endomicroscope, dedicated to intraoperative label-free imaging for brain tumor tissues [173], [257]. This tool is addressed in order to improve the surgical act by helping the neurosurgeon to obtain a real-time, fast, and reliable diagnosis response of the examined tissues.

In parallel, and over several years, we have been establishing an optical tissue database which aims to extract and to specify each brain tissue type with its specific optical signature. These specific signatures are derived from the multimodal analysis of the endogenous fluorescence emission of several fluorophores presented in brain cells. In our past studies, we managed to discriminate, with high specificity and sensitivity, healthy human brain tissues, from secondary and primary brain tumors [98], low and high grade glioma [270], and grade I and grade II meningioma [216]. This database will be associated to the endomicroscope as a standard reference to establish a real time diagnosis during intraoperative imaging. In this context, our endomicroscopic tool is able to efficiently excite four main endogenous fluorophores, that their fluorescence signal is analyzed in the tissue database: Nicotinamide adenine dinucleotide (NADH), Flavins (FAD), Lipopigments and Porphyrins, as well as detecting Second Harmonic Generation (SHG) from non-centrosymmetric molecules such as collagen structures presented in brain tissues.

However, transition from benchtop microscopy to endomicroscopy is challenging. Most of the TPFM scanning systems have been developed using free-space optics and benchtop

microscopes setups while in vivo imaging and clinical applications impose the use of a fiber-optic endoscope, where the laser beam is delivered through a flexible fiber and image acquisition can be performed using a miniature probe. Choosing the proper fiber is essential to ensure the delivery of femtosecond laser pulses to the imaged specimen. This transition also requires the miniaturizing of the distal optics and integration of the scanning device into medical instruments such as trocars that are used to perform tissue biopsy.

Through time, several miniaturized scanning techniques have been developed to acquire images through TPFM- and OCT-based probes. The two main widely used scanning techniques are scanning a fiber or scanning an optical beam in free space. The first one consists of introducing the endoscopic fiber into a piezoelectric (PZT) ceramic tube in order to induce resonance within the fiber and perform scanning patterns [169], [190]. This technique is widely used in TPFM probes due to its low cost and fast scanning speed. However, it suffers from different mechanical constraints that affect its linear displacement [191] and affect its control to acquire homogenous and repetitive scanning patterns and limit its Field Of View (FOV) [181], [190].

The second scanning method is scanning an optical beam using a Micro-Electro-Mechanical System (MEMS) mirror. It is a recent technology widely used for OCT-based endoscopes [197], but not frequently used for TPFM probes due to the high-development cost. The main advantages of this technology reside in its small size, large achievable scanning FOV and stable scanning pattern [197], all of which allow for high scanning frame rates and ease of control. Several groups around the world have designed scanning systems based on MEMS mirrors dedicated mostly for OCT endoscopic imaging [197], [200], [281]. The design of the probe, lens configuration, total outer diameter of the probe, mirror size and actuation type were the most development challenges faced over time [199], [276]. In fact, clinical in vivo imaging and real-time biopsy requires the use of a small diameter probe, with fast acquisition and high resolution. The majority of developed TPFM or OCT probes based on MEMS mirror scanners either have a large diameter due to the use of a large aperture mirror [282], or lack resolution due the non-adapted lens configuration or lack stability and high performance due to the use of a non-adapted actuation type [282].

In our previous works, we managed to overcome the first challenge, i.e., the ultrashort pulse delivery was realized through a homemade micro-structured double-clad photonic crystal fiber (DC-PCF), specially designed for non-linear endomicroscopy [173]. We managed to generate an 810 nm laser beam with a 40-fs pulse duration at the exit of a 5-m long fiber. Briefly, it was composed of a 6.4  $\mu\text{m}$  diameter single mode central core to ensure the excitation with a numerical aperture of 0.097 at 800 nm. The central core was surrounded by an air/silica micro-structured region with a diameter of 40  $\mu\text{m}$  to separate it from the collecting inner cladding. Efficient collection of the fluorescence signals was ensured through this latter waveguide with a numerical aperture of 0.27.

Once the pulse delivery was addressed, our second challenge was to design and manufacture the best performing scanning probe. Our goal is to obtain an intra-operative imaging tool able to perform fast stable scanning acquisition, acquire high resolution images with a large FOV and a miniature probe that is small enough to fit in a surgical tool (surgeon trocar) to perform real-time optical biopsy examination.

In this paper, we report a homemade TPF probe based on a 2D electrothermal MEMS mirror adapted for in vivo clinical imaging in a clear and a defined medical needs context.

This customized probe combines a two-lens configuration design with a new actuators shape consisting of two-level-ladder double S-shaped electrothermal bimorph actuators and employs a small aperture mirror. We discussed the choice of the presented lens configuration, probe design, actuation type and actuators architecture. Critical issues such as the mechanical characteristics of the MEMS mirror actuators and the efficiencies of the laser pulse delivery and fluorescence collection were addressed.

## 4.2.2 Materials and methods

### 4.2.2.1 Probe design

The first step in the fabrication of an intraoperative endoscopic probe is to choose the best design that can ensure a high imaging resolution, large imaging FOV and high packaging flexibility within the smallest possible outer diameter.

In their study, S. Tang et al. [276] presented three different side-viewing imaging incorporating a different lens configuration each. They compared their advantages and disadvantages in order to perform multiphoton endoscopy imaging. Their probes implement an electrostatic MEMS mirror with a large diameter (2 mm), able to achieve a 20° as optical scan angle over 90 V as driving voltage. The three different configurations were tested and used to image 20  $\mu\text{m}$  beads in order to compare the image generated from each design.

The first one presented is a common lens configuration widely used in the reported OCT probes designs [200], [281], and consists of a single focusing GRIN lens placed between the endoscopic fiber and the MEMS mirror. This configuration is the simplest one that could be realized for an endoscopic probe design. It has the advantage of an easy alignment and assembly packaging as well as size efficiency [276]. The achievable imaging FOV of their tested probe was 200  $\mu\text{m}$  while the resolution of the 20  $\mu\text{m}$  beads was  $\sim 5 \mu\text{m}$ . However, this configuration imposes the use of a long working distance GRIN lens in order to let the beam reach the sample, which leads to a poor image resolution.

The second design consists of putting the GRIN focusing lens after the MEMS mirror, very close to the sample, which requires the use of a short working distance focusing lens. Therefore, this design is difficult to optimize and suffers from a small achievable FOV (100  $\mu\text{m}$ ). In fact, and by using only one lens, the path from the endoscopic fiber to the lens and from the lens to the sample is restricted, which limits the flexibility to adjust those distances, so to fit in the MEMS mirror. It also limits the imaging FOV and imposes the use of a large aperture MEMS mirror in this case, which increases the total outer diameter of the probe. However, this design overcomes the resolution problem of the first design due to the short working distance of the lens, where the resolution of the obtained image of the 20  $\mu\text{m}$  beads was  $\sim 2 \mu\text{m}$ .

The third design consists of a two-lens configuration, where a collimation lens was placed between the fiber and the MEMS mirror and a focusing lens was placed after the mirror close to the sample. This design combines the advantages of the previous design a high FOV, image resolution and flexible in packaging. The path between the collimation lens and the focusing lens can be easily varied to fit in the MEMS mirror without changing the beam property due the collimated beam. Therefore, the obtained image FOV was 200  $\mu\text{m}$  with a 2  $\mu\text{m}$  resolution for the 20  $\mu\text{m}$  beads image.



As the two-lens configuration has the best combination of FOV, resolution and packaging flexibility, we decided to adopt it as the design for our TPF handled probe. We tried also to choose the most miniature possible optical elements while preserving a high performance. As the collimation lens, an achromatic doublet lens (NT65-564, Edmund Optics, Barrington, NJ, USA) with 1 mm as diameter and 1.5 mm as focal length was used. As the focusing lens (354140-B, Thorlabs, Newton, NJ, USA), an aspheric lens with a large diameter (2.4 mm), a high Numerical Aperture ( $NA = 0.58$ ) and a short working distance (0.9 mm) was used. Described in the next subsection, the used mirror was a small aperture electrothermal MEMS mirror with a mirror plate size of  $0.52 \text{ mm} \times 0.52 \text{ mm}$ . Afterwards, Zemax simulations were performed for the chosen design. Through these simulations, we managed to reach a  $560 \text{ }\mu\text{m}$  FOV with only  $\pm 10^\circ$  as Optical Scan Angle (OSA). Figure 1a shows the distances set between the collimating lens, the MEMS mirror and the focusing lens. The footprint diagram of the tracked beam at the exit of the focusing lens shows that a  $560 \text{ }\mu\text{m}$  FOV could be reached with a mechanical scan angle of  $\pm 5^\circ$  (Figure 4.1(b)).

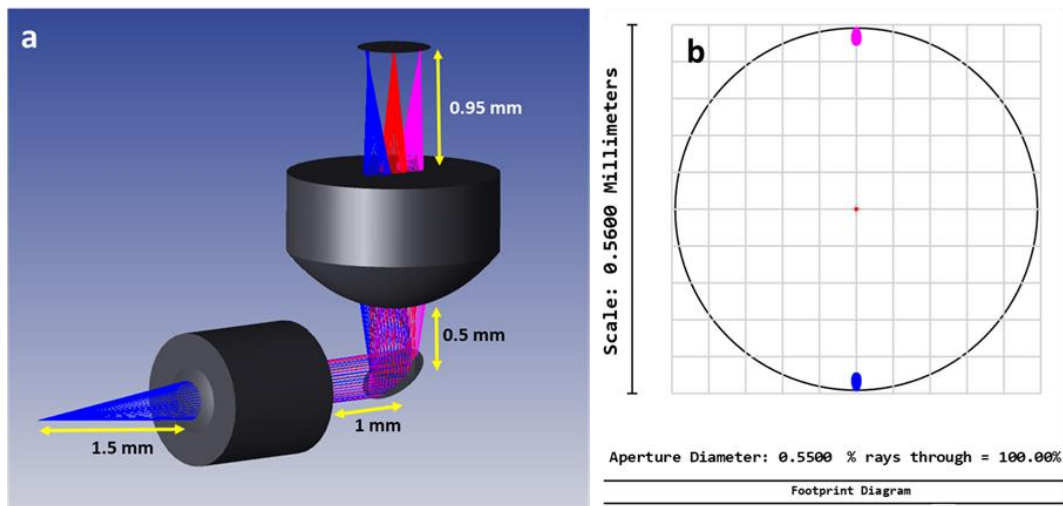


**Figure 4.1:** (a) Zemax shaded model of the probe design. (b) Footprint diagram of the tracked beam at the exit of the focusing lens.

#### 4.2.2.2 MEMS mirror and probe assembly

Moving to the MEMS mirror actuation, several types of MEMS mirrors exist, based on electrostatic [283], [284], piezoelectric [285], electromagnetic [286] or electrothermal actuation [200]. Electrostatic MEMS mirrors are particularly known for their low power consumption and the high operation frequency ( $\sim 10 \text{ kHz}$ ) which enables very fast scanning acquisitions. However, they typically need high driving voltage ( $\sim 100 \text{ V}$ ), their scanning ranges are limited compared to the other types ( $\pm 10^\circ$ ) and their linearity control is complex [197]. Electromagnetic MEMS mirrors have low driving voltages ( $\sim 3 \text{ V}$ ) and large scanning ranges ( $\pm 20^\circ$ ), but they suffer from a low fill factor (5%) and large packaging size due to the need of packaging permanent magnets [197]. Electrothermal MEMS mirrors have several main advantages: high fill factor (25%), low drive voltage ( $< 5 \text{ V}$ ) and larger scanning range (up to  $\pm 30^\circ$ ) compared to the other aforementioned types [197]. In the electrothermal MEMS mirrors family, there are several actuator shapes, such as Z-shape, U-shape [287] and S-shape actuators [281].

A number of electrothermal MEMS mirror-based probes have been reported in the literature, with most of them deploying single-level S-shaped bimorph actuators [200], [281], [288]. This type (single level architecture) can achieve  $\sim \pm 12^\circ$  as optical scan range [281] using a low voltage with a fast response time ( $\sim 4$  ms) [288]. However, it suffers from a short stable frequency range before reaching the resonance regime [281], while the use of a high voltage ( $> 5$  V) may damage the actuators.

Stacking more levels in the actuators architecture has been explored to achieve large piston displacements and to increase the frequency stability and its flat range before resonance [289], [290].

S. Luo et al. [289] used an electrothermal MEMS mirror which employs three levels of dual S-shaped bimorph actuators to develop an OCT imaging probe including a C-lens instead of a GRIN lens in a single-lens configuration for the probe design. It has  $\pm 17.5^\circ$  as an optical scan range at only 5 V, with the ability to use a higher voltage to achieve a larger FOV without damaging the actuators

J. Chai et al. [290] reported a MEMS mirror with three levels of dual S-shaped bimorph actuators dedicated to develop a Fourier transform spectrometer and obtained a more stable scanning with large displacement, but the response time of this shape of actuators was significantly high (28 ms) and needed a high driving voltage (up to 10 V) to achieve a large scanning range [290].

Hence, the use of a new actuator shape, based on a symmetrical two-level ladder of dual S-shaped bimorph actuators (Figure 4.2(a)), is adopted. This allows us to keep the low response time of the actuators and to gain more stability and control of the scanning process following a raster scanning pattern.

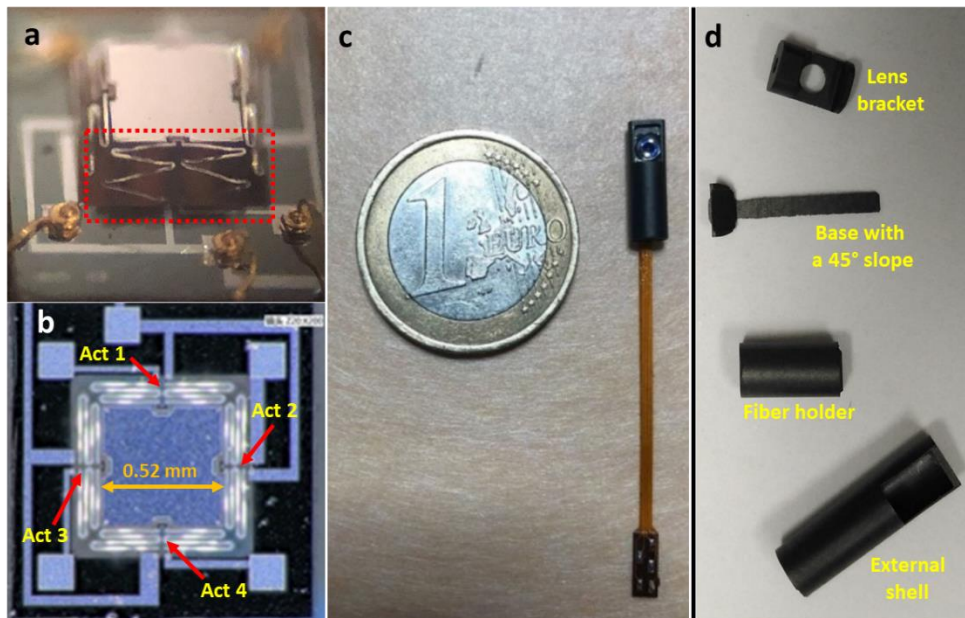


**Figure 4.2:** (a) An optical image of the Micro-Electro-Mechanical System (MEMS) mirror showing one of its two-level-ladder, double S-shaped actuators (red square); (b) Scanning electron microscopic (SEM) image showing the four actuators with the mirror plate; (c) Assembled probe; (d) Probe mechanical components.

Table 4.2 shows the differences among single-level, double-level, and three-level MEMS mirrors with the same Al/SiO<sub>2</sub> bimorph materials as used for our MEMS mirror actuators. The values concerning the double-level MEMS mirror consist of the values obtained in this work and presented in the results section.

	Single Level	Double Level	Three Level
<b>OSA/Voltage</b>	$\pm 13^\circ/4$ V [281]	$\pm 24^\circ/4$ V	$\pm 17.5^\circ/5$ V [289]
<b>Response time</b>	4.3–4.6 ms [288]	~4.5–5.5ms	~28 ms [290]
<b>First order resonant frequency</b>	191 Hz [281]	950hz	1.3 KHz [289]

**Table 4.2:** Comparison of the main mechanical properties between three MEMS mirrors deploying Al/SiO<sub>2</sub> dual S-shaped bimorph electrothermal actuators with a different actuators level architecture each.

A side-view scanning electron microscopic (SEM) image of the MEMS mirror (WiO Technologies, Wuxi, China) is shown in Figure 4.2(a), where the central mirror plate was suspended with four symmetrical two-level-ladder, double S-shaped bimorph electrothermal actuators over a silicon substrate. An Aluminum (Al) layer covered by a SiO<sub>2</sub> layer from each side composes each actuator. Figure 4.2(b) shows a top-view picture of the MEMS mirror whose footprint was 1.3 mm × 1.5 mm. The surface of the mirror plate was coated with a layer of aluminum (thickness: ~0.3 μm). The end result was an assembled probe with a 4 mm outer diameter, as shown in Figure 4.2(c). The pictures of the mechanical components are shown in Figure 4.2(d).

#### 4.2.2.3 Characterization setup

Two different setups were used to measure the optical and mechanical properties of the MEMS scanning mirror. The first one was a reflectivity measurement setup. It consisted of a Xenon light source (HPX-2000, Mikropack, Ostfildern, Germany) coupled with a monochromator (MonoScan 2000, Mikropack, Ostfildern, Germany) delivering a monochromatic beam going from 400 nm to 800 nm with a 1 nm step interval. The outgoing beam was converged to the mirror plate using an objective in order to focus the beam into a 320 μm diameter focal point, smaller than the mirror plate surface, to ensure a total reflection through the mirror. The optical power was measured, using a photodiode sensor (PD300, Ophir photonics, Ophir Spiricon Europe GmbH, Darmstadt, Germany) with a spectral detection range from 350 nm to 1100 nm, before and after the mirror, resulting in the reflectivity at various wavelengths.

To measure the scanning properties of the mirror actuators, the second characterization setup, presented in Figure 4.3, was used. Each pair of the actuators generates the scanning along a single axis, i.e., the actuators 1 and 4 responsible for the Y-axis scanning and the actuators 2 and 3 for the X-axis scanning. A laser beam, going out from a laser diode, was directed into the mirror plate, and reflected toward a charge-coupled device (CCD) camera (Fastcam Mini UX 50, Photron, Photron Deutschland GmbH, Reutlingen, Germany) to track the laser beam's spatial displacement. This camera could reach a recording speed of 160,000 frames per second (fps) and was equipped with a 1.3-Megapixel CMOS Sensor with a pixel size of 10 μm. An AC signal generator (AFG3022C, Tektronix, Beaverton, OR,

USA) was used to provide voltage signals to the mirror actuators. This setup was used to measure the quasi-static angular scan characteristics and frequency response of the MEMS mirror.

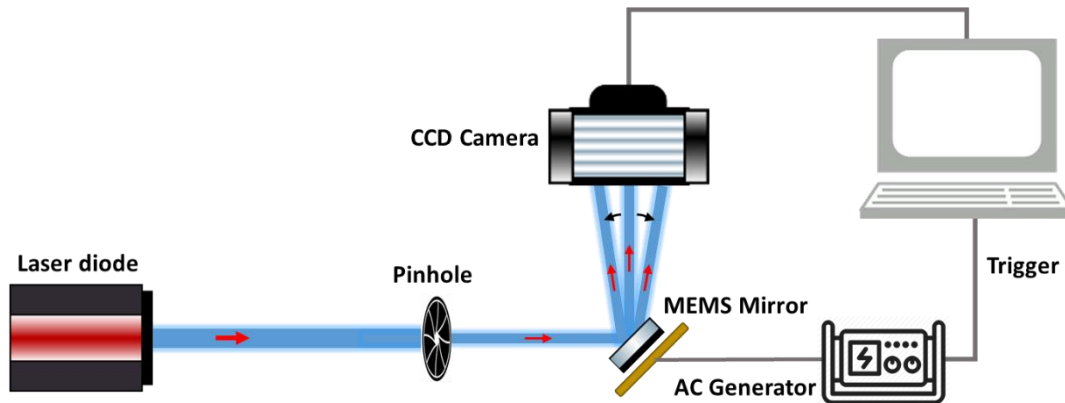


**Figure 4.3:** Schematic of the characterization setup of the mechanical properties of the MEMS actuators.

### 4.2.3 Results

Characterization started by investigating the spectral reflectivity of the mirror plate among a polychromatic signal wavelength range. Quantifying this parameter is required in order to calibrate the detected fluorescence emission spectrum so that accurate spectral fitting can be performed. The measured reflectivity in the wavelength range from 400 nm to 800 nm is plotted in Figure 4.4. The reflectivity at 800 nm, corresponding to the excitation laser, was found to be around 84%. In the collection mode, a similar reflectivity was found at 550 nm, which corresponds to the FAD emission peak [270], while it was found to be lower at 405 nm (74%), which corresponds to the SHG peak when excited at 810 nm. The wavelength range of the TPF signal excited using an 800 nm laser ranges from 400 to 700 nm.

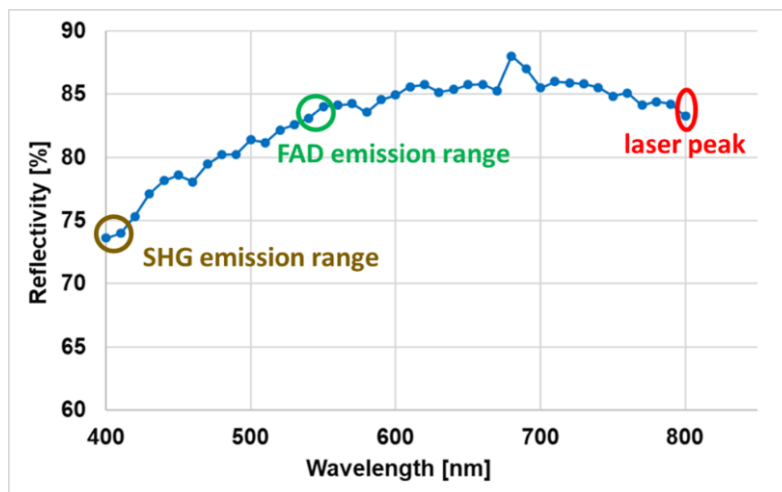


**Figure 4.4:** Measured reflectivity of the MEMS mirror plate.

OSA measurements were performed using several voltages ranging from 0 to 4 V. The measured OSA values of the four actuators were plotted in Figure 4.5. The four obtained

curves, corresponding each to a single actuator, showed a quasi-linearity variation starting from 0.5 V. This linearity was investigated by fitting each curve (starting from 0.5 V) to a polynomial fit curve ( $y = a*x + b$ ) where the fit equations were written and plotted in black (Figure 4.5). The corresponding R-square values were obtained higher than 0.99 for all fitted curves (0.9927, 0.996, 0.9969 and 0.9902 for actuator 1, 2, 3 and 4 respectively). Indeed, the obtained equations show the excellent similarity, in terms of OSA variation, between the actuators of each scanning axis where the obtained slopes of actuator 1 and 4 were very close and symmetrical (6.909 and  $-6.839$  respectively) as well as those of actuator 2 and 3 (4.03 and  $-4.01$  respectively).

It was observed also that the Y-axis actuators had maximum OSAs ( $24.78^\circ$  and  $24.67^\circ$  for actuators 1 and 4 respectively at 4V) larger than the X-axis actuators ( $14.31^\circ$  and  $14.49^\circ$  actuators 2 and 3 respectively at 4V). This difference is occurred due to the non-uniformity in the thickness of the deposited Al/SiO<sub>2</sub> layers in the actuators of each scanning axis. This non-uniformity led to an increase in the thermal resistance of the X-axis actuators, which directly depends on the thicknesses of these layers [277]. Therefore, the vertical displacement of the X-axis actuators was decreased.

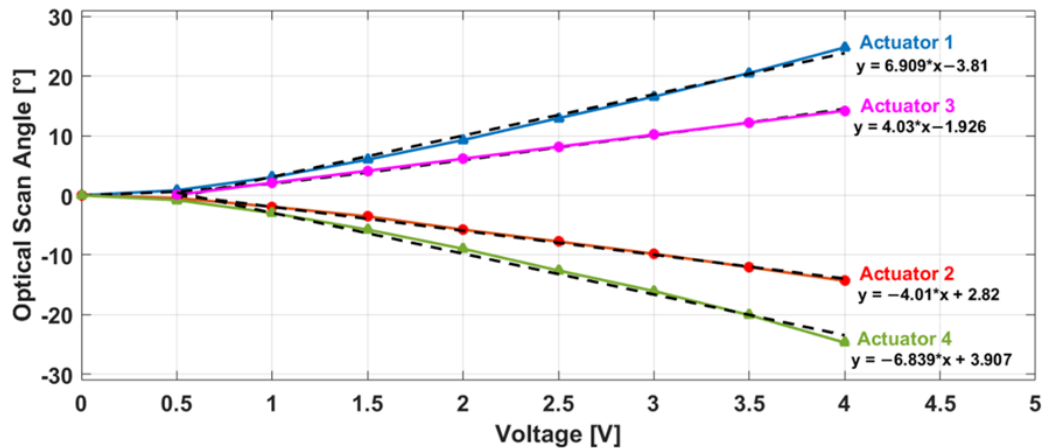


**Figure 4.5:** Optical scan angle variation with the driving voltage for the four actuators with the curve fitting equation of each one (black curves).

However, according to the simulations shown in Figure 4.1(b), a 560- $\mu\text{m}$  FOV only required a  $\pm 5^\circ$  mechanical scan angle, corresponding to  $\pm 10^\circ$  optical scan angle. This angle, and according to the fit equations, could be reached using 2 V as driving voltage for Y-axis scanning actuators (1 and 4) and at 2.95 V for X-axis scanning actuators (2 and 3).

The obtained linearity of the OSA with the driving voltage ensures a constant Pixel Dwell Time (PDT) along a single scan axis. PDT is defined as the time that the laser beam rests on a single pixel and illuminates it. It characterizes the scanning speed of any scanning system. Therefore, the higher the PDT is, the higher the number of photons collected per pixel and vice versa. The PDTs for Y and X scanning axes were extracted using the videos of the displacement of the reflected laser beam recorded with the CCD camera (Figure 4.3). The MEMS actuators were driven by an AC generator, which provided a 2V amplitude triangular wave-form signal with a 10Hz frequency, while the CCD camera frame rate was set at 20,000 fps.

The obtained results, plotted in Figure 4.6, show that a quasi-constant PDT was obtained for both X and Y scanning axes along a straight line. The standard deviation of each distribution of the values did not exceed 10% (100  $\mu$ s) around a calculated mean value of 1000  $\mu$ s. We can conclude that these two pairs of actuators are able to provide a stable scanning pattern with a uniform scanning speed along all scanning lines. Looking at the borders of these two curves, we can observe that the PDT was high at the beginning and started to decrease to become quasi-constant at the rest of the scanning line. This is due to the fact that the actuators have certain thermal response times before moving when they are driven by a voltage. For that, we measured the response time of each actuator using a 1-V amplitude square-wave signal for each actuator. The AC generator and the CCD camera were triggered together in a way that the CCD camera started recording at the same time as the AC generator provided its square signal. Figure 4.7(a–d) shows the obtained rise response times for the four actuators. The orange curve in each figure represents the assumed displacement of the laser beam for an ideal response time. The Y-axis represents the position of the laser spot in the CCD camera sensor referred by its pixel index position. The displacement of the laser spot goes to its final position with an exponential variation. For actuators 1 and 4, the 10–90% rise times were 4.08 ms and 4.10 ms, respectively, while for actuators 2 and 3, the 10–90% rise times were 4.56 ms and 4.40 ms, respectively. The fall response time was also measured for each actuator, where it was found respectively as 5.12 ms and 4.88 ms for actuators 1 and 4 and 5.28 ms and 5.40 ms for actuators 2 and 3. The fall response time was higher than the rise response (20%, 14.8%, 16.67% and 15% higher for actuators 1, 4, 2 and 3, respectively). This difference is believed to be caused by the heat stored in the mirror plate flowing back into the actuators during the cooling phase [278].

The frequency response of the four actuators was measured and presented in Figure 4.7(e). At a fixed amplitude of 1.5 V, the displacement of the laser beam (FOV) decreased with the frequency except for a few resonance peaks. Two main resonance peaks were detected for each actuator at 1400 and 1800 Hz with a secondary peak at 950 Hz. These peaks correspond respectively to the actuators tip–tilt modes and piston mode [277], [278]. At high frequencies, the FOV decreased to reach 10% of its initial value at 10 Hz. We can also observe that in the frequency range between 1100 Hz and 1300 Hz, the FOV maintains a constant variation. In fact, the scanning response is a combination of thermal response and second-order mechanical response. The displacement of the mirror will decrease with increasing frequency, which is caused by the thermal response.

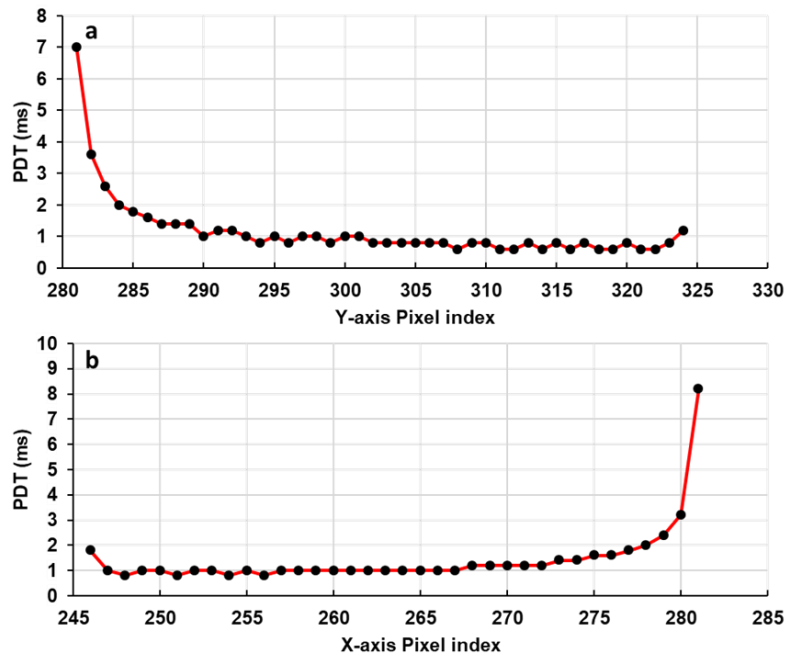


**Figure 4.6:** Measured pixel dwell time along a Y-axis scan line (a) and along an X-axis scan line (b).

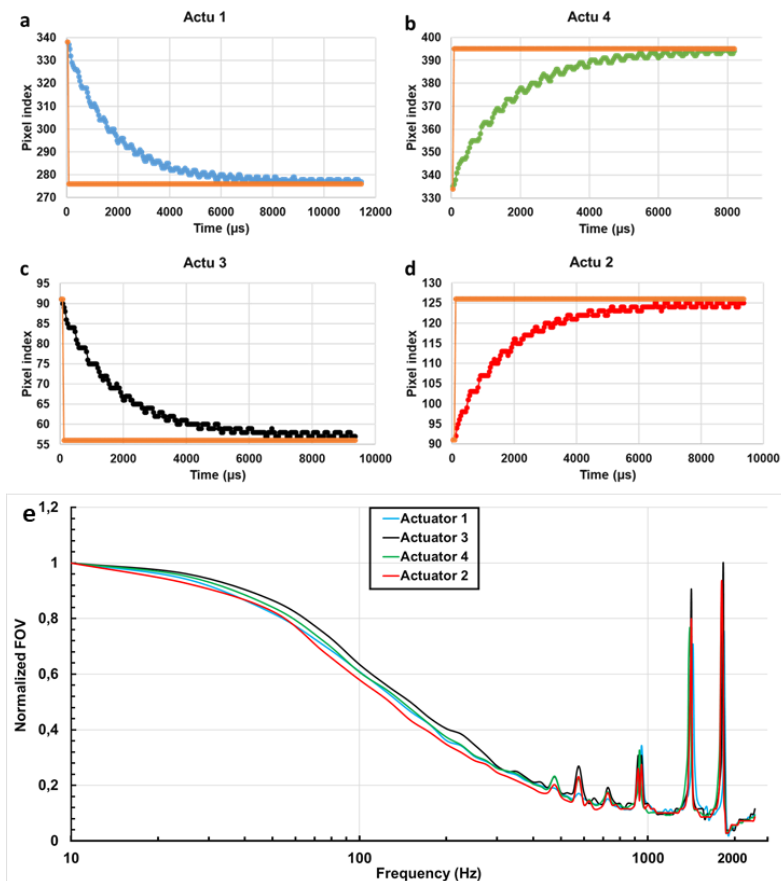


**Figure 4.7:** The dynamic responses of the MEMS mirror actuators. Step response of the MEMS mirror four actuators (a–d) in the rise phase (heating up). Frequency response of the four actuators (e) corresponding to the Normalized displacement of the beam (field of view, FOV) with the frequency variation at a fixed voltage of 1.5 V.

Finally, the impact of our scanning system on the pulse duration of the laser beam was investigated. Using an auto-correlator (Ape, mini) the auto-correlation trace of the laser pulse outgoing from the endoscopic double clad fiber (DCF) fiber was measured and is shown as the black curve in Figure 4.8. The auto correlation function was measured to be 70 fs, which corresponds to a pulse width of 45 fs for a pulse profile in  $\text{sech}^2$ .

The auto-correlation trace of the laser pulse outgoing from the assembled scanning probe was also measured using an objective to collimate the laser beam toward the auto-correlator. Its duration was found to be 89 fs (the blue curve in Figure 4.8), corresponding to a pulse duration of 57 fs for a pulse profile in  $\text{sech}^2$ . It is clear that the laser pulse duration did not greatly expand, suggesting that the scanning components did not alter the pulse duration, ensuring efficient two-photon excitation.

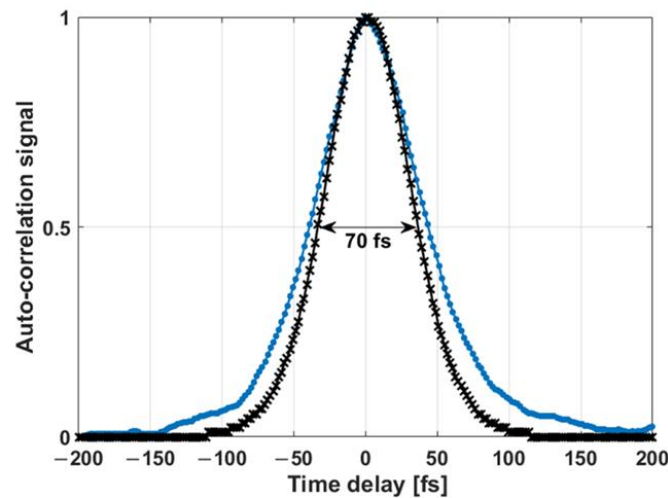


**Figure 4.8:** Autocorrelation trace at the output of the endoscopic double clad fiber (DCF) fiber (black curve) and at the output of the MEMS scanning system (blue curve).

#### 4.2.4 Discussion

Our main research project consists of developing a TPF multimodal endomicroscope dedicated to intraoperative brain imaging. This endomicroscope aims to improve the surgical act by delimitating the tumor infiltrating boundaries. It will be able to provide the neurosurgeon a fast and reliable multimodal quantitative and qualitative information on the tissue's nature in order to establish a real-time diagnosis. This diagnosis information will be extracted through an already-established tissue optical database of several human brain tissue types that has been demonstrated in our past works.

In actuality, our developed endomicroscope is able to perform bimodal measurements of two photon fluorescence spectra and fluorescence lifetime with high efficiency [257]. Since the bimodality is validated, the next step on the track of reaching a multimodal endomicroscope is the scanning system probe development.

In this work, a homemade TPF scanning head probe dedicated to performing optical biopsy and intraoperative brain imaging when coupled with the developed endomicroscope was presented. The imaging probe head combines a miniaturized 2D scanning electrothermal MEMS mirror and micro-optical lenses in a two-lens configuration. This imaging probe is able to ensure, with a small outer diameter, a large imaging FOV as well as performing



stable scanning acquisitions and delivers the shortest possible pulse duration to enhance the image contrast.

The characterization of the mechanical properties of the MEMS mirror starts by measuring the reflectivity of its aluminum-coated plate. It is an important parameter to be measured precisely in order to determine the signal transmission of the mirror and to quantify the excitation and collection efficiency on each wavelength since that the collected fluorescence signal is a polychromatic light. From this, several metabolic ratios could be derived from spectral fitting in order to provide important information about cellular metabolism [98] in different brain tissue types. These ratios are already established as discrimination factors between healthy and cancerous zones [98], [270].

Moving to the actuation characteristics, and as mentioned before, a fast and stable scanning acquisition is required in order to obtain the best image quality. A quasi-linear OSA variation with the voltage drive signal was obtained for both Y and X-axis (Figure 4.5).

Indeed, Zemax simulations showed that a 560  $\mu\text{m}$  FOV can be achieved when a  $\pm 10^\circ$  OSA range is reached by the mirror. Our desired imaging FOV varied from 250 to 500  $\mu\text{m}$  depending on the region of interest in the sample that the neurosurgeon wished to image. Therefore, and regarding the excellent linearity of the OSA variation, the maximum desired 500  $\mu\text{m}$  FOV can be reached with  $\pm 8.9^\circ$  OSA range for both axes which imposes the use of a very low operation voltage to drive the Y-axis actuators (1.84 V) and the X-axis actuators (2.69 V).

In addition, the OSA linearity was configured with a constant PDT variation through the two scanning axes. The standard variation of the obtained PDT values along a scanning axis was less than 10% (100  $\mu\text{s}$ ) around a calculated mean of 1000  $\mu\text{s}$ , which means that our MEMS mirror actuators are able to perform a 90% stable scanning along the two scanning axes. This stability will allow the acquisition of the real representative images of the specimen and will avoid the blurry effects and the distortion of the acquired images.

The dynamic responses of the MEMS mirror actuators including the step response and frequency response were also characterized. Observed from the PDT variation curves, the step response time of each actuator, during the heating and cooling phase, was measured. This parameter is necessary to be known in order to adapt the drive and control system of the MEMS scanner to achieve a precise synchronization and trigger between the MEMS actuators and the photon counting detector. It will allow us to avoid the temporal phase shift between the start of the scan and the start of photon counting, which also aids to avoid the spatial shift that may occur between the pixel rows of an acquired image.

Factually, the response time of the actuators depends on the type of materials that compose the thermal bimorph actuator and their thermal expansion coefficients (TEC). The two materials that are widely used to fabricate the bimorph thermal actuators are Copper (Cu) with tungsten [278], [291] and Aluminum (Al) with silicon dioxide (SiO<sub>2</sub>) [288], [292]. Thus, due to their larger TEC difference ( $23.1 \times 10^{-6}/\text{K}$  for Al and  $0.5 \times 10^{-6}/\text{K}$  for SiO<sub>2</sub>) comparing Cu/W actuators [291], the use of Al/SiO<sub>2</sub> bimorph actuators was favored. In literature, the measured step response time of the widely used Cu/W Bimorph actuators was found at around 7ms [278] and 15 ms [291], while the response time of our Al/SiO<sub>2</sub> actuators was found much lower (4 ms for heating phase and 5 ms for cooling phase).

The frequency response was also investigated for each actuator, where the FOV showed a decreased behavior in function of the scanning frequency. This decrease limits the ability

to change the scanning speed from a low to a fast acquisition without a FOV change. In the highest frequencies, the FOV reaches only 10% of its maximal value (Figure 4.7(e)) which imposes the increase of the used voltage in order to keep the same desired FOV.

This behavior, largely observed in the electrothermal actuators [197], [281], can be surpassed through the drive and control system of the MEMS scanner by accounting for each frequency's corresponding voltage value (amplitude of the control signal) in order to keep the same scanning FOV. However, the maximum advised driving voltage of an electrothermal actuator is around 5 V [197]. Surpassing this voltage overheats the Al/SiO<sub>2</sub> layers and may therefore damage the actuators. For this reason, a value of 4 V was fixed as the maximum driving voltage to prevent the damage of the mirror actuators. This 4 V threshold will be applied and used to drive the fast scanning axis actuators only, since the slow axis is operated with a very low frequency in a raster pattern so no need to increase the voltage. Since the Y-axis actuators (1 and 4) showed a larger OSA value, they will be adopted to ensure the fast axis scanning of the desired raster pattern. Referring to the optical simulations and to the frequency response variation (Figure 4.7), the maximum operating frequency of the Y-axis as well as the maximum frame rate that can be reached for each desired imaging FOV was calculated and presented in Table 4.3. The maximum desired 500  $\mu\text{m}$  FOV can be performed with a 1.8 fps rate, while the 2-fps rate can be reached with a 450  $\mu\text{m}$  FOV.

FOV	Max Frequency Y-axis	Frequency X-Axis	Frame Rate
500 $\mu\text{m}$	450 Hz	0.9 Hz	1.8 fps
450 $\mu\text{m}$	500 Hz	1.11 Hz	2 fps
400 $\mu\text{m}$	550 Hz	1.37 Hz	2.2 fps
320 $\mu\text{m}$	775 Hz	2.42 Hz	3 fps
250 $\mu\text{m}$	1175 Hz	4.69 Hz	4.7 fps

**Table 4.3:** The operating frequencies for both scanning axes for each imaging FOV with the maximum frame rate that can be reached for each FOV.

The last essential parameter that we investigated was the effect of the probe optical components on the sub-fs pulse delivery. Our custom-built fiber-based endomicroscope is able to generate excitation pulses with 45 fs duration delivered to the distal end of a 5-meter length long microstructured double-clad photonic crystal fiber (DC-PCF). At the exit of our developed probe, this duration increased to reach 57 fs. These generated short pulses increase the laser peak power which will improve the generated fluorescence signal [173], and they are also critical to prevent photo-bleaching or photo-induced tissue damage within the focal volume. They are desired also for obtaining superior image quality, enhancing the imaging depth and for faster acquisition times [257].

#### 4.2.5 Conclusion

In summary, a miniature two-photon fluorescence endomicroscopic probe head based on a 2-axis scanning electro-thermally actuated MEMS mirror with a total outer diameter of 4 mm was presented. This probe is dedicated to intraoperative brain imaging as well as performing optical biopsy. A combination of the most performing probe design and lens

configuration with the most performing available electro-thermal actuators was adopted in order to obtain a well suitable tool for in-vivo biomedical imaging. The chosen probe elements (micro-optics and mirror) ensures obtaining a large scanning FOV with high imaging speed, resolution, packaging flexibility, small probe diameter and sub-fs pulse delivery.

As for actuation type and architecture, a small aperture mirror that included electro-thermal actuators that meet our needs was used for a fast and stable scanning acquisition. A high reflectivity of the mirror plate was measured, which ensures a good excitation and signal collection efficiency. A large and linear OSA range was reached at a low drive voltage for horizontal and vertical scan axes which allows for the reaching of a large FOV with a low power consumption. A 450  $\mu\text{m}$  imaging FOV could be achieved with 2 fps as the imaging speed. A quasi-constant pixel dwell time was obtained along both scanning axes leading to a stable and a uniform scanning speed along a scanning pattern. In addition, the frequency response, the time response of the mirror actuators and the impact of the scanning system on the pulse duration were investigated.

Our ongoing work consists of developing an electronic acquisition system to control the developed device and to drive the MEMS mirror, synchronize the mirror with the detectors, perform photon counting and to quickly transfer the data for image reconstruction. Once the control software is finished, image acquisition will be performed, and several parameters will be investigated.

This promising technology has the potential to give birth to a new generation of miniature TPF micro-endoscopic imaging probes that are capable of realizing in vivo early cancer detection as well as performing fast optical biopsy with high performance. MEMS characterization is a prerequisite step before implementing the first multimodal in vivo TPF micro-endoscopic imaging tool based on MEMS scanning micro-mirror technology.

## Chapter 5

# What is the maximal post-operation time which permits to measure correctly the autofluorescence signal? Should a tissue database be acquired using only fresh samples?

### 5.1 Context of the study

The previous three chapters covered the technical development achieved towards building the TPF multimodal endomicroscope and its ability of extracting a reliable quantitative response from intrinsic fluorescence signal. The multimodality feature of our proposed technique is an important way to obtain a reliable and reproducible diagnosis information on the tissue's nature. It is also an important key to reveal the different biological differences that may be extracted from several endogenous fluorophores, NADH, FAD, Lipopigments, Porphyrins (I and II), as well as from non-centro symmetric structures such as collagen fibers, source of SHG signal. These features include the one and two-photon spectral and lifetime fluorescence properties for each endogenous fluorophore as well as the SHG signal. To facilitate the diagnosis establishment during surgery as well to achieve a robust tissue discrimination, a tissue database that gathers the different optical signatures obtained from ex vivo measurement of brain tissues of different brain tissue types (healthy cortical tissue, glioma, meningioma, and metastases) is under construction. Therefore, three different imaging platforms, covering each a different excitation domain (Deep UV, visible and Near Infra-red) are being used to supply this tissue database with multimodal optical contrasts. However, the neurosurgical operation lasts several hours, where a time delay of 3-4 hours typically occurs between the time that tissue is resected, and the time that it takes to be transferred in our laboratory in order to be analyzed. Therefore, it was imperative to study the effect of this delay time on the derived optical features.

Additionally, since our previous multimodal optical imaging studies had mostly involved imaging fixed healthy and brain tumors (meningioma, glioblastoma (GBM)) [215], [216], it was necessary to test if two-photon imaging of freshly excised tissue resulted in different optical signatures from those derived after the samples were fixed with formaldehyde. For the optical tissue database to be reliable therefore, two main questions need to be addressed:

- 1) What is the effect of time of measurement post-excision on the fluorescence properties extracted?
- 2) Are the optical signatures obtained from fresh tissues different from those that are Formalin fixed?

Both questions address primarily whether the derived fluorescence properties change according to the resection time and tissue processing. The first question was imperative to address, as no similar study had been reported in the literature. Despite that changes in the optical properties of tissue are known to change after their excision, due to tissue dehydration and increased blood deoxygenation, changes in the fluorescence properties of the previously cited four endogenous fluorophores within brain tissues has not been investigated. As for the second question, there are limited studies, that have compared changes in the one and two-photon emission signals in brain tissue before and after tissue fixation [241], [293], [294]. A detailed analysis of the effect of tissue preparation on the absorption, scattering, and autofluorescence spectral and lifetime properties will be presented in chapter 6.

**Methods** To monitor the variation of fluorescence properties with the post-excision time, spectral and fluorescence lifetime measurements were conducted on 10 freshly excised cortical tissues hourly for 5 hours in the neuropathology laboratory of Sainte Anne Hospital using a one-photon excitation bimodal endoscope (405 nm pulsed laser source) where the normalized fluorescence spectral shape, the fluorescence intensity, and the fluorescence lifetime of each fluorophore were extracted for each measurement.

For the fresh vs. fixed tissue study, 36 fresh samples were transported in physiological serum our laboratory within 3-4 hrs. after the surgery. TPF, SHG, as well as FLIM measurements were performed using the multimodal benchtop multiphoton microscope on 12 epileptic cortex samples (control), 13 glioblastoma samples (GBM), and 11 metastatic tissue samples. The average TPF and SHG spectra, and the mean lifetime values were obtained for each sample group before and after tissue fixation.

**Results and Discussion** The average one-photon fluorescence intensity decreased of 23% after 1 hour and 33% after 5 hrs. The two main fluorophores that were affected by the structural and metabolic changes due to tissue resection were Lipopigments and Porphyrin I. Interestingly, the fluorescence lifetimes for each fluorophore under 405 nm excitation did not significantly change with time.

On the other hand, the spectral shapes, and intensities of the TPF and SHG signals were different for all tissue groups after undergoing tissue fixation. However, there was still characteristic features present in control, GBM and Metastasis group that enabled tissue discrimination such as the persistent SHG signal in the Metastasis group, the low autofluorescence in the GBM group, and the uniform fluorescence signal in the control group. FLIM analysis showed that fixed tissue had longer mean lifetimes compared to their fresh counterparts. Results of this study suggest that a post-excision time of one hour is necessary to obtain consistent fluorescence intensities and lifetimes. The fresh vs. fixed tissue study indicates that while all optical signals differ after fixation, the characteristic features extracted from one and two-photon excitation still discriminate normal brain cortical tissue, glioblastoma, and metastases. Moving forward based on the results, it is recommended to construct two different optical tissue databases for accurate tissue discrimination depending on the application: if the database is to be used in the operating room to guide the surgery, then the database built from optical properties of fresh tissue should be used, while if the database is to be used for post-excision pathological assessment, then the database built from characterizing fixed tissue is to be used.

## 5.2 Paper: Multimodal imaging to explore endogenous fluorescence of fresh and fixed human healthy and tumor brain tissues

Received: 12 May 2018 | Accepted: 7 September 2018  
DOI: 10.1002/jbio.201800178



FULL ARTICLE

### Multimodal imaging to explore endogenous fluorescence of fresh and fixed human healthy and tumor brain tissues

Hussein Mehdine<sup>1,2</sup> | Mira Sibai<sup>1</sup> | Fanny Poulon<sup>1</sup> | Johan Pallud<sup>3,4,5</sup> | Pascale Varlet<sup>4,5,6</sup> | Marc Zanello<sup>3,5</sup> | Bertrand Devaux<sup>3,5</sup> | Darine Abi Haidar<sup>1,2\*</sup>

<sup>1</sup>IMNC Laboratory, UMR 8165-CNRS/ IN2P3, Paris-Saclay University, Orsay, France

<sup>2</sup>Paris Diderot University, Sorbonne Paris Cité, F-75013, Paris, France

<sup>3</sup>Neurosurgery Department, Sainte-Anne Hospital, Paris, France

<sup>4</sup>IMA BRAIN, INSERMU894, Centre de Psychiatrie et de Neurosciences, Paris, France

<sup>5</sup>Paris Descartes University, Paris, France

<sup>6</sup>Neuropathology Department, Sainte-Anne Hospital, Paris, France

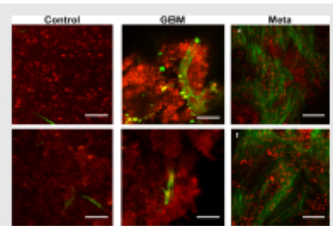
\*Correspondence

Darine Abi Haidar, Paris Diderot University, Sorbonne Paris Cité, F-75013, Paris, France.  
Email: abihaidar@imnc.in2p3.fr

Funding information

"Investissement d'Avenir" run by the "Agence Nationale pour la Recherche", Grant/Award Number: ANR 11-INBS-0006

To complement a project toward label-free optical biopsy and enhanced resection which the overall goal is to develop a multimodal nonlinear endomicroscope, this multimodal approach aims to enhance the accuracy in classifying brain tissue into solid tumor, infiltration and normal tissue intraoperatively. Multiple optical measurements based on one- and two-photon spectral and lifetime autofluorescence, including second harmonic generation imaging, were acquired. As a prerequisite, studying the effect of the time of measurement postexcision on tissue's spectral/lifetime fluorescence properties was warranted, so spectral and lifetime fluorescence of fresh brain tissues were measured using a point-based linear endoscope. Additionally, a comparative study on tissue's optical properties obtained by multimodal nonlinear optical imaging microscope from fresh and fixed tissue was necessary to test whether clinical validation of the nonlinear endomicroscope is feasible by extracting optical signatures from fixed tissue rather than from freshly excised samples. The former is generally chosen for convenience. Results of this study suggest that an hour is necessary postexcision to have consistent fluorescence intensities/lifetimes. The fresh (a,b,c) vs fixed (d,e,f) tissue study indicates that while all optical signals differ after fixation. The characteristic features extracted from one- and two-photon excitation still discriminate normal brain (a,d) cortical tissue, glioblastoma (GBM) (b,e) and metastases (c,f).



#### KEYWORDS

fluorescence, fluorescence lifetime imaging, fresh and fixed human brain tissues, multiphoton microscopy, spectroscopy

#### 1 | INTRODUCTION

Surgical resection, whenever feasible, is the first line of defense against most tumors of the central nervous system [1, 2]. The extent of resection is a significant prognostic factor independent of age, Karnofsky score and tumor grade. Since most patients eventually succumb to the disease, the

goal of maximal safe resection is not only to prolong the time to tumor progression, but rather to optimize the patient's quality of life. Therefore, extensive tumor removal is always balanced with preserving functional tissue. This challenge is exacerbated by the difficulty in delineating tumor to normal boundaries as brain tumors are diffusive and are known to migrate beyond the resection cavity, infiltrating normal

### 5.2.1 Introduction

Surgical resection, whenever feasible, is the first line of defense against most tumors of the central nervous system [28], [295]. The extent of resection is a significant prognostic factor independent of age, karnofsky score and tumor grade. Since most patients eventually succumb to the disease, the goal of maximal safe resection is not only to prolong the time to tumor progression, but rather to optimize the patient's quality of life. Therefore, extensive tumor removal is always balanced with preserving functional tissue. This challenge is exacerbated by the difficulty in delineating tumor to normal boundaries as brain tumors are diffusive and are known to migrate beyond the resection cavity, infiltrating normal parenchyma. As a result, complete resection in patients with glioma, for example, is achieved in less than 30% and 20% of low- and high-grade glioma cases, respectively [28], [296].

To improve surgical outcomes, intraoperative imaging, such as magnetic resonance imaging (iMRI), has become a necessity providing the surgeon with updated plans on the tumor's location and boundaries [297]. However, conventional neuro-navigation through the operating microscope guided by iMRI is currently still time-consuming and lacks the spatial resolution and sensitivity to resolve tissue microstructure or to discriminate between tumor-induced tissue alterations and surgically-induced changes, such as contusion, ischemia or oedema [297]. A more practical solution that provides real-time tumor contrast is intraoperative fluorescence. In its most widely used form, fluorescence-guided resection (FGR) is mediated by the preferential overproduction of the fluorophore protoporphyrin IX (PpIX) in malignant tissue after an oral dose of its precursor 5-aminolevulinic acid (ALA) [139], [148], [298], [299]. 5-ALA-PpIX FGR has been shown to significantly increase the rate of extent of tumor resections in high-grade glioma patients and more recently in meningioma cases [299], but has shown limited efficacy in identifying diffuse low grade gliomas, tumor necrosis and cases of micro-infiltration [148], [299]. PpIX fluorescence, however, is not highly specific to tumors as PpIX is known to leak into peritumoral oedematous areas, which are free of neoplastic cells [299]. Additionally, PpIX is also found in inflammatory cells adjacent to the tumor site [299]. PpIX's suboptimal photo-stability is also a concern since the fluorescence signal can decay to 36% of its initial intensity after 25 minutes of blue light excitation [299]. Intraoperative detection of endogenous fluorescence would be more practical as it eliminates the potential toxicity as well as the non-specific binding of ALA-PpIX and other exogenous dyes. The autofluorescence from reduced nicotinamide adenine dinucleotide (NADH) and flavin adenine dinucleotide (FAD), for example, has been used to differentiate between tumor and normal tissue as the optical redox ratio (NADH/FAD) relates to the tissue's metabolic state [93], [148]. In fact, it has been suggested that metabolic changes typically occur before changes in cellular proliferation [93]. Autofluorescence imaging, however, is not commonly used in brain surgery, because of the limited sensitivity and spectral specificity of endogenous fluorophores, namely, NADH, FAD, Lipopigments and Porphyrins following violet-blue excitation [82], [84].

Two-photon excitation on the other hand, intrinsically has depth sectioning capabilities and enhanced spectral resolution [300]. Although applying two-photon excitation on excised tissue or on the skin has gained momentum, in vivo two-photon excitation via an endoscope is severely lagging as the typical rigid needle-like lenses are not compatible with

intraoperative/intracavitary diagnosis [300]. Moreover, flexible fiber-optic probes typically used for one-photon confocal endomicroscopy, for example, degrade the two-photon excitation pulses so much so that excitation is not possible [300].

To address the above problems, we propose the use of a custom-built multiphoton endomicroscope capable of identifying tumors deep into tissue (up to 1 mm) at a sub-cellular resolution with minimal photo-damage and without the need for exogenous fluorescent dyes. A multiphoton endomicroscope is being designed in house to overcome the technical challenges in delivering energetic near infrared (NIR) ultrashort pulses, necessary for efficient two-photon excitation at the output of a long and flexible optical fiber, while being sensitive enough to detect the intrinsically low autofluorescence signals [173]. Compact nonlinear endoscopes that have been reported for imaging organs such as kidney and bladder in vivo [300] lack the unique multimodality and multiscale capabilities of the endomicroscope built in house, which is equipped to extract morphological and functional information based on multiple fluorescence signals: (1) spectral analysis, (2) two-photon fluorescence lifetime imaging microscopy (FLIM), (3) second harmonic generation (SHG) imaging, highlighting myosin and collagen, and (4) two-photon excitation fluorescence (2PEF) that will ultimately aid neurosurgeons in delineating healthy tissue from solid and infiltrative cancerous tissue at the time of resection.

To achieve accurate tissue diagnosis, a database of optical properties in the visible and NIR excitation range from numerous ex vivo brain tissue samples should be constructed a priori. This bank of information will characterize brain tissue (normal cortex and dura, solid and infiltrative glioma, meningioma and metastasis) by their one-photon and two photon spectral fluorescence emission properties, their one photon and two photon fluorescence lifetimes, as well as by their SHG signatures using model-based clustering, to be reported soon. Collecting multiple optical properties is expected to circumvent the biophysical limitations of individual optical techniques and to increase the overall accuracy in classifying tissue accordingly. Additionally, ex vivo multimodal measurements are necessary to optimize, calibrate, and validate the endomicroscope under development before clinical testing. However, since a delay of 3 to 4 hours typically occurs between the time tissue is biopsied and the time it is transferred to be analyzed, it was imperative to study the effect of this delay on the derived optical features. This was investigated by taking spectral and lifetime measurements, hourly, on the optical setup stationed at Sainte-Anne Hospital in Paris. Since our previous multimodal optical imaging studies had mostly involved imaging fixed healthy and brain tumors (meningioma, glioblastoma, (GBM)) [89], [97], [215], [216], it was necessary to test whether two photon imaging of freshly excised tissue resulted in different

optical signatures from those derived after the samples were fixed with formaldehyde. We investigated 2PEF signals to explore all known endogenous fluorophores emitting visible light, namely NADH, FAD, lipopigments, and porphyrins (I and II), in fresh and fixed brain tissues, including normal (control) brain tissues, primary (GBM), and secondary (metastasis (Meta)) brain tumor tissues from adult patients that were newly-diagnosed with a supratentorial malignant brain tumor.



## 5.2.2 Materials and methods

### 5.2.2.1 Samples

Approval of the Sainte-Anne Hospital, University Paris Descartes Review Board (CPP Ile de France 3, S.C.3227) was obtained for this study in collaboration with the Neurosurgery and the Neuropathology Departments of Sainte-Anne Hospital. All methods were performed in accordance with the relevant guidelines and regulatory requirements of this protocol and informed consent was obtained from all patients. A cohort of 46 samples was used. Ten cortex tissues biopsied from epileptic patients, considered as control samples, were used for the one-photon fluorescence excitation study at Sainte-Anne Hospital, where spectral and lifetime fluorescence signals were acquired hourly for 5 hours. The remaining 36 samples were transported in a physiological serum to the PIMPA (multiphoton imaging platform for small animals) platform at IMNC laboratory within 3 to 4 hours post excision for the nonlinear excitation study. 2PEF, SHG, as well as FLIM measurements were directly performed on these samples comprising of 12 epileptic cortex samples (control), 13 GBM samples and 11 metastatic tissue samples (Meta). Following two-photon imaging, these tissue samples were fixed using 4% formalin according to an established protocol for at least 24 hours. 2PEF, SHG and FLIM measurements were then taken on the fixed tissue samples to compare nonlinear optical properties extracted from fresh and fixed tissue.

### 5.2.2.2 Single-photon emission fluorescence setup

Spectral and fluorescence lifetime measurements were performed on a linear fiber-optic endoscope stationed at Sainte-Anne Hospital's neuropathology department in Paris, France. This setup was used and described thoroughly in our previous work [89], [97], [215] Briefly, the system consists of a 405-nmpulsed laser diode (LDH-P-C-405B, FWHM 60ps; PicoQuantGmbH, Berlin, Germany) controlled by a "Sepia" driver (PDL-808 "Sepia"; PicoQuant GmbH). The repetition rate was chosen to be 40 MHz. Excitation and fluorescence emission signals pass through a double-clad fiber (PC-DCF) [237], where 70% of the collected fluorescence is detected by a cooled computer-controlled spectrometer (QEPro 6500; Ocean Optics, Dunedin, Florida) equipped with a long-pass filter (SR420; Semrock, Rochester, New York). The spectrometer has a spectral resolution of 1.5 nm over its spectral range of 365 to 750 nm. For time-resolved fluorescence measurements, the remaining 30% of the collected fluorescence is directed to a photomultiplier tube (PMA-182 N M; PicoQuant GmbH) equipped with a filter wheel matching the emission maximum of the five endogenous fluorophores: NADH, FAD, Lipopigments, Porphyrin I and Porphyrin II, detected at  $450 \pm 10$  nm,  $520 \pm 10$  nm,  $550 \pm 30$  nm,  $620 \pm 10$  nm and  $680 \pm 10$  nm, respectively. A time-correlated single photon counting data acquisition board (Time correlated single photon emission (TCSPC): TimeHarp 200; PicoQuant GmbH) was used to synchronize the output signal of the diode driver with the start of the photomultiplier tube's signal.

### 5.2.2.3 Acquisition and analysis of spectral and lifetime data

Freshly excised brain tissue from 10 patients was directly brought to the neuropathology department for 1PEF (one photon excitation) spectral and lifetime measurements. Four regions of interest (ROIs) in each sample were measured hourly up to 5 hours. The total fluorescence signals were spectrally decomposed into five characteristic fluorescence spectra using a custom-made Matlab program [97], [215]. To determine the fluorescence lifetimes of each ROI, the temporal decay function of each wavelength emission was best fit to a mono-exponential decay function providing the respective fluorophores' lifetime value. Selecting the same ROIs for the intensity and lifetime measurements was possible at each time interval as the sample was placed on a motorized translation stage. The fit was accepted if  $\chi^2$  was close to 1 and the residual errors were randomly distributed around zero within an upper and lower boundary of  $\pm 2$ .

### 5.2.2.4 Two-photon fluorescence imaging with SHG detection

The multimodal two-photon microscope used for this part of the study was provided by PIMPA (multiphoton imaging platform for small animals) based at the IMNC laboratory. The compound system consists of a Mai Tai DeepSee Ti:Sapphire tunable laser source (690-1040 nm), which is pumped with an average power of 2.4 W and equipped with automated dispersion compensation. The laser is combined with a TCS SP8 MP confocal microscope from Leica Microsystems and is controlled through Leica's acquisition software (LasX; Leica, Wetzlar, Germany). The laser's repetition rate is 80 MHz, and the output pulse duration is 70 fs. Two external nondescanning hybrid detectors (NDD-Hyd; Leica, Germany) are added to the multiphoton confocal microscope for improved two-photon fluorescence emission detection. A  $448 \pm 20$ -nm bandpass filter (FF01-448/20-25; Semrock) was placed in front of the first detector for SHG detection and a  $520 \pm 30$ -nm bandpass filter (FF01-520/35-25; Semrock) was placed in front of the second detector for 2PEF imaging. A water-immersion Leica objective was used (HCX IRAPO L 20X NA 0.95, Leica, Wetzlar, Germany). The field of view at a chosen focal depth is typically  $433 \mu\text{m} \times 433 \mu\text{m}$  for the 20 $\times$  objective. The platform also has FLIM capabilities (PicoHarp 300; PicoQuant GmbH). 2PEF and SHG and FLIM measurements were performed following 890-nm excitation on the same ROIs. 2PEF and SHG images were first acquired simultaneously by their respective detectors. The final image is a result of averaging the two-photon images acquired from four ROIs. Then spectral acquisition was performed using the internal hybrid with a resolution of 10 nm. Finally, FLIM measurements were performed and detected by the NDD-Hyd; 10 images were averaged to produce the final image. The post processing of the images was performed using ImageJ NIH (Bethesda, Maryland), while all the quantitative analysis was performed using a home-made algorithm in MATLAB (MathWorks, Natick, Massachusetts).

## 5.2.3 Results

### 5.2.3.1 Changes in single photon emission fluorescence with time

The total fluorescence emission spectrum acquired from fresh control samples over time with a 405-nm excitation is plotted in Figure 5.1(a) at different time points from  $t = 0$  to  $t = 5$  hrs;  $t = 0$  indicates the time when the sample was available in the department of neuropathology few minutes after excision. The mean peak intensity across the whole spectrum was calculated for each time point and is plotted in Figure 5.1(b), where the error bars are the SDs across all samples. The average fluorescence intensity had a decrease of 23% after 1 hour and 33% after 5 hours.

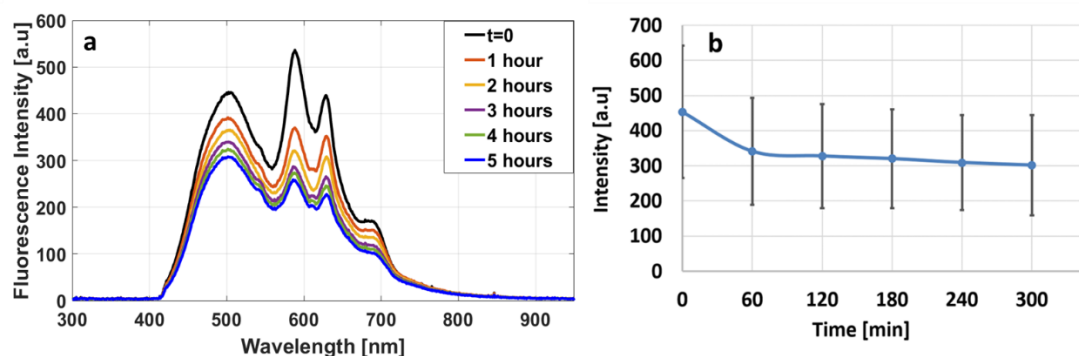


**Figure 5.1:** (a) Spectra from a fresh control sample acquired using 405-nm excitation wavelength at multiple time points. (b) The mean peak fluorescence intensity derived hourly from 10 control samples with their corresponding SDs

A direct comparison between the mean fluorescence lifetimes from all control samples determined at  $t = 0$  and at  $t = 5$  hours for the five endogenous fluorophores (NADH, FAD, Lipopigments, Porphyrin I and Porphyrin II) is shown in Figures 5.2(c). A student's paired t test showed no significant differences ( $p < 0.05$ ) in the respective lifetime values obtained at  $t = 0$  and  $t = 5$  hrs.

Since the total fluorescence spectra changed with time (Figure 5.1(a&b)), a closer look at the individual fluorophore spectra was warranted. Figures 5.2(a&b) illustrates an example of individual fluorescence spectra pertaining to each of the endogenous fluorophores measured at  $t = 0$  and  $t = 5$  hours, respectively. A general decrease in the peak intensity for all five fluorophores was observed. Particularly, the Lipopigments fluorescence intensity relative to NADH and FAD at  $t = 5$  hours differs from that observed at  $t = 0$ . Because of the prominent changes in the Lipopigment's fluorescence signal relative to FAD, a box plot comparing the mean Lipopigments to FAD ratios at both time points is shown in Figure 5.2(d). These ratios were obtained by quantifying the integrated fluorescence intensity from each characteristic spectrum and averaging them across all healthy tissue samples. There is a significant decrease in this ratio at 5 hours compared to that calculated at  $t = 0$  ( $p = 0.021$ ).

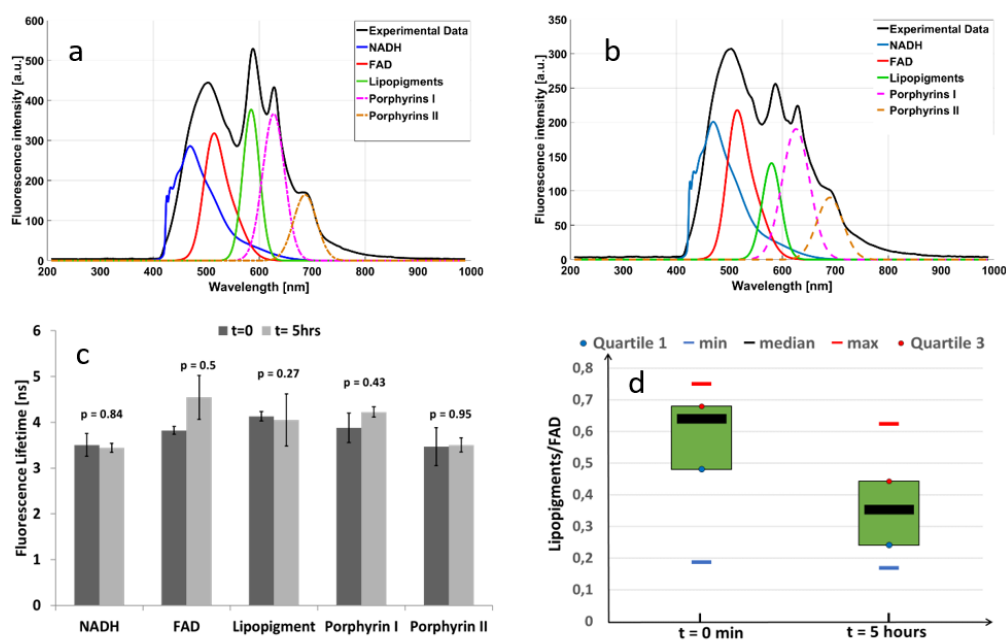


**Figure 5.2:** (a) Spectrally unmixed emission spectra upon 405-nm excitation from the fresh control sample of Figure 1A at  $t = 0$ . (b) Spectrally unmixed emission spectra after 5 hours of resection. (c) Bar graph comparing fluorescence lifetime values for each fluorophore measured at  $t = 0$  and at  $t = 5$  hours post resection. The error bars indicate the SD from all fresh control samples, while the p-values indicate whether the individual lifetimes after 5 hours post resection are significantly different from those obtained at the time of biopsy. (d) Box plot comparing the Lipopigments/FAD ratio at  $t = 0$  and  $t = 5$  hours derived from all control samples. The box plot includes the upper, the upper quartile (upper portion of box), the median (horizontal line in box), the lower quartile (lower portion of box), and the lower extreme (whisker). NADH, nicotinamide adenine dinucleotide; FAD, flavin adenine dinucleotide

### 5.2.3.2 2PEF imaging and spectral analysis

To obtain high 2PEF and SHG signals with our setup, the excitation wavelength of 890 nm was chosen as shown in our previous studies [89], [216]. The mean normalized fluorescence spectra of freshly excised tissue obtained from healthy (control), GBM, and metastatic (Meta) patients are shown in Figure 5.3(a), while the mean normalized fluorescence spectra measured from the same samples after tissue fixation are shown in Figure 5.3(b). The overall spectrum obtained from fresh control samples (Figure 5.3(a)) was characterized over a wider spectral range compared to the spectra from GBM and Meta samples (full width at half maximum (FWHM) of 200 nm vs 113 and 138 nm, respectively). The main contributors were Lipopigments as well as Porphyrin I and II. A weak SHG signal centered at 445 nm is also observed in the control spectrum. The contribution of Lipopigments to the overall fluorescence spectrum in GBM and Meta samples was greatly reduced. The relative peak intensity of Porphyrin I was high in GBM samples and low in Meta samples. The SHG signal and the 2PEF from Meta samples equally contributed to the overall emission spectra in Meta samples only. Fixed GBM, Meta and Control samples (Figure 5.3(b)) on the other hand, exhibited the same spectral shape with a common FWHM around 175 nm. The fixation with formaldehyde induced a loss of the spectral specificity, particularly for the control samples, which precluded subsequent discrimination of the samples' pathology. The

notable exception was the persistence of a strong SHG signal for the Meta samples, which was as strong as the 2PEF signal. Figures 5.3(c-e) show examples of SHG signal (in green) superimposed on the 2PEF (in red) obtained from fresh control, GBM, and Meta samples, respectively, following 890-nm excitation. Figures 5.3(f-h) show the corresponding 2PEF images combined with the SHG signals from the same samples after the tissue fixation process. Following the same trend observed in comparing the spectral features from figures 5.3(a&b), 2PEF and SHG signals change due to the chemical crosslinking during the fixation process in all three tissue types. These imaging results gave also a hint in differentiating between histopathological types; the control samples presented large homogenous cells (red), possibly corresponding to neuron pyramidal cells, whereas the strong SHG signal (green) corresponded to collagen fibers in the vessel walls (Figures 5.3(c&d)). Two-photon images from the GBM fresh and fixed sample showed larger SHG-producing structures (green), indicative of dilated vessels and tissue necrosis. The 2PEF images (Figures 5.3(e&f) showed dark red regions, indicative of necrotic tissue, and the bright red regions signifying neoplastic cells. Two-photon images from Meta samples had a dense network of vessels displaying a strong SHG signal (green) surrounding numerous atypical cells (red) (Figures 5.3(e&h)).

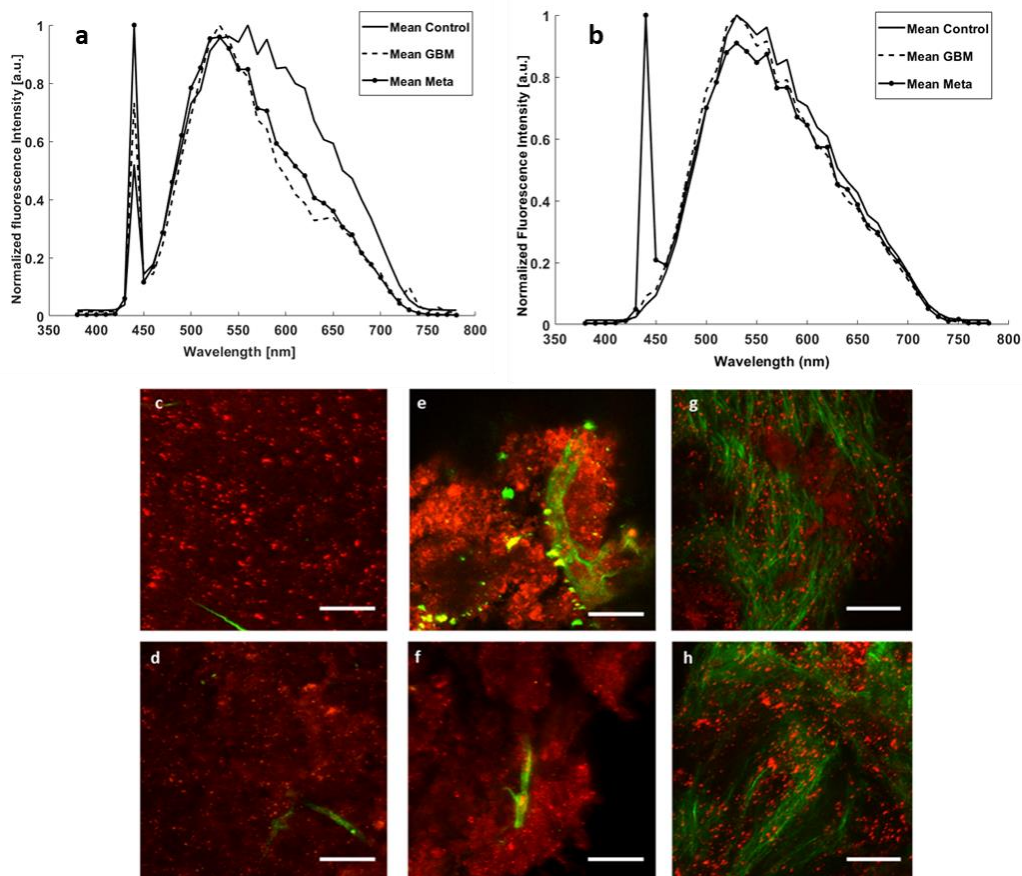


**Figure 5.3:** (a) Averaged two-photon spectra from fresh control samples ( $n = 12$ ), fresh glioblastoma (GBM) samples ( $n = 13$ ), and fresh Meta ( $n = 11$ ) samples after 890-nm excitation; (b) corresponding averaged two-photon spectra for the three sample groups after tissue fixation: two-photon image from (c) a fresh control sample, (d) the control sample after fixation, (e) a fresh GBM sample, (f) corresponding fixed GBM sample, (g) a fresh Meta sample, and (h) corresponding fixed Meta sample. Scale bar:  $100 \mu\text{m}$

### 5.2.3.3 Fluorescence lifetime imaging (FLIM)

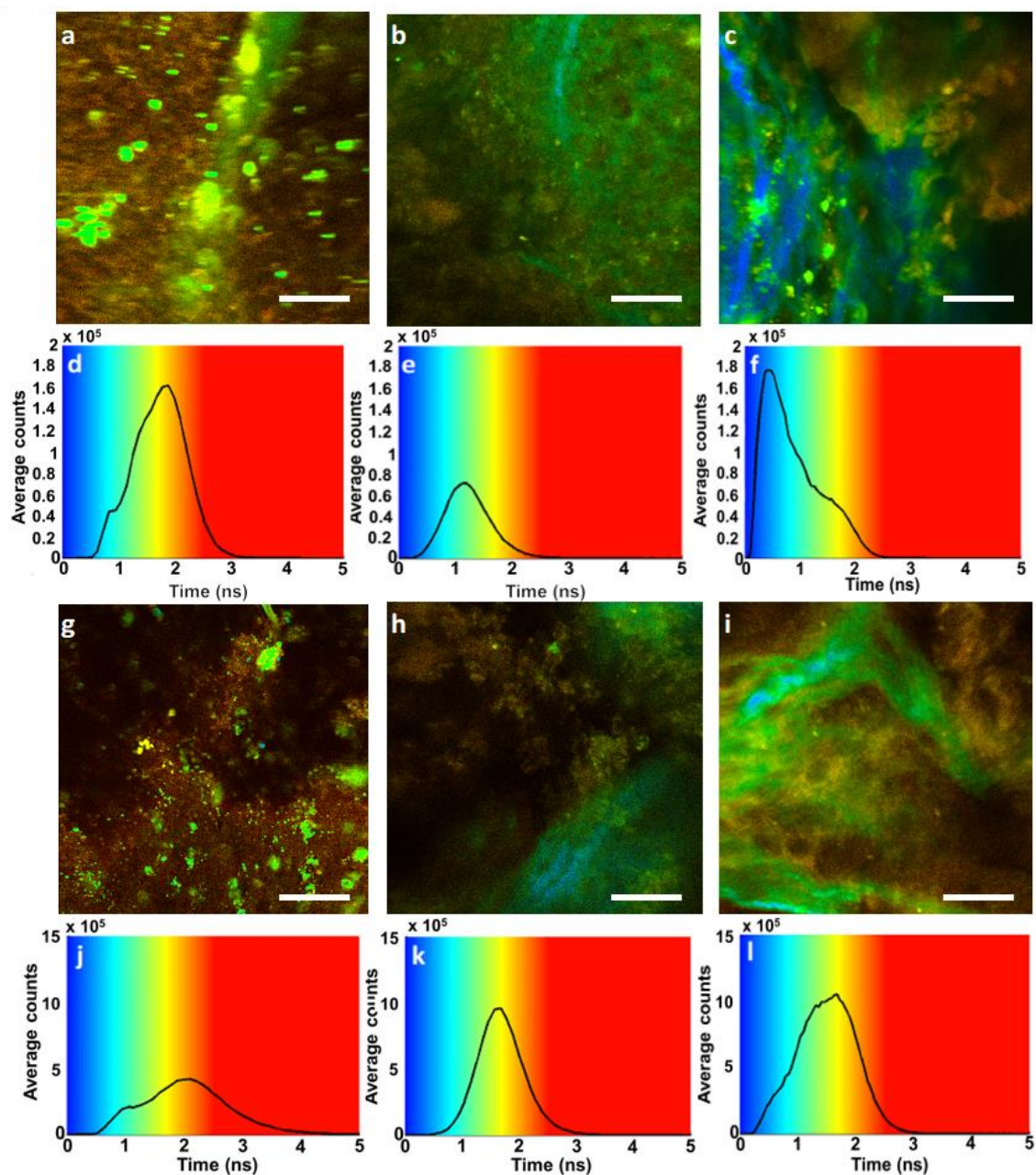


**Figure 5.4:** Fluorescence lifetime imaging microscopy (FLIM) from fresh (a) control, (b) glioblastoma (GBM), and (c) Meta sample; (d-f) histogram of the average lifetime superimposed on a color scale bar for each FLIM image above; (G-I) FLIM after each sample was fixed; (j-l) corresponding histogram. Scale bars = 200  $\mu\text{m}$

For lifetime analysis, specific ROIs were chosen from two photon fluorescence images so that the focal plane and lateral spatial position chosen for imaging fixed samples were somewhat matched to that of their fresh counterparts. FLIM images of a fresh control, GBM, and Meta sample are shown in Figures 5.4(a-c), respectively. Figures 5.4(d-f) are the respective color-scaled images along with the lifetime histogram for each of the above FLIM image. FLIM images taken after fixing each sample are shown in Figures 5.4(g-i), while

their histograms are shown in Figures 5.4(j-l). In general, the lifetime decay curves from both fixed and fresh control samples were broadly distributed, having short and long lifetime values (Figures 5.4(d&j)), while the lifetime decay curves from fresh and fixed GBM samples were more confined toward shorter lifetimes (Figures 5.4(e&k)). Fresh Meta samples were also characterized with a broad lifetime decay spectrum (Figures 5.4(f&l)), which generally had shorter lifetime values compared to normal tissue due to the enhanced SHG diffuse signal resulting in a short lifetime peak ( $\sim 0.5$  ns). Looking at the difference between fresh and fixed control and GBM samples, the peak lifetimes were longer in fixed tissue for both cases, respectively, 1.7 to 2.2 ns in the control samples and 0.9 to 1.12 ns in GBM cohort. For the Meta samples, the secondary peak in Figure 5.4(f) also appears at a shorter lifetime than the peak in Figure 5.4(l), 1.5 to 1.6 ns. In any case, FLIM images as well as the lifetime histograms both indicate that tissue fixation affects the average fluorescence lifetime with longer lifetime in all three types.

### 5.2.4 Discussion and conclusion

The emitted fluorescence following 405-nm excitation wavelength was measured *ex vivo* every hour up to 5 hours to study the effect of time, post-tissue resection, on the tissue's intrinsic properties, particularly as related to the spectral and lifetime signals of five endogenous fluorophores: NADH, FAD, Lipopigments, Porphyrin I and Porphyrin II, whereby the first two fluorophores are indicative of tissue's metabolic state. After compensating for measurement geometry and the excitation power density, the corrected fluorescence intensity is proportional to the fluorophores' concentrations, while also being modulated by changes in tissue's light absorption and scattering properties at both the excitation and emission wavelengths. The fluorescence intensity was found to noticeably decrease during the first hour after tissue extraction (Figures 5.1(a&b)) and remain somewhat stable thereafter for up to 5 hours. The 5-hour observation window was chosen to simulate the maximum time required for tissue preparation post-biopsy for the fluorescence measurements. The shape of the emission spectra also changed during the first hour post-harvest, but remained consistent thereafter, suggesting that tissue optical property measurements become more reproducible 1 hour after tissue extraction. This observation is expected as structural and functional changes occur in the sample immediately after tissue removal. In particular, blood becomes more de-oxygenated, while tissue dehydration increases the density of chromophores as well as tissue structural properties, thereby affecting both tissue absorption and scattering properties. Analyzing individual fluorophore

signatures indicate that the spectral distortion with time is mostly caused by changes in the relative concentrations of Lipopigments and Porphyrin I (Figures 5.2(a&b)). Lipopigments

are particularly sensitive to the tissue's metabolic state of tissue and decrease when metabolic processes such as oxidative and glycolytic metabolisms are stopped following resection [301]. There is no similar study in the literature that has investigated the changes in the spectral shape and fluorescence intensity that may occur in fresh brain tissue samples as a function of excision time. This is probably because *ex vivo* fluorescence measurements are typically performed on fixed tissue, while histopathological analysis immediately after needle biopsy based on two-photon fluorescence microscopy has only been recently realized

[300], further highlighting the importance of this study. Interestingly, the fluorescence lifetimes following visible excitation did not yield significant ( $p > 0.05$ ) differences between the time points tested including at 1 hour (data not shown) for all five fluorophores (Figure 5.2(c)) even though fluorophore lifetime properties highly depend on the microenvironment such as temperature, pH, and the fluorophore's binding state, all affected by altered metabolic conditions [301]. This finding highlights the particular advantage of using fluorescence lifetime as a reliable and self-referenced technique compared to fluorescence intensity measurements within the time span post-harvest tested here. The limited sample size for this part of the study should not undermine the above observations as similar conclusions were found in our previous studies [89], [215], [271]. The second arm of the study aimed at investigating the effect of tissue fixation on the nonlinear optical properties of excised tissue. Fresh and fixed healthy cortex, GBM, and Meta samples were imaged under two-photon excitation to test whether fixed tissue provided similar 2PEF and SHG signatures. The latter would be more practical for optical biopsy and histopathological analysis. It was observed that the fixed brain tissue samples did not have 2PEF and SHG patterns similar to their fresh counterparts (Figures 5.3(c-h)).

Nevertheless, relying on either fresh or fixed tissue was sufficient in differentiating between healthy, GBM, and metastatic tissue as there are consistent hallmarks in their corresponding two-photon images. This is in accordance to the work by Croce and colleagues [302], where the autofluorescence intensity and lifetime analysis from fixed samples after two-photon fluorescence excitation discriminated neoplastic brain tissue from normal tissue sections as efficiently as that obtained via an intraoperative probe, despite the fluorescence spectral shapes and intensity being altered after fixation. For example, while the 2PEF spectra obtained from fixed control, GBM and Meta are almost indistinguishable (Figure 5.3(b)), there is a persistent SHG peak in the Meta sample adequate for identification. The high SHG signal in Meta samples refer to the collagen structures and dilated vessel walls necessary for tumors originating from other parts of the body to migrate and settle in the brain [303]. Ongoing studies aim to determine the orientation of these collagen fibers [304] to correlate the SHG signal with tumor stage optically. Healthy tissue typically exhibits a homogenous fluorescence distribution corresponding to large neuron pyramidal cells, while GBM tissue shows a more heterogeneous fluorescence distribution [16]. Strong fluorescence is due to the high density of neoplastic cells, while weak fluorescence corresponds to necrotic tissue [89], [215], [216]. The sparse but strong SHG signal in GBM images typically signifies dilated vessel walls [303], [304]. FLIM imaging under two-photon excitation also proved that tissue fixation altered lifetime properties of each tissue type (Figure 5.4). This was expected as formalin acts as a crosslinking agent at the molecular level by linking together soluble and structural proteins, thereby particularly affecting lifetime decays of endogenous fluorophores. Interestingly fresh and fixed GBM consistently preserved a narrow distribution of lifetime values, which were both generally shorter than control and Meta samples, again suggesting lifetime measurements were more sensitive and specific to tissue type compared to intensity-based measurements, yet further studies would have to confirm this observation.

In summary, this study highlights the unique advantages of multiphoton imaging in differentiating between normal, glioma and metastatic tissue at a cellular level, while also



showing the need to perform optical measurements on fresh tissue if the objective is to obtain an optical biopsy. On the other hand, if the morphological and structural information is aimed at classifying tissue after surgery, two-photon images can still potentially classify tissue in a similar way to standard histology.

## Chapter 6

# **Does the multimodality of contrast in NIR window permits to define reliable discrimination parameters between healthy and tumors tissues? Investigation of scattering, absorption, and anisotropy properties of human brain tumoral tissues in the NIR wavelength range.**

### **6.1 Context of the study**

Similar to other forms of light-tissue interaction, fluorescence emission is related on scattering and absorption of tissue main components (water, hemoglobin, melanin ...) as well as other structures (vascular structures, collagen fibers). This emission varies with the variation of these optical properties within the tissues and may be affected as well with the alteration of tissue structures. Furthermore, fluorescence generation depends also on light wavelength which determine its ability to penetrate in the tissue and to interact with fluorescent molecules. Two-photon fluorescence imaging employs an excitation light within the NIR window, also known as phototherapeutic window, that ranges between, 650 nm and 950 nm. As described in the introduction, within this window, the excitation light has its maximum penetration depth in biological tissues, where water and hemoglobin have their lowest absorption values (figure 1.19). However, and as part of the multimodal tissue characterization that are carried for tissue database establishment, it was necessary to investigate scattering and absorption properties of the different human brain tissue types that we are characterizing.

Determining these properties in the NIR window allows to understand the variation of fluorescence emission that occurs from one tissue type to another. It is necessary also to determine the wavelength where tissues have the lower scattering and absorption coefficients within the NIR window and therefore to determine the optimal wavelength for tissue excitation. It will be useful also for optimizing the spectral response of each tissue type as well as to establish discrimination factors between the tissues that are related to these properties.

Optical properties characterization of brain tissues was reported in different studies in the literature [305]–[309]. These studies, performed on human brain tumor samples and healthy white or grey matter, have highlighted differences between healthy regions and tumors. However, these studies lack of statistical significance and the obtained values were non consistent and varies from a study to another due to using different experimental conditions, different tissue preparation process as well as different data analysis methods. Seen this variation in reported values and since that these values were specific to each study conditions as well the nature of inspected brain tissue, it was best for us to extract these values in-house using our own method and setup.

Previously, we have reported scattering, absorption and anisotropy coefficients of healthy, low grade glioma, GBM, meningioma and metastatic tumors in the visible excitation wavelength range at 375 and 432 nm [215], in correlation with spectral and fluorescence lifetime measurements in the same range.

In this study we are extending the previously work into the NIR window where scattering, absorption and anisotropy coefficients were determined in parallel with two-photon spectroscopic and lifetime analysis. Optical redox ratio, optical index (OI) ratio highlighting NADH over porphyrins content, the lipopigment to porphyrins (LP) ratio, relative collagen density defined as the ratio of SHG over TPF signal following 890 nm excitation as well as the fluorescence lifetimes of Flavins (FAD) were compared.

**Methods** Intrinsic optical properties of twenty-seven ethanol fixed samples were investigated in a wavelength range starting from 720 nm to 890 nm. The samples were cryosectioned into 200  $\mu\text{m}$  and 600  $\mu\text{m}$  slices with 7 cortical healthy tissues, 5 low grade diffuse glioma, 6 high grade glioma, 5 meningioma and 4 metastatic tumors. A pulsed tunable laser source (same laser source used in the endomicroscope setup) coupled with a single integrating sphere setup was used to determine the optical coefficients at 720, 760, 800, 850 and 890 nm. The absorption ( $\mu\text{a}$ ), scattering ( $\mu\text{s}$ ) and anisotropy ( $g$ ) coefficients were extracted from the measured diffuse reflectance, diffuse transmittance, and collimated transmittance measured using the inverse added-doubling method [305], [310], [311]

**Results and conclusion** As expected, the optical property measurements showed that all three optical parameters, absorption, scattering and the anisotropy coefficient, were significantly lower in healthy samples than in the tumor ones. This difference from tumor to healthy tissue in scattering property could be described by the difference in tissue architecture between healthy and tumor tissue especially the denser networks of collagen fibers that forms in cancerous zones which constitute an important source of scattering.

However, in term of  $\mu\text{a}$  variation, no distinction could be made between GBM and low-grade gliomas, metastases or meningiomas. It was noticed also that  $\mu\text{s}$  was lower in GBM samples than other tumor types and even little bit close to healthy values. Similar to scattering increase explanation, the increase in absorption property could be attributed to the presence of denser vascularization structures in tumor tissues leading to higher hemoglobin presence which are considered as a strong light absorber.

These conclusions were validated by observing the H&E stained images that were compared to the combined TPF+SHG images. Distinctive features of each tumor type in the H&E stained images were reflected in TPF+SHG images including high cellular density, a denser

vascularization and necrosis zones. The combined TPF+SHG images had the added benefit of showing the disorganization of blood vessels and collagen structures mainly present in GBM, metastases and meningioma. When relating the intrinsic optical properties with the spectral differences, we found that  $\mu_a$  and  $\mu_s$  had limited effect on the TPF spectrum at both 810 and 890 nm excitation. The quantitative parameters derived from these spectral results following 720 nm and 890 nm excitation were particularly useful in providing tissue discrimination. The optical index ratio was found increasing with tumor malignancy, while the LP ratio had an opposite trend. The collagen density differentiates healthy samples from other tumors except low grade glioma. However, this ratio was useful in differentiating between GBM and low-grade glioma, while the optical redox ratio did not provide any potential for differentiation. Phasor FLIM analysis reveals the Long Lifetime Intensity Factor ( $\alpha$ ) which describes the relative contribution of free FAD to its protein-bound form in the imaged sample. This factor decreased with malignancy increasing, suggesting protein-bound FAD is implicated in driving malignancy, as is further demonstrated in the next study described in chapter 7 on low grade and high grade glioma investigation.

To this end, this study illustrates the necessity of deriving multiple optical signatures to identify the different characteristics of a brain tumor. The limited tissue discrimination between the tumor types further confirms the importance of constructing a tissue database from a large number of tissue samples. Finally, as seen in the previous chapter, we expect to obtain more robust tissue discrimination capabilities when the database comprises optical signals from fresh tissue compared to the fixed tissue presented in this study.

## 6.2 Paper: Comparison of optically-derived biomarkers in healthy and brain tumor tissue under one- and two-photon excitation


Received: 25 March 2019 | Revised: 2 July 2019 | Accepted: 4 July 2019

DOI: 10.1002/jbio.201900111

FULL ARTICLE

JOURNAL OF  
BIOPHOTONICS

### Comparison of optically-derived biomarkers in healthy and brain tumor tissue under one- and two-photon excitation

Mira Sibai<sup>1,2</sup> | Hussein Mehdine<sup>1,2</sup> | Emile Kaadou Moawad<sup>1,2</sup> | Marjorie Juchaux<sup>1,2</sup> | Pascale Varlet<sup>3,4,5</sup> | Bertrand Devaux<sup>5,6</sup> | Darine Abi Haidar<sup>1,2\*</sup> 

<sup>1</sup>Imagerie et Modélisation en Neurobiologie et Cancérologie (IMNC), CNRS, Univ Paris Sud, Université Paris-Saclay, Orsay, France

<sup>2</sup>Université de Paris, IMNC, Orsay, France

<sup>3</sup>Neuropathology Department, Sainte-Anne Hospital, Paris, France

<sup>4</sup>IMA BRAIN, INSERMU894, Centre de Psychiatrie et de Neurosciences, Paris, France

<sup>5</sup>Paris Descartes University, Paris, France

<sup>6</sup>Neurosurgery Department, Sainte-Anne Hospital, Paris, France

\*Correspondence

Darine Abi Haidar, Université de Paris, IMNC, F-91400, Orsay, France.  
Email: abihaidar@imnc.in2p3.fr

Funding information

Applicable Funding Source Institut National de la Santé et de la Recherche Médicale (National Institute of Health and Medical Research), Grant/Award Number: 201601; Synchrotron SOLEIL for beam time, Grant/Award Numbers: 20160978, 20160206; Agence Nationale pour la Recherche, Grant/Award Number: Infrastructure d'avenir en Biologie Santé – ANR – 11-INBS-0006; Institut National de Physique Nucléaire et de Physique des Particules (IN2P3); ligue nationale contre le cancer (LNCC); TMO Cancer AVIESAN

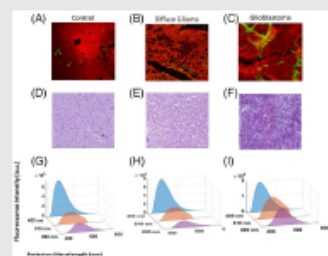
#### Abstract

The surgical outcome of brain tumor resection and needle biopsy is significantly correlated to the patient's prognosis. Brain tumor surgery is limited to resecting the solid portion of the tumor as current intraoperative imaging modalities are incapable of delineating infiltrative regions. For accurate delineation, in situ tissue interrogation

at the submicron scale is warranted. Additionally, multimodal detection is required to remediate the genetically and molecularly heterogeneous nature of brain tumors, notably, that of gliomas, meningioma and brain metastasis. Multimodal detection, such as spectrally- and temporally-resolved fluorescence under one- and two-photon excitation, enables characterizing tissue based on several endogenous optical contrasts. In order to assign the optically-derived parameters to different tissue types, construction of an optical database obtained from biopsied tissue is warranted. This report showcases the different quantitative and semi-quantitative optical markers that may comprise the tissue discrimination database. These include: the optical index ratio, the optical redox ratio, the relative collagen density, spectrally-resolved fluorescence lifetime parameters, two-photon fluorescence imaging and second harmonic generation imaging.

#### KEYWORDS

absorption coefficient, anisotropy coefficient, fluorescence, multiphoton microscopy, scattering coefficient, spectroscopy



#### 1 | INTRODUCTION

The challenges in the clinical management of brain tumors arise from their aggressive and heterogeneous nature, even within a single tumor [1]. Brain tumors, such as gliomas, comprise of solid tumor foci with possible necrotic portions

at the core and infiltrative regions at the periphery, where tumor cells often travel along the white matter tracks reaching the contralateral side [1]. The genetic expression of each region differs, resulting in unique histopathological properties that manifest as varying degrees of nuclear abnormalities, endothelial proliferation, increased cell density, and

### 6.2.1 Introduction

The challenges in the clinical management of brain tumors arise from their aggressive and heterogeneous nature, even within a single tumor [312]. Brain tumors, such as gliomas, comprise of solid tumor foci with possible necrotic portions at the core and infiltrative regions at the periphery, where tumor cells often travel along the white matter tracks reaching the contralateral side [312]. The genetic expression of each region differs, resulting in unique histopathological properties that manifest as varying degrees of nuclear abnormalities, endothelial proliferation, increased cell density, and vascularity [313], [314]. Consequently, the accuracy of brain tumor diagnosis following needle biopsy and standard histopathological assessment is limited leading to a misdiagnosis in 10% to 30% of the cases [315]. As a result, repeat procedures are required, which increase the patient's risk of morbidities including hemorrhage and infection. Hence, there is a critical need for an intraoperative modality that can non-invasively assess tissue microscopically to accurately identify the different facets of brain tumors, preferably along with their corresponding histopathology. At the macroscopic scale, 5-Aminolevelunic acid induced protoporphyrin IX fluorescence imaging has significantly aided surgeons to improve biopsy and tumor surgery outcomes, yet non-fluorescent satellite tumor cells are left undetected causing recurrence [148], [316]. For enhanced tumor visualization at the meso and microscale, other optical techniques are applied, usually through an endomicroscope [316].

State of the art endomicroscopes can be equipped with confocal reflectance and fluorescence imaging [317], Raman spectroscopy [75] and coherent anti-Stokes Raman scattering (CARS) microscopy [318][9], fluorescence lifetime imaging (FLIM) [319] and two-photon microscopy [312]. Although each modality has its own advantages and limits when utilized in the surgical field, a recent solution has been to combine two or more modalities to alleviate their limitations on one hand, and to increase the information depth retrieved enabling more differentiated diagnostics. FLIM, for example, is a form of metabolic imaging, where changes in the fluorescence lifetime reflect perturbations in the tissue microenvironment such as hypoxia, abnormal metabolism, perturbed local pH, as well as changes in the protein binding properties of endogenous fluorophores, all of which are altered in diseased tissue before any structural abnormalities develop [148], [319]. FLIM is particularly appropriate for intraoperative application, because the time-resolved fluorescence images are minimally affected by confounding factors such as non-uniform illumination, illumination angle, as well as light attenuation/scattering within the imaged volume [123].

The first FLIM-enabled endoscope tested for brain tumor surgery was reported by Sun et al., where the fluorescence intensity, mean fluorescence lifetime and the first four Laguerre coefficients were found to be significantly different between neoplastic and normal brain tissue [320]. FLIM however does not directly display morphological features of the sampled region and is thus best combined with other microscopic imaging modalities such as CARS [318] or two photon imaging [127]. Multimodal detection through an endomicroscope has mostly been applied to imaging of the upper and lower gastrointestinal tract [321] or the heart [319], where microscopic features similar to that depicted by stained histopathological images are visualized. Limited research has been conducted on brain tissue due to the additional technical requirements including probe size and acquisition time. More importantly, few of these multimodal studies have derived quantitative markers that can define tissue status despite the added information retrieved.

We are developing a multi-scale multimodal nonlinear endomicroscope that can characterize tissue based on several endogenous optical contrasts [173] in tandem with constructing an optical database that can define different brain tissue types. The detected optical signatures pertain to: the spatially-resolved two-photon emission fluorescence (TPEF), the second harmonic generation (SHG), the spectrally-resolved two-photon fluorescence, as well as spatially and spectrally-resolved fluorescence lifetime. The multimodal detection of the endomicroscope should provide complimentary information enabling the identification of multiple brain tumor biomarkers in vivo. As eluded above, two-photon imaging (TPEF and SHG) can provide detailed cytological, histological, and molecular information competitive with histopathological staining with the added advantage of being label-free and non-invasive [217]. Low TPEF signals in neoplastic cells typically correspond to hypercellularity and angiogenesis, while high SHG intensities can indicate the presence of microcalcifications, increased vasculature and dense extracellular matrices characteristic of infiltrative and metastatic phenotypes [215], [322]. Overall, this endomicroscope will sample the brain at the tissue, cellular, and subcellular scale to identify microstructural, metabolic, and physiological properties pertaining to different brain tumor types. We hypothesize that including multiple optical biomarkers, which individually show significant, albeit limited efficiency should enhance the accuracy of in situ tissue diagnosis and better inform treatment decision-making. To this end, in order to assign the optically-derived parameters extracted from multimodal imaging to different markers of oncogenesis, an optical database is being built by data obtained from ex vivo brain tissue samples. We have previously reported on the intrinsic tissue optical and spectral fluorescence properties of neurological tissue under 375 to 435 nm excitation [215]. In this study we extend the database to include tissue optical properties in the near infrared regime (NIR) as well as the spectral and fluorescence lifetime properties of endogenous fluorophores under two photon excitation. Two-photon imaging was performed on a commercial multiphoton microscope and optical parameters, such as the optical redox ratio, the optical index (OI) ratio, the lipopigment to porphyrins (LP) ratio, the collagen density, as well as the fluorescence lifetimes of flavins (FAD) were compared. Optical properties based on brain tissue type/disease is scarce, and thus the intrinsic absorption and scattering coefficients of tissue were extracted from a well-established method based on the total diffuse reflectance and transmission signals measured with an integrating sphere setup at multiple wavelengths. The excised tissue samples were histologically identified as noncancerous cortical tissue, low-grade diffuse glioma, glioblastoma, meningioma, or metastatic tissue.

## 6.2.2 Materials and methods

### 6.2.2.1 Samples

Tissue samples were collected during surgery from the Department of Neurosurgery and Neuropathology at Sainte-Anne Hospital (S.C.3227) with approval from the Sainte-Anne Hospital – University Paris Descartes Review Board (CPP Ile de France 3). The following protocol was performed accordingly, and informed consent was obtained from all participants and/or their legal guardians. A total of 28 samples were biopsied from 21 patients with different brain tumor types and from 7 cancer-free patients who underwent epilepsy surgery. The samples were stored at  $-80_{\circ}\text{C}$  before preparation. The samples were

cryosectioned into 200  $\mu\text{m}$  slices (CM 1950, Leica Microsystems) and then fixed with ethanol. To correlate changes in optical properties with structural abnormalities, 10  $\mu\text{m}$  specimens were stained with Hematoxylin-Eosin (H&E) and digitized (NanoZoomer 2.0, Hamamatsu Photonics K.K, Hamamatsu, Japan). A summary of the cohort brain specimens is provided in Table 6.1.

Tissue Type	Description	Number of Samples
Cortical tissue	Biopsied from epileptic patients	7
Diffuse glioma	Anaplastic oligo-astrocytoma, oligo-astrocytoma, astrocytoma (grades II and III)	5
High-grade glioma	Glioblastoma	6
Meningioma	Grades II and III	5
Metastatic tissue	Thyroid and adenocarcinoma	4

**Table 6.1:** Summary of the cohort brain specimens included in this study

### 6.2.2.2 Optical property measurements with a single integrating sphere set-up

The spectrally-resolved diffuse reflectance ( $RD[\lambda]$ ), and the total diffuse transmission ( $TD[\lambda]$ ) measurements were performed using a typical single integrating sphere set-up [215], while another setup was used to collect the collimated transmission ( $TC[\lambda]$ ). A Ti:sapphire femtosecond laser source (Chameleon, Coherent, Santa Clara, California) tunable from 690 to 1040 nm served as the illumination source. For the integrating sphere measurements, two neutral density filters were placed between the laser and the integrating sphere to decrease the laser beam mean power to 5 mW. The sectioned tissue was placed on a custom sample holder fixed in front or behind the sphere for the diffuse transmission and reflectance measurements, respectively. The integrating sphere (IS200-4 Thorlabs) had a diameter of 56.8 mm with four possible sample/entrance ports, each being 12.7 mm in diameter. The entrance diameter of the sample port was reduced to 6 mm. The sphere was coupled to a spectrometer (HR2000-Ocean optics) at the 3 mm detector port. The same four regions of interest (ROI) were chosen for both transmission and reflectance measurements per sample. For the collimated transmission measurements, the laser beam was further attenuated with a third neutral density filter ( $OD = 0.85$ ) before illuminating the sample. Three equidistant pinholes between the sample holder and the spectrometer ensured that the collected spectra were from collimated and not diffusely transmitted photons. For each ROI, the reflectance/transmittance spectra were obtained at multiple excitation wavelengths in the NIR: 720, 760, 800, 850 and 890 nm, which encompassed the same excitation wavelengths used in the multimodal nonlinear microscope. Under the same experimental conditions, the



collimated transmission and integrating sphere measurements were first validated on tissue simulating liquid phantoms that matched the range of optical properties reported in brain tissue [323]. The phantoms consisted of a mixture of intralipid, India ink and water poured in to a 1 mm quartz cuvette that was fixed with the same sample holder as used for the ex vivo measurements. For each ROI, the inverse added-doubling method was used to solve for three intrinsic tissue optical properties, the absorption coefficient,  $\mu_a$ , the scattering coefficient,  $\mu_s$ , and the anisotropy factor  $g$  [215], [310], [311]. Optical properties extracted at 405 nm were reported previously [215] using a similar setup and are added for comparison.

### 6.2.2.3 Multimodal imaging with the multiphoton benchtop microscope

A Mai Tai DeepSee Titanium:sapphire femtosecond laser (Mai Tai DeepSee, Spectra-Physics, Santa Clara) with automated dispersion compensation and an average power of 2.4 W (at 800 nm) was coupled to the TCS SP8 MP confocal microscope (Leica Microsystems, Wetzlar, Germany). The repetition rate and output pulse duration was set to 80 MHz and 70 fs, respectively. The laser is tunable from 690 to 1040 nm. The 720 nm, 800 nm, and 890 nm excitation wavelengths were chosen to optimally excite NADH, FAD, as well as the SHG signal from the fixed tissue sections. A 25X water immersion microscope objective (HCX IRAPO L 25X NA 0.95, Leica Microsystems, Wetzlar, Germany) provided a 433  $\mu\text{m}$  by 433  $\mu\text{m}$  field of view at a working distance of 1.5 mm. The internal 405 nm LEDsource was used for applying confocal fluorescence microscopy. Time-correlated single-photon counting (PicoQuant TCSPC module, Berlin, Germany) technique was added to measure time-resolved fluorescence data. Two external Leica hybrid, non descanned detectors (Leica Hyd-RLD 2, Leica Microsystems, Wetzlar, Germany) were added for improved detection of TPEF/SHG and FLIM, and each detector had a band-pass filter (FF01-448/20-25 and FF01-520/35-25, Semrock, New York) to separate the TPEF from SHG signal, and to separate the fluorescence signal into two spectral bandwidths,  $448 \pm 25$  nm and  $520 \pm 30$  nm, respectively. The spectrally-resolved confocal and two-photon fluorescence were imaged using the internal hybrid detector from 400 to 780 nm in steps of 10 nm. For each sample, TPEF and SHG images required 2 minute per sample at a chosen focal plane across the whole spectral range, while each lifetime image took 10 to 15 seconds at a given excitation wavelength. The time to acquire a confocal fluorescence image under one-photon excitation took around 2 seconds, while spectrally-resolved one- and two-photon fluorescence images acquired at the focal plane took 15 minutes.

### Multimodal image analysis

2D confocal and two-photon intensity images were treated and analyzed through ImageJ and a custom-made MatLab program. Spectral and image analysis was performed. ImageJ was used to convert the images saved on Leica's acquisition software to. TIFF image extensions. The custom program allowed automatic image analysis, which included recovering the mean redox ratio and the collagen content, for a chosen ROI. The redox ratios were based on the TPEF images following 720 nm excitation; the fluorescence intensity detected at  $448 \pm 25$  nm was assumed to be mainly from NADH, while the fluorescence intensity detected at  $520 \pm 30$  nm was assumed to be mainly from FAD. The

SHG to TPEF signal following 890 nm excitation is defined as the relative collagen density, since the SHG signal from brain tissue originates from collagen structures pertaining to the extracellular matrix and vasculature. The number of green SHG pixels and the number of red TPEF pixels were counted using the plugin color pixel counter in ImageJ for each composite image and the SHG/TPEF ratio was determined. For spectral analysis, spectrally-resolved images were averaged across 20 frames, and the mean intensity per spectral bin was extracted to produce the mean fluorescence spectra following one and two-photon excitation at the chosen wavelengths. Two additional optical ratios, the optical index ratio and the Lipopigment to Porphyrins ratio, were determined after fitting the autofluorescence spectrum with five Gaussians pertaining to NADH, FAD, Lipopigments, Porphyrins I and Porphyrins II [215] with central peaks at  $470 \pm 40$  nm,  $540 \pm 30$  nm,  $580 \pm 10$  nm,  $620 \pm 10$  nm, and  $680 \pm 10$  nm under 810 nm excitation: Optical index (OI) = Porphyrins/NADH and Lipopigment to Porphyrins (LP) = Lipopigments/Porphyrins (I & II). At the same focal plane, fluorescence lifetime data was collected at  $520 \pm 30$  nm. This was performed for nine ROIs per sample. The phasor approach was applied to the FLIM data of all tissue samples similar to [239] as an unbiased model-free data analysis method. The algorithm reduces the initial image size from  $512 \times 512$  pixels to  $16 \times 16$  pixels. Each reduced pixel corresponds to one phasor count on the phasor plot directly related to the fluorescence decay profile pertaining to that pixel. Additionally, the long lifetime intensity fraction,  $\alpha$ , was also determined.  $\alpha$  corresponds to the fraction of fluorescence emitted by the fluorophore (FAD) with the longer lifetime and is obtained from projecting the phasor counts to the line that intersects the universal circle [129]. In this study, this line pertains to the free and protein-bound forms of FAD. The distances between each projected phasor count and the two lifetime values are calculated. The  $\alpha$  value is the relative distance to the long lifetime and thus corresponds to the fraction of free FAD. A two-sided student t-test analysis was used to test whether the above molecular ratios and  $\alpha$  values from different tissue types vary from one another.

### 6.2.3 Results

The bar plots of Figures 6.1 (a, b) show the variation of the absorption ( $\mu_a$ ) and scattering coefficients ( $\mu_s$ ) as a function of excitation wavelength averaged for each tissue type and for each ROI: noncancerous cortical tissue, diffuse glioma, glioblastoma, meningioma, and metastatic tissue. For all five categories,  $\mu_a$  decreases with excitation wavelength as expected when the main chromophore is hemoglobin. The minor peak at 760 nm coincides with the absorption peak of deoxygenated hemoglobin that is present in all five tissue groups. Comparing the mean  $\mu_a$  values of all tissue types, Figure 6.1(a) clearly shows a difference in  $\mu_a$  between noncancerous cortical tissue and malignant tissue across the whole spectral range; Specifically, the absorption coefficient modulated by oxy- and deoxy-hemoglobin concentrations is consistently lower in control samples across the visible and NIR range compared to malignant tissue yet, differentiating between the different tumor types is not readily evident, where  $\mu_a$  can vary up to 33% for specimens of similar pathology. The spectral trend of  $\mu_s$  mirrors that of  $\mu_a$ , where  $\mu_s$  decays slowly with increasing wavelength as expected due to the increased mie scattering relative to Rayleigh scattering [240], [305]–[307]. Similar to  $\mu_a$ , the differences between healthy and diseased tissue is evident. Clear discrimination between the different tumor samples are confounded by the

wide spread of values obtained for each tissue group. In fact, the inter and intra-tumor variance was found to be 25 and 23% on average. Interestingly, glioblastoma specimens had significantly

lower scattering coefficients than those of other cancerous tissue, including gliomas of lower grade. The mean anisotropy factor,  $g$ , is plotted as a function of wavelength in Figure 6.1 (c). For all tissue types,  $g$  is between 0.86 and 0.96, where forward scattering is increasingly favored in the NIR spectral range compared to that in the visible regime. Beyond 720 nm illumination,  $g$  does not greatly vary with increasing wavelengths. On average, control samples had lower  $g$  values ( $g < 0.9$ ) compared to their tumor counter parts.

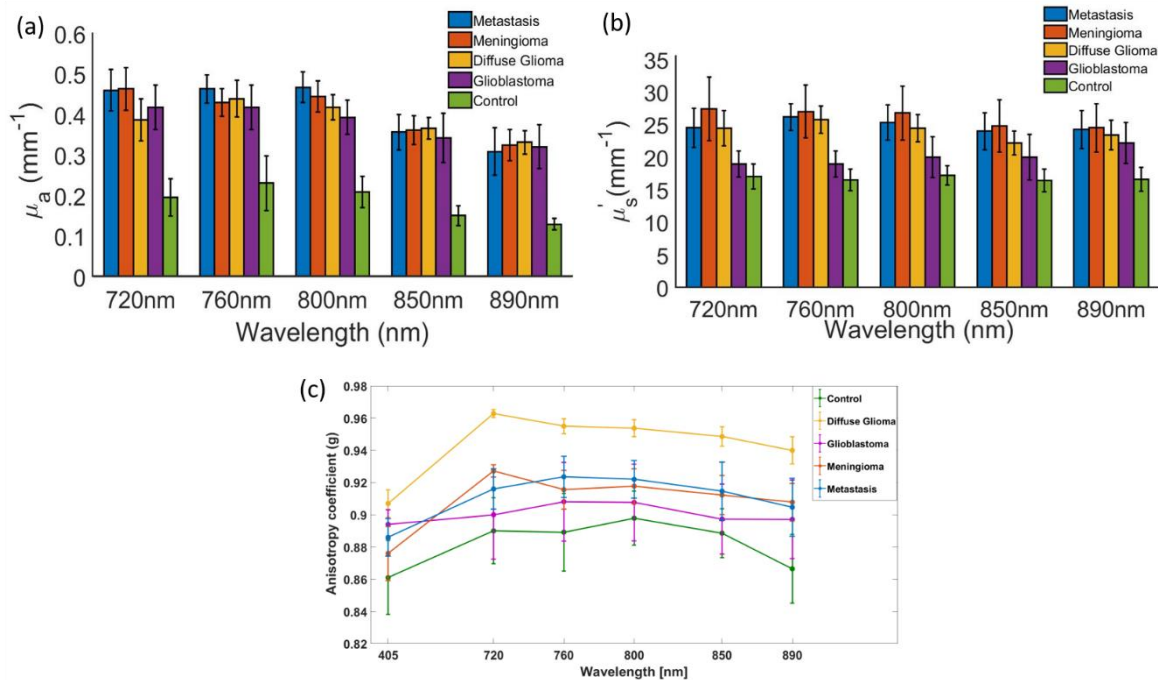


**Figure 6.1:** (a) Mean absorption coefficient,  $\mu_a$  (mm<sup>-1</sup>), as a function of excitation wavelength derived from integrating sphere measurements of control, diffuse glioma, glioblastoma, metastasis, and meningioma samples. (b) Histogram comparing the scattering coefficient,  $\mu_s$ , across all tissue types for each wavelength. (c) Anisotropy coefficient,  $g$ , derived from collimated transmission measurements and averaged among each tissue category. The error bars are the corresponding standard deviations from all tissues within the same category in all three figures

### 6.2.3.1 Qualitative examination of two-photon signals and correspondence to histopathology

First row of Figure 6.2 depicts the different two-photon imaging features characteristic of each tissue pathology. The images are a result of superimposing the two-photon images collected at  $520 \pm 20$  nm and  $448 \pm 20$  nm for optimal detection of TPEF and SHG, respectively after 890 nm excitation. The images were collected under the same mean laser power, acquisition time, pulse duration, and repetition rate. Figure 6.2(f-j) are the corresponding H&E stained histology images extracted from the same patients as those used for two-photon excitation. Figure 6.2(k-o) show the one- and two photon emission spectrum from 380 to 760 nm following 405, 810 and 890 nm excitation across the spectral range averaged across different ROIs. The control sample was derived from an epileptic

patient with hippocampal sclerosis showing no signs of necrosis, dedifferentiation, or angiogenesis as depicted in the H&E stained images. The uniform TPEF signal (red in figure 6.2(a)) confirms normal neuronal cells and the SHG signal (green) indicates blood vessel

walls. The diffuse glioma sample corresponding to the second column was excised from a patient with grade II oligo-astrocytoma. The H&E stained image depicts diffused cellular proliferation with no signs of necrosis and angiogenesis. This is also mirrored in the two-photon image with minimal SHG signal and relatively large tumor cells presented as hypo-intense regions. The histological image of Figure 6.2(h) depicts the common microscopic features of GBM, namely the prominent anaplasia, the microvascular proliferation, and the palisading of tumor cells around necrotic regions observed at the center of the image. The two-photon image (Figure 6.2(c)) also highlights the dense microvasculature as portrayed by the intense green SHG signal, which surrounds a dense network of endothelial cells. The fourth column of Figure 6.2 corresponds to images sampled from a patient suffering from brain metastasis, while the fifth column pertains to a patient with recurrent meningioma. The dense vascular network surrounding tumor cells is equally shown in both the histological and two-photon image (Figures 6.2(d&e)), while the thick stroma characteristic of metastatic tissue is better depicted in the latter. The hyper intense SHG signal in figure 2E correspond to collagen structures surrounding tumors organized as whorls as also shown in figure 6.2(j). Similarly, the hyper-cellularity of this tumor is shown in both the two-photon and H&E stained images. The fluorescence emission spectrum for each tissue type (Figure 6.2(k-o)) shows that the fluorescence emission under one-photon excitation (405 nm) is distinct from that under two-photon excitation (810 nm). Qualitatively, the latter is seen to have a broader spectrum, is redshifted and is generally less intense. By comparing the fluorescence spectra according to tissue type, the malignant tissue (glioblastoma, metastases, and meningioma) tend to have lower autofluorescence, which was more evident under one-photon excitation. Differences in the spectral shape on the other hand, are better delineated

under two-photon excitation. For example, the fluorescence emission from glioblastoma at 810 nm excitation depicts unique spectral features different from that of low-grade diffuse glioma and healthy cortical tissue. Moreover, exciting tissue at 890 nm is seen to be particularly useful to identify meningioma and metastatic tissue based on the SHG peak at 445 nm.

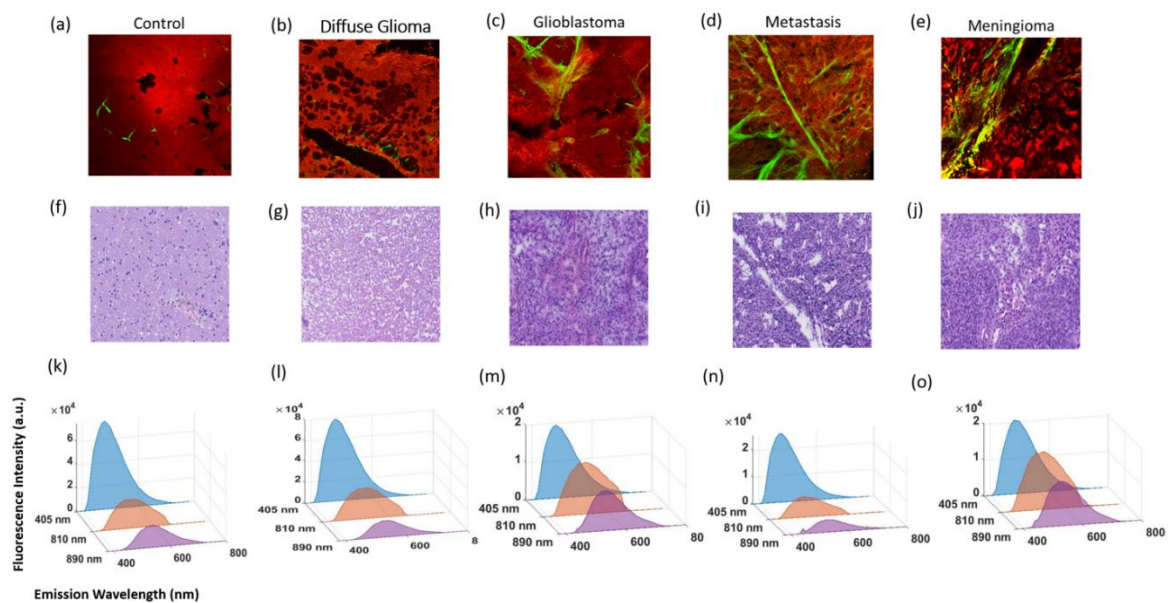


**Figure 6.2:** First row: Two-photon images representative of (a) control, (b) diffuse glioma, (c) glioblastoma, (d) metastasis and (e) meningioma samples following 890 nm excitation. Red and green colors correspond to the TPEF and SHG intensities, respectively. Second row: (f-j) H&E stained images obtained from the same patient; (k-o) the autofluorescence spectra following 405 nm one-photon excitation, and the TPEF spectra following 810 and 890 nm excitation

### 6.2.3.2 Quantitative examination of multimodal optical signatures for tissue characterization

The optical index (OI) ratio, defined as porphyrins/NADH, was determined from the spectrally-resolved TPEF images after 810 nm excitation. The bar plot in Figure 6.3(a) shows that the OI ratio increases as a function of malignancy, where GBM samples had the highest values. The Lipopigment/Porphyrins (LP) ratio (Figure 6.3(b)) had the opposite trend, where low grade glioma and control tissue had the highest values. The redox ratio,  $FAD/(FAD+NADH)$ , was determined from the TPEF images after 720 nm excitation at a given ROI. The fluorescence signal collected by the second detector ( $520 \pm 30$  nm) was assumed to be mainly attributed to FAD, while the fluorescence collected by the first detector ( $448 \pm 20$  nm) was assumed to be mainly from NADH. This way, both fluorophores were excited under the same experimental conditions, and the redox ratio becomes a quantitative biomarker of tissue metabolism. Figure 6.3(c) shows that the redox ratios for all tissue types extend from 0.21 to 0.34. There is no significant difference in the ratios among the tissue groups. The redox ratios obtained after 810 nm excitation (not shown here) resulted in similar conclusions. The collagen density was obtained by measuring the SHG/TPEF ratio under 890 nm excitation. Collagen is not fluorescent under 890 nm excitation, but it is a strong SHG emitter. Hence the SHG/TPEF signal corresponds to the relative collagen content. The SHG signal was separately detected at  $448 \pm 20$  nm, while the fluorescence from other fluorophores (FAD, lipopigments, and porphyrins I and II) was detected at  $520 \pm 30$  nm. For this cohort, the best indicator of diffuse glioma is the low collagen density ( $<0.05$ ) and high LP ratio ( $>1.3$ ). In the more malignant case, GBM was characterized with high optical index ratio ( $>0.7$ ), low LP ratio ( $<1.4$ ), and rich collagen density ( $>0.7$ ). Meningioma was best differentiated by the high collagen density ( $>0.12$ ).

Non-cancerous tissue was characterized with high LP ratio ( $>1.8$ ), low collagen density ( $<0.07$ ), and relatively low optical index ratio ( $<0.5$ ).

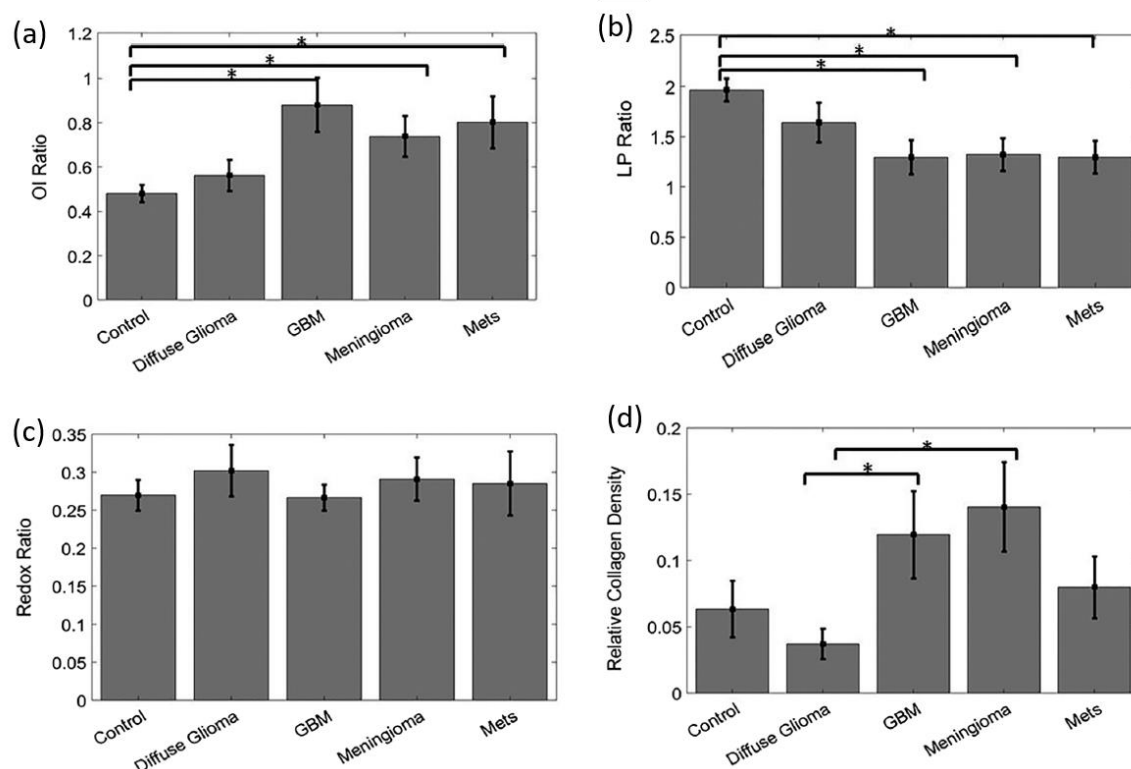


**Figure 6.3:** Bar plots of the optical index (OI) ratio (a), the lipopigment to porphyrin (LP) ratio (b), the redox ratio (c) and the collagen density (d) for each tissue group. The error bars correspond to the standard error averaged across the samples within each tissue group and the asterisks indicate significant differences with a p-value of 0.05

### 6.2.3.3 Lifetime analysis

The capabilities of the multimodality of the two-photon microscope extend to measuring the fluorescence lifetime of endogenous fluorophores related to impaired cellular metabolism and microenvironment. The raw FLIM data culminated from all samples following 890 nm excitation is graphed as a phasor plot in Figure 6.4(a). The distribution of the phasor points indicates that the lifetimes of all samples were well characterized with the same fluorophore as indicated by having most phasor counts clustered at a small region (red) inside the universal circle. The line connecting the phasor distribution intersects the universal circle at two points, which correspond to two mean lifetimes, 2.1 ns and 0.67 ns. Since images were collected at 520 nm, FAD is the expected fluorophore and the two mean lifetimes correspond to free (2.10 ns) and protein-bound (0.67 ns) FAD. After projecting all phasor counts onto the intersecting line, the Long Lifetime Intensity Fraction ( $\alpha$ ) was calculated and is plotted in Figure 6.4(b) according to tissue type. The statistical difference ( $p < 0.05$ ) in the  $\alpha$  values between two categories is indicated by \*. The control and diffuse glioma samples showed minimal variations and relatively higher  $\alpha$  values compared to the malignant samples. GBM tissue had the lowest  $\alpha$  values, which were statistically separated from normal tissue and gliomas of lower grade. A student t-test analysis also showed that metastatic samples had significantly different  $\alpha$  values than their control.

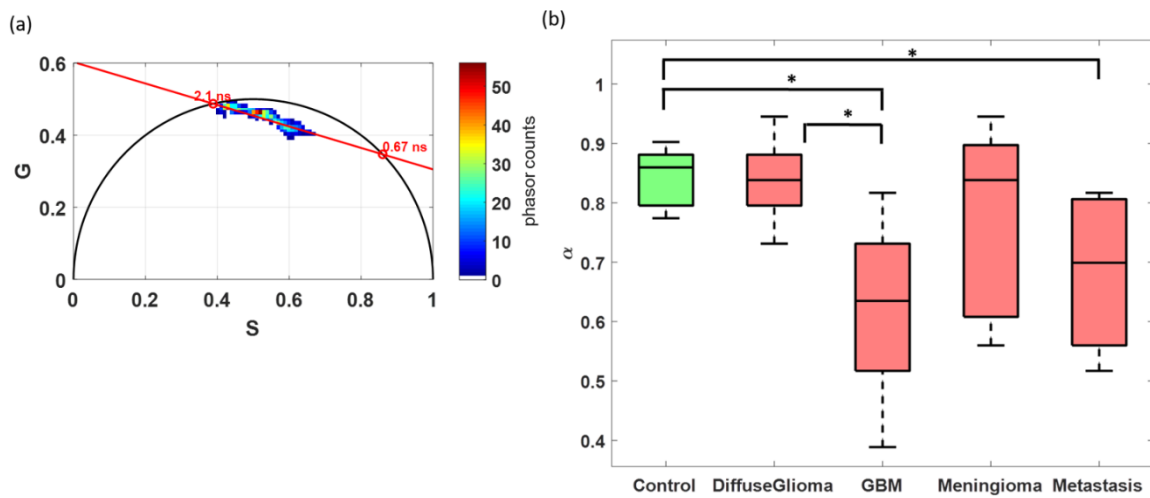


**Figure 6.4:** (a) Phasor plot of FLIM data obtained from all tissue samples following 890 nm excitation and 520 nm detection. (b) Box plot comparing the long lifetime intensity fraction ( $\alpha$ ) determined for each category

## 6.2.4 Discussion and conclusion

This paper investigates the utility of multimodal optical imaging to identify optical signatures of different brain tissue pathologies from fixed samples obtained intraoperatively from cancer and epileptic patients. Specifically, cancer patients were diagnosed with GBM, diffuse glioma (grades II and III), meningioma (grades II and III) or metastases. Cortical tissue from epileptic patients was considered as the control as they did not have a history of brain tumors and the samples had no sign of dysplasia. Local optical properties of cortical tissue have been shown to drastically change prior to and leading up to an epileptic event due to hyper perfusion, glial activation and cell swelling [324]. However, since these biological effects are temporary (in the order of minutes post-seizure),  $\mu_a$  and  $\mu_s$  are not expected to change post-seizure and at the time of biopsy [324]. The integrating sphere measurements showed that tissue optical properties from non-cancerous tissue differed from those of cancerous ones across the whole spectral range. All three optical properties,  $\mu_a$ ,  $\mu_s$  and  $g$ , were consistently higher in the tumor samples, as also observed in vivo [240], [306], [323]. Specifically, pleomorphism, the presence of densely packed chromatin and necrotic tissue all contribute to enhanced scattering, where the scatter centers (nuclei and organelles) are larger in size, more heterogeneous and more abundant in tumors compared to non-tumorigenic cells [325]. Hyper-vascularization driven by angiogenesis result in higher absorption coefficients found in the tumor samples [323]. Interestingly, diffuse glioma did not have optical property values between those from healthy and GBM samples, as the diffuse glioma samples comprised of both abnormal oligodendrogloma and astrocytoma cells. Furthermore, the large variation in the optical properties within the same category (up to 33%) hindered further differentiation between tumor types in this cohort. This is particularly true for gliomas as they are known to have different histological properties (degree of necrosis, endothelial proliferation and genetic atypia) even within the same tumor grade [313]. The limited capability of discriminating between tumor types based solely on tissue optical properties has also been reported elsewhere [240], [305], [307], [326], where in

vivo, frozen and fixed brain tissue samples were examined. Our absorption and scattering coefficients of GBM, meningioma and cortical tissue are similar to those reported by Honda et al. [326], where integrating sphere measurements were performed on freshly excised samples and are generally higher than the in vivo results reported by Bevilacqua et al. [306]. Additionally, they are higher than those obtained by Gebhart et al on frozen tissue due to the change in hemodynamics upon snap freezing [305]. The varying techniques in preserving tissue directly affect the optical properties and thus explain the discrepancies [294]. In fact, changes in the optical properties due to tissue handling are wavelength [294] and tissue type dependent [240]. For brain tissue, the spectral diffuse reflectance shapes across the visible range were drastically altered due to significant loss of oxy and deoxy hemoglobin following tissue fixation by Formalin [293]. In the NIR regime on the other hand Formalin fixation was found to have a minimal effect, where  $\mu_a$  increased by 15% and  $\mu_s$  increased by 5% compared to their in vivo values [240] as a result of tissue shrinkage. Cryogenation drastically reduces both coefficients by 20% to 30% due to the formations of intra- and extra-cellular crystals

that can damage cell walls and cause blood drain as well as oxidation of deoxy-hemoglobin [240], [327]. Therefore, it is possible that the enhancing effects of Formalin fixation partly compensated for the attenuating effects of freezing. Since the tissue optical property study resulted in limited tissue differentiation among tumor types, additional optically-derived signatures were examined based on two photon excitation. This was motivated by our preliminary two photon imaging studies, which demonstrated that fixed/fresh meningioma and glioblastoma samples display certain features correlated to their unique phenotypes, such as intense green SHG signals surrounding hypo-intense fluorescence regions [214], [274]. These were corroborated here and extended to other brain tissue types, diffuse glioma, cortical tissue, and metastases. Conflicting results are reported regarding the effect of tissue fixation and cryogenation on the fluorescence and SHG signals according to a review by Perry et al. [300]. However, it was reported that both Formalin fixation and cryogenation did not significantly impact the ability to obtain useful information including those from NADH and FAD measurements [300]. We have also shown previously that although the TPEF signal of freshly excised brain tissue was systemically higher from that after Formalin fixation, the optical features of each tissue type were still characteristic to each group (cortical tissue, GBM, and metastases) [274].

This study, among others [319], [321], [322], [328]–[330], shows that qualitative examination of TPEF images not only mirrors the histological features observed by the gold standard (anaplasia, necrosis, and increased cellular density), but rather provides additional information related to tissue architecture such as the (dis)organization of blood vessels and collagen structures surrounding tumor cells (Figure 6.2(c-e)). The added advantage of interrogating tissue non-invasively, and in real-time, without the need of exogenous, contrast further motivates the development of a non-linear multimodal endomicroscope for intraoperative pathological assessment in lieu of repeat biopsy sampling. In fact, previous studies have reported on the ability of trained pathologists to identify gallbladder [328], breast [329], and liver tumors [330] from TPEF images with an accuracy of ~90%, while being blind to the histopathological assessment. In neuro-oncology, untrained pathologists correctly identified GBM and metastatic tissue with a sensitivity and specificity of 50% and 75%, respectively, before training the neuropathologists [214]. It is evident that qualitative



assessment of the overall autofluorescence spectra is not sufficient in identifying different brain tissue types even after exciting with different wavelengths (Figure 6.2(k-o)). The purpose of comparing the spectra for each tissue type was to rather delineate unique spectral features such as the SHG signal after 890 nm excitation in the meningioma and metastatic samples, identify any shifts in the fluorescence peaks or broadening in the spectral distribution such as in the GBM samples after 810/890 nm excitation. Spectral shifts in the FAD and NADH peaks, for example, are explained by a change in the ratio between their free and bound forms associated with tumorigenesis [331]. Interestingly, one- and two-photon excitation (405 nm vs. 810 nm) did not result in the same emission spectrum opposite of what Bestvater and colleagues had observed [332]. The one- and two-photon fluorescence spectra of diffuse glioma (Figure 6.2(k)) were closer to that exhibited by normal tissue, indicating that the spectral analysis was performed on regions with almost normal cell differentiation. The spectral shapes and fluorescence intensity from the malignant samples under 810 and 890 nm indicate that the intrinsic optical properties (Figure 6.1(a&b)) do not greatly modulate the TPEF and SHG signal, while the opposite is true for one-photon excitation, where higher  $\mu_a$  and  $\mu_s$  values in malignant tissue result in a decrease in the observed autofluorescence compared to that of healthy tissue. From the spatially-resolved TPEH/SHG images, two

quantitative biomarkers were extracted: the optical redox ratio and the relative collagen density. The first parameter reflects the metabolic state of tissue. Changes in the redox ratio can be interpreted as a metric for the relative change in the rate of glucose catabolism to oxidative phosphorylation [123]. The particularly large variation in the redox ratio of diffuse glioma and metastatic tissue found here mirrors the large variation in the scattering properties measured with the integrating sphere (Figure 6.1(b)) at 720 nm. This was the wavelength used to extract the aforementioned ratios. The redox ratio did not significantly decrease with tumor status in this cohort (Figure 6.3(c)), which is in agreement with Skala et al. who found variability in the optical redox ratios as a result of heterogeneous mitochondrial function and microenvironment [93]. This further highlights the heterogeneous nature of brain tumors and the need to extract multiple markers of disease. As for the collagen density, Jiang et al. reported similar collagen ratios in Glioma samples to that obtained in the GBM group (Figure 6.3(d)), where collagen was shown through imaging to deposit in the tumor microenvironment, i.e. the connective stroma within brain vessels and extracellular matrix promoting angiogenesis and infiltration, respectively [215], [300]. Similar to the SHG/TPEF images of Figure 6.2(a-e), the bar plot of Figure 6.3(d) shows that meningioma and GBM have the most abundant collagen structures. However, on average the metastatic samples had only slightly higher collagen content than cortical tissue compared to what was deduced from the qualitative composite image of Figure 6.2(e). From the spectrally-resolved TPEF images, two additional optical ratios were investigated: the optical index ratio (OI) and the Lipopigment to Porphyrins ratio (LP). The OI ratio is a marker of vasculature, where higher values indicate hyper-vascularization [215]. This ratio is used to differentiate bladder tumor cells from their healthy counterparts [96]. The LP ratio has only been recently investigated and relates both metabolic and vascular properties into one metric [215]. The malignant tumor samples had significantly higher OI ratios and lower LP ratios. Based on all four molecular ratios, a threshold of 1.4 for the LP ratio, 0.6

for the OI ratio, and a threshold of 0.08 for the collagen density can discriminate malignant tumors vs. non-malignant tissue. GBM and diffuse glioma are best differentiated by their collagen density. Secondary brain tumors are modestly differentiated from meningioma and gliomas by their collagen density. As for FLIM analysis, the fluorescence lifetime reflects tumor microenvironment including local PH, temperature, polarity of biomolecules as well as conformational changes that have occurred in the fluorophore [320]. The phasor plot approach provides a simple and robust interface to analyze the raw FLIM data quantitatively without being limited to the errors associated with typical fitting routines [129], [130]. Two mean lifetimes were extracted, a short lifetime of 0.67 ns and a longer lifetime of 2.1 ns, both of which correspond to the fingerprint of FAD (protein bound vs free FAD) [300]. The long lifetime intensity fraction,  $\alpha$ , indicates the contribution of free FAD. This  $\alpha$  factor was chosen as it has been suggested to be a more specific biomarker than the commonly used average lifetime, the amplitude-weighted lifetime and average arrival time [333]. Free FAD was predominant in control and low-grade diffuse glioma tissue (Figure 6.4(b)). The distribution of this factor starts to shift towards lower values for malignant tissue, suggesting protein-bound FAD dominance is implicated in malignancy. A similar conclusion was found by Nazeer et al., in fresh and fixed astrocytoma, glioma and meningioma samples, where a blue shift in the FAD fluorescence spectrum from these tumors was attributed to the increase in the bound state of coenzyme FAD due to angiogenesis [331]. The potential use of the  $\alpha$  value as a classifier of malignancy as well as an indicator to tumor grade of the same tumor type is currently under investigation.

The results presented in this study suggest that deriving multiple optical signatures is not only useful but is required to identify the multifaceted characteristics of brain tumors. Each optical contrast (tissue optical properties, one and two photon autofluorescence spectra, shifts in the spectral peaks, SHG/TPEF signal, the redox ratio, the OI ratio, the LP ratio and the lifetime fractional intensity value) identified in the different tissue groups correlates to different properties of tumors. These include angiogenesis, infiltration, enhanced cell growth and proliferation. Despite, performing different optical and fluorescence measurements at multiple excitation wavelengths and spatial scales, efficient discrimination between the five groups was not achieved. Therefore, a larger database is warranted so that a multivariate classification algorithm can be applied. Nevertheless, the spectral specificity characterizing each brain tissue type is greatly enhanced when measurements are performed on fresh tissue, and thus the qualitative and quantitative optical markers identified here should result in more efficient discrimination *in vivo* [274]. Additionally, these optically derived biomarkers should be measured *in situ* in both suspect tissue regions as well as adjacent normal tissue in order to overcome the inter- and intra-patient variability, thereby bringing the recently developed multimodal endomicroscope to the OR, for improved brain cancer diagnosis, treatment, and post-resection evaluation.

# Chapter 7

## **Towards a more specific tissue database: Could quantitative multimodal and multiscale optical analysis discriminate low grade and high grade glioma from healthy brain tissues?**

### **7.1 Context of the study**

In the previous chapters (chapter 5 and 6), we addressed the issues of studying the effect of the fixation process and the post-excision measurements time on the autofluorescence of neuronal tissues. Indeed, we enlarged our tissue database by determining new optical related parameters such the optical coefficients (scattering, absorption, and anisotropy) of fixed brain tissue in the photo-therapeutic window wavelength range.

The next challenge is to render the discrimination more robust and specific. In our previous works, our discrimination studies were focused on looking for discrimination factors between healthy and tumor tissues, without separating the different grades of each type. In the next two chapters, we are categorizing each tumor type into two different types following their grades, low grade, and high grade. The investigation methodology will be focused on discriminating healthy from low grade tumor and these two latter from high grade tumors. This specification challenge started by investigating the different grade of glioma, the most malignant brain tumor types. One of the most challenging and unmet needs in glioma surgery is to accurately identify the infiltrating margins of the tumor mass. Delineating these zones from healthy tissue zones is crucial to achieve maximum safe resection and to prevent tumor recurrence [28], [227]. However, the strong diffusive nature of these tumors makes them visually indistinguishable from normal regions during surgery. Indeed, differential diagnosis between malignant zones and non-malignant one is essential as the line of treatment may differ [28], [227].

In this study we gathered grade I and grade II glioma tumors in the category of Low Grade (LG) glioma, while grade III and grade IV (GBM) under the category of high grade glioma. Therefore, this study was designed to collect the multimodal optical signatures obtained from multiple optical imaging modalities and at different excitation domains: from the deep UV (DUV), the visible light domain, to the NIR domain. In the DUV domain, the endogenous spectrally-resolved autofluorescence signal originating mainly from tyrosine (Tyr), tryptophan (Tryp), collagen (coll), and NADH (table 7.1) was highlighted. In the visible and NIR domain, we have access to autofluorescence signal of four main four

fluorophores; NADH, FAD, Lipopigments, and Porphyrins as well as the SHG signal generated from collagen structures when non-linear excitation in NIR domain is used.

**Methods** This multimodal study involved a thirty-six fresh samples cohort that consist of 16 control healthy samples, 6 low grade and 14 high grade samples. Located in Sainte Anne hospital, the visible one-photon bimodal endoscope was used to extract the spectral and lifetime fluorescence properties following 375 nm and 405 nm excitation. A second collaboration that is established with Synchrotron SOLEIL (Saint-Aubin, France) provided an access to their DUV excitation platform within DISCO beamline. 10  $\mu\text{m}$  slices were sectioned and fixed in order be analyzed on a spectroscopic setup using 275 nm as excitation wavelength. Thereby NIR measurements were performed using a multiphoton multimodal benchtop microscope able to perform: (1) two-photon fluorescence imaging (2) two-photon FLIM measurement, (3) SHG imaging and (4) one and two-photon Spectral imaging. For all three domains, spectral fitting into Gaussian curves was used to extract the different molecular ratios. In the NIR domain, and similar to the FLIM study realized in chapter 6, phasor FLIM analysis and LLIF extraction of FAD and NADH was performed to further characterize the different interrogated tissue types.

Indeed, in this chapter, the spectral phasor approach was used for spectral unmixing of fluorophore contributions in the spectral images which offers a global visualization of the spectral variation between each tissue type.

**Results and discussion** A summary of the spectral extracted molecular ratios and mean fluorescence lifetime values for each tissue type are shown in the tables below for all three excitation domains.

Tissue Type	Tryp/collagen	Tryp/NADH	Tryp/Tyr	Vis Redox	Vis Index	Vis LP	NIR Redox ratio	NIR OI ratio	NIR LP ratio
Control	2.8	8	6	0.42	-0.7	0.1	0.65	1.6	0.55
LGG	3.2	25	5	0.55	0.1	-0.9	0.6	1	0.8
HGG	4.2	12	4	0.6	0	0	0.68	1.5	0.55

Table 7.1: Summary of the median values of the investigated molecular ratios extracted from DUV, visible and NIR excitation domains

Tissue Type	$\tau_{\text{NADH 375nm}}$	$\tau_{\text{FAD 375nm}}$
Control	$5.3 \pm 0.6$	$4.4 \pm 0.4$
LGG	$4.8 \pm 0.4$	$4.2 \pm 0.3$
HGG	$6.0 \pm 0.8$	$6.0 \pm 0.8$

**Table 7.2:** Summary of the mean fluorescence lifetime values of NADH and FAD extracted through the visible one-photon endoscope following 375 nm

Through these multimodal extracted parameters, several differentiation conclusions would be attributed: HG glioma tissue could be differentiated from normal cortical tissue by its higher Tryp/collagen and Tryp/NADH ratio, lower Tryp/Tyr ratio, longer fluorescence lifetime at 375 nm, higher FAD and lower Porphyrin 2 content at 405 nm excitation, higher visible optical redox ratio, and lower LLIF values.

Importantly, HG glioma can be distinguished from LG glioma by its higher Tryp/collagen, lower Tryp/NADH ratio, lower Tryp/Tyr ratio, higher visible and NIR redox ratio, higher NIR index ratio, lower NIR LP ratio, and longer fluorescence lifetime value at 375 nm, and lower LLIF values.

Discrimination between normal cortical tissue and diffuse LG glioma was also possible. LG glioma had higher Tryp/collagen and Tryp/NADH ratio, lower median value of Tryp/Tyr ratio, higher visible redox and optical index ratios, lower NIR redox and optical index ratios, higher NIR LP ratios and longer NADH fluorescence lifetimes at 375 nm.

Obtained results from DUV excitation domain were the most significant in terms of discrimination between the three interrogated tissue types. Therefore, the DUV molecular were implemented in a 3D cloud-based discrimination algorithm to discriminate control, LG, and HG glioma. Therefore, a sensitivity of 94% and a specificity of 84% were obtained when healthy vs tumor discrimination is needed.

A crucial finding, apart from the quantitative indicators derived from the three excitation domains, was that the acquired TPF+SHG images successfully showed the tumor microenvironment supporting tumor invasion and infiltration by the high SHG signal originating from dense vasculature. This feature will help in delineating the infiltrated brain regions from that of non-infiltrated brain regions.

The main aspect that could be concluded from this study was that using several excitation wavelengths in different spectral domains provide important complementary properties that characterize histologically healthy brain tissue, low and high-grade glioma. The quantitative indicators derived from visible and NIR excitation domain will be directly extracted through our multimodal endomicroscope. Although, DUV excitation is not implemented in the developed endomicroscope, but exciting within this spectral domain was useful to highlight the properties of other endogenous fluorophores such as tryptophan and collagen crosslinks that play a role in malignant transformation brain tissues. Seen the significant discrimination provided by DUV molecular ratios, this excitation domain was also used in the next chapter to interrogate meningioma samples with different grades.

## 7.2 Paper: Optical Signatures Derived from Deep UV to NIR Excitation Discriminates Healthy Samples From Low and High Grades Glioma

www.nature.com/scientificreports

# SCIENTIFIC REPORTS

OPEN

## Optical Signatures Derived From Deep UV to NIR Excitation Discriminates Healthy Samples From Low and High Grades Glioma

Received: 25 January 2019  
Accepted: 29 May 2019  
Published online: 19 June 2019

Hussein Mehdine<sup>1,2</sup>, Audrey Chalumeau<sup>2</sup>, Fanny Poulon<sup>2</sup>, Frédéric Jamme<sup>3</sup>,  
Pascale Varlet<sup>4,5,6</sup>, Bertrand Devaux<sup>5,7</sup>, Matthieu Refregiers<sup>3</sup> & Darine Abi Haidar<sup>1,2</sup>

Among all the tumors of the central nervous system (CNS), glioma are the most deadly and the most malignant. Surgical resection is the standard therapeutic method to treat this type of brain cancer. But the diffusive character of these tumors create many problems for surgeons during the operation. In fact, these tumors migrate outside the tumor solid zone and invade the surrounding healthy tissues. These infiltrative tissues have the same visual appearance as healthy tissues, making it very difficult for surgeons to distinguish the healthy ones from the diffused ones. The surgeon, therefore, cannot properly remove the tumor margins increasing the recurrence risk of the tumor. To resolve this problem, our team has developed a multimodal two-photon fibered endomicroscope, compatible with the surgeon trocar, to better delimitate tumor boundaries by relying on the endogenous fluorescence of brain tissues. In this context, and in order to characterize the optical signature of glioma tumors, this study offers multimodal and multi-scaled optical measurements from healthy tissues to high grade glioma. We can interrogate tissue from deep ultra-violet to near infrared excitation by working with spectroscopy, fluorescence lifetime imaging, two-photon fluorescence imaging and Second Harmonic Generation (SHG) imaging. Optically derived ratios such as the Tryptophan/Collagen ratio, the optical redox ratio and the long lifetime intensity fraction, discriminated diseased tissue from its normal counterparts when fitted by Gaussian ellipsoids and choosing a threshold for each. Additionally two-photon fluorescence and SHG images were shown to display similar histological features as Hematoxylin-Eosin stained images.

Brain cancer is one of the deadliest cancers which prevails in humans. Its survival rate is lower than other types of cancer, among ten patients suffering from brain cancer only two survives<sup>1</sup>. Originating from brain neoplastic glial cells, glioma presents 30% of brain tumors and 80% of all malignant brain tumors<sup>2</sup>. They are categorized referring to their location, their cell types and their grades<sup>3</sup>: Low Grade (LG) and High Grade (HG), which is determined by the malignancy and the pathological evaluation of the tumor. This evaluation is performed according to World Health Organization (WHO) classification of CNS tumors<sup>3</sup>. To treat glioma, maximal safe surgical resection is the standard practice used today<sup>4</sup>. The success of this kind of surgery relies on the accurate identification of the solid tumor mass. But actual tumor margins are not well defined as tumor cells diffuse into adjacent normal tissue. This cell diffusion leads to the emergence of infiltrating zones, which overlap with the healthy zones with no distinguishing appearance, thus making their delineation very difficult. The inability to fully visualize the margins of a diffusive glioma results in subtotal surgical resections, which negatively affects the survival rate of the patient<sup>5</sup> and causes a fast recurrence of the tumor. Similarly, unnecessary removal of healthy functional brain tissue that does not contain cancer cells can lead to major neurological deficits that affect the life quality of the patient.

<sup>1</sup>Université de Paris, IMNC Laboratory, UMR 0165-CNRS, IN2P3, Paris, France. <sup>2</sup>Université Paris-Saclay, IMNC Laboratory, UMR 0165-CNRS, IN2P3, Orsay, France. <sup>3</sup>DISCO Beamline, Synchrotron SOLEIL, GIF-sur-Yvette, France. <sup>4</sup>Neuropathology Department, Sainte-Anne Hospital, Paris, France. <sup>5</sup>IMA BRAIN, INSERMU894, Centre de Psychiatrie et de Neurosciences, Paris, France. <sup>6</sup>Paris Descartes University, Paris, France. <sup>7</sup>Neurosurgery Department, Sainte-Anne Hospital, Paris, France. Correspondence and requests for materials should be addressed to D.A.H. (email: abihaidar@imnc.in2p3.fr)

### 7.2.1 Introduction

Brain cancer is one of the deadliest cancers which prevails in humans. Its survival rate is lower than other types of cancer, among ten patients suffering from brain cancer only two survives [16]. Originating from brain neoplastic glial cells, glioma presents 30% of brain tumors and 80% of all malignant brain tumors [297]. They are categorized referring to their location, their cell types and their grades [19]: Low Grade (LG) and High Grade (HG), which is determined by the malignancy and the pathological evaluation of the tumor. This evaluation is performed according to World Health Organization (WHO) classification of CNS tumors [19]. To treat glioma, maximal safe surgical resection is the standard practice used today [28]. The success of this kind of surgery relies on the accurate identification of the solid tumor mass. But actual tumor margins are not well defined as tumor cells diffuse into adjacent normal tissue. This cell diffusion leads to the emergence of infiltrating zones, which overlap with the healthy zones with no distinguishing appearance, thus making their delineation very difficult. The inability to fully visualize the margins of a diffusive glioma results in subtotal surgical resections, which negatively affects the survival rate of the patient [261] and causes a fast recurrence of the tumor. Similarly, unnecessary removal of healthy functional brain tissue that does not contain cancer cells can lead to major neurological deficits that affect the life quality of the patient.

Most brain cancers are diagnosed by conventional imaging techniques such as computed tomography (CT), magnetic resonance imaging (MRI) and positron emission tomography (PET) [263], [297], [298]. These imaging techniques characterize the location and the anatomical property of the tumor solid area, but they cannot give structural or metabolic information at the cellular level. In addition, these imaging techniques cannot be practically used intraoperatively. Over time, different techniques have been developed to guide the surgery and to improve the surgical outcome like Intra-MRI which gives the surgeon an updated plan on the tumor's location and its solid boundaries [280]. However, intra-MRI are resource intensive as they require 20–30 minutes for each acquisition, thereby lengthening the duration of the procedure.

A more practical technique that provides real-time information on the tumor boundaries, is the intra-fluorescence guided surgery which uses exogenous fluorescent markers to acquire fluorescence images [139], [299]. Fluorescence guided surgery, using Protoporphyrins IX and its precursor, the 5-Aminolevulinic Acid (5-ALA), increases the extent of tumor resections in patients with Glioblastoma (GBM) (Grade IV glioma) patients [82], but has shown limited efficacy in identifying the diffuse low-grade gliomas and the micro-infiltration cases [299]. In addition, the fluorescence of this fluorophore is not highly specific to tumors, as PpIX fluorescence is also present in inflammatory cells within the resection cavity [299]. In addition to this, protoporphyrin IX can escape into peritumoral oedematous areas which are healthy regions that are free of tumor cells. To this end, histological Hematoxylin-Eosin (H&E) staining is still the gold standard for an accurate diagnosis of any brain tissue type. Unfortunately, the results of such methods can only be communicated a few days after the surgery. There is therefore an immense need to develop a more efficient for tissue diagnosis that can be obtained during surgery. This method should be able to sample tissue non-invasively and provide morphological structural and functional information at the tissular, molecular, and cellular level to be sensitive enough to detect isolating diffuse low and high grade glioma cells. One and two-photon excitation can satisfy this need.

Over time, the reliance on endogenous fluorescence has strongly evolved to explore brain tissues, in order to discriminate tumoral from healthy tissues [82], [84], [85]. The autofluorescence of the Nicotinamide Adenine Dinucleotide (NADH) and the Flavins (FAD) with its related metabolic ratios shows the importance of getting reliable information on the tissue's nature [82], [84], [85], [89]. The redox ratio highlights the accretion of NADH in tumor tissues by rationing NADH to FAD content (NADH/FAD). In Previous works, this ratio was shown to discriminate between healthy and tumoral tissues in the bladder [96], breasts [334], and brain [215]. Other metabolic ratios investigated are the NADH to Porphyrin levels and the Lipopigments to Porphyrin relating metabolic activity with vasculature [96], [215].

The fluorescence lifetime of these fluorophores have also been studied to discriminate tumor from healthy tissues. Fluorescence lifetime of NADH was found higher in GBM than normal cortex ones [124], while it was found lower in carcinoma than that found in normal ones [335]. Most studies found in literature focus either on analyzing spectrally-resolved autofluorescence [85], [336] or the temporally-resolved fluorescence [125], [126], [337], but few studies tried to implement the complementarity between both methods to better discriminate the different types of brain tissues.

To this end, and to address all these problems cited, we aim to build a multimodal endomicroscope based on non-linear excitation in Near Infra-Red (NIR) range where the tissue therapeutic window is located, resulting in better penetration depth and less photodamage. This endomicroscope will be able to perform different fluorescence imaging modalities by detecting several contrasts: 1) Two-Photon Fluorescence Emission (2PEF) imaging of five endogenous fluorophores: NADH, FAD, Lipopigments, Porphyrins I and Porphyrins II; 2) The Fluorescence Lifetime Imaging (FLIM) of these five fluorophores; 3) The autofluorescence spectra and 4) The Second Harmonic Generation (SHG) detection. With two-photon imaging, TPEF/SHG images at the submicron resolution is expected to identify isolated tumor cells that have infiltrated the parenchyma within the field of view, either during open surgery after macroscopically complete surgical removal of the tumor, or during biopsy procedure, using an optic fiber mounted biopsy forceps. Therefore, we hypothesize that tumor microenvironment supporting tumor invasion and infiltration can be differentiated from that of non-infiltrated brain parenchyma.

Although multiscale (DUV to NIR) one and two photon images were acquired from fresh tissue on benchtop systems, our multimodal endomicroscope prototype is currently being developed with imaging capabilities using MEMS mirror scanning technology. This endomicroscope will be able to characterize the nature of all types of human brain tumors through its multimodality in order to give the surgeon fast, accurate and specific information at a subcellular scale on the histological nature of the examined tissue during the operation. In parallel, and to validate the instrumental development, we are building a big optical database of the fluorescence response of brain tissues in order to explore the different optical signatures of all types of human brain tissues, healthy or tumor, and to characterize each type of tumor with its specific multimodal signature. This database will be used to develop discriminating algorithms giving the surgeon more criteria to make an informed decision.

Most studies focuses on discriminating healthy from tumor tissue [85], [336], however, there are no studies which try to discriminate tumor types from each other, or to define a specific



signature for each tumor type and for each grade. In some previous work, we were able to discriminate Grade I from Grade II meningioma through their 2PEF images and their spectral emission analysis [216]. We also managed to discriminate primary from secondary brain tumors using deep UV and NIR excitation [214]. The use of deep UV excitation is particularly efficient in studying the autofluorescence of bio-macromolecules due to its high absorption rate in this wavelength range [338], for example tryptophan, whose fluorescence signal gives an additional marker for monitoring cellular status [338]. Although, our endomicroscope will use visible and NIR excitation, the excitation in deep UV highlights the fluorescence of different fluorophores which cannot fluoresce if excited in visible or NIR [338]. Collagen crosslinks emit a fluorescence signal when they are excited in deep UV, while they are a strong source of SHG signal using NIR excitation, indicating the presence of vascularized structures. So, by using different excitation wavelength and adding deep UV excitation, our ability to relate the fluorescence response of the different molecules and to study the alteration of the fluorescence signal of each molecule during cancerogenesis will be improved. All this information will allow us to better follow the metabolic state of the tissue and to find a better discriminative indicator of cancerous tissue.

Many studies were also conducted to discriminate GBM from healthy tissues using different imaging modalities including the autofluorescence spectroscopy over the visible range [85], [125], [126], [336], but it is difficult to find a multimodal study which can delineate diffuse LG gliomas from parenchyma or HG from LG gliomas, or to find a specific optical signature for each type by relying on the autofluorescence of brain cells.

For that reason, we have decided to launch a multiscale study in order to discriminate LG from HG glioma and to try to define a specific signature for each grade. This study was performed in collaboration with Sainte-Anne hospital center (Paris, France), providing all fresh samples and with Synchrotron SOLEIL (Saint-Aubin, France), where we have access to the DISCO beamline platform for deep UV excitation. We performed the NIR measurements using our two-photon multimodal benchtop microscope. We, therefore, present a multimodal study which combines the results and the data obtained from these three imaging platforms. Also included in our study, different molecular ratios analysis and a 3D discrimination algorithm was established for deep UV molecular ratios. Finally, another study was established combining the three molecular ratios derived from different excitation wavelengths in order to discriminate, with high sensitivity and high specificity, the HG, LG glioma from healthy tissues.

## 7.2.2 Materials and methods

### 7.2.2.1 Samples

Samples were collected from the Neurosurgery and Neuropathology department at Sainte-Anne Hospital upon the approval of the Sainte-Anne Hospital – University Paris Descartes Review Board. (CPP Ile de France 3, S.C.3227). All methods were carried out in accordance with relevant guidelines and regulations. Informed consents were obtained from all the samples coming from human subjects whose clinical data were recorded (Table 7.3). Different diffuse glioma grades were compared to control samples extracted during epileptic surgery. These samples were maintained in normal saline solution to avoid desiccation, in a temperature-controlled dark room dedicated to optical imaging. Firstly, these samples

were studied on a visible setup at the CHSA Platform then on a nonlinear multimodal setup at the PIMPA Platform. The whole process took less than two hours. After this procedure, the fresh samples were fixed with 4% paraformaldehyde, embedded in paraffin, and stained with H&E then digitized using Digital Slide Scanner NanoZoomer 2.0 (Hamamatsu Photonics K.K, Hamamatsu, Japan).

Secondly, these samples were stored at  $-80\text{ }^{\circ}\text{C}$  after being freshly analyzed. Few hours before cutting, the tissues were put at  $-20\text{ }^{\circ}\text{C}$ , after which they were cut at  $-18\text{ }^{\circ}\text{C}$  into  $10\text{ }\mu\text{m}$  slices using a cryostat (CM 1950, Leica Microsystems). The tissues were then fixed with ethanol at  $100^{\circ}\text{C}$  and stored at  $4\text{ }^{\circ}\text{C}$  until experimentation. The  $10\text{ }\mu\text{m}$  fixed slices were then used at the PIMPA Platform and on Deep UV setup at the DISCO Platform.

Sample	Number	Mean of patients age
Control	16	30.6
Low grade glioma	6	35
High grade glioma	14	56.6

**Table 7.3:** Clinical Characteristics of our sample's cohort

### 7.2.2.2 Deep UV setup

The deep UV spectral data have been acquired on DISCO beamline at Synchrotron Soleil (Saint Aubin, France), where we performed full field imaging and spectral measurements using  $275\text{ nm}$  as an excitation wavelength on  $10\mu\text{m}$  thick samples. Using this excitation wavelength, we were able to excite four different molecules: Tyrosine, Tryptophan, collagen and NADH. The setup details were described in a previous experiment conducted by our team [214]. For each sample, measurements were conducted on 1 to 4 selected zones (depending on the sample volume). Therefore, the data issued from each zone were taken into consideration separately.

### 7.2.2.3 Visible setup

A detailed description of the visible setup has been published elsewhere [215], [274]. Located at Sainte-Anne Hospital (CHSA), this setup consists of a bi-modal endoscope which uses  $375$  and  $405\text{ nm}$  as the excitation wavelengths. Spectral and lifetime measurements were performed on freshly extracted tissues. In this range we excited five fluorophores, NADH, FAD, Lipopigments and Porphyrins I and Porphyrins II. Spectral acquisition was accomplished for several longitudinal lines of each sample, while the lifetime measurements accomplished five different Regions of Interest (ROI) for each sample. Measurements for each sample were taken between 10 to 15 minutes.

### 7.2.2.4 NIR setup

The NIR multimodal optical setup was described in our previous work [89], [216]. It consists of a two-photon multimodal benchtop microscope (Leica SP8, Leica microsystems) able to perform four different optical imaging modalities: (1) One and two-photon fluorescence

imaging (2) two-photon FLIM measurement, (3) SHG imaging and (4) one and two-photon Spectral imaging.

Analyses were conducted using the dedicated Leica software (LAS-X) as well as Matlab and imageJ. For FLIM measurements, 3\*3 images mosaic per sample were analyzed using 810 and 890 nm the excitation wavelengths. The same technique was used also for 2PEF and spectral imaging, where 2PEF images were acquired using 890 nm and the spectral images using 810 nm. The collected fluorescence signal is divided into two detection channels. Each detection channel contains a super sensitive hybrid non descanned (HyD NDD) detector. In the first detection channel (channel 1), a bandpass filter with a bandwidth of  $448\pm 20$  nm (FF01-448/20-25, semrock, USA) was used to select the NADH fluorescence signal, and in the second detection channel (channel 2) another bandpass filter with a bandwidth of  $520\pm 35$  nm (FF01-520/35-25, Semrock, New York, USA) was used to select the FAD fluorescence signal.

### 7.2.2.5 Data analysis

#### Spectral fitting and molecular ratios analysis

Spectral data processing was conducted using a new homemade matlab interface whose development is based on matlab data processing codes used in previous work by our team [215].

The excitation under 275 nm highlight the fluorescence emission of four fluorophores: tyrosine (tyr), tryptophan (tryp), collagen (col) and NADH. Each emission was represented by a Gaussian fit (Fig 7.1(a)) whose maximum wavelength and bandwidth follows the given values as shown in Table 7.4.

Fluorophores	Maximum wavelength (nm)	Spectral bandwidth (nm)
Tyrosine	301-311	0-50
Tryptophan	335-345	0-10
Collagen	380-420	0-50
NADH	430	0-60

**Table 7.4:** Gaussian Parameters considered to fit the fluorescence emission spectrum of each fluorophore excited with 275 nm

On the other hand, the visible excitation under 405 nm and the two-photon excitation at 810, highlight the fluorescence emission of five fluorophores: NADH (Free and protein bound), FAD, lipopigments, porphyrin I and porphyrins II. These molecules were chosen through a literature review [82]. Six components were fitted by Gaussian curves thanks to this review (Fig 7.5(b&c)). A recapitulation table of the Gaussian parameters is given in Table 7.5.

Fluorophores	Maximum wavelength (nm)	Spectral bandwidth (nm)
NADH free	460-470	45-50
NADH bound	443-445	40-48

FAD	520-530	30-50
Lipopigments	570-600	0-180
Porphyryns I	615-630	0-10
Porphyryns II	675-690	0-10

**Table 7.5:** Gaussian Parameters used to fit the fluorescence emission spectrum of each fluorophore excited with 405 nm.

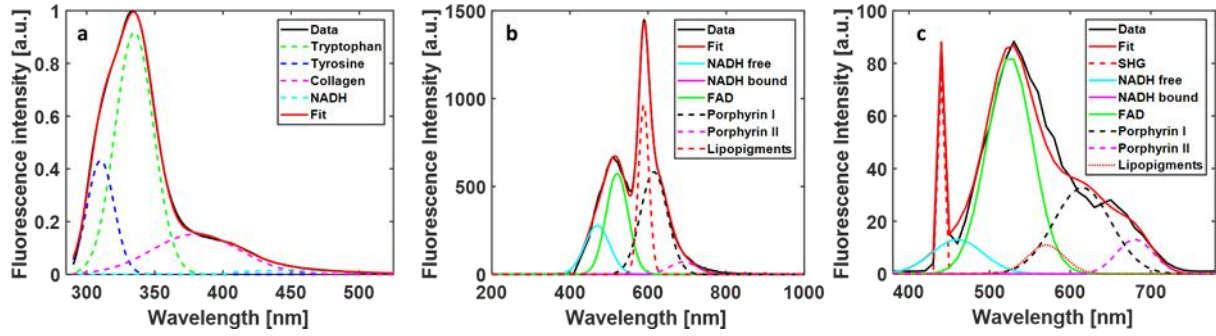


**Figure 7.1:** Fitting examples of the spectral data collected during Deep-UV excitation (275 nm) (a), for Visible excitation (405 nm) (b) and for NIR excitation (890 nm) (c).

In addition, and for all spectral data, the integral proportion of each endogenous fluorophore was then determined: it is defined by the ratio of the integral under the emission curve of the fluorophore contribution on the integral under the curve of the total fit. spectrum. Using this type of analysis, we were able to calculate different molecular ratios.

For deep UV measurements, three molecular ratios were extracted:

$$\frac{\text{Tryp}}{\text{Tyr}} = \frac{\text{Tryptophan}}{\text{Tyrosine}}$$

$$\frac{\text{Tryp}}{\text{NADH}} = \frac{\text{Tryptophan}}{\text{NADH}}$$

$$\frac{\text{Tryp}}{\text{coll}} = \frac{\text{Tryptophan}}{\text{Collagen}}$$

For visible (405 nm) and for NIR (810 nm) spectral measurements, other three molecular ratios were extracted:

$$\text{Redox ratio} = \frac{\text{FAD}}{\text{NADH} + \text{FAD}}$$

$$\text{Optical index} = \frac{\text{Porphyryns}}{\text{NADH}}$$

$$\text{Ratio LP} = \frac{\text{Lipopigments}}{\text{Porphyryns}}$$

## Spectral Phasor

NIR spectral images acquired using 810 nm excitation were treated and extracted through ImageJ. In the spectral phasor analysis, the fluorescence emission signal of each pixel in the image was reduced to a “phasor” that is made up of two numbers: the real and imaginary parts of the Fourier transform of the fluorescence signal [339], [340]. These two numbers are used as coordinates in a histogram plot, known as the phasor plot. The grid of the figure covers the maximum emissions from the spectral range of 380–780 nm by 10 nm steps, and the spectral width varies from 20 to 100 nm by steps of 20 nm each. Using this method, we obtain one histogram for each sample imaged on the NIR setup. A global type histogram was plotted afterwards by adding all the histograms belonging to the same type. To obtain a better description and a better analysis of our spectra, we measured under the same conditions the fluorescence emissions of two standard fluorophores in solution: NADH (1 mM in Tris Buffer, pH=8.5, Grade I, disodium salt, ref: 10107735001 sigma aldrich) and FAD (1 mM in PBS, pH=7.4, Flavin adenine dinucleotide disodium salt hydrate  $\geq 95\%$  (HPLC), powder, F6625, sigma aldrich). These measurements facilitate the tracking on the phasor, with one point and one 95%-confidence Gaussian ellipsoid for each standard.

## Fluorescence lifetime and Phasor FLIM

Fluorescence lifetime measurements were realized using the Time Correlated Single Photon Counting (TCSPC) technique. For visible lifetime measurements data, lifetime decay curves were adjusted by a mono-exponential fit using fluofit software (PicoQuant, GmbH, Berlin, Germany). For an acceptable fit, the two criteria considered were: 1)  $0.8 \leq \chi^2 \text{ value} \leq 1.2$  and 2) residuals distribution around 0 within the interval +4 and -4.

In NIR, FLIM images data were acquired via Symphotime software (PicoQuant, GmbH, Berlin, Germany), the phasor technique was used to treat this data. The procedure of plotting the figure started by collecting the fluorescence decay curve of each pixel of a FLIM 3\*3 images mosaic of each sample, so for each sample we had nine FLIM images. For each FLIM image we selected, for 810 nm excitation, the signal of FAD filter ( $520 \pm 35$  nm) and the NADH filter ( $448 \pm 20$  nm), while for 890 nm we only selected the signal of FAD filter. Each image was also treated and extracted using ImageJ. Each FLIM image is constituted of  $512 * 512$  pixels, each pixel containing one decay curve. We reduced the size of each image from  $512 * 512$  to  $16 * 16$  pixels. So, the new reduced pixel has a real size of  $32 * 32 = 1024$  pixels. The decay curves of each 1024 pixels were added together to obtain one decay curve  $I(t)$ . The phasor approach was used to treat lifetime data where the decay curve  $I(t)$  of each reduced pixel is represented in a graphical view. This approach works in a new "space", each decay is represented by a unique vector, called phasor, in the “phasor plot”, and it have its unique location in the phasor plot [129], [131], [132]. Following the equations (7.7 and (7.8), each decay  $I(t)$  is converted into two coordinates in a Cartesian plot:

$$S_i(\omega) = \int_0^{\infty} I(t) \cdot \cos(\omega t) \cdot dt / \int_0^{\infty} I(t) \cdot dt \quad (7.7)$$

$$G_i(\omega) = \int_0^{\infty} I(t) \cdot \sin(\omega t) \cdot dt / \int_0^{\infty} I(t) \cdot dt \quad (7.8)$$

where,  $Si(\omega)$  and  $Gi(\omega)$  correspond respectively to the x and y coordinates of the phasor, and the index “i” identify a pixel of the image;  $\omega$  is the laser repetition angular frequency which is related to the sampling period ( $T_s$ ) and to the signal length ( $L$ ) using the equation (7.9):

$$\omega = 2\pi/(L \cdot T_s) \quad (7.9)$$

These sets of numbers provided the phasor histogram with the initial reduced 3\*3 mosaic image. Each reduced pixel of the FLIM image gives a point (or a count) in the phasor plot. After this procedure, the global phasor histogram was plotted. It grouped the phasor counts of all the samples and for each selected molecule. Then, the local maxima of the histogram was identified in order to draw the best fitting line. The two intersections between this line and the circle segment are linked to the two fluorescence lifetimes values [129]. A projection on the line of each phasor count (vector) was accomplished to calculate, for each type of tissue, the Long Lifetime Intensity Fraction (LLIF) marked with a symbol alpha ( $\alpha$ ) [129] in Figure 7.6, in order to estimate the similarities or the dissimilarities between the different tissue types. This parameter helps us to determine the fraction of fluorescence emitted by each component presented in our excited zone.

### Deep UV discriminative algorithm

Three molecular ratios (Tryptophan-Collagen, Tryptophan-NADH and Tryptophan-Tyrosine) were presented in the 3D-scatter plot of deep UV measurements for the three groups of tissues (Figure 7.2). The scatter cloud of each group was approached by a Gaussian ellipsoid using the mean and the standard deviation as parameters for the covariance with the ellipse to cover 60% of the total probability mass. The overlap volume between the three ellipses was then reported as a percentage to assess the performance of such an algorithm. A blind analysis was conducted, and the sensitivity (Se) and the specificity (Sp) of the discrimination criteria were calculated using the equation (7.10) and (7.11) cited below:

$$Se = \frac{TP}{TP+FN} \quad (7.10)$$

$$Sp = \frac{TN}{TN+FP} \quad (7.11)$$

where :

TP : True Positive, defined as tumoral tissue classified as tumoral.

FP : False Positive, defined as control tissue classified as tumoral.

TN : True Negative defined as control tissue classified as healthy.

FN: False Negative, defined as tumoral tissue classified as healthy.

### Statistical analysis

A student test (t-test) was performed for all molecular ratios data series to analyze statistically the different indicators statistically in order to obtain a p-value with a criteria of significance. On each boxplot figure, a table with stars “\*” icon indicator was displayed showing the p-value obtained comparing each couple of tissue type, where :

\* correspond to a p-value  $> 0.05$ .

\*\* correspond to  $0.01 < \text{p-value} < 0.05$

\*\*\* correspond to a p-value  $< 0.01$

A p-value  $< 0.05$  was considered as discriminating for two data series of two different tissue types.

## 7.2.3 Results

### 7.2.3.1 Deep UV

Concerning the UV spectral measurements, we used spectral measurements for 10 $\mu\text{m}$  thick control, and we used 275 nm as an excitation wavelength for LG and HG glioma samples. With these wavelengths, we can excite four molecules: Tryptophan (Tryp), tyrosine (Tyr), collagen (col) and NADH. A fitting process was then done for all obtained spectra to get different molecular ratios data. Figure 7.2 gathers the main results of the deep-UV study; it shows the possible discrimination extracted based on this excitation range. Three boxplots of three molecular ratios for the tissue types are displayed. Tryptophan/Collagen ratio is shown in Figure 7.2(a), Tryptophan/NADH ratio in Figure 7.2(b) and Tryptophan/Tyrosine ratio in Figure 7.2(c)

As shown, Control tissues were discriminated from tumoral tissues thanks to Tryptophan/Collagen and Tryptophan/NADH ratio, because the control tissues have a lower ratio than LG and HG glioma. Tryptophan/Tyrosine ratio could not discriminate control from tumor, but LG and HG can be separated with this ratio. Based on the observations of these ratios, a discrimination algorithm which combines these three ratios was applied to the spectral data and is displayed in Figure 7.2(d). So, each point in this 3D graph has three coordinates, which are the three molecular ratios cited above. Each cloud of points was then approximated by an ellipsoid giving an overlap between these groups, as shown in Table 7.6. As we can see in this 3D plot, control, and LG glioma ellipsoid overlap only 4% of the common volume, however, this percentage increases slightly to reach 14% between control and HG glioma ellipsoid. But this percentage increases sharply to reach 46% between HG and LG glioma. So, it is clear that this 3D algorithm discriminates between control and tumor tissues very efficiently, while it does not discriminate very well HG from LG glioma.

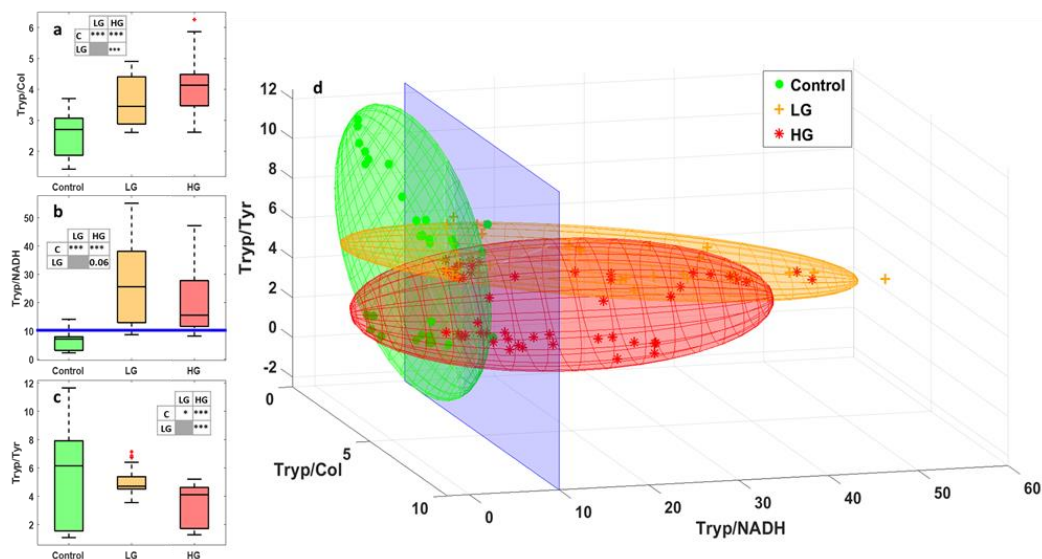


**Figure 7.2:** Analysis of the Deep-UV data. Boxplots of three molecular ratios acquired from spectral data under 275 nm excitation wavelength: (a) shows the Tryptophan/Collagen ratio, (b) shows the Tryptophan/NADH ratio and (c) shows the Tryptophan/Tyrosine ratio for control, LG, and HG glioma. The central mark in each box represents the median while the box edges represent the first and the third quartile, respectively. The tables recap the p-values corresponding to the t-test of a couple of values distribution (see statistical analysis). (d) represent the 3D-discrimination clouds of the three molecular ratios comparing control, LG, and HG glioma.

	<b>LG</b>	<b>HG</b>
<b>Control</b>	4%	14%
<b>LG</b>		46%

**Table 7.6:** Overlap volume percentage between the different ellipsoids

### 7.2.3.2 Visible

Concerning the visible spectral range, we used spectral and lifetime measurements for our three types of tissues. Figure 7.3(a) presents the mean emission of fluorescence spectra of control using LG and HG glioma samples under 405 nm excitation wavelength. At this wavelength, we excited five endogenous fluorophores highlighted in our study. Differences were noticed concerning the maximal fluorescence emission intensity of each type, and each type had its specific spectral signature which is interesting. Control presented higher fluorescence emission intensity that overlapped with the HG glioma spectra in the NADH, FAD and lipopigments emission range (centered at 445 nm, 520 nm, and 580 nm respectively). This overlapping disappeared in the porphyrins I and II emission range where the HG glioma spectra started to decrease and became lower than control spectrum. The lower fluorescence emission spectrum was observed in the LG glioma. In addition, by calculating the integral proportion of the emission contribution of each fluorophore using our homemade Matlab program, we plotted a histogram (Figure 7.3(b)) gathering the contribution of each molecule in the total of each tissue type. Unlike with our previous results on rats [97] and fixed tissues [215], when the contribution of all molecules was higher



in control tissues, the contribution of NADH and FAD seems to increase with the malignancy of the tissue, while they are lower in control tissues and higher in HG. Porphyrins I and II were almost similar to the three examined tissue types with no significant differences, except that the lipopigments are more present in the control samples.

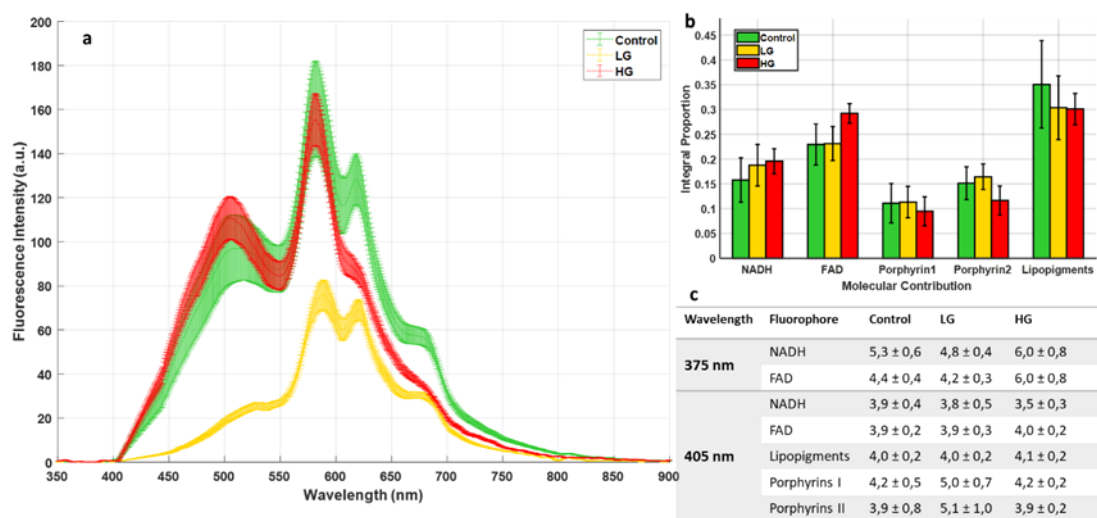


**Figure 7.3:** Analysis of Visible data. (a) shows the mean type spectrum of control, LG, and HG glioma under 405 nm excitation. (b) shows the Integral proportion of the five endogenous fluorophores: NADH, FAD, Lipopigments, Porphyrins I and Porphyrins II. (c) shows the average lifetime of the five endogenous fluorophores excited in each tissue type at 405 nm and for NADH and FAD excited at 375 nm.

For fluorescence lifetime measurements, another excitation wavelength of 375 nm was added. At this wavelength, only the lifetime values of NADH and FAD were considered. Lifetime values for each molecule at 375 nm and 405 nm are displayed in Figure 7.3(c). At 405 nm, the obtained lifetime values of NADH and FAD were similar to the three tissue types, even the lifetime values of the other molecules were similar, except the lifetime of porphyrins was found to be a bit higher in LG glioma than control and HG glioma. This similarity disappeared in the lifetime values of NADH and FAD at a 375 nm excitation wavelength, where HG glioma presents a higher lifetime value for these two molecules than for control and LG glioma. However, by using 375 nm as an excitation wavelength, we excite more efficiently NADH and FAD than by using a 405 nm wavelength, thus the population of excited NADH and FAD molecules increase, which improves the precision of the results and the obtained lifetime values.

The last analysis made on the visible spectral data was the exploitation of three molecular ratios. Redox ratio ( $FAD/(NADH+FAD)$ ), optical index ( $Porphyrins/NADH$ ) and ratio LP ( $Lipopigments/Porphyrins$ ) displayed in Figure 7.4(a, b, and c respectively). Looking at these boxplots, redox ratio and optical index discriminate significantly control tissues from low grade glioma ( $0.01 < p\text{-value} < 0.05$  and  $p\text{-value} < 0.01$  respectively), while the redox ratio only discriminate control from HG glioma ( $0.01 < p\text{-value} < 0.05$ ). Between LG and HG glioma, only the optical index discriminates these two tissue types ( $p\text{-value} < 0.01$ ).

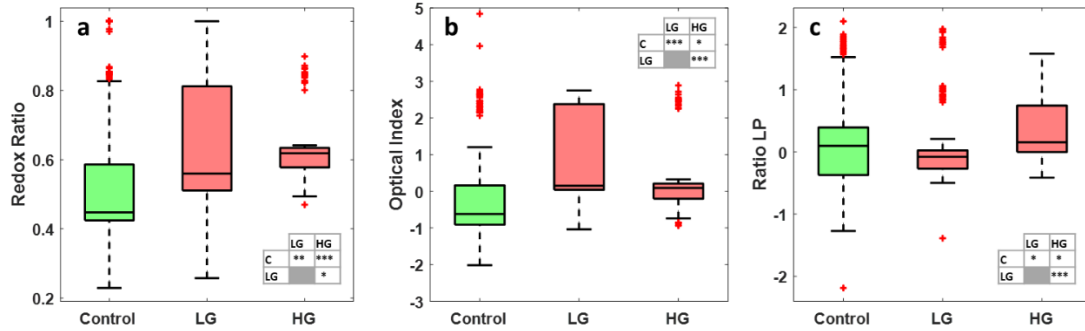


**Figure 7.4:** Boxplots of three molecular ratios acquired from spectral data at 405 nm excitation: (a) shows the redox ratio ( $FAD/(NADH+FAD)$ ), (b) shows the optical index (Porphyrins/NADH) and (c) shows the ratio LP (Lipopigments/Porphyrins) for control, LG glioma and HG glioma. The central mark in each box represents the median while the box edges represent the first and the third quartile, respectively. The values outside the box (red “+”) are considered as outliers. The tables recap the p-values corresponding to the t-test of a couple of values distribution. (see statistical analysis)

### 7.2.3.3 Near Infra-Red

The last spectral range in our study was the NIR. The data gathered under NIR excitation reflects the wide multimodality that is achievable through autofluorescence. Figure 7.5 assembles different images issued from 2PEF+SHG images, FLIM images and a comparison of these two imaging modalities with H&E histological images for each type of samples. This comparison shows the reliability of 2PEF+SHG and mostly FLIM imaging modalities as a diagnosis technique to provide similar information to those acquired from histological H&E images. Similar structures were noticed for each type in these three images. Control samples present a clear H&E image with a low cell density and some small vessels. These similar properties appear in a 2PEF image with strong red spots as well as in FLIM images where we observe spaced green spots. LG glioma presents a high cell density and a compact structure which appears clearly in the FLIM image where we observe a fluorescence carpet with some big spots. Big vessels and strong SHG emission characterize the HG glioma in 2PEF images and the same zone in blue on FLIM images which corresponds to a low fluorescence lifetime. This strong SHG emission can be a good indicator of tumor infiltration in a HG glioma sample, where the dense vascular network support tumor cell invasion.

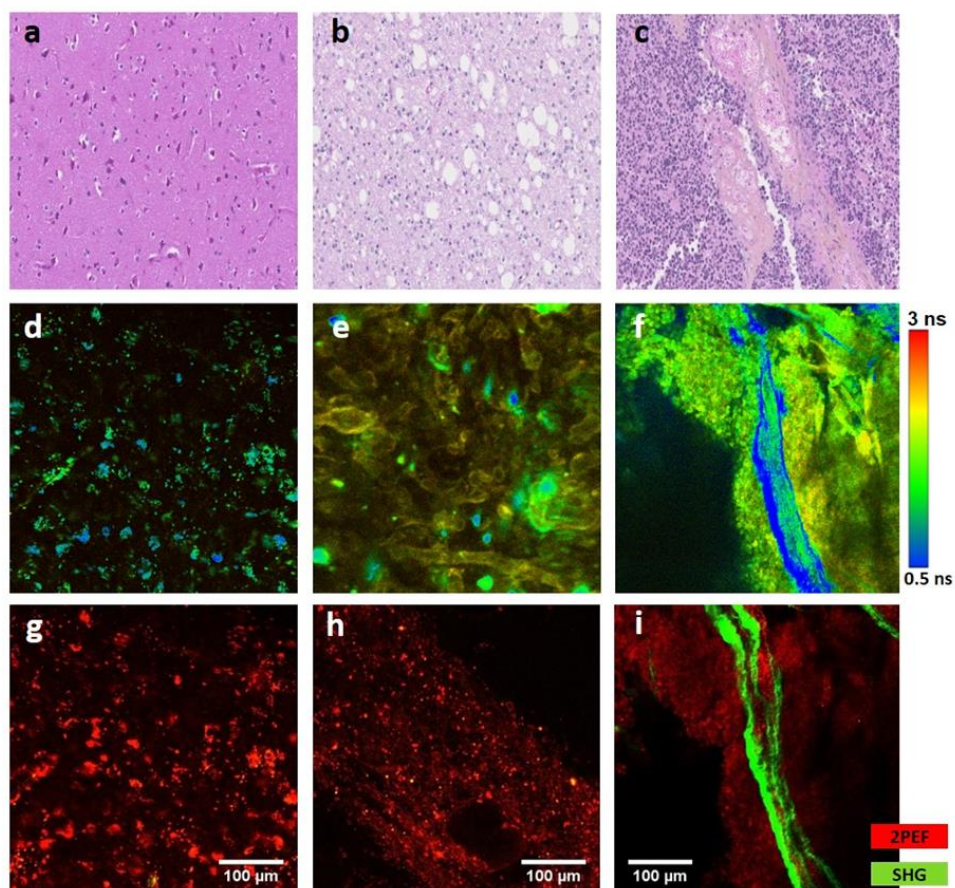


**Figure 7.5:** Image comparison through the NIR set-up showing a comparison between control (a,d,g), LG (b,e,h) and HG (c,f,i) glioma using different imaging techniques: Hematoxylin-Eosin staining Images (a,b,c) ; FLIM images acquired at 890 nm (d,e,f), color bar represents the lifetime value. 2PEF + SHG images at 890 nm showing 2PEF signal in red and SHG signal in green (g,h,i). Scale bar: 100  $\mu\text{m}$ .

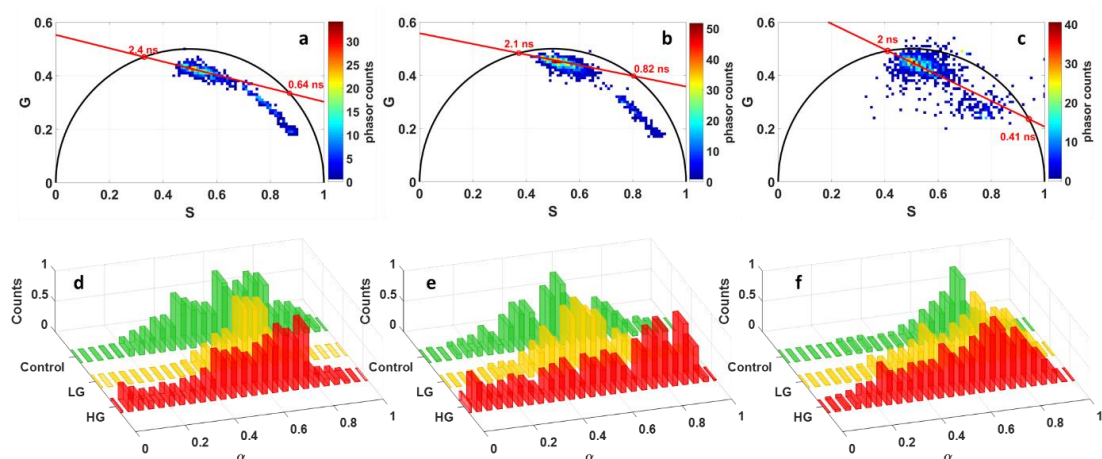


**Figure 7.6:** Phasor FLIM Analysis of NIR data. Global histogram of FLIM phasor plot (a,b,c) and Long Lifetime Intensity Fraction distribution ( $\alpha$ ) for Control, LG and HG (d,e,f) at 810 nm (b,c,e,f) at 890 nm (a,d) excitation for FAD (a,b,d,e) and NADH (c,f) channels.

Since FLIM images were clearly different for each tissue type, we decided to analyze the fluorescence lifetime through a non-fitting technique, the phasor FLIM. The Control, LG and HG glioma fluorescence decay curves taken from FLIM images data were grouped on different global phasor counts (Figure 7.6(a,b,c)).

The selected FLIM data was divided into two parts: NADH data acquired from channel 1 and FAD data acquired from channel 2. The global phasor FLIM histogram of FAD acquired at 890 nm excitation in all tissue types was plotted and is shown in Figure 7.6(a) while that which was acquired at 810 nm excitation was plotted and is shown in Figure 7.6(b). Using 810 nm as the excitation wavelength the NADH global phasor FLIM histogram in all tissue types was plotted and is shown in Figure 7.6(c). Then these global phasor FLIM histograms were used to plot the histogram of Long Lifetime Intensity Fraction (LLIF) ( $\alpha$ ) distribution of each molecule in each tissue type. The LLIF of FAD in each tissue type, which is acquired from 890 nm and 810 measurements, is shown in Figure 7.6(d) and (e) respectively. While the LLIF of NADH in each tissue type acquired from 810 nm measurements is shown in Figure 7.6(f).

Looking at the FAD LLIF histogram at 890 nm (Figure 7.6(d)), we noticed that HG glioma histogram shifted the most towards the lower LLIF values of FAD at 890 nm, while control samples shifted more toward higher LLIF values. In NADH LLIF histograms at 810 nm (Figure 7.6(f)), we noticed that the contribution of lower LLIF values is low in control samples where its histogram shifts sharply toward higher LLIF values. This contribution starts to be higher in LG glioma and reaches its height in the HG glioma histogram.

Moving to the spectral imaging results at 810 nm, the spectral phasor histogram for each tissue type was plotted and is shown in Figure 7.7 for control (Figure 7.7(a)), LG glioma (Figure 7.7(b)) and HG glioma (Figure 7.7(c)). Fingerprints of standard NADH and FAD measured in standard solutions were added to each phasor histogram respectively at 495 nm and 535 nm. The spectral phasor approach is used for spectral unmixing of fluorophore contributions in the spectral images. Regarding the three phasors shown, a maximum wavelength shift between the phasor clouds of each type was noticed. The control spectral phasor counts shifted toward an interval higher than the FAD fingerprint. In the LG glioma it was contained between NADH and the FAD fingerprint, while in HG glioma the phasor cloud was centered and close to the FAD fingerprint.

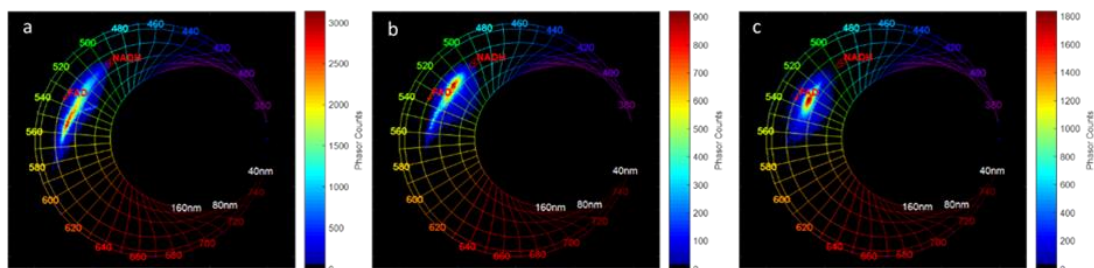


**Figure 7.7:** Spectral Phasor Analysis of NIR data at 810 nm excitation wavelength. Comparison of three spectral phasor histogram for: Control (a), LG glioma (b) and HG glioma (c).

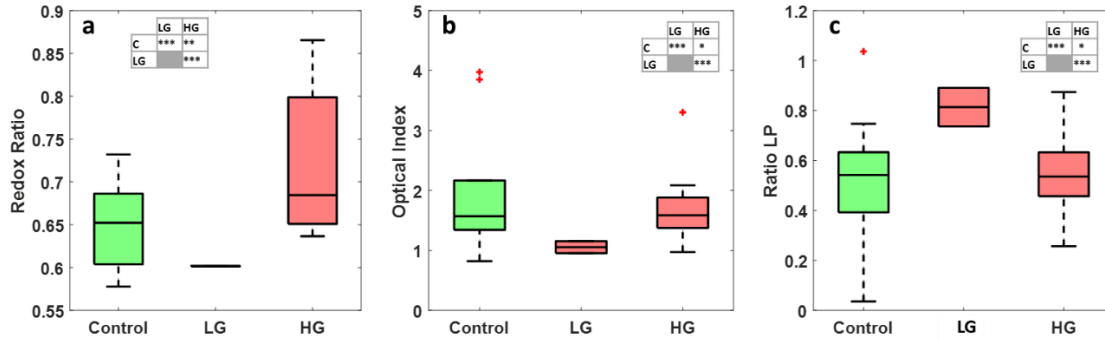


**Figure 7.8:** Boxplots of the three molecular ratios acquired from spectral images data acquired at 810 nm: (a) shows the redox ratio (FAD/(NADH+FAD)), (b) shows the optical index (Porphyrins/NADH) and (c) shows the ratio LP (Lipopigments/Porphyrins) for control, LG glioma and HG glioma. The central mark in each box represents the median while the box edges represent the first and the third quartile, respectively. The values outside the box (red “+”) are considered as outliers. The tables recap the p-values corresponding to the t-test of a couple of values distribution. (see statistical analysis).

Finally, molecular ratios were calculated for all tissue types at 810 nm excitation wavelength: Redox ratio (Figure 7.8(a)), optical index (Figure 7.8(b)) and Ratio LP (Figure 7.8(c)). Analyzing these boxplots, redox ratio discriminates significantly control from HG glioma. Optical index discriminates control from LG glioma, while the ratio LP discriminates control from LG and discriminates LG from HG glioma.

#### 7.2.3.4 UV-VIS-NIR discrimination

The last analysis consisted of combining three molecular ratios, each issued from a different spectral range in order to plot a discriminative 3D scatter cloud able to discriminate healthy from tumoral tissues, and LG from HG glioma.

For that we choose Tryptophan/collagen from deep UV spectral range as X axis. Redox ratio from NIR spectral range which as Y axis and redox ratio from visible (VIS) spectral range as Z axis. In order to get a 100% sensitivity, we did not take into account all the molecular ratio values in the distribution of each type, however, we took the median value of each distribution along with the first 5 values that were bigger than and the first 5 values that were smaller than the median value, and using these values we plotted our 3D scatter cloud as shown in Figure 7.9(a). So, in terms of median region values, control LG and HG glioma were clearly discriminated. Figure 7.9(b) represents the 3D scatter cloud with a different view angle than Figure 7.9(a), where a horizontal threshold plane was plotted ( $z=0.503$ ). This plane discriminates healthy from tumoral tissues. We acknowledge that if our scatter point is above this plane the tissue is tumoral, and if it is under it, the tissue is healthy. Figure 7.9(c) also represents the 3D scatter cloud with another view angle, where a vertical threshold plane was plotted ( $y=0.607$ ). This plane was plotted to discriminate LG from HG glioma tissues. We acknowledge that if the scatter point has a NIR redox ratio of less than 0.607, the sample is a LG glioma, and if it has a NIR redox ratio which is bigger than 0.607, it is considered as HG glioma tissue.

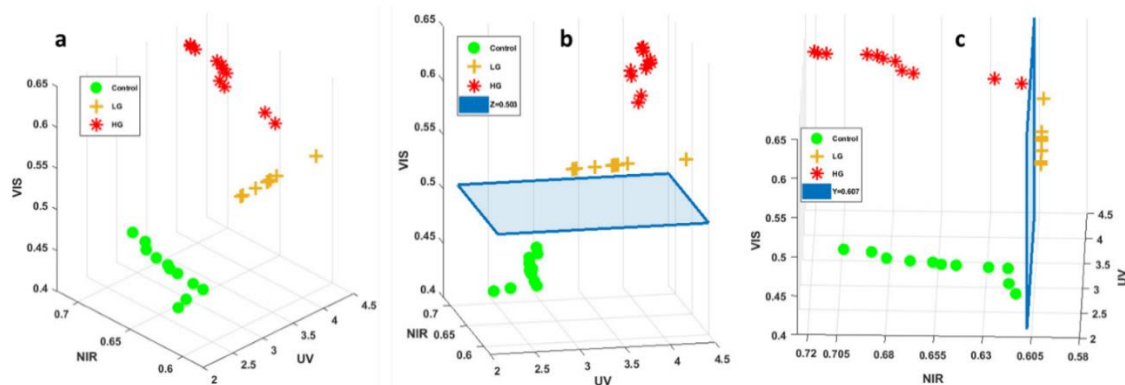


**Figure 7.9:** 3D scatter cloud of three molecular ratios : Tryp/collagen from UV as X axis (UV), redox ratio from NIR as Y axis (NIR) and redox ratio from Visible as Z axis (VIS). a) general view of the 3D scatter cloud of control, LG, and HG glioma. b) Right side view of the 3D scatter cloud showing the Control-tumor threshold plane ( $z=0.503$ ). c) Left side view of the 3D scatter cloud showing the HG-LG threshold plane ( $y=0.607$ ).

## 7.2.4 Discussion and conclusion

In this study, our main goal is to discover, analyze and achieve the best method to discriminate between healthy brain tissues, LG, and HG glioma tissues. Relying on the endogenous fluorescence of several molecules in brain cells, different excitation wavelengths were used, ranging from deep UV to NIR passing by visible wavelengths. Different imaging modalities on several setups and multiple methods of analysis were performed on our cohort of freshly extracted and fixed brain samples: control samples, low grade glioma and high grade glioma.

Few studies have used deep UV excitation to study the endogenous fluorescence emission of human tissues [341], [342]. Tryptophan is being considered as a good internal standard of tissue autofluorescence, the Tryptophan/Collagen and Tryptophan/NADH ratios could be considered as good indicator of cancer proliferation. Indeed, NADH redox state and propensity to bound to proteins affects its fluorescence level and was monitored for epithelial cells [342]. Moreover, under near-UV excitation, collagen fluorescence decreases in Barrett's esophagus versus normal epithelium [341]. Therefore, even if results obtained from single cells or endoscopy may not be directly related to biopsies results, those two balances (Tryp/Coll and Tryp/NADH) are good indicators of glioma. Pu et al. [343] for example, analyzed the Tryptophan and NADH principal components using 300 nm excitation. However, they only showed the preliminary study and used in-vitro cells. While Pradhan et al. analyzed the Tryp/NADH intensity ratio using 310 and 350 nm excitation and found this ratio higher in metastatic cell lines than in non-metastatic and normal cell lines, similar to our findings on glioma tissues. So, we proposed to calculate and analyze three molecular ratios related to the tryptophan molecule: Tryp/NADH, Tryp/tyrosine and Tryp/collagen. Tryp/collagen discriminates control from tumor, when control had a significantly lower ratio ( $p\text{-value} < 0.01$ ), however, Tryp/NADH presents the best results. A Tryp/NADH threshold value of around 10 could be defined to separate control from tumor (Figure 7.2(c)). Through these results, we built a 3D discriminative algorithm using the ellipsoids and the discrimination threshold value of Tryptophan/NADH ratio (Tryp/NADH), where the three molecular ratios values correspond to the 3 coordinates of

each point. We assumed that if the point is inside a tumor ellipsoid (HG or LG) and its Tryp/NADH is above 10, tumors can be detected and confirmed. With a low percentage of volume overlapping between control and tumor ellipsoids (4% control-LG and 14% control-HG), this test is not able to attribute a value for the percentage of points under 9 and has a sensitivity (Se) of 94% and a specificity (Sp) of 84%.

Concerning the visible spectral range, we conducted spectral and fluorescence lifetime analysis on our cohort. On the one hand, we explored the spectral properties of the fluorescence emission by comparing the molecular contribution of each fluorophore in each tissue type. On the other hand, we performed a fluorescence lifetime study using six band pass filters to select the specific emission spectral band of each fluorophore to measure the lifetime of each fluorophore separately. Each tissue type seems to have a specific spectral signature. We can particularly underline a difference in the fluorescence intensity between LG and control tissues. The lower fluorescence intensity in LG could be attributed to the angiogenesis, which is a high source of absorption [344] so less fluorescence is emitted and detected by our setup. The gap between control and tumoral tissues can be noticed as well after 600 nm.

Regarding the proportion of each molecule in the total spectra, the higher value of FAD and NADH in tumorous tissues indicates a higher malignancy. Even though, different studies have shown that the redox ratio decreases in tumor cells as compared to the norm [345], [346], we raised the problem that this ratio seems to decrease between control and low grade but at the same time seems to remain stable between control and glioblastoma. The prevalence of glycolytic pathway over oxidative phosphorylation might not be respected in non-invasive tissues due to the Warburg effect [347].

Lifetime values are not consistent with the literature on human brain samples [125], [126], however, the values remained in the same order of magnitude. As an example, Butte et al. [125], [126] investigated the evolution of the average lifetime in brain tissues as a function of the excitation wavelength. Under 375 nm and 405 nm excitation, they found an average lifetime of around 2.2 ns and 2 ns, respectively. It is twice as short as the values that we obtained. Nevertheless, they pointed out the fact that the average lifetime of the three types demonstrated a peak centered at 370-380 nm. We noticed that the average lifetimes are higher in the case of 375 nm excitation than at 405 nm excitation, as well. The Control and Glioma groups did not show significant differences.

The last and the wider spectral range in term of imaging modalities and analysis is the NIR. We performed three types of measurements on our samples cohort: 1) 2PEF + SHG detection imaging at 890 nm; 2) FLIM imaging at 810 nm and 890 nm and 3) Spectral Imaging at 810 nm excitation wavelength. In addition, H&E histological images were recovered from the neuropathology department in Sainte hospital to compare our images (Figure 7.5) with the gold standard technique of histological diagnosis. The similar structures observed in H&E, FLIM and 2PEF+SHG images is very encouraging. In control samples images, the classical cortical arrangement of neurons with a low cell density is visible through clear fluorescent and spaced red spots on the 2PEF and FLIM images. In LG glioma samples, we observed some holes in H&E images due to cysts, a cell density higher than control noticed in 2PEF images and a more compact tissue structure observed in FLIM image. In the HG glioma samples, a very high density of tumor cells, identified in

H&E image, surrounds an enlarged vessel observed in 2PEF image by its strong SHG emission (Green) and its lower lifetime in FLIM image (Blue).

The phasor approach shown in this work has the potential to simplify the analysis of FLIM, avoid the fitting errors associated with mono-exponential or multi-exponential analysis, and to give a graphical global view of the processes which affects the fluorescence decays occurring at each pixel in the FLIM image [131], [132].

In the FAD channel, the phasor FLIM histogram at 810 nm and 890 nm excitation wavelengths were similar. Free FAD lifetimes were slightly close (2.4 ns for 890 and 2.1 ns for 810 nm) but protein-bound FAD lifetimes were different (0.64 ns at 890 nm and 0.82 ns at 810 nm). We observed that the HG glioma LLIF histogram of FAD was the only histogram which is shifted to lower LLIF values. Based on this observation, we assumed that there is more protein-bound FAD in glioblastoma tissues than control ones. While in the NADH channel, the calculated free and protein-bound NADH lifetime were respectively 0.4 ns and 2 ns. We also noted that the LLIF repartition shifted to the Lower LLIF values according to the tumor grade. So, it seems that the contribution of free NADH increases with the malignancy of the tissue. Thus, it can be assumed that the higher grade gliomas increases free NADH concentration. All of these results are in line with the study of Skala et al. [93]. In their study, FAD and NADH lifetimes were in the same order of magnitude. They also noticed that the proportion of protein-bound FAD and NADH decrease with the grade.

In addition to the FLIM phasor analysis, spectral phasor analysis is applied also to the data issued from spectral images at 810 nm for each tissue type. This technique is a fast and representative way to extract two characteristic parameters from a spectrum that are related to the maximum emission wavelength and the width of the spectrum. It can also be used to separate the contributions of the different fluorophores presented in one fluorescent sample. With this in mind, we decided to apply the method as a standard. NADH (1 mM in Tris Buffer pH=8.5) and FAD (1 mM in PBS pH=7.4) were tested and converted as points, respectively at 495 nm and 535 nm on the phasor plot (Figure 7.7).

We noticed that these values are red-shifted in comparison with the values in brain tissues we have recovered from the literature. (see spectral fitting). The difference is less significant for FAD than for NADH. despite this, it could be clarified by the spectral red-shift of free form from bound form of the fluorophore [348]. First of all, higher phasor counts on all types (of tissues) which are located on a straight line crossing NADH and 580-600 nm (Lipopigments, Porphyrins). Spectrum shapes are quite different for each tissue type because the peak of low and high grade glioma is closer to NADH, while it is closer and even farther from FAD fingerprint. The lack of information from any previous work using this method, makes a comparison to literature more difficult. Nevertheless, these results are in line with the observations under visible excitation. Furthermore, a widening of the Gaussian ellipsoid and, consequently, of the spectral bandwidth sets the tumoral tissues apart.

Finally, we gathered our molecular ratios results derived from the different excitation wavelength, in order to plot a multiscale discrimination algorithm with a 100% sensitivity able to, on the one hand discriminate control from tumors, and on the other hand to discriminate LG from HG glioma. We, therefore, choose the best discriminator molecular ratio from each spectral range excitation, considering the median range values. Tryp/col



was chosen from deep UV, redox ratio from Visible and redox ratio from NIR measurements. Then a 3D scatter cloud was plotted (Figure 7.9). What we obtained, relying on the median values range of each molecular ratio, is very interesting. Each scatter cloud of each type was separated from every other scatter cloud, which means a 100% sensitivity. A threshold was then defined to discriminate healthy from tumor ( $z=0.503$ ) and another one to discriminate LG from HG glioma ( $y=0.607$ ). So finally, we can admit that if a sample has a visible (VIS) redox ratio  $< 0.503$ , it is considered as a healthy tissue. If the sample has a VIS redox ratio  $> 0.503$  and a NIR redox ratio  $< 0.607$  it is considered as a LG glioma, and if the sample has a VIS redox ratio  $> 0.503$  and a NIR redox ratio  $> 0.607$  it is considered as HG glioma.

Throughout our study, we have brought new approaches to analyze the endogenous fluorescence of different human brain tissue types ranging from deep UV to NIR. Regarding our results, we can conclude that using a large panel of contrast sources is essential in order to achieve the best discrimination between tumor and healthy tissues and between the different grades of the same tumor type. Moreover, this study highlights numerous discrimination criteria between healthy and different grade tumor tissues. The combination of different quantitative and qualitative measurements of fluorescence microscopy allowed us to reach this goal. But there is still a lack in the number of collected data. A larger database would be crucial in the future in order to build a more robust analysis program with different discrimination thresholds and particularly through NIR-Visible molecular ratios where the set of values of these ratios was not robust enough to discriminate control from tumor and to offer a sensitivity and a specificity higher than 80%.

We are currently enriching our optical database with more biopsied samples. A sample size larger than 50 was enough to differentiate between primary and secondary brain tumors, with a sensitivity of 97% and a specificity of 100% based on the Optical Index ratio, the redox ratio and the mean lifetime value [98]. Since the morphological and metabolic difference in low grade glioma vs. normal and low grade glioma vs. high grade glioma is more subtle (figure 7.5, for instance), we expect that a sample size larger than 50 is necessary to obtain clinically useful statistical significance. In fact, a power analysis was performed for the three ratios used in the UV-visible-NIR study to determine the sample size necessary to test whether these ratios (Tryptophan/Collagen, visible redox ratio, and NIR redox ratio) were statistically different for each pathology by setting the type I and II error at 0.05 and 0.2 respectively [349]. Interestingly, the Tryptophan/Collagen ratio required the lowest number of samples to reach statistical significance, while the visible redox ratio needed the highest number of samples. Specifically, 107 samples were required to compare healthy tissue with LG glioma, while only 35 samples were needed to compare healthy tissue with HG glioma. As one would expect, more samples are needed to discriminate between HG and LG glioma, specifically 118 samples. For this reason, the sensitivity and specificity values were not calculated for the NIR and visible data.

The final objective is to apply this technique in real-time during surgical resection, so that the tissue can be analyzed immediately in a way to facilitate the resection. This study brings us closer to our goal and opens the door for a pilot in vivo study.

In tandem to constructing an optical database based on one- and two-photon fluorescence excitation and on multiscale detection, a nonlinear endoscope prototype is being optimized with imaging capabilities. The custom-built fibered endoscope is already capable of

generating excitation pulses below 100 fs delivered to the distal end of a 5-meter-long microstructured double-clad photonic crystal fiber [173]. A miniature MEMs system is being incorporated to extend the endoscope's capabilities to perform spatially- and depth-resolved imaging. Visible and NIR excitation is possible with the non-linear endoscope and thus results pertaining to both regimes can be directly translated to future in vivo measurements, where NADH, FAD, lipopigments and porphyrins I & II are the molecules of interest. DUV excitation on the other hand, was useful to highlight the properties of other endogenous fluorophores that play a role in malignant transformation such as collagen and tryptophan. Although, the enhanced SHG signal observed in brain tumors is known to result from increased disorganization of collagen fibers in the extracellular matrix facilitating invasion, spectral analysis of the autofluorescence spectra under DUV excitation [214] informed us that collagen levels themselves are elevated according to tissue grade. This further supports the hypothesis that the high SHG signal in Figure 7.5(i) signifies tumor infiltration.

So, in summary, the three excitation regimes provided complimentary properties that histologically characterize healthy brain tissue, low and high grade glioma. The quantitative parameters derived from visible and NIR excitation will be directly measured with the multimodal endomicroscope so that in situ tissue discrimination beyond the solid tumor will be possible. This is paramount for delineating diffuse LG, which is not feasible under conventional 5-ALA fluorescence. Specifically, since the endomicroscope is equipped with two-photon imaging, TPEF/SHG images at the submicron resolution is expected to identify isolated tumor cells that have infiltrated the parenchyma within the field of view, either during open surgery after macroscopically complete surgical removal of the tumor, or during biopsy procedure, using an optic fiber mounted biopsy forceps. Additionally, tumor microenvironment supporting tumor invasion and infiltration can be differentiated from that of non-infiltrated brain parenchyma by the former's high SHG signal from dense vasculature.

## Chapter 8

# Could quantitative multimodal and multiscale optical analysis discriminate grade I and grade II meningioma from healthy brain tissues

### 8.1 Context of the study

In continuity of the challenge presented in the previous that consists of specifying our tissue database, we are interrogating in this chapter the different grades of meningioma tumor. This type was categorized into two categories: grade I meningioma and grade II meningioma.

Although meningioma is the most diagnosed common central nervous system tumor. It is a slow-growing tumor derived from the meningeal membrane that covers the brain and the spinal cord [25]. Because of its slow growth, an early diagnosis, that is, delineating invasive borders of meningioma from healthy zones, can significantly impact prognosis. Additionally, performing a differential diagnosis, i.e., differentiating between grade I and grade II, allows for the optimal choice of treatment [25]. We have tackled this objective before in a qualitative previous study of our group by comparing the TPF + SHG imaging findings in meningioma grades [216]. In that study, TPF + SHG images from meningioma grade II showed strong SHG emission from solid perivascular and interstitial collagen structures, which sometimes converged into large acellular zones. Meningioma grade I samples revealed spindled tumor cells forming parallel and interlacing bundles in a various amount of intercellular collagen rich matrix. Control samples displayed uniform red fluorescence with minimal SHG signal. The strong SHG signal observed in these samples have been attributed to the collagen-rich dense vascularized structures that seemed increasing with malignancy. Through these observations, it was interesting to focus on investigating quantitatively the collagen presence in grade I and grade II meningioma, in order to achieve a robust differentiation and a specific discrimination.

Therefore, the motivation of this study arise from the need to expand on the previous study using more robust quantitative analysis along with the molecular information provided through DUV excitation that can complement the imaging findings observed using NIR excitation. Molecular ratios extracted using DUV domain showed the most significant discriminations between the tissue type that were interrogate in the previous chapter. Furthermore, exciting tissue at 275 nm allows investigating the contribution and changes of the collagen fluorescence emission that occur during malignancy and to be correlated with their SHG emission when exciting in NIR domain which corresponds to the degree of vascularization. Indeed, tryptophan, for example, may correlate with the degree of phosphorylation related to cell growth, proliferation, and transformation [214], [338].

**Methods** A cohort of forty-nine fresh samples was provided by Sainte-Anne Hospital. NIR measurements were performed using a multiphoton benchtop microscope on 24 control samples, 14 meningioma grade I, and 11 meningioma grade II samples. DUV measurements were performed at Synchrotron Soleil within the DISCO beamline widefield fluorescence imaging and spectroscopic platforms, where 10 control samples, 7 grade I and 8 grade II meningioma samples were imaged.

This study follows similar quantitative analysis performed on the glioma study detailed in the previous chapter. That is, the spatially and spectrally resolved fluorescence measurements were produced from DUV and NIR excitation. The quantitative discrimination indicators were extracted from the spectra acquired at 275 nm and 810 nm excitation. Similar to the glioma grade specification study presented in the previous chapter, spectral phasor, phasor FLIM and LLIF extraction were applied to exploit the autofluorescence variation at a molecular level in order to differentiate the different interrogated tissue types.

**Results and conclusion** Spectral analysis at 275 nm showed the changes in the contribution of tryptophan and collagen corresponding to each tissue group. Similarly, spectral phasor analysis at 810 nm highlighted the different fluorophore contributions (NADH, FAD, Lipopigments, and Porphyrins) present according to each pathology. Phasor FLIM analysis provided more specific information on the different metabolic properties since changes in the relative protein-bound to free NADH and FAD can be characterized for each tissue group based on their short and long fluorescence lifetimes. Finally, a 3D discriminatory algorithm was applied to evaluate the ability to differentiate between control vs. meningioma and between the two grades based on quantitative indicators related to collagen density within each tissue type.

Overall, there is a linear trend in the total fluorescence signal, fluorescence lifetime, and in the molecular ratios as a function of pathology. This trend is in contrast to what we observed in the low and high-grade glioma discrimination study, possibly because of the heterogeneous nature of glioma. Specifically, the overall DUV fluorescence spectrum, the Tryp/Collagen ratio, and the Tryp/NADH ratio decrease linearly with increasing malignancy. The spectral phasor analysis and the above results point toward the prevalence of collagen and NADH in the malignant tissue. In the NIR domain, the decrease in the PN ratio (The same OI ratio in glioma study) and the increase in the LP ratio indicated an overall decline in the porphyrins and Lipopigments content with increasing grade. Phasor FLIM analysis of the samples after 810 nm excitation showed that the fluorescence lifetime of NADH and FAD decrease with degree of malignancy, and the global LLIF values had the opposite trend. The latter suggests protein-bound NADH is dominant in malignant tissue.

Finally, a 3D discrimination algorithm was used and based on collagen related indicators: the SHG integral proportion (SHG-Int), the integrated collagen content (coll-Int), and the collagen emission maximum intensity peak (coll-peak). This algorithm provided robust tissue discrimination between control vs. tumor with sensitivity and specificity rates of 100% and 90%, respectively, and between grade I meningioma and grade II meningioma with sensitivity and specificity rates of 94.7% and 95 %, respectively.

To conclude, we were able in this chapter to quantitatively track different molecular transformations driving pathogenesis in the meninges by using two different complementary imaging methods to sample the different endogenous fluorophores found in brain tissue: DUV excitation with spectral analysis and NIR excitation with spectral and lifetime analysis. Significant quantitative parameters were found that divide the three tissue groups, mainly based on tracking collagen density and metabolic markers (NADH and FAD). The thresholds extracted from these parameters were summarized in table 8.1 below. Furthermore, the strong SHG signal seen in meningioma exactly correlates with the increase in collagen content based on the DUV spectral analysis.

<b>Quantitative Indicator</b>	<b>Control</b>	<b>Grade I meningioma</b>	<b>Grade II Meningioma</b>
<b>Relative Collagen Content (a.u)</b>	$\leq 28$	$\geq 28$	$\geq 43$
<b>Relative SHG content (a.u)</b>	$\leq 2.5$	$2.5 \leq \text{SHG-Int} \leq 22$	$\geq 22$
<b>Protein-bound NADH Lifetime (ns)</b>	$\geq 2.1$	$1.9 \leq \tau \leq 2.1$	$\leq 1.9$
<b>Protein-bound FAD Lifetime (ns)</b>	$\leq 0.7$	$0.7 \leq \tau \leq 1$	$\geq 1$

**Table 8.1:** Summary of the significant quantitative discrimination thresholds obtained in this chapter to differentiate healthy, grade I and grade II meningioma

## 8.2 Paper: Molecular changes tracking through multiscale fluorescence microscopy differentiate Meningioma grades from healthy brain tumor tissue

Accepted for publication in scientific reports journal.

### 8.2.1 Introduction

Being one of the most common cancer that affects humans, Central Nervous System (CNS) tumors are the deadliest and have the lower survival rate compared with other cancer types [350]. Numerous types of CNS tumors exist, they are classified into different categories referring to their originating cell and to their pathological class [19]. Meningioma, known also as meningeal tumors, are one of the most frequently diagnosed primary CNS tumor, they present more than 30% of all CNS tumor cases [25], [350]. This type is a slow growing tumor which derives from arachnoidal cap cells in the meningeal membranous layers, covering of the brain and the spinal cord, also known as the meninges [25]. In the last edition of WHO classification of CNS tumors (2016) [19], meningiomas were classified into three major groups which differ in grade and biological behavior: Grade I, a benign tumor recognized by its histologic subtype and the absence of anaplastic features; Grade II, an atypical tumor known by its chordoid histologic subtype, its invasive development towards brain, surrounding dura matter and that sometimes reaches the skull bone; and Grade III, a rare tumor with about 1-6% of the diagnosed meningiomas being grade III [25], is known as an anaplastic tumor and the most malignant grade defined by its rhabdoid subtypes and a very high rate of mitoses [23].

These aggressive subtypes of tumors expose faster tumor progression, invasiveness and recurrence [351]. However, even benign meningiomas commonly invade adjacent anatomical structures, especially the dura matter, although the rate and extent of local spread are often greater in the more aggressive subtypes [25]. Thus, depending on location and grade, some benign meningioma types can become deadly and fatal, due to their progressive growth in the skull, if they are not treated or excised quickly [25], [350].

For initial diagnosis, contrast CT scan, MRI with gadolinium contrast and arteriography are the modalities of choice, due to the fact that meningiomas are extra-axial and present a dense vascularized tissue structure. After imaging (CT or MRI), a biopsy is performed to confirm the diagnosis. After diagnosis confirmation, the standard therapeutic indication is a total surgical resection followed by chemotherapy and radiotherapy treatments for aggressive subtypes [352]. Despite this aggressive treatment, the mean overall survival is dismal for patients suffering from aggressive meningioma tumors.

During surgery, the neurosurgeon aims to remove the entire solid tumor detected by MRI. However, recurrence rate has been shown to correlate with the extent of tumor resection [351], [352]. This correlation was presented by Donald Simpson which described a grading system that has been validated for recurrence rate prediction in grade I-III meningioma [353].

To improve the quality of resection, many intraoperative tools have been implemented to help the surgeon with their work such as Intraoperative MRI and neuro-navigation [280] or operating microscope [298], which offers a global view of the surgical cavity with a clear visualization and improves the determination of anatomical structures.

However, these techniques are resource intensive and time consuming. They can't offer sufficient information on the histopathological nature of the examined region on a subcellular scale, or to provide a real-time multiple information on dural infiltration and extrinsic brain invasion, in order help the neurosurgeon to achieve a gross total removal of all the tumor volume [216]. While the histopathological analysis, based on Hematoxylin and Eosin (H&E) staining, is still the standard used technique to acquire a specific and exact diagnosis, this analysis intervenes after the operation and takes several days to provide the final confirmed diagnosis response.

On the other side, advanced optical imaging such as confocal microscopy and optical coherence tomography (OCT) present advanced bio-imaging capabilities with cellular and subcellular level resolution for in vivo imaging applications such as optical biopsy or in vivo brain imaging in animals [354], [355]. In addition, Two-Photon Microscopy (TPM) provides high-resolution (submicron) imaging with lower phototoxicity and deeper penetration depth in tissues [354], [355].

Tracking of endogenous fluorophores and their fluorescence signal has been widely developed to explore the optical features of cancerous brain tissue, in order to discriminate tumoral from healthy tissues [85], [302] or to discriminate healthy tissues from tumoral and infiltrating tissues [85].

Excited in Near Infra-Red (NIR) through two-photon excitation, the auto-fluorescence of several endogenous molecules has been studied to understand and track the metabolism of tumor tissues. The Nicotinamide Adenine Dinucleotide (NADH) and the Flavins (FAD) with their related metabolic ratios can provide reliable information on tissue metabolism [82], [84], [85], [89]. These ratios have also shown their ability to be an efficient discriminative indicator in order to discriminate properly between healthy and tumoral tissues in bladder [96], breasts [334], and brain tissues [98], [215].

The fluorescence lifetimes of these fluorophores have also been investigated to explore the variation of this quantitative parameter in cancerous tissues. The phasor approach used in a past study has shown its reliability to track the chemical state variation (free and protein-bound) of NADH and FAD in high and low grade glioma [270].

Excitation in Deep UV (DUV), efficient to expose the auto-fluorescence of bio-macromolecules such as tryptophan and collagen crosslinks, provides an additional marker for monitoring cellular and metabolic status [270], [338]. It highlights the fluorescence of several fluorophores that do not fluoresce if excited in visible or NIR [338] which constitute a good base to correlate the auto-fluorescence of all these fluorophores. While collagen crosslinks fluoresce in DUV, the collagen polymers are a strong source of Second Harmonic Generation (SHG) signal when using NIR excitation, indicating the presence of vascularized structures. So, using NIR excitation wavelength and correlating with DUV excitation, the ability to relate the fluorescence response of this molecule with its SHG emission will improve the robustness of our markers and the determination of the metabolic alteration and the structural variation in cancerous tissues.

To this end, and to answer the neurosurgeon needs, a two-photon fluorescence endomicroscopic probe is under development in our laboratory. It relies on the endogenous fluorescence of cerebral tissues to offer a multimodality of contrasts: Two-Photon Fluorescence (TPF) imaging, Second Harmonic Generation (SHG) imaging, Fluorescence Lifetime Imaging (FLIM) and Spectral analysis. This multimodality will bring more

reliability and will increase the sensitivity and the specificity of our imaging tool. Additionally, this endomicroscope will be able to perform a fast diagnosis acquisition and to provide a sub-cellular resolution information on the examined tissue. Compatible with the surgeon trocar, it will be able to perform an optical biopsy diagnosis, so a pre-surgery diagnosis test which will improve the ability of the surgeon to choose the optimal therapeutic management of the tumor.

In parallel to the instrumental endomicroscope development, we are building a large tissue database, that will be integrated in the endomicroscope. These specific multimodal signatures will help obtain robust optical discrimination factors between healthy and cancerous tissues. In past studies, and in the context of our database using multiscale excitation, we managed to discriminate quantitatively and qualitatively healthy tissues from primary and secondary tumors [97], [98]. We managed also to discriminate low and high grade glioma [270] through tracking molecular changes in both types of tumors. Concerning meningioma, we have conducted a study to discriminate grade I and grade II meningioma qualitatively through TPF imaging at NIR excitation analysis [216]. In this work, we aim to complete this preliminary study and to apply our new quantitative advanced analysis methods to robustly discriminate grade I and II meningioma tissues from healthy ones. For that purpose, we added the deep UV excitation range to combine its results with visible and NIR ones. We have multiplied the discriminants by focusing on the collagen variations observed in different grades, adding molecular ratios, indicators, and thresholds and by using advanced analysis method for spectral and lifetime results. Full field imaging and spectral analysis were conducted using deep UV excitation range to study the fluorescence response of the tryptophan and collagen crosslinks in order to relate its fluorescence emission with its Second Harmonic Generation (SHG) emission at NIR excitation. In addition, Phasor approach were applied to investigate the fluorescence lifetime of NADH and FAD and to track their chemical state variation.

## 8.2.2 Materials and methods

### 8.2.2.1 Samples

In cooperation with the neurosurgery and the neuropathology department of Sainte Anne hospital (Paris), 49 fresh samples from were acquired according to the approval of the Sainte-Anne Hospital – University Paris Descartes Review Board (CPP Ile de France 3, S.C.3227). All methods were carried out in accordance with the relevant guidelines and regulations of this approval and informed consents were obtained from all patients. For NIR measurements we used a samples cohort which consisted of 14 grade I meningioma, 11 grade II meningioma and 24 control samples obtained from epileptic surgeries, while for DUV measurements the number of samples were 10 control, 7 grade I and 8 grade II meningioma samples.

After the surgery, each sample was directly sent in a normal saline solution to the neuropathology department where our visible endoscope is located. After the acquisition of the spectral measurements, the sample was sent to the IMNC laboratory (Orsay-France) where our NIR excitation multimodal setup is located. After the NIR excitation measurements, these samples were stored at  $-80\text{ }^{\circ}\text{C}$ . For deep UV measurements, the samples were put at  $-18\text{ }^{\circ}\text{C}$  few hours before to be prepared to cutting, after that, and using



a cryostat (CM 1950, Leica Microsystems), they were cut into 10  $\mu\text{m}$  slices then fixed with ethanol (100°C) and stored at 4 °C until experimentation. These fixed slices were then used for full field imaging and spectral measurements on the Deep UV setup at DISCO Beamline.

### 8.2.2.2 Deep UV excitation setup

Deep UV spectral measurements were carried out on DISCO beamline [356] at Synchrotron SOLEIL (Saint-Aubin, France). On this beamline, spectral and full-field imaging measurements were performed using 275 nm as excitation wavelength. The experimental setup consists of a full-field microscope (Zeiss Axio-observer Z-1) to acquire images and a micro-spectrofluorimeter (Olympus IX71) to perform spectral measurements.

For each sample, a large mosaic was selected to perform Tryptophan + Collagen full field imaging acquisitions. Two band-pass filters, (1) 323-357nm and (2) 408-438nm (Semrock, USA) were serially positioned in front of a CCD camera (Pixis BUV, Princeton Instrument, USA) to select respectively the fluorescence signal of tryptophan and collagen.

The obtained full field images were reconstructed and merged through an open source-image-processing software “FIJI”. Afterwards we used Masson’s trichrome (MT3) model to generate virtual stained images from the merged Tryptophan + collagen images. This model consists of a deep-learning-based virtual histology staining method of label-free human tissue samples [357].

The network models for Masson’s trichrome (MT3) stain alongside sample test-image data are available through a Fiji-based plugin [357]. This plugin is publicly available and can be downloaded through DeepImageJ website in bundled models’ section: <https://deepimagej.github.io/deepimagej/models.html>.

For spectral measurements, several Regions of Interest (ROI) in the acquired mosaic were then selected to perform spectral measurements through the micro-spectrofluorimeter. Each ROI have a size of 160x160  $\mu\text{m}$  with 4  $\mu\text{m}$  as pixel size. From each pixel, the collected spectrum is the sum of the fluorescence emission of four endogenous fluorophores: Tyrosine, tryptophan, collagen and NADH.

### 8.2.2.3 Multimodal NIR excitation setup

This multimodal setup is able to perform four different optical imaging modalities: (1) TPEF imaging, (2) two-photon spectral imaging, (3) SHG imaging and (4) two-photon Fluorescence Lifetime Imaging (FLIM) measurements. It consists of a Mai Tai DeepSee Ti:Sa laser (Spectra-Physics, Santa Clara, USA) tunable from 690 nm to 1040. This laser is able to deliver a 70 fs laser pulse duration due to its automated dispersion compensation with 2.4 W as average power at 800 nm. It is coupled with a TCS SP8 MP benchtop microscope (Leica Microsystems, Wetzlar, Germany) to perform confocal two-photon microscopy through a water-immersion Leica objective (HCX IRAPO L 25X NA 0.95). In addition, a FLIM module from PicoQuant (GmbH, Berlin, Germany) is integrated this benchtop microscope which uses Time Correlated Single Photon Counting (TCSPC) technique to carry out the FLIM acquisition through its dedicated software (Symphotime, Picoquant, Germany). The collected fluorescence signal is split by a dichroic cube (FF495-Di03-25  $\times$  36, Semrock, New York, USA) and collected into two detection channels. Each one contains a supersensitive Leica hybrid non-descanned (HyD NDD) detector. In the first detection channel (channel 1) a 448 nm centered band pass filter (FF01-448/20-25, Semrock,

USA) was introduced, while in the second detection channel (channel 2), a 520 nm centered band pass filter (FF01-520/35-25) was introduced.

The TPEF + SHG images acquisition were performed using 890 nm as excitation wavelength. Using this wavelength, the channel 1 allows to select the SHG emission signal while the channel 2 allows to select the FAD emission signal. These images were acquired through the microscope dedicated Leica software (LAS-X) and then reconstructed through the open source-image-processing software “FIJI”.

FLIM images acquisition were performed using 810 nm as excitation wavelength. Using this wavelength, the channel 1 allows to select the NADH emission signal instead of SHG, while the channel 2 always selects the FAD emission signal.

For spectral imaging acquisition, and instead of using channel 1 and channel 2, an internal hybrid detector was used. It covers a detection range from 380 nm to 790 nm with 10 nm as chosen spectral resolution, which remains to a total of 41 images for each acquisition.

### 8.2.2.4 Data analysis

#### DUV spectral analysis

DUV Spectral data processing was conducted using a matlab interface developed in DISCO beamline at Soleil synchrotron, based on matlab data processing codes used in several previous works [215], [270].

The excitation under 275 nm highlight the fluorescence emission of four fluorophores: tyrosine (tyr), tryptophan (tryp), collagen (coll) and NADH. For each collected spectra, a spectral fitting process was performed to extract the emission contribution of each fluorophore. This emission was represented by a gaussian fit whose maximum wavelength and spectral bandwidth follows the values shown in table 8.2, DUV section. An example of a fitted DUV spectrum is shown in figure 8.1(a).

Through this spectral fitting process, the Integral proportion (Int) of each fluorophore emission can be determined. It is defined as the ratio of the integral under the emission curve of the fluorophore contribution on the integral under the total fitted spectrum curve. Rationing the different calculated integral proportion, we were able to extract three different DUV molecular ratios:

$$\text{Tryp/Tyr} = \text{Tryptophan-Int/Tyrosine-Int} \quad (8.1)$$

$$\text{Tryp/NADH} = \text{Tryptophan-Int/NADH-Int} \quad (8.2)$$

$$\text{Tryp/coll} = \text{Tryptophan-Int/Collagen-Int} \quad (8.3)$$

#### NIR spectral analysis

NIR Spectral images were extracted first using the image processing software “FIJI” and then processed using a homemade Matlab interface for molecular ratios extraction and for phasor plot analysis.

For spectral phasor analysis, the fluorescence spectrum of each pixel in each spectral image was recovered. Two coordinates can be extracted through the Fourier transform of each spectrum: the real and imaginary parts. These two coordinates were used to plot the

corresponding “phasor” (or count) of the pixel in a histogram plot known as the phasor plot [339], [340]. The grid of the phasor plot covers the maximum emission peaks of the spectrum from the spectral range of 380–790 nm by 10 nm steps, and the spectral width varies from 20 to 100 nm by steps of 20 nm each. Therefore, one total histogram can be obtained for each sample, and afterwards all the histograms belonging to the samples of the same type were added together in order to plot global type histogram.

In addition, standard phasor histograms of NADH and FAD, measured through standard fluorophores solutions (1 mM in Tris Buffer, pH=8.5 for NADH and 1 mM in PBS, pH=7.4 for FAD), were added to each global type histogram and marked in red on the grid in order facilitate the tracking of the tissues emission peaks.

For NIR molecular ratios extraction, the same spectral fitting technique used for DUV spectral data processing was applied to fit the NIR spectral data. The mean fluorescence spectrum of all pixels in each spectral image was fitted to extract the integral proportion of each fluorophore emission. At 810 nm excitation wavelength, six fluorophores were chosen and fitted by Gaussian curves through a literature review [82]: NADH free, NADH protein bound, FAD, lipopigments, porphyrin I and porphyrins II. While at 890 nm excitation wavelength, the NADH bound was removed and replaced by SHG emission. The Gaussian parameters used for these fluorophore emission fitting is recapitulated in table 8.2, NIR section. An example of two fitted NIR spectrum is shown in figure 8.1(a&b). Rationing the different calculated integral proportion (Int) of these fluorophores, we were able to extract three different NIR molecular ratios:

$$\text{Redox ratio} = \text{FAD-Int} / ((\text{NADH-free-Int} + \text{NADH-bound-Int}) + \text{FAD-Int}) \quad (8.4)$$

$$\text{PN ratio} = (\text{PorphyrinsI-Int} + \text{PorphyrinsII-Int}) / (\text{NADH-free-Int} + \text{NADH-bound-Int}) \quad (8.5)$$

$$\text{LP ratio} = \text{Lipopigments-Int} / (\text{PorphyrinsI-Int} + \text{PorphyrinsII-Int}) \quad (8.6)$$

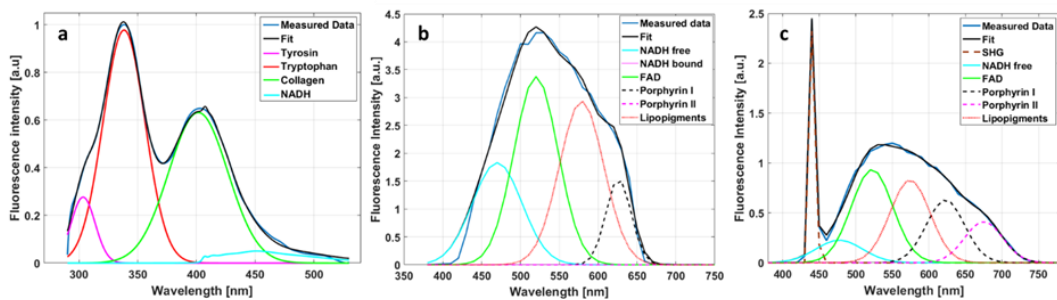


**Figure 8.1:** Examples of spectral fitting of DUV and NIR collected data. (a) Fitted spectrum acquired using 275 nm as excitation wavelength (a); (b) Fitted spectrum acquired using 810 nm as excitation wavelength; (c) Fitted spectrum acquired using 890 nm as excitation wavelength.

DUV Fluorophores	Maximum wavelength (nm)	Spectral bandwidth (nm)
Tyrosine	301-311	0-50
Tryptophan	335-345	0-10
Collagen	380-420	0-50
NADH	430	0-60
NIR Fluorophores	Maximum wavelength (nm)	Spectral bandwidth (nm)
SHG (890 nm only)	440-450	0-5
NADH free	460-470	45-50
NADH bound (810 nm only)	443-445	40-48
FAD	520-530	30-50
Lipopigments	570-600	0-180
Porphyrins I	615-630	0-10
Porphyrins II	675-690	0-10

**Table 8.2:** Gaussian Parameters considered to fit the fluorescence emission spectrum of the endogenous fluorophores excited in DUV range (275 nm) and in NIR range (810 nm and 890 nm)

### FLIM analysis

FLIM acquisition were performed using 810 nm as excitation wavelength. The acquired data were extracted through Symphotime software (PicoQuant, GmbH, Berlin, Germany), then a Matlab interface was used to treat these data.

For protein-bound NADH lifetime, the channel 1 FLIM images were selected where several Region of Interest (ROI) were chosen in each image. In each ROI, the decay curves of its pixels were averaged and adjusted by a bi-exponential fit. To get an acceptable fit, two criteria were considered: 1) having  $\chi^2$ -values of around 1.0 ( $\chi^2$  range 0.8 to 1.2) and 2) the residuals had to be randomly distributed around 0 within the intervals +4 and -4.

For free and protein bound FAD, the channel 2 FLIM image were selected where the phasor approach was used to extract their lifetime values. For each sample, FLIM measurements were performed on a 3x3 mosaic images (9 images). Each image was extracted and treated using "FLJJ" software, the size of each image was reduced from 512x512 pixels to 16x16 pixels. So, each new reduced pixel presents a real size of 32x32=1024 pixels. The decay curves of each 1024 pixels were added together to obtain one decay curve  $I(t)$ . Each decay curve  $I(t)$  is represented in a graphical view by a unique vector having its unique location, called phasor (or count) in the "phasor plot" [129], [130], [132].

Then each decay curve  $I(t)$  is converted in a Cartesian plot into two coordinates using the equations (8.7) and (8.8) below:

$$S_i(\omega) = \int_0^{\infty} I(t) \cdot \cos(\omega t) \cdot dt / \int_0^{\infty} I(t) \cdot dt \quad (8.7)$$

$$G_i(\omega) = \int_0^{\infty} I(t) \cdot \sin(\omega t) \cdot dt / \int_0^{\infty} I(t) \cdot dt \quad (8.8)$$

The x and y coordinates of each phasor are represented by  $S_i(\omega)$  and  $G_i(\omega)$  while the index “i” refers to a pixel in the reduced image; The laser repetition angular frequency is represented by  $\omega$  and it's related to the sampling period ( $T_s$ ) and to the signal length ( $L$ ) through the equation (9) below:

$$\omega = \frac{2\pi}{L.T_s} \quad (8.9)$$

These sets of numbers provided the phasor histogram of the initial reduced 3x3 mosaic image where each reduced pixel of the FLIM image present a count in the phasor plot histogram.

After this procedure, phasor counts of all the samples belonging to the same type were grouped to plot the global phasor histogram for each tissue type where the local maxima of the histogram were localized in order to draw the best fitting line. The two intersections points between the circle segment and this fitting line are related to the two fluorescence FAD components lifetime values [129], [130].

Another procedure was performed in order to calculate, for each tissue type, the Long Lifetime Intensity Fraction (LLIF) of NADH and FAD. This parameter is calculated in order to determine the fluorescence fraction emitted by each molecule component (free and protein-bound) presented in a FLIM image, so to track the emission changes of these two components with the tissue grade.

For that, we selected together all channel 1(NADH) FLIM images belonging to the three tissue types, where a global molecule phasor histogram was plotted used these selected images. The local maxima of this histogram was localized, and the fitting line was drawn. Then, for each tissue type, a projection on the line of its phasor counts was performed to calculate the (LLIF) histogram of NADH [129]. The same procedure was also applied on all channel 2 (FAD) FLIM images to calculate the LLIF histogram of FAD.

### Collagen 3D discrimination algorithm

Extracted from DUV and NIR spectral fitted data, three parameters related to collagen emission: SHG integral proportion (SHG-Int) of 890 nm NIR spectra, collagen integral proportion (Coll-Int) of DUV spectra and normalized collagen maximum peak (Coll-Peak) were combined and presented as a 3D-scatter plot for the three groups of tissues (Figure 8.7). Each point in the scatter cloud has SHG-Int as X axis coordinate, Coll-Peak as Y coordinate and Coll-int as Z axis coordinated. The scatter cloud of each tissue was approached by a Gaussian ellipsoid using the mean and the standard deviation as parameters for the covariance with the ellipse to cover 60% of the total probability mass. Two discrimination tests were conducted on 10 control samples, 7 grade I meningioma samples and 8 grade II meningioma samples, where the sensitivity (Se) and the specificity (Sp) of the discrimination criteria were calculated using the equation (8.10) and (8.11) cited below:

$$Se = \frac{TP}{TP + FN} \quad (8.10)$$

$$Sp = \frac{TN}{TN + FP} \quad (8.11)$$

The first test was realized between control ellipsoid and tumor ellipsoid using 2.5 value of SHG-Int as threshold to discriminate healthy from tumor tissues, where:

TP: True Positive, defined as tumoral tissue classified as tumoral.

FP: False Positive, defined as control tissue classified as tumoral.

TN: True Negative defined as control tissue classified as healthy.

FN: False Negative, defined as tumoral tissue classified as healthy

The second test was realized between grade I meningioma ellipsoid and grade II meningioma ellipsoid using 22 value of SHG-Int as threshold to discriminate grade I from grade II samples, where:

TP: True Positive, defined as grade II tissue classified as grade II.

FP: False Positive, defined as grade I tissue classified as grade II.

TN: True Negative defined as grade I tissue classified as grade I.

FN: False Negative, defined as grade II tissue classified as grade I

## 8.2.3 Results

### 8.2.3.1 Spectral analysis

Using 275 nm as excitation wavelength, we are able to excite efficiently three endogenous fluorophores: Tyrosine, Tryptophan and Collagen crosslinks, emitting respectively around 315 nm, 340 nm and 410 nm [214]. Normalized mean fluorescence intensity (NFI) curves were plotted to observe the variation of the spectral shape between healthy (n=10), grade I (n=7) and grade II (n=8) meningioma. For each spectrum we can observe two main peaks (Figure 8.2(a)): The Tryptophan emission dominant peak around 340 nm and a secondary peak around 410 nm corresponding to collagen crosslinks emission. Control samples presented the lowest fluorescence emission of collagen crosslinks, while this emission increased in grade I and achieved a strong intensity level in grade II meningioma.

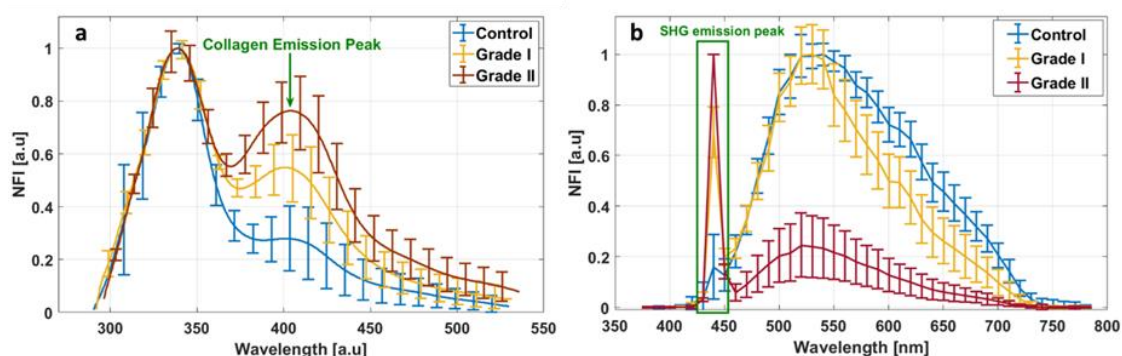


**Figure 8.2:** Spectral Analysis using Deep UV and NIR excitation range. (a) Normalized mean Fluorescence Intensity (NFI) spectra of 10 control, 7 grade I and 8 grade II meningioma samples acquired at 275 nm excitation. (b) Normalized mean Fluorescence Intensity (NFI) spectra of 24 control, 14 grade I and 11 grade II meningioma samples acquired at 890 nm excitation.

In NIR excitation range, spectral measurements were performed on all tissue types to highlight the Two-Photon Emission Fluorescence (TPEF) of NADH and FAD using 810 nm as excitation wavelength, and to underline the SHG emission of collagen structures using 890 nm as excitation wavelength.

Figure 8.2(b) show the Normalized mean Fluorescence Intensity (NFI) curves using 890 nm as excitation wavelength for control (n=24), grade I (n=14) and grade II (n=11) meningioma tissues. Observing the plotted spectra extracted from spectral images, a remarkable variation of SHG emission peak around 445 nm is noticed. This peak is very weak in control spectrum, it increases strongly in grade I spectrum, while it dominates the fluorescence spectra in grade II meningioma. The fluorescence signal on these three tissue types (detection range from 460 nm to 740 nm) also shows an important variation. The control tissues present a wider mean spectrum covering all the detection range, while grade I mean spectrum is narrower, with an intensity starting to decrease from 550 nm. This decrease corresponds to a lower emission of lipopigments, porphyrins I and porphyrins II, emitting respectively around 580 nm, 620 nm, and 680 nm, in grade I compared to control samples.

In addition, and since the obtained spectra reveal that collagen emission signal undergoes a remarkable variation with tumor grade, we decided to track the molecular changes of this macromolecule and to focus our discrimination study on it in order to extract more parameters based on its two types of emission signals and its concentration in tumors samples.

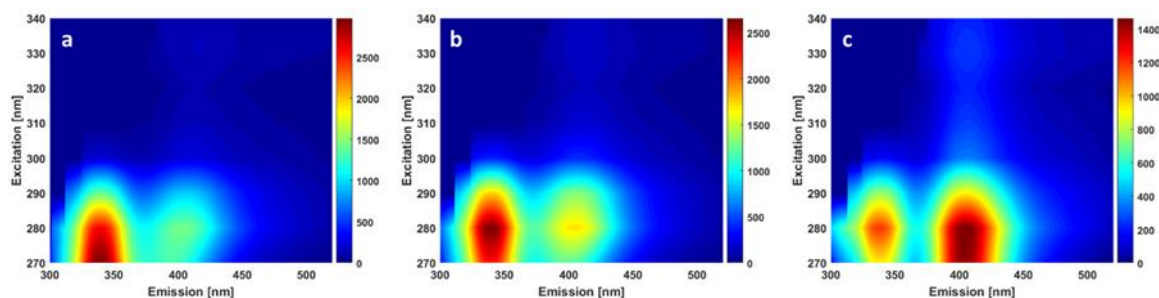


**Figure 8.3:** (a) Excitation-Emission Matrix map in DUV excitation range for control (a), grade I (b) and grade II meningioma (c).

In the DUV excitation range, Excitation-Emission Matrix (EEM) were recorded to track the evolution of the spectral emission of collagen crosslinks with the excitation wavelength. Starting from 270 nm excitation, with a 10 nm step, toward 340 nm, one sample was chosen from each tissue type to perform EEM measurements. EEM map for control, grade I and grade II meningioma are plotted respectively in figure 8.3(a, b, and c). The three maps show that 270-280 nm is the most efficient range to excite tryptophan and collagen simultaneously. Each map presents two main emission zones, the first one around 340 nm corresponding to tryptophan emission, and the second one around 410 nm corresponding to collagen emission. These maps clearly show the increase of collagen fluorescence with the tissue grade, confirming the hypothesis concluded from NIR and DUV normalized spectra. In control and grade I EEM maps, the tryptophan peak dominates the collagen one, while this latter dominates the EEM map of grade II meningioma. In addition, and looking to the intensity scale range, we can conclude that the total emission of control is higher, followed

by grade I which presents a slightly lower fluorescence intensity than the control, while grade II present a low emission intensity comparing to other tissue types, with a map dominated by collagen emission.

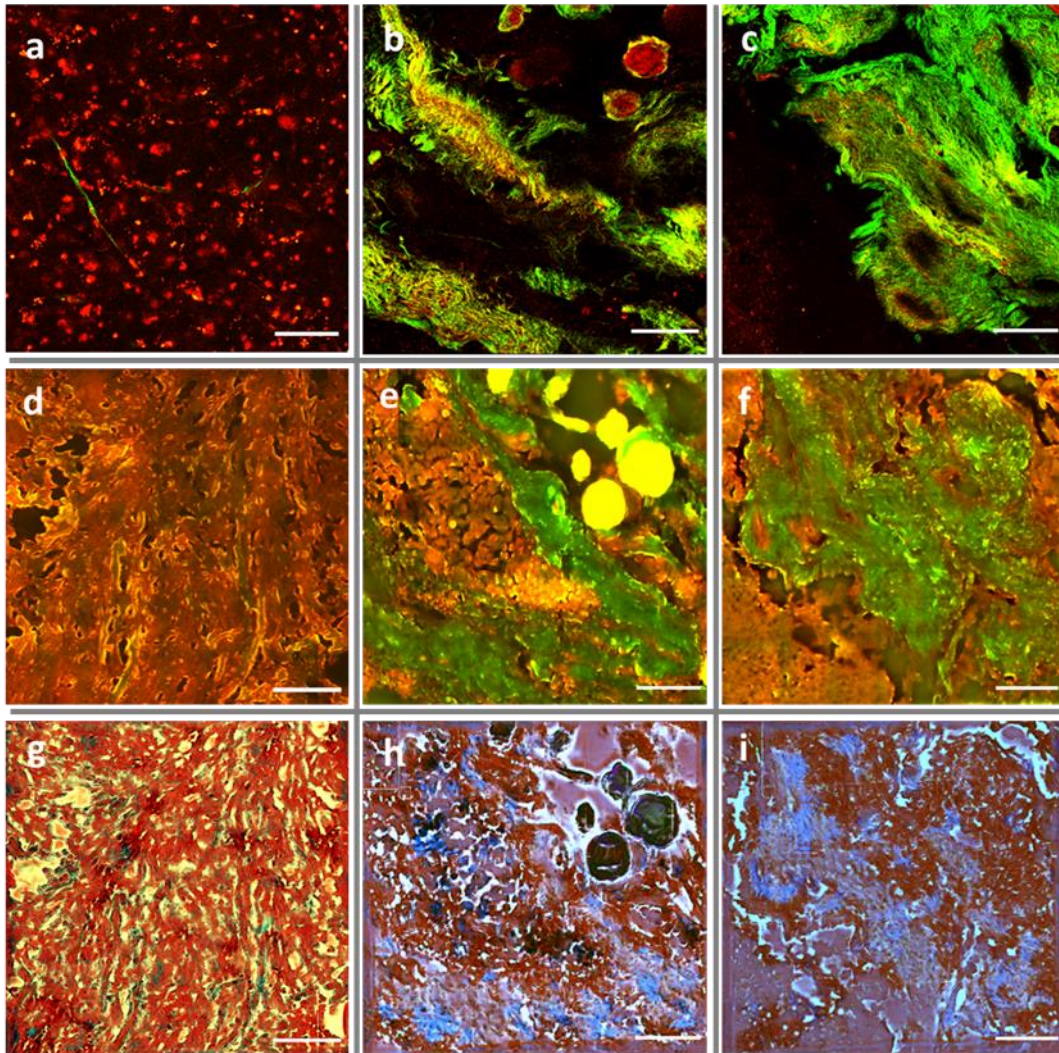


**Figure 8.4:** Image comparison through the NIR and DUV imaging set-up presenting a comparison between control (a,d,g), Grade I meningioma (b,e,h) and Grade II meningioma (c,f,i) through NIR confocal TPEF + SHG images (a, b and c) 890 nm as excitation wavelength, and through DUV Tryptophan + Collagen full field images (d,e,f) using 275 nm as excitation wavelength. MT3 virtual staining Images (g,h,i); scale bar: 100  $\mu$ m

To complete our quantitative analysis and to illustrate spectral results, image acquisitions were performed on all samples using two different imaging setups. TPEF (in red) and SHG (in green) images were acquired using 890 nm as excitation wavelength by merging images of two different detection channels (Figure 8.4(a, b, and c)). These merged images are a qualitative illustration of 890 nm spectral phasors. Control TPEF+SHG images (Figure 8.4(a)) are dominated by the fluorescence and confirm the absence of collagen structures. TPEF+SHG images of grade I meningioma (Figure 8.4(b)) show the classical features of different grade I meningioma types where tumor cells forming fascicle whorls with various amount of intercellular collagen structures can be noticed, while grade II image (Figure 8.4(c)) present a stronger SHG presence with a very dense collagen fibers network,



dominating the fluorescence signal. These observations match with the H&E staining meningioma images presented in our previous works, where TPEF+SHG images were compared to their corresponding H&E images [216], [358].

In the DUV excitation range, full field images of all tissue types were performed using 275 nm as excitation wavelength. Images acquired through the tryptophan emission band-pass filter (307-223 nm) and through the collagen emission band-pass filter (408-438 nm) were merged and presented in figure 8.4(d,e,f). Similar structures were observed in the NIR images and the DUV full-field images. These images present a qualitative and visual translation of the 275 nm spectral results (figure 8.2(a)) where control image are dominated by tryptophan emission (in red) with a low collagen intensity. For grade I and grade II images, the structures highlighted by SHG in the NIR images can be seen in DUV images (in green).

The last row consists of the virtual staining images generated from DUV full field images using Masson's Trichrome (MT3) virtual staining method [357]. The generated images of control, grade I and grade II meningioma (Figure 8.4(g, h and i respectively)) were well matched to their equivalent DUV images noticing that collagen zones were clearly stained in blue and differentiated from the other images' structures.

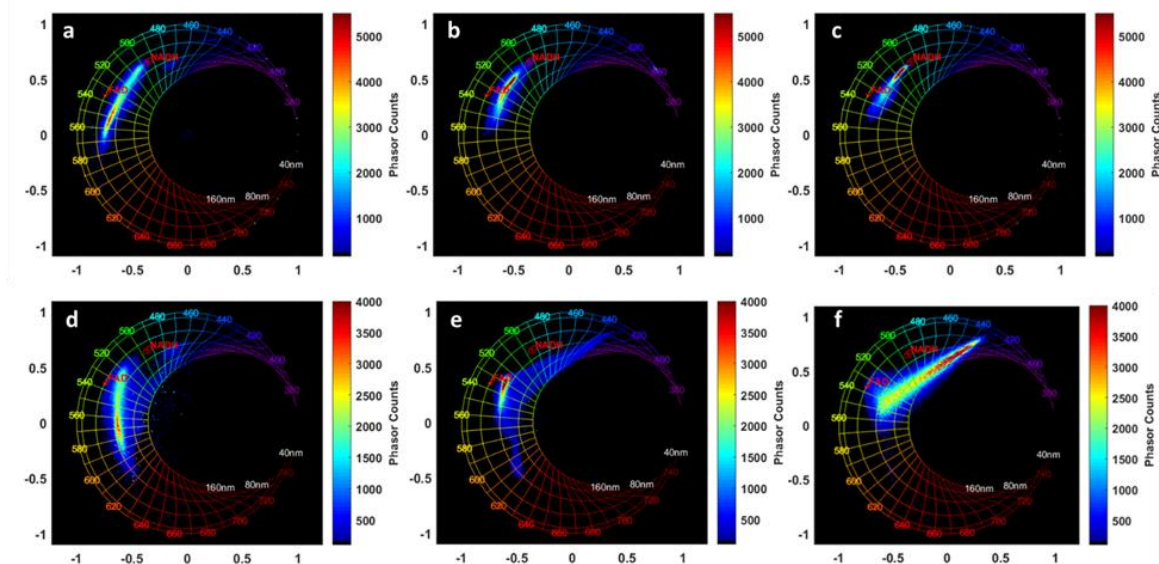


**Figure 8.5:** Spectral Phasor histograms using 810 nm (a,b,c) and 890 nm (d,e,f) for: Control (a,d), Grade I meningioma (b,e) and Grade II meningioma (c,f).

To better visualize the spectral variations, and since we cannot excite NADH at 890 nm, we performed spectral measurements using 810 nm on regions interest for 890 nm spectral measurements. The spectral phasor technique was used to analyze the spectral images acquired under both 810 and 890 nm excitation wavelengths. This approach simplifies the analysis of the global emission spectra of each tissue type with an unmixed view of the spectral contributions of each molecule. Based on spectral images acquired at 810 nm, spectral phasor histograms of each tissue type were plotted in figure 8.5 for control (Figure 8.5(a)), grade I meningioma (Figure 8.5(b)) and grade II meningioma (Figure 8.5(c)). In addition, fingerprint Phasors of NADH and FAD measured in standard solutions were added in red at 495 nm and 535 nm respectively for each histogram to better visualize the emission of each molecule in each tissue type phasor histogram.

From control tissues to higher grade, we observed that the emission cloud undergoes a shift towards NADH fingerprint. In control phasor histogram the emission peak cloud is strongly shifted toward FAD and even more toward the lipopigments emission zone around 570 nm. In grade I phasor histogram, the cloud is focused around the FAD fingerprint while in grade II phasor histogram the emission peak cloud continues its crawling toward the NADH fingerprint, pointing a variation in the concentration of these molecule when going from a grade to another.

The same analysis is shown in Figure 8.5(d, e, and f) but for 890 nm excitation wavelength. At this wavelength we are able to detect and highlight the SHG emission of collagen structures. The same trend is observed for 810 nm and 890 nm phasor histograms. In control samples, the emission cloud is strongly shifted toward the FAD and lipopigments emission zone without detecting a strong SHG emission. In grade I meningioma histogram, the emission is also focused near the FAD fingerprint with a shift tail toward the SHG emission zone, while the grade II meningioma emission cloud is strongly shifted toward the SHG zone due to a strong emission of this signal.

### 8.2.3.2 Molecular ratios

To complete the molecular emission tracking, and several molecular ratios related to the excited molecules were compared through 275 nm and 810 nm spectral measurements.

Figure 8.6(a) gathers the molecular ratios extracted from DUV spectral data using 275 nm excitation. Three molecular ratios for control, grade I and grade II meningioma are displayed. Tryptophan/Collagen ratio (Figure 8.6(a) N°1), Tryptophan/NADH ratio (Figure 8.6(a) N°2), and Tryptophan/Tyrosine ratio (Figure 8.6(a) N°3). As expected, a decrease in the Tryptophan/Collagen ratio from Control to grade I and grade II meningioma discriminates significantly these three tissue types. The Tryptophan/NADH ratio was clearly higher in control tissues and discriminates significantly these three tissue types in a descending behavior with tumor grade. This descending behavior indicates that the NADH level increase with the tumor grade to reach a higher presence in grade II meningioma. This results are weakly detectable on the EEM map of grade II meningioma (Figure 8.3(c)), where at 340 nm excitation, a faint emission tail around 450 nm appears close to the collagen emission zone. This tail is very low in control EEM map, and slightly present in grade II EEM map, confirming the observed behavior in Tryptophan/NADH ratio.

As for DUV, exploitation of the three molecular ratios extracted from NIR spectral data using 810 nm excitation wavelength reveals and confirms another molecular variation behavior with the tumor grade; PN ratio (Porphyrins/NADH), LP ratio (Porphyrins/Lipopigments+Porphyrins) and redox ratio (FAD/ (NADH+FAD)) are displayed in Figure 8.6(b) (N°3, 4 and 5 respectively). The PN ratio decreases from control to grade II, revealing a loss in porphyrins contribution in the meningioma samples. Similarly, the LP ratio reveals a decrease of the lipopigments contribution in grade I and grade II meningioma, translated by an increasing variation of the ratio from control to grade II. This molecular variation in term of emission contribution of lipopigments and porphyrins confirms the changes in the mean normalized spectra acquired at 890 nm (which is better than 810 nm to excite these two molecules) of the three tissue types in the emission range of the cited molecules.

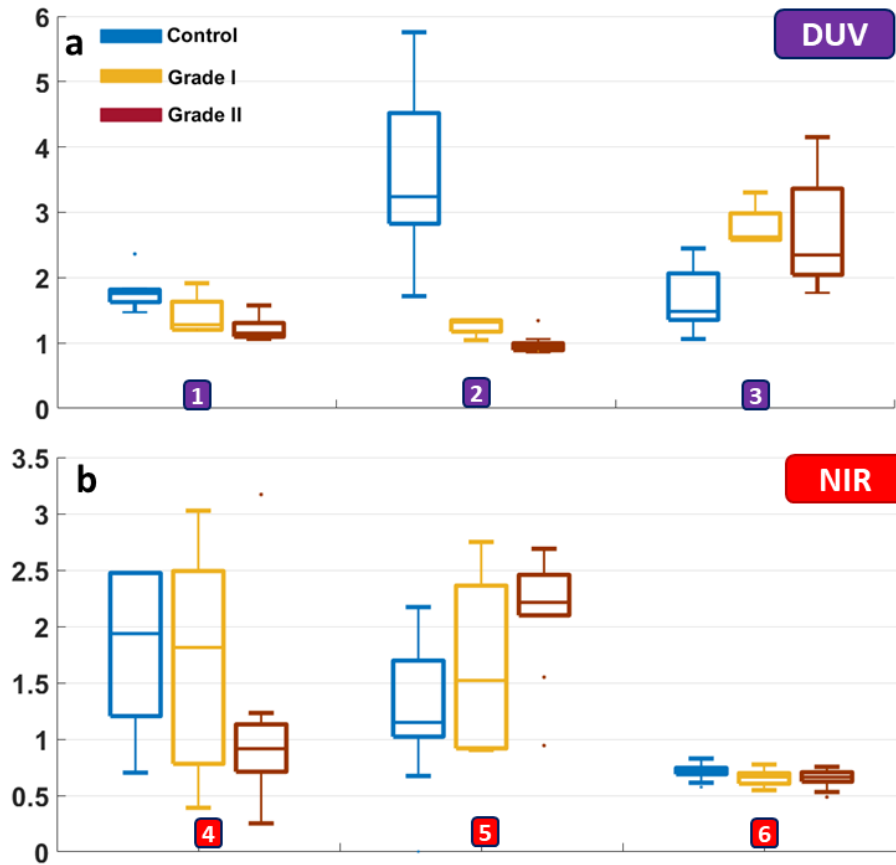


**Figure 8.6:** Group boxplots of six molecular ratios acquired from spectral data at 275nm (DUV) and 810 nm excitation (NIR) for control, grade I and grade II meningioma. DUV part shows Tryptophan/Collagen (N°1), Tryptophan/NADH (N°2) and Tryptophan/Tyrosine (N°3) ratios. NIR part shows PN ratio (Porphyrins/NADH) (N°4), ratio LP (Porphyrins/Lipopigments+Porphyrins) (N°5) and redox ratio (FAD/ (NADH+FAD)) (N°6) ratios.

### 8.2.3.3 Collagen 3D discrimination

Based on the previous observation, all results concerning the collagen emission tracking in NIR and DUV were grouped to build a discriminative algorithm between control-tumor and between grade I-grade II meningioma. First, a boxplot representing the SHG integral proportion (SHG-Int) in the total emission spectrum at 890 nm of each tissue type was plotted in figure 8.7(a). We observed, the same trend than normalized plotted spectra and spectral phasor histograms in NIR excitation domain, with a significant increase of the SHG emission observed from control samples to grade II meningioma. Secondly, boxplots plotted in figure 8.7(b) and figure 8.7(c) show the integral proportion of collagen emission (coll-int) in the total emission spectra and the normalized maximal emission collagen peak (coll-peak) respectively, acquired from 275 nm spectral results in the DUV excitation domain. These two boxplots highlight the increase of the collagen emission with tumor grade, from a low contribution on control samples to a higher emission in grade II meningioma.

Based on the obtained differentiation, a homemade 3D discrimination algorithm, used in previous works [270], was applied to these set of data. This algorithm considers three parameters and combine them to plot a 3D scatter cloud which is then approximated by

an ellipsoid. As threshold, we choose SHG-Int to establish a Control-tumor diagnosis response (Figure 8.7(d)) and a grade I-grade II discrimination.

For the coordinates, we choose the SHG emission as X axis parameter, Coll-Peak as Y axis parameter and Coll-int as Z axis parameter. The results obtained were encouraging, a 100 % sensitivity and 90% specificity for Control-Tumor discrimination was reached, while a 94.7% sensitivity and 95% specificity for grade I-grade II discrimination was achieved (figure 8.7(e)).

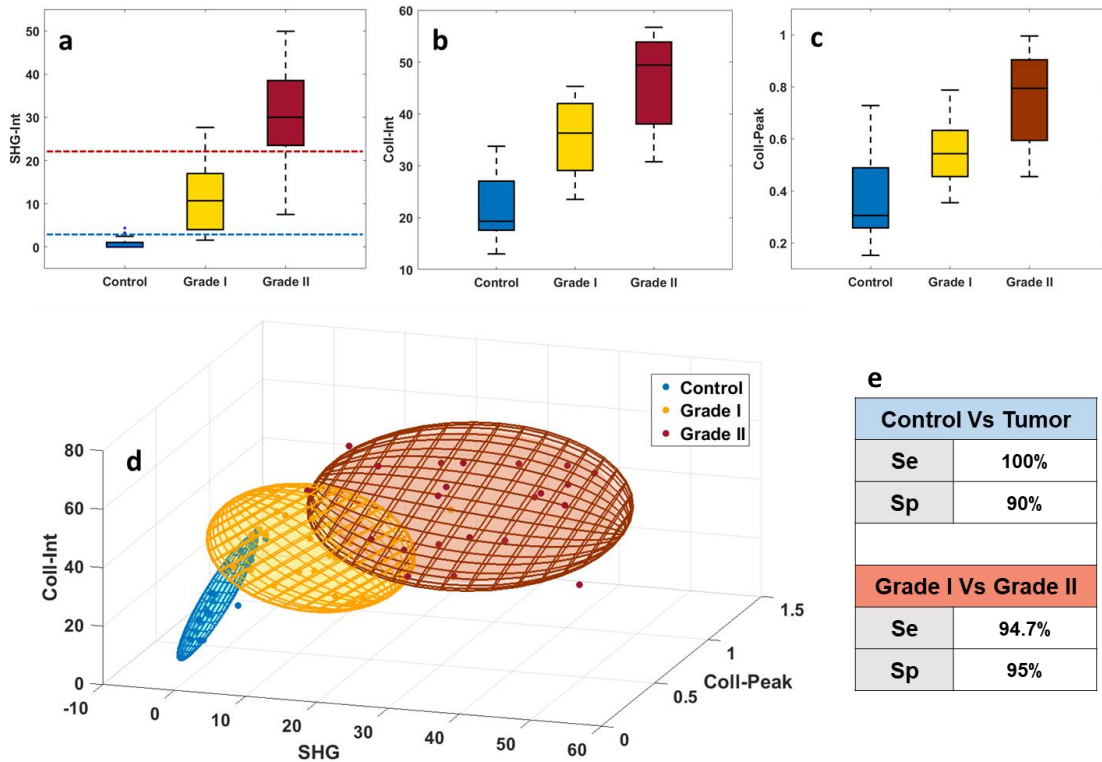


**Figure 8.7:** (a) Boxplot view of SHG integral proportion (SHG-int) in the total spectra at 890 nm excitation wavelength for control, grade I and grade II meningioma; (b) collagen maximum intensity peak (Coll-peak) using 275 nm as excitation wavelength for control, grade I and grade II meningioma; (c) Collagen integral proportion (Coll-int) in the total spectra acquired using 275 nm Control, Grade I and Grade II meningioma. (d) 3D-discrimination ellipsoids of control, grade I and grade II meningioma where SHG-int, Coll-peak and Coll-int were taken as 3D coordinates. (e) table gathering the sensitivity and specificity of discrimination test results realized for 10 control vs 15 tumor samples and for 7 grade I vs 8 grade II meningioma samples.

### 8.2.3.4 Fluorescence Lifetime analysis

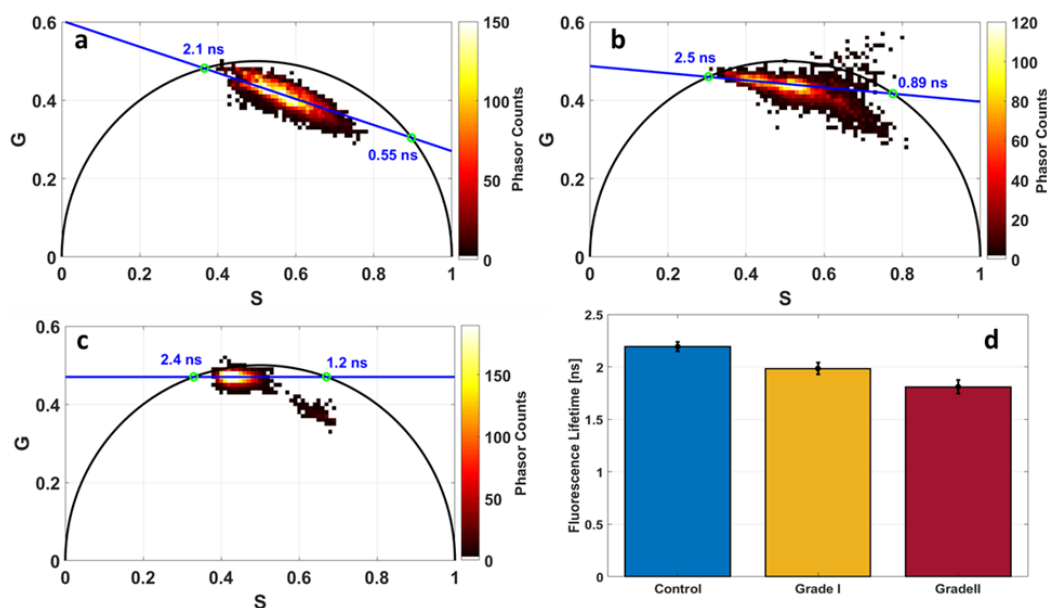


**Figure 8.8:** Fluorescence lifetime analysis of FAD (a,b,c) and NADH (d). Phasor FLIM histogram of FAD using 810 nm as excitation wavelength for control (a), grade I meningioma (b) and grade II meningioma (c), free and protein-bound FAD lifetime values are drawn as green circles intersecting with the universal circle; mean lifetime histogram of protein-bound NADH at 810 nm for control, grade I and grade II meningioma.

Since the spectral phasor analysis using 810 nm (figure 8.5(a)) shows a modification in the emission contribution of the NADH and FAD with tumor grade, we decided to analyze the fluorescence lifetime of these two molecules at 810 nm to track their chemical state (free and protein-bound) changes with tissue grade. Phasor FLIM analysis was performed to investigate FAD lifetime through its FLIM images. This approach was used to simplify the FLIM analysis and to obtain a graphical global view of the processes affecting the fluorescence decays occurring at each pixel in the FLIM image [131], [132]. Each phasor histogram presents a cloud including the repartition of all phasor counts extracted from each reduced pixel of a FLIM image. A fitting line is additionally plotted through the identified local maxima of each phasor histogram. Through this fitting line we can determine the lifetime of each component presented in our image [129].

Figure 8.8(a,b,c) shows respectively the phasor FLIM histograms of FAD using 810 nm for the three tissue types: control, grade I and grade II meningioma. Different lifetime values of the two FAD components were obtained: control samples had the lower free FAD lifetime (2.1 ns) while grade I and grade II had higher values (2.5 and 2.4 respectively). The same trend was obtained for protein-bound FAD lifetime, where control samples presents the lowest value (0.55 ns) and the grade I and grade II had higher values (0.89 and 1.2 respectively).

For NADH lifetime, we used a bi-exponential fit to extract the fluorescence lifetime of its two components. Histograms representing the lifetime of this component were plotted in figure 8.8(d). It is clear that the lifetime of protein-bound NADH decreases with the tumor grade, and can discriminate significantly control from tumors, and grade I from grade II

meningioma. A mean value of  $2.19 \pm 0.046$  ns was found for control,  $1.98 \pm 0.055$  ns for grade I and  $1.8 \pm 0.065$  ns for grade II meningioma.

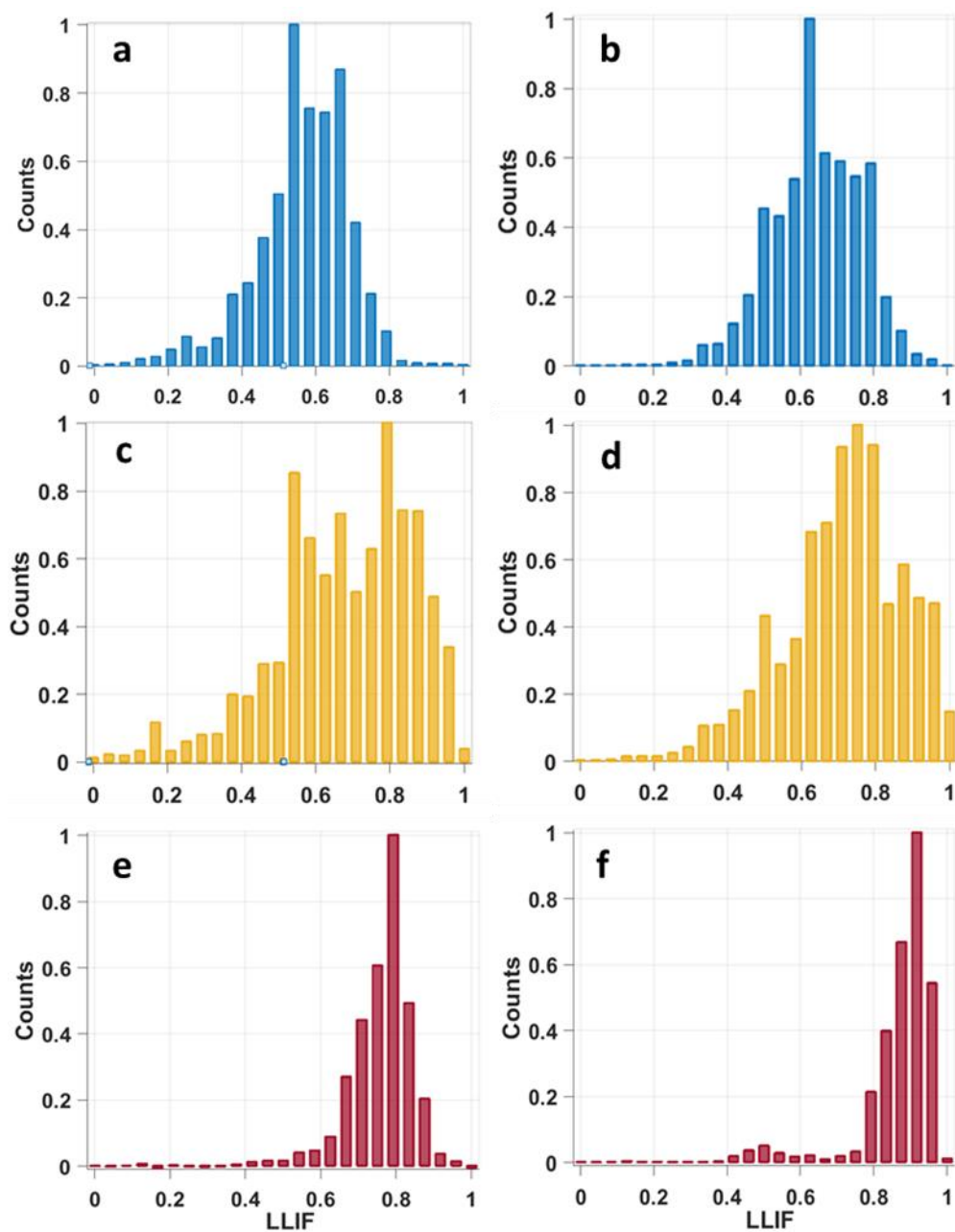


**Figure 8.9:** Long Lifetime Intensity Fraction (LLIF) histogram of NADH (a,c,e) and FAD (b,d,f) issued from phasor FLIM analysis at 810 nm for Control (a,b), grade I meningioma (c,d) and grade II meningioma (e,f).

In addition to the lifetime values extraction, we tracked the variation of the contribution of each molecule component in each tissue type through their FLIM phasor histograms. For that purpose, we regrouped all FAD and all NADH FLIM images from all types, in order to build a global phasor histogram for each molecule. Then these global phasor histograms were used to plot the histogram of Long Lifetime Intensity Fraction (LLIF) distribution of each molecule component in each tissue type (see data analysis). This parameter helps us to determine the fraction of fluorescence emitted by each molecule component presented in

a FLIM image in each tissue type. LLIF histogram of NADH (figure 8.9(a,c,e)) and FAD (figure 8.9(b,d,f)) are shown respectively in figure 8.9 for control (a,b), grade I (c,d) and grade II meningioma samples (e,f).

Observing the plotted histograms, we can clearly notice that the distribution of LLIF of these two molecules present the same variation behavior from grade II to control and undergoes a shift from high LLIF values toward lower values. For grade II meningioma, figure 8.9(e&f) show a strong accumulation of higher LLIF values with a narrow distribution. While in grade I, the histogram undergoes a shift toward lower LLIF values with a wider distribution than grade II including high and lower LLIF values in figure 8.9(c&d). In control samples, the histogram shifts even more toward lower LLIF values presenting a decrease of the counts in high LLIF values region (Figure 8.9(e&f)).

## 8.2.4 Discussion and conclusion

To complement a past study [216], we aimed in this work to discover, analyze and track changes at the molecular level through an advanced multimodal quantitative analysis of tissue auto-fluorescence; and to correlate those changes with the tumor grade. Our goal was to establish several discrimination parameters between healthy, grade I and grade II meningioma tissues. We used multiscale excitation, from DUV to NIR, and different imaging instruments to investigate the fluorescence emission of several endogenous fluorophores from a large cohort of samples. Advanced analysis was performed on the results of those various imaging modalities, they consisted in analyzing and correlating the spectral and time-resolved variations of the auto-fluorescence response of the three tissue types.

We investigated at first the spectral response changes of meningioma grades using three excitation wavelengths, 275 nm, 810 nm, and 890 nm. Under DUV excitation, the auto-fluorescence of two major molecules was highlighted: tryptophan and collagen crosslinks. Emitting around 340 nm, tryptophan residues have been proposed as a fluorescent marker in the study of phosphorylation of cellular mechanisms that regulate cell growth, proliferation and transformation [214], [338]. Therefore, many studies relied on the auto-fluorescence signal of this molecule and its related metabolic ratios to discriminate cancer cells [214], [338]. Emitting a fluorescence signal around 415 nm when excited in the DUV range, collagen plays multiple roles in the composition of the different tissue compartments of the central nervous system [359]. Indeed, Type VI collagen can be found in the connective tissue, mainly consisting of the central nervous system basal lamina associated with the meninges and the brain blood vessels and it's considered as a good marker for tissue vascularization [359].

Through the obtained spectral results in the DUV range (figure 8.2(a)), an important variation of the collagen crosslink fluorescence emission was observed, from a low emission in healthy samples to an increase with the tumor grade to reach a strong emission close and even higher than the tryptophan emission peak in grade II meningioma samples (figure 8.3(c)). The same trend was observed in NIR spectral phasor results in term of SHG emission (figure 8.5(f)). This variation was also visualized through the acquired confocal and full-field images (figure 8.4(c&f)), where the collagen fibers structures were not present in healthy samples while they started to be dense and more concentrated with higher tumor grade. In fact, grade II meningioma tissues feature prominent blocky perivascular and interstitial collagen, which occasionally coalesces into large acellular zones or forms brightly

eosinophilic amianthoid-like collagen [25]. These coalescing blocks increase the ability of such structures to generate a non-linear signal such as SHG. These blocks hide the tumor cells zones and decrease their capacity to absorb light, explaining the strong and dominant SHG signal emission and the weak fluorescence response in grade II meningioma samples (figure 8.2(b)). On the other side, grade I meningioma features spindled tumor cells forming parallel and interlacing bundles in a various amount of intercellular collagen rich matrix [25]. This fact could explain the presence of a high fluorescence signal in grade I samples with a low emission (comparing to grade II) of SHG signal due to a more homogenous repartition of collagen matrix in these samples.

These interesting spectral variations have been confirmed with qualitative visualization through confocal and full-field images acquired using 890 nm and 275 nm excitation wavelengths respectively (figure 8.4). The same trends were observed than with spectral results. In a previous work, a proof-of-concept study was conducted on fresh human samples where TPEF + SHG images were compared to their corresponding H&E stained images in order to validate the efficiency of two-photon microscopy to provide a reliable diagnosis information on tissue's nature [98]. In this this previous study, a blind diagnosis test was realized by a neuropathologist on a large group of TPEF and SHG images revealing a high sensitivity (100%) and specificity (50%) for discriminating control brain tissues from glioblastoma and brain metastasis tumors [98].

Therefore, and since H&E staining of tissue samples is time consuming and involves laborious preparation, we tried in this study to attempt the use of virtual staining for microscopy images through deep learning to compare its resulting images with our DUV full-field images. In their recent work, Y. Rivenson et al [357] shows that a convolutional neural network trained using a generative adversarial-network model can transform wide-field auto-fluorescence images of unlabeled tissue sections into images that are equivalent to the bright-field images of histologically stained versions of the same samples. Realized on a large cohort of liver and lung tissue samples, the staining efficiency of their approach, was blindly evaluated by a group of pathologists who were able to recognize histopathological features in their output images, and achieved a high level of agreement with the H&E stained images [357]. In addition, this approach can be applied to other microscopy modalities that use other endogenous or exogenous contrast markers [357]. So as a first step, we decided to test this approach on our full-field images generated using 275 nm in order to explore its ability to recognize same features as H&E stained images of brain samples. The obtained images were encouraging in term of collagen network staining, but the staining of isolated cells was not sufficiently effective. This test opens the door to realize a large study using this virtual staining method and impose the training of this approach on the corresponding H&E stained brain images of our full-field images and the use of large cohort of sample images of different tissue types, before applying it on confocal NIR images. Concerning metabolic ratio indicators, the extracted ratios translated the same variations of collagen concentration observed by spectral analysis. In addition, it was noticed from Tryptophan/NADH ratio (figure 8.6(a)  $N^{\circ}2$ ) and from the EEM map of meningioma samples that an increase of NADH levels appears in grade II meningioma compared to control samples.

But since the absorption cross section of NADH is low in the DUV range [83], spectral measurements were acquired using two-photon excitation in NIR at 810 nm to efficiently



excite this molecule and to better track its variation with tissue type. Through spectral phasors at 810 nm (figure 8.5(a,b,c)), the increase of NADH level with tissue grade was confirmed and clearly noticed. This increasing behavior of NADH levels in tumor tissues was reported in several studies in literature and observed in rat brain tissues [97], human fixed tissues [34] and in tumoral esophageal epithelium cells [342]. In fact, NADH is the reduced form of Nicotinamide Adenine Dinucleotide (NAD) which is a coenzyme that is central to metabolism and found ubiquity in all living cells [83]. This molecule is involved in cell metabolism processes as an electron carrier in redox reactions [83]. It had been widely monitored to evaluate oxidative metabolic state in cells and tissues [360] and considered as the most prevalent endogenous molecule. In meningioma tumors, the mitotic activity and cellular proliferation increase in proportion with the grade [25], leading to an increase of metabolic activity with the grade, explaining the increase of NADH level in proportion to tissue grade, reaching a high level of NADH in grade II meningioma.

Another molecular change in meningioma grades was noticed through NIR spectral results. Phasor histograms of spectral data acquired using 810 nm (figure 8.3(a,b,c)) and normalized mean spectra curves of spectral data acquired using 890 nm as excitation wavelength show a variation of lipopigments and porphyrins levels in tumor tissues. The fluorescence signal of these two molecules was more important in control tissues and decrease in tumor samples. The same trend was observed also through the ratio LP

In literature, lipid levels in brain tissues were found decreasing with tumor grade, this decrease is linked to the sensitivity of lipopigments to the metabolic state of the tissue even if it is not tumoral and that they are affected by several metabolic processes such as oxidative and glycolytic metabolism [274], [301]. Our past studies have shown a spectral distortion and a strong decrease of lipopigments level in fresh tissues five hours after resection due to the metabolism alteration after the resection and the end of the processes cited above [274].

In the light of the obtained results of collagen variation in the DUV and NIR excitation range, we decided to use a homemade 3D discriminative algorithm, already tested in a previous work [270] with DUV molecular ratios related to tryptophan, tyrosine, collagen and NADH. This 3D algorithm combines 3 different parameters extracted from each tissue type in order to plot a scatter cloud and to approach by a Gaussian ellipsoid using the mean and the standard deviation as parameters for the covariance with the ellipse covering 60% of the total probability mass.

We choose three different parameters related to collagen to plot our three ellipsoids, SHG-Int extracted from NIR spectral measurements as an X-coordinate, collagen emission maximum intensity peak (coll-peak) and its molecular integral proportion (coll-int) through deep UV spectral data as Y and Z-coordinate respectively.

Two discrimination tests were performed, the first one is a control-tumor diagnosis using the 2.5 value of SHG-Int as threshold. Applied on the sets of data, we assumed in this test that if the point is inside a grade I or grade II ellipsoid and its SHG-Int is higher than 2.5, tumor can be diagnosed and confirmed. With 0% of overlapping volume between control and tumor ellipsoids this test reaches a 100% sensitivity and a 90% specificity. The second test was a grade I-grade II meningioma discrimination using the 22 value of SHG-Int as discrimination threshold. Applied only on grade I and grade II sets of data, we assumed that if the point is inside the grade I ellipsoid and its SHG-Int is lower or equal than 22,

grade I is detected; while if the point is inside the grade II ellipsoid and present a SHG-Int value higher than 22, grade II is detected and confirmed. This test reaches a 94.7% sensitivity and 95% specificity. These excellent percentages constitute a strong encouragement to train more this algorithm with a larger number of samples to confirm its robustness. It will constitute an important tool that will serve for future blind analysis in order to acquire fast diagnosis on tissues nature and its grade.

Moving to lifetime results, protein-bound NADH lifetime were extracted from decay curves of different region of interest (ROI) in FLIM images through a bi-exponential fit process. This component presents the majority of NADH presence in human cells [342]. In control samples, this component lifetime was found high and decreased with the tumor grade. The same variation was obtained in our past study using 810 nm as excitation wavelength [216]; where the NADH lifetime value was higher in grade I than grade II ( $2.67 \pm 0.15$  for grade I and  $2.55 \pm 0.14$  for grade II at 810 nm; and  $4.00 \pm 0.18$  for grade I and  $3.64 \pm 0.10$  for grade II at 405 nm [216]). The difference between the two works is due to the fact that mono-exponential fit was used to fit the decay curves in the previous work, while in the present one, we used bi-exponential fitting to calculate precisely the protein-bound NADH lifetime. The bound-NADH lifetime values obtained in this study were significantly different between control-tumor discrimination (student test: p-value = 0.00013 for control vs grade I) or between grade I-grade II discrimination (student test: p-value = 0.0077 for grade I vs grade II). The increase of fluorescence lifetime can be correlated with an increase of NADH concentration in tumor tissues, confirmed through 810 nm spectral analysis, and considered as a reliable discrimination threshold criterion in a diagnosis rapid test. So a high NADH level with a lifetime value lower than 1.9 ns leads to a grade II meningioma diagnosis; a low level of NADH and a lifetime value higher than 2.1 ns leads to a healthy zone diagnosed while if these two criteria were in between, a grade I could be diagnosed.

Phasor FLIM technique was also used to analyze FLIM data acquired at 810 nm to study FAD and its two components, free and protein-bound, lifetime values in the NIR domain. Similar to NADH lifetime values, the two FAD components lifetime values (free and protein-bound) evolved with the tissue type. Not only lifetime values were different in each type, but the phasor cloud shape varies from a narrow ellipse shape for control to a widespread ellipse in grade I and a focused circle cloud close to free FAD region in grade II. This variation in the shape of the phasor cloud led us to conclude that the repartition of the two FAD components seems to be changing from one type to another. Therefore, we investigated the fluctuations of the two components of FAD and NADH in order to determine the variation in term of the contribution of each component in each tissue type. The histogram of Long Lifetime Intensity Fraction (LLIF) distribution of NADH and FAD in each tissue type is shown in figure 8.9 It is remarkable that the histograms of these two molecules follow a similar trend from control to higher grades. Free FAD, which corresponds to higher LLIF values, was more present in grade II meningioma than protein-bound FAD (lower LLIF values), inducing a strong shift of the histogram toward the right side (figure 8.9(e&f)). In grade I meningioma this strong shift is not present while the histogram is wider (figure 8.9(d)) shifted toward lower LLIF values, therefore free FAD is more concentrated in grade II than grade I. Control samples present a histogram shape (figure 8.9(f)) similar to grade I but with a lower accumulation of high LLIF values and an increase of low LLIF values, which means a higher protein-bound FAD occurrence and a decrease

of free FAD concentration. Similar shift and variation in protein-bound and free components presence is observed for NADH histograms (figure 8.9(a,c,e)). Protein-bound NADH is less present in control samples, its level increase in grade I samples, while it was strongly presented in grade II samples with a strong decrease of free NADH levels. These observations allow to conclude that NADH and FAD LLIF repartition shift to higher values with the meningioma tumor grade. We can assume and confirm, through our two works on low and high grade glioma [270] and through this work on grade I and grade II meningioma, that the concentration NADH and FAD components follow a variation behavior with the tumor grade and with the malignancy of the tissue and can become a good discriminative indicator between tumor grades.

We presented in this study an advanced multimodal approaches to analyze and track the molecular variation between healthy, grade I and grade II meningioma tumor. We can conclude at the end this work, that the tracking of several molecules individually (collagen, tryptophan, Lipopigments, NADH, FAD) and their analysis through multiscale and multimodal analysis could lead to better extraction of discriminative parameters for future diagnosis of brain tumors. Other molecules, such as porphyrins and tyrosine, will have to be tracked in a future work to discover the alteration of these fluorophores in brain cancer tissues.

Moreover, this study offers several discrimination quantitative factors between healthy tissues and meningioma tumor tissues:

- (1) increase of collagen fluorescence signal with the tissue grade: a tissue with a collagen contribution (Coll-Int) lower than 28 is considered as healthy, while a tissue with a Coll-Int higher than 28 is considered as tumor.
- (2) increase of SHG contribution with the tissue grade: a tissue with a SHG contribution (SHG-Int) less than 2.5 is diagnosed as healthy, between 2.5 and 22 is diagnosed as grade I, and higher than 22 is diagnosed as grade II meningioma.
- (3) increase of protein-bound NADH concentration with the tissue grade with a decrease of this NADH component lifetime: a tissue with a bound-NADH lifetime higher than 2.1 ns is diagnosed as healthy; between 1.9 ns and 2.1 ns is diagnosed as grade I, while lower than 1.9 is diagnosed as grade II.
- (4) increase of free FAD concentration with the tissue grade and an increase of this FAD component lifetime: a tissue with bound-FAD lifetime lower than 0.7 ns is diagnosed as healthy; between 0.7 and 1 ns is diagnosed as grade I, while higher than 1 ns is diagnosed as grade II.

The combination of these factors with qualitative parameters allowed us to reach our goal and to strengthen our optical database. And to build a discrimination parameters bank of different cancerous aspects in brain tissues.

We have shown that the study and the tracking of endogenous brain fluorescence through multiple excitation and relying on several modalities of optical contrasts offers a reliable response with high sensitivity and specificity to overcome limits of actual technics and is essential to achieve the best discrimination between different tumor grades and healthy tissues. We confirmed the clinical relevance of such multimodal optical analysis, which can be easily applied to neurosurgical purpose for a better diagnosis of surgical margins for brain tumors. Each specific multimodal multiscale optical signature of a tissue type, established

in our database, will be implemented in the endomicroscope to differentiate healthy tissues from tumor ones in a robust way.

A first prototype of this intraoperative surgical tool is under development in our laboratory and has shown great performances in term of exciting and signal collection efficiency, and its ability to provide a discrimination response was proved. This endomicroscopic probe could be directly implemented in the human brain while performing its measurements. The rapidity of acquisition of this tool is an advantage over the actual used tools (extemporaneous examination, intra-MRI... etc.). Additionally, our tool does not require the use of any exogenous markers which simplify the surgery workflow and limits any biased classification.

# Chapter 9

## Discussion and conclusion

During this thesis, I had the opportunity to work on two different aspects that complement each other in a research project that aims to improve the diagnosis of brain tumors margins intraoperatively. The first aspect was the instrumental development of a fibred endomicroscope based on a non-linear excitation to perform TPF and SHG imaging for brain surgery guidance. The second one is the construction of tissue database that will be associated with the endomicroscope to provide it the ability of establishing a real-time intraoperative diagnosis of the imaged areas.

In these two aspects, my work is a continuation of the work carried by former members of our team. During these three years, I worked to achieve three main goals that were defined for my thesis work:

- 1) Improving the existing endomicroscope setup and developing a new prototype with higher performance.
- 2) Moving to the stage of a multimodal endomicroscope translated by designing and characterizing a miniature scanning system dedicated for image acquisition.
- 3) Improving the tissue database to render it more robust, by looking for new tissue discrimination factors, and more specific, by specifying each tumor grade with its specific multimodal optical signature.

In this chapter, the different addressed tasks in the instrumental aspect as well in the tissue database construction will be enumerated and their significance will be discussed. The encountered obstacles during my work in each aspect will be cited as well as the short and long term prospects for each one to get closer and to reach the clinical use stage.

### 9.1 A TPF endomicroscope with a high potential for quantitative diagnosis establishment

One of the main goals of my PhD was to improve the instrumental capacities of the endomicroscope setup. As described in the introduction, a first prototype has been set up before my arrival to the laboratory. This prototype served to perform several important characterizations for the endoscopic fiber choice, the pre-compensation unit, and the pulse delivery process. A customized PC-DCF fiber that meets our needs in term of high resolution, high collection efficiency, negligible fiber-autofluorescence and that reduces as much as possible the non-linear effects, was conceived and built through a collaboration with the group of Professor Alexandre Kudlinsky in PHLAM laboratory, specialized in optical fibers fabrication.

For excitation, this fiber includes a non-doped silica central core, to avoid the fiber autofluorescence, with a diameter of 6.4  $\mu\text{m}$  (single-mode at 800 nm) and a NA of 0.097 (at



However, the usefulness of such imaging system does not just lie in its instrumental aspect or its ability to generate high quality images, but as well in its ability to exploit the generated fluorescence signal. For this reason, the validation of the medical/biological aspect of our developed endomicroscope is necessary before moving to a next stage. This aspect is translated by investigating first the effect of the two-photon excitation process on human brain tissues.

In chapter 2, a large *ex vivo* study was conducted on four different types of brain tissue samples to investigate the effect of ultrashort two-photon excitation pulses, generated through our developed TPF endomicroscope, on the autofluorescence signal from neuronal tissues. We aimed to inspect whether these pulses, induced any changes in the biochemical state of the excited fluorophores or induced any morphological or metabolic changes in the excited tissues. Therefore, we have shown the ability of our endomicroscope to excite with ultrashort pulse durations without inducing any distortion in the spectral emission of the inspected fluorophores and without observing any photo-induced local heating, or changes in the pH or protein-binding states of the relevant molecules.

The second inspected aspect was the ability of our endomicroscope to generate and to collect high intensity and exploitable TPF + SHG signals was well its potential to extract the needed reliable quantitative response that should be relied on for a future diagnosis establishment. This potential is translated by providing a spectrally and time-resolved fluorescence signal that is similar to the one provided by the tissue database reference setup, the multiphoton multimodal benchtop microscope.

In chapter 3, and to demonstrate this potential, we conducted a study, on a cohort of forty-nine human brain fresh samples with different tumor types. We compared the spectral and the fluorescence lifetime signal generated via the endomicroscope with its counterpart generated by the benchtop multiphoton microscope that was used for the tissue data base establishing.

This study showed a high performance of our developed system in exciting and collecting high quality TPF and SHG signals. Quantitative extracted parameters such as spectral emission intensity, extracted molecular ratios and fluorescence lifetime distributions highlighted the potential need of the endomicroscope. However, our endomicroscope setup have a more efficient excitation thanks to the ability to excite with a very short pulse duration and a high excitation mean power. Furthermore, the collection of the fluorescence signal is faster, more precise, and more efficient than the benchtop microscope setup. To our knowledge, the combination of quantitative TPF and SHG analysis and lifetime measurements through a TPF fibered endomicroscope on a large number of human fresh samples using these short energetic pulses has never been reported before.

## 9.2 Toward a multimodal TPF endomicroscope

Once the quantitative bimodality is approved and its ability to be analyzed is validated, the transition to obtain a qualitative modality in our endomicroscope is the next step to complete our aimed multimodality. Therefore, the next stage in the instrumental development aspect is to develop an imaging probe head which employs a scanning system, necessary for image acquisition. Such system should respond to several specifications; it should be as miniature as possible while able to perform fast imaging acquisition with the highest possible resolution.

Since that the MEMS-based scanner was our justified method to develop our scanning system of the probe head, due to several reasons explained in the introduction and in chapter 4, our work started first by looking to the most adapted probe design to perform TPF imaging. We looked in the state of the art of MEMS probe designs, where most the developed probe were based on a one-lens configuration and designed for OCT imaging. Two-lens configuration was the most adapted for our mission, so Zemax simulations were done following this configuration and similarly, the most adapted and miniature micro-lenses that are commercially available were chosen to respond our needs.

The next step was obtaining the MEMS mirror and its associated chip, so a collaboration has been set up with the group Prof Huikai Xie, head of the biophotonics and microsystems laboratory of the university of Florida. Probe components as well the MEMS electronic chip were fabricated by our collaborators, while the assembly process was done in our laboratory. Once received, all necessary characterizations were performed to determine the mechanical properties and the scanning performance of the MEMS mirror. These characterizations reveal a good ability of the probe including its mirror to perform stable scanning with a relative high frame rate (2 images per second) over a 450x450  $\mu\text{m}$  FOV.

However, this mirror suffers from several drawbacks such as the non-stable frequency response where the FOV is strongly reduced when increasing the drive frequency which limited the maximal achieved speed into 2 images per second. Indeed, the optical scan angle variation of the horizontal and the vertical axis was not symmetrical ( $\pm 24^\circ$  for vertical axis and  $\pm 14^\circ$  for horizontal axis as maximal scanning range at 4 V) due to a non-uniformity of the deposited Al/SiO<sub>2</sub> layers on each axis actuators, which requires driving each axis with a different signal (in term of amplitude). Despite these minor drawbacks, this system has the ability to be coupled with the endomicroscope and to be tested for image acquisition.

However, my work on this part of my thesis was not simple where several difficulties and challenges have been encountered to achieve this stage. The main challenge was the lack of expertise to deal with MEMS devices and its components fabrication in our team and our laboratory. For that, the manufacturing of the MEMS components of the customized probe was entrusted to international experts in the field as an external service delivery, which took a long time to ensure the for delivery and unfortunately with different broken prototype. The fragility of the MEMS mirror made its transportation too complicated as well to its manipulation with high precautions.

**Short term prospects** Since that the characterizations measurements have not finished yet; the next step is to test the excitation and the collection efficiency of the probe head through fluorescent solutions and through fresh tissues later. Furthermore, a control and drive station is currently under development in order to ensure the MEMS mirror driving, synchronizing the scanning process with the photon counting detectors as well analogic to digital converting for image matrix reconstruction. A user interface will be implemented in this station to achieve a real-time display of the acquired image.

**Medium/Long term Prospects** Our long term intended goal is to get closer to the operating room and to reach the clinical trials phase with the best adapted instrument. This phase requires a more compact endomicroscope setup with the best performing scanning system as well as a biocompatible probe head. Actually, our developed probe head



components are fabricated through 3D printing materials that are not biocompatible. For this reason, developing a new probe head adapted to the clinical use is necessary. The new probe should overcome the drawbacks of the actual one in term of scanning speed and a stable FOV with the frequency variation.

### 9.3 A more robust and specific Tissue Database

Moving to the second part of this thesis work: the tissue database construction. Tissue characterization and data collection for this database started since the start of this research project. As described in the introduction, this tissue database aims to discriminate each brain tissue type, whether was a tumor or healthy, by its specific multimodal optical signature. To extract this multimodal signature, three different platforms are currently under our disposal, where with each we used a different excitation wavelength to cover a range from DUV to NIR passing through visible.

Therefore, the multimodality of contrasts is our investigation methodology and the proposed solution (table 1.3) that we are relying on in order to establish a reliable diagnosis response of an examined tissue. This multimodality is translated by collecting multiple optical parameters, is expected to overcome the biophysical limitations of individual optical modalities and to increase the overall accuracy in classifying the different tissue types.

Indeed, combining other excitation ranges with the NIR such as excitation in the DUV give the access to investigate supplementary fluorophores, that their autofluorescence could be correlated with the autofluorescence of NIR excited fluorophores. For instance, collagen fibers emit an SHG signal when exciting with NIR wavelengths, while these structures could fluoresce when exciting in the DUV range.

Through these platforms, a large database has been established and several discriminative parameters were extracted in previous works of our team members. Qualitative analysis studies were conducted in order to inspect the ability of TPF + SHG imaging to provide a reliable diagnosis that could the standard H&E stained images. Obtained results showed an accuracy of 72% to discriminate tumor from healthy tissues [98]. This accuracy was obtained when neuropathologists tried to establish a diagnosis result by looking on our TPF+SHG images instead of H&E images. However, a 28% false positive rate was the major limitation to obtain higher accuracy. This high false positive rate imposes the training of the neuropathologist on establishing diagnosis issued from our TPF+SHG images with the use of a larger cohort of tissues and a variety of images for a same tumor tissue type.

Consequently, the use of quantitative analysis became an important complementary to qualitative image analysis. In our previous works, this type of analysis has shown its importance and its ability to discriminate healthy, primary, and secondary brain tumors with high specificity and sensitivity. Spectral extracted parameters (molecular ratios, spectral intensity, proportion of a fluorophore emission) were combined with fluorescence lifetime parameters in order to establish such discrimination [98].

In my thesis work, we aimed to continue enlarging the tissue data base as well as to complete it with the non-investigated tasks. Through the study conducted and presented in chapter 4, the necessity of reducing the time of measurement post-excision on fresh tissues was pointed out in order to have consistent fluorescence signal to analyze. Furthermore, this study indicates that even with the alteration of the fluorescence and optical properties that occurs after sample fixation, the extracted properties from one and two-photon

excitation still have the ability to discriminate healthy brain tissues from tumor ones. Indeed, and through the study conducted in chapter 5, optical coefficients in the NIR window (scattering, absorption and anisotropy) were extracted and correlated with NIR spectral results after that were extracted within the visible wavelength range in previous works [215].

The second goal of my thesis work was to render the tissue database more specific and more robust by focusing on extracting multimodal parameters to discriminate the grades of each tumor type which help us to better understand the problematic linked to each type of tumor. In the first stage, we focused on two main tumor types that are the most widely incident between brain tumor types, glioma, and meningioma tumors. To reach this goal, we focused on quantitative analysis by investigating new molecular ratios, tracking molecular changes of each molecule and the variation of its different chemical form (free and protein-bound). New methods of analysis and data treatment were developed (phasor spectra, phasor FLIM, Long Lifetime Intensity Fraction extraction) to better visualize these variations and to track each component.

### 9.3.1 Spectral analysis for tissue discrimination

Spectral analysis of the detected fluorescence spectra is the simplest and the fastest technique used in for tissue characterization and that is accessible through the three different measurement platforms. Since the start of the tissue database establishment, spectral fitting with Gaussian curves, based on several parameters extracted from literature (table 1.4) was the standard treatment method used to analyze the spectral response at a molecular level. It allows to reveal and to quantify the emission proportion of each fluorophore in the total detected spectra, permitting therefore to monitor the emission variation of each molecule within the imaged tissue. Using this fitting method, all molecular ratios could be extracted and quantified allowing thus to follow the metabolic changes in tumor tissues.

However, this method suffers from the fitting associated errors which decrease its precision. Indeed, this method could offer a global vision of the spectral intensity variation within the compared tissue types but do not permits a global vision at a molecular level.

A new treatment method was developed and implemented in our analysis protocol: the spectral phasor analysis. This non fitting method allows rapid and reliable un-mixing of our NIR spectral images where each pixel in the image is Fourier transformed. It offers a global visualization of the spectral emission in each tissue type and permits to observe the spectral variation at a molecular level between the compared types [339], [340]. This treatment method was applied first on the glioma grades differentiation study presented in chapter 7, where it showed an excellent visual discrimination between the spectral emission changes of low grade glioma and healthy tissues. Similarly, high grade glioma had a specific phasor plot that differentiate it from low grade glioma and from healthy tissues. Seen its encouraging results, this method was then extended to be used for meningioma grades differentiation study in chapter 8. The obtained results in this study confirmed the usefulness of this graphical representation method to track precisely the global spectral variation within the tissue types.

Moving to molecular ratios, the standard ratio that was extensively inspected in the literature and in our previous works to monitor the alteration of metabolic process in tissues

is the redox ratio [98], [215]. This ratio considers the accumulation of NADH in cancer cells by rationing the content of NADH over FAD content to give an amount of the extent of the Warburg effect. It has shown its ability to discriminate between healthy and cancerous cells as well between healthy brain tissues from different tumor types but not to discriminate a tumor type from another. Despite being a promising factor to be relied on for tissue discrimination, this ratio is not sufficient alone to be a confident discrimination factor in the operating room. Correlation of this metabolic indicator with other parameters and molecular ratios could be a complementary add to the metabolic response inspection as well as to bring more reliability to the discrimination response extracted from the intrinsic optical response. Optical index ratio, which consist of rationing the NADH content over the porphyrins content, links the metabolic and the vascular aspect of the tissue. Using visible excitation range, this ratio has been observed varying significantly between healthy and cancerous bladder tissues [96] as well between healthy and brain cancerous tissues [215]. Therefore, larger inspections of this porphyrin related ratio should be performed in NIR excitation range. Another molecular ratio was also investigated which consist of rationing the lipopigments content over the porphyrin's contents. These two ratios led to an interesting differentiation between glioma and meningioma grades and also showed a variation between healthy and these different grades. However, this variation was not consistent but not significantly enough to be used as discrimination reliable thresholds or to be integrated in our 3D discrimination algorithms. Despite that these three presented molecular ratios led sometimes to relevant conclusions on tissue metabolism and their molecular composition variation, they were not reliable enough to be relied on to be used to establish a definite diagnosis.

Consequently, we headed towards the investigation of DUV extracted molecular ratios, where they showed a better discrimination ability than the NIR extracted one. Within the glioma study, the variation of these ratios was significant to be defined as discrimination threshold. These ratios managed to discriminate healthy tissues from tumor ones with high sensitivity and specificity (94% and 84% respectively) but did not manage to discriminate low grade from high grade glioma.

Seen this heterogeneity in molecular ratios, investigation of new biomarkers and diagnostic ratios based on specific structures within the tissues and that permits a significant discrimination was necessary. Therefore, we opened the door for a new factor to be investigated: the collagen presence in brain tissues and its variation within the cancerous tissues. These structures have a particular usefulness for our tissue database, where they present a high SHG source when excited non-linearly in NIR range, while they are an autofluorescence source when excited in DUV, which facilitate the tracking of the alteration of these proteins with the tumor growth as well with the tissue malignancy.

Firstly, the collagen density ratio between SHG and maximum fluorescence intensity was inspected in chapter 6, were SHG/TPF discriminated significantly fixed healthy tissues from other cancerous tissues and especially glioblastoma and meningioma tumors. However, low grade glioma was not discriminated due to the structure similarity of this type of tumor with healthy cortex tissues. Therefore, this factor has a strong potential to discriminate low grade glioma from high grade glioma. Thus, combining this factor with DUV ratios, could discriminate healthy, low grade and high grade glioma.

Seen this result, we extended the use of collagen density tracking toward meningioma grades discrimination by using the SHG intensity peak, the SHG content and the collagen fluorescence content extracted through DUV excitation. This type of tumors, arising from dura matter, is known by the presence of high collagen fibred organization. The obtained results were encouraging and showed a significant discrimination between healthy, grade I and grade II meningioma allowing thus its definition as a consistent discrimination threshold. From these observations, a quantitative indicator of SHG was used in the study of fresh biopsies from grade I and grade II tumor. It was chosen to track the intensity of SHG and resulted in significant discrimination of these grade (95% and 94.7%).

To this end, we can conclude that spectral analysis have provided interesting indicators to discriminate tumor from healthy tissue and has proven its high ability to be relied on for diagnosis tissue establishment. But despite its relevance for a global visualization of the spectral variation and to monitor the metabolic changes within the tissue, it's limited by several factors such as the difficulty to separate the fluorescence response at a molecular level due to the spectral overlap between the fluorescence emission of each fluorophore. Fluorophores like NADH could be presented in two forms within the tissues, free or protein-bound, where the spectral emission of each form is only separated by less than 20nm shift, making it very difficult to separate them through the fitting process or to be precisely tracked through the spectral phasor. Furthermore, spectral analysis depends strongly on the fluorophores within the tissues, which make the significant discrimination of regions with a low density too difficult. However, combining other analysis methods with the spectral one is necessary to improve our tissue database ability for tissue discrimination.

### 9.3.2 Fluorescence lifetime analysis for tissue discrimination

Similar to the spectral analysis, fluorescence lifetime analysis has proven ability to provide interesting indicators to discriminate tumor from healthy tissues. Fluorescence lifetime extracted parameters were correlated and combined with the spectral extracted parameters in order to obtain reliable discriminative response [98].

Contrary to the spectral analysis, fluorescence lifetime is independent from the fluorophores concentration while it depends mainly on its chemical microenvironment such pH, temperature, chemical binding to other molecules ... etc. In addition, the tissue metabolic state could be also monitored by inspecting the fluorescence lifetime of the free protein-bound components of each molecule as well to track their concentration changes.

As for treatment method, exponential fitting of the fluorescence decay curve is the standard method to determine the fluorescence lifetime of a single molecule. This method has been extensively used for fluorescence lifetime changes tracking in tumor tissues whether in our previous works [89], [215], [216]. However, this analysis method is limited by its fitting errors and did not provide a large marge of reliability. Consequently, and similar to the spectral analysis, we headed toward a non-fitting method: the phasor FLIM method, already described in the introduction. This method was implemented first in the study described in chapter 6, looking for a discrimination between healthy and different fixed tumor tissues. It was extended also the specific discrimination study of glioma and meningioma grades in chapters 7 and 8. This method overcomes the limitations of exponential fitting method and offers better visualization and a more precise analysis of all examined regions within the tissues. Furthermore, and to take advantage of the graphical representation of phasor

FLIM, a method to extract the Long Lifetime Intensity Fraction (LLIF) through the phasor FLIM plot was developed. Adding the LLIF extraction to our tissue database allows us to easily determine the free and protein-bound fraction of FAD and NADH within the tissue. It permits also to track the variation of these components between the different tissue types. Obtained results showed an interesting variation of these two components, where free NADH was observed increasing with the tissue malignancy in glioma grades, while free FAD increasing indicates a higher grade of meningioma.

To this end, combination of spectral and fluorescence lifetime related parameters constitute a powerful tool for tissue diagnosis. In this work, a variety of spectral and lifetime extracted parameters were largely investigated. A summary of the obtained variation in terms of all investigated parameters in glioma and meningioma grades is presented in table 9.1.

	Glioma		Meningioma	
	LG	HG	GI	GII
<b>Spectral intensity</b>	--	~~	-	--
<b>redox ratio</b>	+	+	--	--
<b>OI ratio</b>	+	+	~~	++
<b>LP ratio</b>	~~	+	+	++
<b>Tryp/NADH</b>	++	++	-	--
<b>Tryp/Tyr</b>	~~↓	~~↓	++	++
<b>Tryp/Coll</b>	+	+	-	--
<b>Collagen density</b>	~~	+	+	++
<b>NADH FLT</b>	~~	++	-	--
<b>FAD FLT</b>	~~	~~	+	++
<b>free FAD</b>	~~	-	+	++
<b>bound FAD</b>	~~	+	-	-
<b>free NADH</b>	+	++	-	-
<b>bound NADH</b>	~~	~~	+	++
<b>3D discrimination</b>				<b>GII vs GI</b>
<b>specificity</b>	84%		90%	94.7%
<b>sensitivity</b>	94%		100%	95%

**Table 9.1:** Summary of all the discrimination indicators in this thesis work to differentiate the grades of glioma and meningioma tumors. FLT: Fluorescence lifetime. The used signs indicate the variation of each indicator comparing with its counterpart in healthy tissues. + : slight increase/ ++ : significant increase/ - : slight decrease/ -- : significant decrease/ ~~ : similar/ ~~↓ : similar with a decrease trend. Specificity and sensitivity corresponds to the discrimination of tumor vs healthy.

Similar to the scanning probe head development, this part of my work was accompanied with several obstacles. Several needs should be addressed to simplify the work on this part. Firstly, the post-excision measurements time should be decreased, and therefore the delivery

time of the resected sample. Increasing the statistics by increasing the samples numbers is too important also. In addition, a more control on the provided sample location within the resection tissues should be obtained. This requires the presence of a member of our team in the operating room to choose the sample that we have access on. Indeed, an important need should be highlighted with the hospital, which consist to have access to tumor margins samples, or to healthy samples that are not extracted from epileptic tissues as well as healthy dura matter for meningioma grade differentiation. This access will enable the last step in our tissue characterization work before moving to in-vivo measurements. But, with the complicated administrative procedures to obtain the required certifications and approvals as well the very long time that it takes, it seems complicated to address these needs in the short term.

**Short term prospects** Maintaining the same methodology of looking for new discriminatory parameters between the different tissue types. To be more robust, this methodology requires increasing the statistics and therefore the samples number.

Categorizing each tumor type will continue. A large investigation study is currently underway in order to differentiate metastatic tumors types based on its originating organ and to try to specify each subtype in order to be discriminated.

**Medium/Long term prospects** Seen the huge multimodal data sets, it is necessary to develop an automated global data treatment interface with implementing artificial intelligence diagnosis methods, that enables a rapid and real-time information provide. This interface will facilitate the implementation of the tissue database with the endomicroscope setup. Therefore, it will constitute the link between the instrument which collect the real-time information, and the tissue data-base that establish the diagnosis response.

In this work, a two-photon fluorescence endomicroscope dedicated for intraoperative imaging during brain surgery was presented. On the road of reaching a multimodal intraoperative imaging device, different instrumental and biological problematics were addressed. In addition, an optical tissue database, that aims to collect, discriminate, and specify each brain tissue type by its specific optical signature, was also presented. This work, added to the previous works done by former members of our team, presents the largest autofluorescence-based tissue database specific to a human organ that is known until this day. Actually, this tissue database groups six different brain tissue types: control healthy tissues, low grade glioma, high grade glioma, grade I meningioma, grade II meningioma and metastasis. To discriminate these types, the multimodal measurements used, as well the different analysis methods, were presented. These multimodal data sets associated with several treatment and analysis methods were developed to establish significant discrimination thresholds between these tissue types and to highlight their ability of providing reliable and reproducible real-time diagnosis. Combining this constructed tissue database with the developed TPF endomicroscope will open the door to its clinical transfer and will support it with a real-time fast and automatic diagnosis establishment.

**Personal conclusion** I am grateful to have had the chance to do my PhD in France and at IJCLab laboratory. This lab gave me a great opportunity and helped me get introduced

to significant people and researchers in my domain. In addition, my stay in this lab affected my integration with the French community strongly. I had the opportunity to do my PhD in a multidisciplinary field and a research project that gather two different scientific aspects. During these three years, I have developed keen knowledge in the field of optical instrumentation, imaging as well in in the treatment and presentation of data. I have also discovered the MEMS devices development domain, that I have never worked on before. Through the interaction and discussion with our MEMS expert collaborators, I acquired strong knowledge in this field, especially in the development of imaging probes that involve MEMS mirrors. Indeed, I had the opportunity to work at one of the biggest research infrastructures in France and worldwide, “Synchrotron Soleil”. Through our collaboration, I had access to discover such structure and to meet, discuss and interact with bioimaging experts at DISCO beamline. Furthermore, I had gladly the chance to interact with neurosurgeons and to discover the hospital world. With every meeting or discussion with neurosurgeons and neuropathologists, I had new information to learn and a new knowledge to acquire in neuro-oncology which helped me to realize the concrete needs and expected benefits of the development in which I am involved. All these rich and multidisciplinary interactions were possible thanks to the several national and international collaborations elaborated by our team. Thus, I had the chance to attend national and international conferences in France, Germany, Canada and Portugal which helped me to more discover the different aspects of my domain and to meet as well international researchers which with we share the same problematic to respond through our research work.

As a personal opinion, my PhD thesis was successful since it provided me a rich and a strong learning experience. Integrating a dynamic research team and working within an ambitious research project led to this success. I have committed to this project during the past three years and I would gladly dedicate my time and effort after graduation to develop more this project and make it more clinically applicable.

# Bibliography

- [1] V. S. says, ‘Cancer History’, *News-Medical.net*, Dec. 02, 2009. <https://www.news-medical.net/health/Cancer-History.aspx> (accessed Jul. 24, 2020).
- [2] H. Ritchie and M. Roser, ‘Causes of Death’, *Our World in Data*, Feb. 2018, Accessed: Jul. 24, 2020. [Online]. Available: <https://ourworldindata.org/causes-of-death>.
- [3] ‘Top 7 most curable cancers based on 5-year relative survival rate’, Aug. 07, 2018. <https://www.medicalnewstoday.com/articles/322700> (accessed Jul. 24, 2020).
- [4] ‘How cancer starts, grows and spreads - Canadian Cancer Society’. <https://www.cancer.ca/en-ca/cancer-information/cancer-101/what-is-cancer/how-cancer-starts-grows-and-spreads/?region=qc> (accessed Jul. 24, 2020).
- [5] ‘Cell Division, Cancer | Learn Science at Scitable’. <https://www.nature.com/scitable/topicpage/cell-division-and-cancer-14046590/> (accessed Jul. 24, 2020).
- [6] ‘How cancer starts | Cancer Research UK’. <https://www.cancerresearchuk.org/about-cancer/what-is-cancer/how-cancer-starts> (accessed Jul. 24, 2020).
- [7] ‘Cancer’. <https://www.who.int/news-room/fact-sheets/detail/cancer> (accessed Jul. 24, 2020).
- [8] E. Y. Lin and J. W. Pollard, ‘Tumor-Associated Macrophages Press the Angiogenic Switch in Breast Cancer: Figure 1.’, *Cancer Res*, vol. 67, no. 11, pp. 5064–5066, Jun. 2007, doi: 10.1158/0008-5472.CAN-07-0912.
- [9] ‘What Is Cancer? - National Cancer Institute’, Sep. 17, 2007. <https://www.cancer.gov/about-cancer/understanding/what-is-cancer> (accessed Jul. 24, 2020).
- [10] ‘Le cancer en chiffres | Fondation ARC pour la recherche sur le cancer’. <https://www.fondation-arc.org/le-cancer-en-chiffres> (accessed Jul. 24, 2020).
- [11] F. Bray, J. Ferlay, I. Soerjomataram, R. L. Siegel, L. A. Torre, and A. Jemal, ‘Global cancer statistics 2018: GLOBOCAN estimates of incidence and mortality worldwide for 36 cancers in 185 countries’, *CA: A Cancer Journal for Clinicians*, vol. 68, no. 6, pp. 394–424, Nov. 2018, doi: 10.3322/caac.21492.
- [12] ‘IARC – INTERNATIONAL AGENCY FOR RESEARCH ON CANCER’. <https://www.iarc.fr/> (accessed Jul. 24, 2020).
- [13] M. Arnold *et al.*, ‘Progress in cancer survival, mortality, and incidence in seven high-income countries 1995-2014 (ICBP SURVMARK-2): a population-based study’, *Lancet Oncol.*, vol. 20, no. 11, pp. 1493–1505, 2019, doi: 10.1016/S1470-2045(19)30456-5.
- [14] ‘Survival Rates for Breast Cancer’. <https://www.cancer.org/cancer/breast-cancer/understanding-a-breast-cancer-diagnosis/breast-cancer-survival-rates.html> (accessed Jul. 24, 2020).
- [15] chief-editor, ‘Malignant Mesothelioma Cancer | Stages, Prognosis, Treatment’, *Mesothelioma.com*. <https://www.mesothelioma.com/mesothelioma/> (accessed Jul. 24, 2020).
- [16] ‘Home’, *Australian Institute of Health and Welfare*. <https://www.aihw.gov.au/> (accessed Jul. 24, 2020).
- [17] ‘Brain topics - patient education from Mayfield Brain & Spine’. [https://mayfieldclinic.com/ht\\_brain.htm](https://mayfieldclinic.com/ht_brain.htm) (accessed Jul. 24, 2020).



- [18] ‘Despite “incremental” progress, long-term survival rates “have not budged” in glioblastoma’. <https://www.healio.com/news/hematology-oncology/20190703/despite-incremental-progress-longterm-survival-rates-have-not-budged-in-glioblastoma> (accessed Jul. 24, 2020).
- [19] D. N. Louis *et al.*, ‘The 2016 World Health Organization Classification of Tumors of the Central Nervous System: a summary’, *Acta Neuropathol*, vol. 131, no. 6, pp. 803–820, Jun. 2016, doi: 10.1007/s00401-016-1545-1.
- [20] ‘Department of Neurosurgery Tokai University Hospital’. <http://neurosurgery.med.u-tokai.ac.jp/en/patients/bt/index.html> (accessed Jul. 24, 2020).
- [21] ‘Brain metastases - Symptoms and causes’, *Mayo Clinic*. <https://www.mayoclinic.org/diseases-conditions/brain-metastases/symptoms-causes/syc-20350136> (accessed Jul. 24, 2020).
- [22] ‘Brain Tumor - an overview | ScienceDirect Topics’. <https://www.sciencedirect.com/topics/neuroscience/brain-tumor> (accessed Jul. 24, 2020).
- [23] T. Backer-Grøndahl, B. H. Moen, and S. H. Torp, ‘The histopathological spectrum of human meningiomas’, p. 12.
- [24] ‘Meningiomas - Classifications, Risk Factors, Diagnosis and Treatment’. <https://www.aans.org/> (accessed Jul. 24, 2020).
- [25] D. N. Louis, H. Ohgaki, O. D. Wiestler, and W. K. Cavenee, *WHO classification of tumours of the central nervous system*, 4ème. Lyon-France: International Agency for research on cancer, 2016.
- [26] T. Siegal, ‘Clinical Relevance of Prognostic and Predictive Molecular Markers in Gliomas’, *Adv Tech Stand Neurosurg*, no. 43, pp. 91–108, 2016, doi: 10.1007/978-3-319-21359-0\_4.
- [27] K. Ichimura, Y. Narita, and C. E. Hawkins, ‘Diffusely infiltrating astrocytomas: pathology, molecular mechanisms and markers’, *Acta Neuropathol*, vol. 129, no. 6, pp. 789–808, Jun. 2015, doi: 10.1007/s00401-015-1439-7.
- [28] T. Wilson, M. Karajannis, and D. Harter, ‘Glioblastoma multiforme: State of the art and future therapeutics’, *Surg Neurol Int*, vol. 5, no. 1, p. 64, 2014, doi: 10.4103/2152-7806.132138.
- [29] Q. T. Ostrom *et al.*, ‘CBTRUS Statistical Report: Primary brain and other central nervous system tumors diagnosed in the United States in 2010-2014’, *Neuro-oncology*, vol. 19, no. suppl\_5, pp. v1–v88, 06 2017, doi: 10.1093/neuonc/nox158.
- [30] D. Krex *et al.*, ‘Long-term survival with glioblastoma multiforme’, *Brain*, vol. 130, no. 10, pp. 2596–2606, Oct. 2007, doi: 10.1093/brain/awm204.
- [31] L. Nayak, E. Q. Lee, and P. Y. Wen, ‘Epidemiology of brain metastases’, *Curr Oncol Rep*, vol. 14, no. 1, pp. 48–54, Feb. 2012, doi: 10.1007/s11912-011-0203-y.
- [32] R. A. Patchell, ‘The management of brain metastases’, *Cancer Treat. Rev.*, vol. 29, no. 6, pp. 533–540, Dec. 2003, doi: 10.1016/s0305-7372(03)00105-1.
- [33] W. A. Hall, H. R. Djalilian, E. S. Nussbaum, and K. H. Cho, ‘Long-term survival with metastatic cancer to the brain’, *Med. Oncol.*, vol. 17, no. 4, pp. 279–286, Nov. 2000, doi: 10.1007/BF02782192.
- [34] A. C. Tan, A. B. Heimberger, A. M. Menzies, N. Pavlakis, and M. Khasraw, ‘Immune Checkpoint Inhibitors for Brain Metastases’, *Curr Oncol Rep*, vol. 19, no. 6, p. 38, Jun. 2017, doi: 10.1007/s11912-017-0596-3.

- [35] ‘What Are the Actual Warning Signs of a Brain Tumor?’, *Health Essentials from Cleveland Clinic*, Feb. 27, 2020. <https://health.clevelandclinic.org/what-are-the-actual-warning-signs-of-a-brain-tumor/> (accessed Jul. 24, 2020).
- [36] ‘Warning Signs of Brain Tumor: Early Symptoms and More’, *Healthline*, Jun. 25, 2018. <https://www.healthline.com/health/brain-tumor-warning-signs> (accessed Jul. 24, 2020).
- [37] ‘Brain tumor - Symptoms and causes’, *Mayo Clinic*. <https://www.mayoclinic.org/diseases-conditions/brain-tumor/symptoms-causes/syc-20350084> (accessed Jul. 24, 2020).
- [38] J. E. Villanueva-Meyer, M. C. Mabray, and S. Cha, ‘Current Clinical Brain Tumor Imaging’, *Neurosurgery*, vol. 81, no. 3, pp. 397–415, Sep. 2017, doi: 10.1093/neuros/nyx103.
- [39] ‘Treatments, Tests and Therapies’. <https://www.hopkinsmedicine.org/health/treatment-tests-and-therapies> (accessed Jul. 24, 2020).
- [40] M. C. Mabray, R. F. Barajas, and S. Cha, ‘Modern Brain Tumor Imaging’, *Brain Tumor Res Treat*, vol. 3, no. 1, p. 8, 2015, doi: 10.14791/btrt.2015.3.1.8.
- [41] G.-H. Jahng, K.-L. Li, L. Ostergaard, and F. Calamante, ‘Perfusion Magnetic Resonance Imaging: A Comprehensive Update on Principles and Techniques’, *Korean J Radiol*, vol. 15, no. 5, p. 554, 2014, doi: 10.3348/kjr.2014.15.5.554.
- [42] S. R. Chandana, S. Movva, M. Arora, and T. Singh, ‘Primary brain tumors in adults’, *Am Fam Physician*, vol. 77, no. 10, pp. 1423–1430, May 2008.
- [43] M. N. Gurcan, L. E. Boucheron, A. Can, A. Madabhushi, N. M. Rajpoot, and B. Yener, ‘Histopathological image analysis: a review’, *IEEE Rev Biomed Eng*, vol. 2, pp. 147–171, 2009, doi: 10.1109/RBME.2009.2034865.
- [44] A. H. Fischer, K. A. Jacobson, J. Rose, and R. Zeller, ‘Hematoxylin and eosin staining of tissue and cell sections’, *CSH Protoc*, vol. 2008, p. pdb.prot4986, May 2008, doi: 10.1101/pdb.prot4986.
- [45] ‘Surgery for Brain Tumors’, *txo*. <https://www.texasoncology.com/types-of-cancer/brain-cancer/surgery-for-brain-tumors> (accessed Jul. 24, 2020).
- [46] T. Yoshimoto, M. Fujimura, T. Kumabe, T. Tominaga, H. Jokura, and R. Shirane, ‘Routine clinical adoption of magnetic resonance imaging was associated with better outcome after surgery in elderly patients with a malignant astrocytic tumour: a retrospective review’, *Acta Neurochirurgica*, vol. 146, no. 3, pp. 251–255, Mar. 2004, doi: 10.1007/s00701-003-0191-2.
- [47] H. Duffau *et al.*, ‘Intraoperative mapping of the subcortical language pathways using direct stimulations. An anatomo-functional study’, *Brain*, vol. 125, no. Pt 1, pp. 199–214, Jan. 2002, doi: 10.1093/brain/awf016.
- [48] G. E. Keles, D. A. Lundin, K. R. Lamborn, E. F. Chang, G. Ojemann, and M. S. Berger, ‘Intraoperative subcortical stimulation mapping for hemispherical perirolandic gliomas located within or adjacent to the descending motor pathways: evaluation of morbidity and assessment of functional outcome in 294 patients’, *J. Neurosurg.*, vol. 100, no. 3, pp. 369–375, Mar. 2004, doi: 10.3171/jns.2004.100.3.0369.
- [49] A. Majos, K. Tybor, L. Stefańczyk, and B. Góraj, ‘Cortical mapping by functional magnetic resonance imaging in patients with brain tumors’, *Eur Radiol*, vol. 15, no. 6, pp. 1148–1158, Jun. 2005, doi: 10.1007/s00330-004-2565-0.

- [50] P. C. Reinacher and V. van Velthoven, ‘Intraoperative ultrasound imaging: practical applicability as a real-time navigation system’, *Acta Neurochir. Suppl.*, vol. 85, pp. 89–93, 2003, doi: 10.1007/978-3-7091-6043-5\_12.
- [51] G. Delaney, S. Jacob, C. Featherstone, and M. Barton, ‘The role of radiotherapy in cancer treatment: estimating optimal utilization from a review of evidence-based clinical guidelines’, *Cancer*, vol. 104, no. 6, pp. 1129–1137, Sep. 2005, doi: 10.1002/cncr.21324.
- [52] ‘Radiation Therapy for Brain Tumors’, *txo*. <https://www.texasoncology.com/types-of-cancer/brain-cancer/radiation-therapy-for-brain-tumors> (accessed Jul. 24, 2020).
- [53] ‘Brain Cancer’, *txo*. <https://www.texasoncology.com/types-of-cancer/brain-cancer> (accessed Jul. 24, 2020).
- [54] P. N. Prasad, *Introduction to Biophotonics*. Hoboken, NJ, USA: John Wiley & Sons, Inc., 2003.
- [55] D. Huang *et al.*, ‘Optical coherence tomography’, *Science*, vol. 254, no. 5035, pp. 1178–1181, Nov. 1991, doi: 10.1126/science.1957169.
- [56] M. E. Brezinski and J. G. Fujimoto, ‘Optical coherence tomography: high-resolution imaging in nontransparent tissue’, *IEEE J. Select. Topics Quantum Electron.*, vol. 5, no. 4, pp. 1185–1192, Aug. 1999, doi: 10.1109/2944.796345.
- [57] J. M. Schmitt, M. J. Yadlowsky, and R. F. Bonner, ‘Subsurface imaging of living skin with optical coherence microscopy’, *Dermatology (Basel)*, vol. 191, no. 2, pp. 93–98, 1995, doi: 10.1159/000246523.
- [58] F.-J. Kao, G. Keiser, and A. Gogoi, *Advanced optical methods for brain imaging*. 2019.
- [59] J. Men *et al.*, ‘Optical Coherence Tomography for Brain Imaging and Developmental Biology’, *IEEE J Sel Top Quantum Electron*, vol. 22, no. 4, Aug. 2016, doi: 10.1109/JSTQE.2015.2513667.
- [60] J. F. de Boer, B. Cense, B. H. Park, M. C. Pierce, G. J. Tearney, and B. E. Bouma, ‘Improved signal-to-noise ratio in spectral-domain compared with time-domain optical coherence tomography’, *Opt. Lett.*, vol. 28, no. 21, p. 2067, Nov. 2003, doi: 10.1364/OL.28.002067.
- [61] W. Drexler, U. Morgner, R. K. Ghanta, F. X. Kärtner, J. S. Schuman, and J. G. Fujimoto, ‘Ultrahigh-resolution ophthalmic optical coherence tomography’, *Nat. Med.*, vol. 7, no. 4, pp. 502–507, Apr. 2001, doi: 10.1038/86589.
- [62] M. Ibne Mokbul, ‘Optical Coherence Tomography: Basic Concepts and Applications in Neuroscience Research’, *J Med Eng*, vol. 2017, p. 3409327, 2017, doi: 10.1155/2017/3409327.
- [63] E. M. Frohman, J. G. Fujimoto, T. C. Frohman, P. A. Calabresi, G. Cutter, and L. J. Balcer, ‘Optical coherence tomography: a window into the mechanisms of multiple sclerosis’, *Nat Clin Pract Neurol*, vol. 4, no. 12, pp. 664–675, Dec. 2008, doi: 10.1038/ncpneuro0950.
- [64] K. L. Thomson, J. M. Yeo, B. Waddell, J. R. Cameron, and S. Pal, ‘A systematic review and meta-analysis of retinal nerve fiber layer change in dementia, using optical coherence tomography’, *Alzheimer’s & Dementia: Diagnosis, Assessment & Disease Monitoring*, vol. 1, no. 2, pp. 136–143, Jun. 2015, doi: 10.1016/j.dadm.2015.03.001.
- [65] A. Giese *et al.*, ‘Non-invasive intraoperative optical coherence tomography of the resection cavity during surgery of intrinsic brain tumors’, San Jose, CA, Feb. 2006, p. 60782Z, doi: 10.1117/12.674436.
- [66] H. J. Böhringer, E. Lanckenau, F. Stellmacher, E. Reusche, G. Hüttmann, and A. Giese, ‘Imaging of human brain tumor tissue by near-infrared laser coherence tomography’,

- Acta Neurochir (Wien)*, vol. 151, no. 5, pp. 507–517; discussion 517, May 2009, doi: 10.1007/s00701-009-0248-y.
- [67] H. J. Böhringer, E. Lanke, V. Rohde, G. Hüttmann, and A. Giese, ‘Optical coherence tomography for experimental neuroendoscopy’, *Minim Invasive Neurosurg*, vol. 49, no. 5, pp. 269–275, Oct. 2006, doi: 10.1055/s-2006-954574.
- [68] O. Assayag *et al.*, ‘Imaging of non-tumorous and tumorous human brain tissues with full-field optical coherence tomography’, *Neuroimage Clin*, vol. 2, pp. 549–557, 2013, doi: 10.1016/j.nicl.2013.04.005.
- [69] C.-P. Liang *et al.*, ‘Concurrent multiscale imaging with magnetic resonance imaging and optical coherence tomography’, *J Biomed Opt*, vol. 18, no. 4, p. 046015, Apr. 2013, doi: 10.1117/1.JBO.18.4.040506.
- [70] C. S. Carignan and Y. Yagi, ‘Optical endomicroscopy and the road to real-time, in vivo pathology: present and future’, *Diagn Pathol*, vol. 7, no. 1, p. 98, Dec. 2012, doi: 10.1186/1746-1596-7-98.
- [71] H. J. Böhringer *et al.*, ‘Time-domain and spectral-domain optical coherence tomography in the analysis of brain tumor tissue: TIME-DOMAIN AND SPECTRAL-DOMAIN OPTICAL COHERENCE TOMOGRAPHY OF GLIOMA TISSUE’, *Lasers Surg. Med.*, vol. 38, no. 6, pp. 588–597, Jul. 2006, doi: 10.1002/lsm.20353.
- [72] D. DePaoli *et al.*, ‘Rise of Raman spectroscopy in neurosurgery: a review’, *J Biomed Opt*, vol. 25, no. 5, pp. 1–36, May 2020, doi: 10.1117/1.JBO.25.5.050901.
- [73] ‘Lesson 1. Basic of Raman scattering’, *Nanophoton corp*, Mar. 12, 2019. <https://www.nanophoton.net/raman-spectroscopy/lessons/lesson-1> (accessed Jul. 24, 2020).
- [74] M. Brusatori, G. Auner, T. Noh, L. Scarpace, B. Broadbent, and S. N. Kalkanis, ‘Intraoperative Raman Spectroscopy’, *Neurosurg. Clin. N. Am.*, vol. 28, no. 4, pp. 633–652, Oct. 2017, doi: 10.1016/j.nec.2017.05.014.
- [75] J. Desroches *et al.*, ‘A new method using Raman spectroscopy for in vivo targeted brain cancer tissue biopsy’, *Sci Rep*, vol. 8, no. 1, p. 1792, Dec. 2018, doi: 10.1038/s41598-018-20233-3.
- [76] M. Jermyn *et al.*, ‘Intraoperative brain cancer detection with Raman spectroscopy in humans’, *Sci Transl Med*, vol. 7, no. 274, p. 274ra19, Feb. 2015, doi: 10.1126/scitranslmed.aaa2384.
- [77] M. Jermyn *et al.*, ‘Raman spectroscopy detects distant invasive brain cancer cells centimeters beyond MRI capability in humans’, *Biomed. Opt. Express*, vol. 7, no. 12, p. 5129, Dec. 2016, doi: 10.1364/BOE.7.005129.
- [78] J. Desroches *et al.*, ‘Characterization of a Raman spectroscopy probe system for intraoperative brain tissue classification’, *Biomed Opt Express*, vol. 6, no. 7, pp. 2380–2397, Jul. 2015, doi: 10.1364/BOE.6.002380.
- [79] ‘ODS MEDICAL | Developing AI-enabled optical detection systems for tumor margin assessment’. <https://odsmc.com/> (accessed Jul. 24, 2020).
- [80] Y. Zhang, H. Hong, and W. Cai, ‘Imaging with Raman spectroscopy’, *Curr Pharm Biotechnol*, vol. 11, no. 6, pp. 654–661, Sep. 2010, doi: 10.2174/138920110792246483.
- [81] K. Eberhardt, C. Stiebing, C. Matthäus, M. Schmitt, and J. Popp, ‘Advantages and limitations of Raman spectroscopy for molecular diagnostics: an update’, *Expert Rev. Mol. Diagn.*, vol. 15, no. 6, pp. 773–787, Jun. 2015, doi: 10.1586/14737159.2015.1036744.
- [82] A. C. Croce and G. Bottiroli, ‘Autofluorescence spectroscopy and imaging: a tool for biomedical research and diagnosis’, *Eur J Histochem*, vol. 58, no. 4, Dec. 2014, doi: 10.4081/ejh.2014.2461.

- [83] A. M. Chorvatova and D. Chorvat, ‘Tissue fluorophores and their spectroscopic characteristics’, in *Fluorescence Lifetime Spectroscopy and Imaging*, 2014.
- [84] G. Papayan, N. Petrishchev, and M. Galagudza, ‘Autofluorescence spectroscopy for NADH and flavoproteins redox state monitoring in the isolated rat heart subjected to ischemia-reperfusion’, *Photodiagnosis and Photodynamic Therapy*, vol. 11, no. 3, pp. 400–408, Sep. 2014, doi: 10.1016/j.pdpdt.2014.05.003.
- [85] S. A. Toms, W.-C. Lin, R. J. Weil, M. D. Johnson, E. D. Jansen, and A. Mahadevan-Jansen, ‘Intraoperative Optical Spectroscopy Identifies Infiltrating Glioma Margins with High Sensitivity’, *Operative Neurosurgery*, vol. 57, pp. 382–391, Oct. 2005, doi: 10.1227/01.NEU.000176855.39826.2D.
- [86] W. H. Koppenol, P. L. Bounds, and C. V. Dang, ‘Otto Warburg’s contributions to current concepts of cancer metabolism’, *Nat. Rev. Cancer*, vol. 11, no. 5, pp. 325–337, May 2011, doi: 10.1038/nrc3038.
- [87] Y. Malthièry and F. Savagner, ‘Métabolisme énergétique de la cellule cancéreuse: exemple des tumeurs endocrines riches en mitochondries’, *Annales d’Endocrinologie*, vol. 67, no. 3, pp. 205–213, Jun. 2006, doi: 10.1016/S0003-4266(06)72588-4.
- [88] B.-H. Li and S.-S. Xie, ‘Autofluorescence excitation-emission matrices for diagnosis of colonic cancer’, *World J. Gastroenterol.*, vol. 11, no. 25, pp. 3931–3934, Jul. 2005, doi: 10.3748/wjg.v11.i25.3931.
- [89] M. Zanella *et al.*, ‘Multimodal optical analysis discriminates freshly extracted human sample of gliomas, metastases and meningiomas from their appropriate controls’, *Sci Rep*, vol. 7, no. 1, p. 41724, Mar. 2017, doi: 10.1038/srep41724.
- [90] W. H. Yong *et al.*, ‘Distinction of brain tissue, low grade and high grade glioma with time-resolved fluorescence spectroscopy’, *Front. Biosci.*, vol. 11, pp. 1255–1263, May 2006, doi: 10.2741/1878.
- [91] Z. Liu *et al.*, ‘Mapping metabolic changes by noninvasive, multiparametric, high-resolution imaging using endogenous contrast’, *Sci. Adv.*, vol. 4, no. 3, p. eaap9302, Mar. 2018, doi: 10.1126/sciadv.aap9302.
- [92] Q. Liu *et al.*, ‘Compact point-detection fluorescence spectroscopy system for quantifying intrinsic fluorescence redox ratio in brain cancer diagnostics’, *J. Biomed. Opt.*, vol. 16, no. 3, p. 037004, 2011, doi: 10.1117/1.3558840.
- [93] M. C. Skala *et al.*, ‘In vivo multiphoton microscopy of NADH and FAD redox states, fluorescence lifetimes, and cellular morphology in precancerous epithelia’, *Proc. Natl. Acad. Sci. U.S.A.*, vol. 104, no. 49, pp. 19494–19499, Dec. 2007, doi: 10.1073/pnas.0708425104.
- [94] R. Drezek *et al.*, ‘Autofluorescence Microscopy of Fresh Cervical-Tissue Sections Reveals Alterations in Tissue Biochemistry with Dysplasia¶’, *Photochemistry and Photobiology*, vol. 73, no. 6, pp. 636–641, Jun. 2001, doi: 10.1562/0031-8655(2001)0730636AMOFCT2.0.CO2.
- [95] A. Varone *et al.*, ‘Endogenous two-photon fluorescence imaging elucidates metabolic changes related to enhanced glycolysis and glutamine consumption in precancerous epithelial tissues’, *Cancer Res.*, vol. 74, no. 11, pp. 3067–3075, Jun. 2014, doi: 10.1158/0008-5472.CAN-13-2713.
- [96] S. Palmer, K. Litvinova, A. Dunaev, J. Yubo, D. McGloin, and G. Nabi, ‘Optical redox ratio and endogenous porphyrins in the detection of urinary bladder cancer: A patient biopsy analysis’, *J. Biophotonics*, p. 12, 2016.
- [97] D. A. Haidar, B. Leh, M. Zanella, and R. Siebert, ‘Spectral and lifetime domain measurements of rat brain tumors’, p. 15, 2015.

- [98] F. Poulon *et al.*, ‘Real-time Brain Tumor imaging with endogenous fluorophores: a diagnosis proof-of-concept study on fresh human samples’, *Sci Rep*, vol. 8, no. 1, p. 14888, Dec. 2018, doi: 10.1038/s41598-018-33134-2.
- [99] ‘Widefield Fluorescence Microscopy: What you need to know’, *Scientifica*. <https://www.scientifica.uk.com/learning-zone/widefield-fluorescence-microscopy> (accessed Jul. 24, 2020).
- [100] ‘Confocal Microscopy - Introduction | Solutions Olympus pour les sciences de la vie’. <https://www.olympus-lifescience.com/fr/microscope-resource/primer/techniques/confocal/confocalintro/> (accessed Jul. 24, 2020).
- [101] ‘Confocal Microscopy | Principle & Applications | ibidi’. <https://ibidi.com/content/216-confocal-microscopy> (accessed Jul. 24, 2020).
- [102] J. Jonkman, C. M. Brown, and R. W. Cole, ‘Quantitative confocal microscopy: beyond a pretty picture’, *Methods Cell Biol.*, vol. 123, pp. 113–134, 2014, doi: 10.1016/B978-0-12-420138-5.00007-0.
- [103] R. K. P. Benninger and D. W. Piston, ‘Two-Photon Excitation Microscopy for the Study of Living Cells and Tissues’, *Current Protocols in Cell Biology*, vol. 59, no. 1, pp. 4.11.1-4.11.24, Jun. 2013, doi: 10.1002/0471143030.cb0411s59.
- [104] J. M. Dąbrowski *et al.*, ‘Engineering of relevant photodynamic processes through structural modifications of metallotetrapyrrolic photosensitizers’, *Coordination Chemistry Reviews*, vol. 325, pp. 67–101, Oct. 2016, doi: 10.1016/j.ccr.2016.06.007.
- [105] A. M. Smith, M. C. Mancini, and S. Nie, ‘Bioimaging: second window for in vivo imaging’, *Nat Nanotechnol*, vol. 4, no. 11, pp. 710–711, Nov. 2009, doi: 10.1038/nnano.2009.326.
- [106] H. Bao, A. Boussioutas, R. Jeremy, S. Russell, and M. Gu, ‘Second harmonic generation imaging via nonlinear endomicroscopy’, *Opt. Express*, vol. 18, no. 2, p. 1255, Jan. 2010, doi: 10.1364/OE.18.001255.
- [107] G. Thomas, J. van Voskuilen, H. C. Gerritsen, and H. J. C. M. Sterenborg, ‘Advances and challenges in label-free nonlinear optical imaging using two-photon excitation fluorescence and second harmonic generation for cancer research’, *J. Photochem. Photobiol. B, Biol.*, vol. 141, pp. 128–138, Dec. 2014, doi: 10.1016/j.jphotobiol.2014.08.025.
- [108] D. A. Dombeck, K. A. Kasischke, H. D. Vishwasrao, M. Ingelsson, B. T. Hyman, and W. W. Webb, ‘Uniform polarity microtubule assemblies imaged in native brain tissue by second-harmonic generation microscopy’, *Proc. Natl. Acad. Sci. U.S.A.*, vol. 100, no. 12, pp. 7081–7086, Jun. 2003, doi: 10.1073/pnas.0731953100.
- [109] P. Campagnola, ‘Second harmonic generation imaging microscopy: applications to diseases diagnostics’, *Anal. Chem.*, vol. 83, no. 9, pp. 3224–3231, May 2011, doi: 10.1021/ac1032325.
- [110] I. Freund, M. Deutsch, and A. Sprecher, ‘Connective tissue polarity. Optical second-harmonic microscopy, crossed-beam summation, and small-angle scattering in rat-tail tendon’, *Biophys. J.*, vol. 50, no. 4, pp. 693–712, Oct. 1986, doi: 10.1016/S0006-3495(86)83510-X.
- [111] G. Cox, E. Kable, A. Jones, I. Fraser, F. Manconi, and M. D. Gorrell, ‘3-dimensional imaging of collagen using second harmonic generation’, *J. Struct. Biol.*, vol. 141, no. 1, pp. 53–62, Jan. 2003, doi: 10.1016/s1047-8477(02)00576-2.
- [112] P. Stoller, B.-M. Kim, A. M. Rubenchik, K. M. Reiser, and L. B. Da Silva, ‘Polarization-dependent optical second-harmonic imaging of a rat-tail tendon’, *J Biomed Opt*, vol. 7, no. 2, pp. 205–214, Apr. 2002, doi: 10.1117/1.1431967.

- [113] A. Zoumi, X. Lu, G. S. Kassab, and B. J. Tromberg, ‘Imaging coronary artery microstructure using second-harmonic and two-photon fluorescence microscopy’, *Biophys. J.*, vol. 87, no. 4, pp. 2778–2786, Oct. 2004, doi: 10.1529/biophysj.104.042887.
- [114] S.-P. Tai *et al.*, ‘Optical biopsy of fixed human skin with backward-collected optical harmonics signals’, *Opt Express*, vol. 13, no. 20, pp. 8231–8242, Oct. 2005, doi: 10.1364/opex.13.008231.
- [115] J. Han, J. C. Daniel, and G. D. Pappas, ‘Expression of type VI collagen during glioblastoma cell invasion in brain tissue cultures’, *Cancer Letters*, vol. 88, no. 2, pp. 127–132, Jan. 1995, doi: 10.1016/0304-3835(94)03627-U.
- [116] K. B. Pointer, P. A. Clark, A. B. Schroeder, M. S. Salamat, K. W. Eliceiri, and J. S. Kuo, ‘Association of collagen architecture with glioblastoma patient survival’, *J. Neurosurg.*, vol. 126, no. 6, pp. 1812–1821, Jun. 2017, doi: 10.3171/2016.6.JNS152797.
- [117] H. Li, J. Yu, R. Zhang, X. Li, and W. Zheng, ‘Two-photon excitation fluorescence lifetime imaging microscopy: A promising diagnostic tool for digestive tract tumors’, *J. Innov. Opt. Health Sci.*, vol. 12, no. 05, p. 1930009, Sep. 2019, doi: 10.1142/S179354581930009X.
- [118] S. Coda, P. D. Siersema, G. W. H. Stamp, and A. V. Thillainayagam, ‘Biophotonic endoscopy: a review of clinical research techniques for optical imaging and sensing of early gastrointestinal cancer’, *Endosc Int Open*, vol. 3, no. 5, pp. E380-392, Oct. 2015, doi: 10.1055/s-0034-1392513.
- [119] ‘Institut de Biologie Intégrative de la Cellule - FLIM@Gif’. <https://www.i2bc.paris-saclay.fr/spip.php?article1494> (accessed Jul. 24, 2020).
- [120] L. Marcu, P. M. W. French, and D. S. Elson, Eds., *Fluorescence lifetime spectroscopy and imaging: principles and applications in biomedical diagnostics*. Boca Raton: CRC Press/Taylor & Francis Group, 2014.
- [121] L.-C. Chen, W. R. Lloyd, C.-W. Chang, D. Sud, and M.-A. Mycek, ‘Fluorescence lifetime imaging microscopy for quantitative biological imaging’, *Methods Cell Biol.*, vol. 114, pp. 457–488, 2013, doi: 10.1016/B978-0-12-407761-4.00020-8.
- [122] D. Elson *et al.*, ‘Biomedical Applications of Fluorescence Lifetime Imaging’, *Optics & Photonics News*, vol. 13, no. 11, p. 26, Nov. 2002, doi: 10.1364/OPN.13.11.000026.
- [123] S. R. Kantelhardt *et al.*, ‘In vivo multiphoton tomography and fluorescence lifetime imaging of human brain tumor tissue’, *J Neurooncol*, vol. 127, no. 3, pp. 473–482, May 2016, doi: 10.1007/s11060-016-2062-8.
- [124] L. Marcu *et al.*, ‘Fluorescence Lifetime Spectroscopy of Glioblastoma Multiforme’, *Photochemistry and Photobiology*, vol. 80, no. 1, pp. 98–103, Apr. 2007, doi: 10.1111/j.1751-1097.2004.tb00055.x.
- [125] P. V. Butte *et al.*, ‘Intraoperative delineation of primary brain tumors using time-resolved fluorescence spectroscopy’, *J Biomed Opt*, vol. 15, no. 2, p. 027008, Apr. 2010, doi: 10.1117/1.3374049.
- [126] P. V. Butte, A. N. Mamelak, M. Nuno, S. I. Bannykh, K. L. Black, and L. Marcu, ‘Fluorescence lifetime spectroscopy for guided therapy of brain tumors’, *Neuroimage*, vol. 54 Suppl 1, pp. S125-135, Jan. 2011, doi: 10.1016/j.neuroimage.2010.11.001.
- [127] Y. Sun *et al.*, ‘Fluorescence lifetime imaging microscopy for brain tumor image-guided surgery’, *J Biomed Opt*, vol. 15, no. 5, p. 056022, Oct. 2010, doi: 10.1117/1.3486612.
- [128] M. Y. Berezin and S. Achilefu, ‘Fluorescence lifetime measurements and biological imaging’, *Chem. Rev.*, vol. 110, no. 5, pp. 2641–2684, May 2010, doi: 10.1021/cr900343z.

- [129] M. A. Digman, V. R. Caiolfa, M. Zamai, and E. Gratton, ‘The Phasor Approach to Fluorescence Lifetime Imaging Analysis’, *Biophysical Journal*, vol. 94, no. 2, pp. L14–L16, Jan. 2008, doi: 10.1529/biophysj.107.120154.
- [130] Ottavia Golfetto, ‘PHASOR APPROACH TO FLUORESCENCE LIFETIME MICROSCOPY TO MEASURE STEM CELL DIFFERENTIATION’, Magistrali biennali, UNIVERSITÀ DEGLI STUDI DI PADOVA, 2010.
- [131] G. I. Redford and R. M. Clegg, ‘Polar Plot Representation for Frequency-Domain Analysis of Fluorescence Lifetimes’, *J Fluoresc*, vol. 15, no. 5, pp. 805–815, Sep. 2005, doi: 10.1007/s10895-005-2990-8.
- [132] A. H. A. Clayton, Q. S. Hanley, and P. J. Verveer, ‘Graphical representation and multicomponent analysis of single-frequency fluorescence lifetime imaging microscopy data’, *J Microsc*, vol. 213, no. 1, pp. 1–5, Jan. 2004, doi: 10.1111/j.1365-2818.2004.01265.x.
- [133] C. G. Hadjipanayis, G. Widhalm, and W. Stummer, ‘What is the Surgical Benefit of Utilizing 5-Aminolevulinic Acid for Fluorescence-Guided Surgery of Malignant Gliomas?’, *Neurosurgery*, vol. 77, no. 5, pp. 663–673, Nov. 2015, doi: 10.1227/NEU.0000000000000929.
- [134] S. R. Ennis *et al.*, ‘Transport of 5-aminolevulinic acid between blood and brain’, *Brain Res.*, vol. 959, no. 2, pp. 226–234, Jan. 2003, doi: 10.1016/s0006-8993(02)03749-6.
- [135] E. Belykh *et al.*, ‘Intraoperative Fluorescence Imaging for Personalized Brain Tumor Resection: Current State and Future Directions’, *Front. Surg.*, vol. 3, Oct. 2016, doi: 10.3389/fsurg.2016.00055.
- [136] R. Díez Valle, S. Tejada Solis, M. A. Idoate Gastearena, R. García de Eulate, P. Domínguez Echávarri, and J. Aristu Mendiroz, ‘Surgery guided by 5-aminolevulinic fluorescence in glioblastoma: volumetric analysis of extent of resection in single-center experience’, *J. Neurooncol.*, vol. 102, no. 1, pp. 105–113, Mar. 2011, doi: 10.1007/s11060-010-0296-4.
- [137] P. P. Panciani *et al.*, ‘Fluorescence and image guided resection in high grade glioma’, *Clin Neurol Neurosurg*, vol. 114, no. 1, pp. 37–41, Jan. 2012, doi: 10.1016/j.clineuro.2011.09.001.
- [138] P. P. Panciani, M. Fontanella, D. Garbossa, A. Agnoletti, A. Ducati, and M. Lanotte, ‘5-aminolevulinic acid and neuronavigation in high-grade glioma surgery: results of a combined approach’, *Neurocirugia (Astur)*, vol. 23, no. 1, pp. 23–28, Feb. 2012, doi: 10.1016/j.neucir.2012.04.003.
- [139] W. Stummer, A. Novotny, H. Stepp, C. Goetz, K. Bise, and H. J. Reulen, ‘Fluorescence-guided resection of glioblastoma multiforme by using 5-aminolevulinic acid-induced porphyrins: a prospective study in 52 consecutive patients’, *J. Neurosurg.*, vol. 93, no. 6, pp. 1003–1013, Dec. 2000, doi: 10.3171/jns.2000.93.6.1003.
- [140] L. Alston *et al.*, ‘Spectral complexity of 5-ALA induced PpIX fluorescence in guided surgery: a clinical study towards the discrimination of healthy tissue and margin boundaries in high and low grade gliomas’, *Biomed. Opt. Express*, vol. 10, no. 5, p. 2478, May 2019, doi: 10.1364/BOE.10.002478.
- [141] W. Stummer *et al.*, ‘Fluorescence-guided surgery with 5-aminolevulinic acid for resection of malignant glioma: a randomised controlled multicentre phase III trial’, *Lancet Oncol.*, vol. 7, no. 5, pp. 392–401, May 2006, doi: 10.1016/S1470-2045(06)70665-9.



- [142] ‘Intraoperative Imaging of Glioblastoma | Neupsy Key’. <https://neupsykey.com/intraoperative-imaging-of-glioblastoma/> (accessed Jul. 25, 2020).
- [143] P. A. Valdés *et al.*, ‘Quantitative fluorescence using 5-aminolevulinic acid-induced protoporphyrin IX biomarker as a surgical adjunct in low-grade glioma surgery’, *J. Neurosurg.*, vol. 123, no. 3, pp. 771–780, Sep. 2015, doi: 10.3171/2014.12.JNS14391.
- [144] B. Montcel, L. Mahieu-Williams, X. Armoiry, D. Meyronet, and J. Guyotat, ‘Two-peaked 5-ALA-induced PpIX fluorescence emission spectrum distinguishes glioblastomas from low grade gliomas and infiltrative component of glioblastomas’, *Biomed Opt Express*, vol. 4, no. 4, pp. 548–558, Apr. 2013, doi: 10.1364/BOE.4.000548.
- [145] N. Sanai *et al.*, ‘Intraoperative confocal microscopy in the visualization of 5-aminolevulinic acid fluorescence in low-grade gliomas’, *J. Neurosurg.*, vol. 115, no. 4, pp. 740–748, Oct. 2011, doi: 10.3171/2011.6.JNS11252.
- [146] S. Utsuki *et al.*, ‘Fluorescence-guided resection of metastatic brain tumors using a 5-aminolevulinic acid-induced protoporphyrin IX: pathological study’, *Brain Tumor Pathol*, vol. 24, no. 2, pp. 53–55, 2007, doi: 10.1007/s10014-007-0223-3.
- [147] A. Nabavi *et al.*, ‘Five-aminolevulinic acid for fluorescence-guided resection of recurrent malignant gliomas: a phase ii study’, *Neurosurgery*, vol. 65, no. 6, pp. 1070–1076; discussion 1076–1077, Dec. 2009, doi: 10.1227/01.NEU.0000360128.03597.C7.
- [148] P. A. Valdés, D. W. Roberts, F.-K. Lu, and A. Golby, ‘Optical technologies for intraoperative neurosurgical guidance’, *Neurosurg Focus*, vol. 40, no. 3, p. E8, Mar. 2016, doi: 10.3171/2015.12.FOCUS15550.
- [149] T. Kuroiwa, Y. Kajimoto, and T. Ohta, ‘Development of a Fluorescein Operative Microscope for use During Malignant Glioma Surgery’, *Surgical Neurology*, vol. 50, no. 1, pp. 41–49, Jul. 1998, doi: 10.1016/S0090-3019(98)00055-X.
- [150] C. Chi *et al.*, ‘Intraoperative Imaging-Guided Cancer Surgery: From Current Fluorescence Molecular Imaging Methods to Future Multi-Modality Imaging Technology’, *Theranostics*, vol. 4, no. 11, pp. 1072–1084, 2014, doi: 10.7150/thno.9899.
- [151] J. T. C. Liu, D. Meza, and N. Sanai, ‘Trends in Fluorescence Image-Guided Surgery for Gliomas’, *Neurosurgery*, vol. 75, no. 1, pp. 61–71, Jul. 2014, doi: 10.1227/NEU.0000000000000344.
- [152] P. A. Valdés *et al.*, ‘ $\delta$ -aminolevulinic acid-induced protoporphyrin IX concentration correlates with histopathologic markers of malignancy in human gliomas: the need for quantitative fluorescence-guided resection to identify regions of increasing malignancy’, *Neuro-oncology*, vol. 13, no. 8, pp. 846–856, Aug. 2011, doi: 10.1093/neuonc/nor086.
- [153] T. Sankar *et al.*, ‘Miniaturized Handheld Confocal Microscopy for Neurosurgery’, *Neurosurgery*, vol. 66, no. 2, pp. 410–418, Feb. 2010, doi: 10.1227/01.NEU.0000365772.66324.6F.
- [154] J. Georges *et al.*, ‘Label-free microscopic assessment of glioblastoma biopsy specimens prior to biobanking’, *FOC*, vol. 36, no. 2, p. E8, Feb. 2014, doi: 10.3171/2013.11.FOCUS13478.
- [155] A. Zehri *et al.*, ‘Neurosurgical confocal endomicroscopy: A review of contrast agents, confocal systems, and future imaging modalities’, *Surg Neurol Int*, vol. 5, no. 1, p. 60, 2014, doi: 10.4103/2152-7806.131638.
- [156] ‘FIVE2’, *OptiScan*. <https://www.optiscan.com/products/five2/> (accessed Jul. 25, 2020).
- [157] ‘Cellvizio Biopsie Ciblée - Mauna Kea Technologies’. <https://www.maunakeatech.com/fr/cellvizio> (accessed Jul. 25, 2020).

- [158] N. Sanai *et al.*, ‘Intraoperative Confocal Microscopy for Brain Tumors: A Feasibility Analysis in Humans’, *Operative Neurosurgery*, vol. 68, no. suppl\_2, pp. ons282–ons290, Jun. 2011, doi: 10.1227/NEU.0b013e318212464e.
- [159] K. I. Swanson and B. G. Rocque, ‘Journal Club: Intraoperative Confocal Microscopy for Brain Tumors’, *Neurosurgery*, vol. 71, no. 2, pp. E514–E517, Aug. 2012, doi: 10.1227/NEU.0b013e31825d2c5b.
- [160] N. L. Martirosyan *et al.*, ‘Prospective evaluation of the utility of intraoperative confocal laser endomicroscopy in patients with brain neoplasms using fluorescein sodium: experience with 74 cases’, *FOC*, vol. 40, no. 3, p. E11, Mar. 2016, doi: 10.3171/2016.1.FOCUS15559.
- [161] N. L. Martirosyan *et al.*, ‘Potential application of a handheld confocal endomicroscope imaging system using a variety of fluorophores in experimental gliomas and normal brain’, *FOC*, vol. 36, no. 2, p. E16, Feb. 2014, doi: 10.3171/2013.11.FOCUS13486.
- [162] F. Helmchen, M. S. Fee, D. W. Tank, and W. Denk, ‘A miniature head-mounted two-photon microscope. high-resolution brain imaging in freely moving animals’, *Neuron*, vol. 31, no. 6, pp. 903–912, Sep. 2001, doi: 10.1016/s0896-6273(01)00421-4.
- [163] Y. Wu and X. Li, ‘Two-photon Fluorescence Endomicroscopy’, in *Advances in Lasers and Electro Optics*, N. Costa and A. Cartaxo, Eds. InTech, 2010.
- [164] H. Bao, J. Allen, R. Pattie, R. Vance, and M. Gu, ‘Fast handheld two-photon fluorescence microendoscope with a  $475\ \mu\text{m} \times 475\ \mu\text{m}$  field of view for in vivo imaging’, *Opt. Lett.*, vol. 33, no. 12, p. 1333, Jun. 2008, doi: 10.1364/OL.33.001333.
- [165] L. Fu, A. Jain, H. Xie, C. Cranfield, and M. Gu, ‘Nonlinear optical endoscopy based on a double-clad photonic crystal fiber and a MEMS mirror’, *Opt. Express*, vol. 14, no. 3, p. 1027, Feb. 2006, doi: 10.1364/OE.14.001027.
- [166] Y. Wu, Y. Leng, J. Xi, and X. Li, ‘Scanning all-fiber-optic endomicroscopy system for 3D nonlinear optical imaging of biological tissues’, *Opt. Express*, vol. 17, no. 10, p. 7907, May 2009, doi: 10.1364/OE.17.007907.
- [167] Y. Wu, J. Xi, M. J. Cobb, and X. Li, ‘Scanning fiber-optic nonlinear endomicroscopy with miniature aspherical compound lens and multimode fiber collector’, *Opt. Lett.*, vol. 34, no. 7, p. 953, Apr. 2009, doi: 10.1364/OL.34.000953.
- [168] C. Lefort, H. Hamzeh, F. Louradour, F. Pain, and D. A. Haidar, ‘Characterization, comparison, and choice of a commercial double-clad fiber for nonlinear endomicroscopy’, *J. Biomed. Opt.*, vol. 19, no. 7, p. 076005, Jul. 2014, doi: 10.1117/1.JBO.19.7.076005.
- [169] M. T. Myaing, D. J. MacDonald, and X. Li, ‘Fiber-optic scanning two-photon fluorescence endoscope’, *Opt. Lett.*, vol. 31, no. 8, p. 1076, Apr. 2006, doi: 10.1364/OL.31.001076.
- [170] J. C. Knight, ‘Photonic crystal fibres’, *Nature*, vol. 424, no. 6950, pp. 847–851, Aug. 2003, doi: 10.1038/nature01940.
- [171] L. Fu, A. Jain, C. Cranfield, H. Xie, and M. Gu, ‘Three-dimensional nonlinear optical endoscopy’, *J. Biomed. Opt.*, vol. 12, no. 4, p. 040501, 2007, doi: 10.1117/1.2756102.
- [172] W. Jung *et al.*, ‘Miniaturized probe based on a microelectromechanical system mirror for multiphoton microscopy’, *Opt. Lett.*, vol. 33, no. 12, p. 1324, Jun. 2008, doi: 10.1364/OL.33.001324.

- [173] A. Ibrahim, F. Poulon, R. Habert, C. Lefort, A. Kudlinski, and D. A. Haidar, ‘Characterization of fiber ultrashort pulse delivery for nonlinear endomicroscopy’, *Opt. Express*, vol. 24, no. 12, p. 12515, Jun. 2016, doi: 10.1364/OE.24.012515.
- [174] H. Choi, S.-C. Chen, D. Kim, P. T. C. So, and M. L. Culpepper, ‘Design of a Non-linear Endomicroscope Biopsy Probe’, in *Biomedical Optics*, Fort Lauderdale, Florida, 2006, p. TuI69, doi: 10.1364/BIO.2006.TuI69.
- [175] H. Hamzeh, C. Lefort, F. Pain, and D. Abi Haidar, ‘Optimization and characterization of nonlinear excitation and collection through a gradient-index lens for high-resolution nonlinear endomicroscopy’, *Opt. Lett.*, vol. 40, no. 5, p. 808, Mar. 2015, doi: 10.1364/OL.40.000808.
- [176] M. Lelek, E. Suran, F. Louradour, A. Barthelemy, B. Viellerobe, and F. Lacombe, ‘Coherent femtosecond pulse shaping for the optimization of a non-linear microendoscope’, *Opt. Express*, vol. 15, no. 16, p. 10154, 2007, doi: 10.1364/OE.15.010154.
- [177] T. Le, G. Tempea, Z. Cheng, M. Hofer, and A. Stingl, ‘Routes to fiber delivery of ultra-short laser pulses in the 25 fs regime’, *Opt. Express*, vol. 17, no. 3, p. 1240, Feb. 2009, doi: 10.1364/OE.17.001240.
- [178] E. Treacy, ‘Optical pulse compression with diffraction gratings’, *IEEE J. Quantum Electron.*, vol. 5, no. 9, pp. 454–458, Sep. 1969, doi: 10.1109/JQE.1969.1076303.
- [179] Guillaume Ducourthial, ‘Développement d’un endomicroscope multiphotonique compact et flexible pour l’imagerie in vivo haute résolution de tissus biologiques non marqués. <https://hal.archives-ouvertes.fr/tel-01086081/>’, Université de Limoges, 2014.
- [180] C. Lefort, T. Mansuryan, F. Louradour, and A. Barthelemy, ‘Pulse compression and fiber delivery of 45 fs Fourier transform limited pulses at 830 nm’, *Opt. Lett.*, vol. 36, no. 2, p. 292, Jan. 2011, doi: 10.1364/OL.36.000292.
- [181] C. J. Engelbrecht, R. S. Johnston, E. J. Seibel, and F. Helmchen, ‘Ultra-compact fiber-optic two-photon microscope for functional fluorescence imaging in vivo’, *Opt. Express*, vol. 16, no. 8, p. 5556, Apr. 2008, doi: 10.1364/OE.16.005556.
- [182] B. A. Flusberg, J. C. Jung, E. D. Cocker, E. P. Anderson, and M. J. Schnitzer, ‘In vivo brain imaging using a portable 39?gram two-photon fluorescence microendoscope’, *Opt. Lett.*, vol. 30, no. 17, p. 2272, Sep. 2005, doi: 10.1364/OL.30.002272.
- [183] X. Liu, M. J. Cobb, Y. Chen, M. B. Kimmey, and X. Li, ‘Rapid-scanning forward-imaging miniature endoscope for real-time optical coherence tomography’, *Opt. Lett.*, vol. 29, no. 15, p. 1763, Aug. 2004, doi: 10.1364/OL.29.001763.
- [184] G. Ducourthial *et al.*, ‘Development of a real-time flexible multiphoton microendoscope for label-free imaging in a live animal’, *Sci Rep*, vol. 5, no. 1, p. 18303, Dec. 2015, doi: 10.1038/srep18303.
- [185] J. Xi, Y. Chen, Y. Zhang, K. Murari, M.-J. Li, and X. Li, ‘Integrated multimodal endomicroscopy platform for simultaneous en face optical coherence and two-photon fluorescence imaging’, *Opt. Lett.*, vol. 37, no. 3, p. 362, Feb. 2012, doi: 10.1364/OL.37.000362.
- [186] Y. Zhang *et al.*, ‘A compact fiber-optic SHG scanning endomicroscope and its application to visualize cervical remodeling during pregnancy’, *Proceedings of the National Academy of Sciences*, vol. 109, no. 32, pp. 12878–12883, Aug. 2012, doi: 10.1073/pnas.1121495109.
- [187] Y. Wang, Z. Li, X. Liang, and L. Fu, ‘Four-plate piezoelectric actuator driving a large-diameter special optical fiber for nonlinear optical microendoscopy’, *Opt. Express*, vol. 24, no. 17, p. 19949, Aug. 2016, doi: 10.1364/OE.24.019949.

- [188] N. Zhang *et al.*, ‘Compact piezoelectric transducer fiber scanning probe for optical coherence tomography’, *Opt. Lett.*, vol. 39, no. 2, p. 186, Jan. 2014, doi: 10.1364/OL.39.000186.
- [189] Pierre Leclerc, ‘Développement d’un endomicroscope multiphotonique à deux couleurs pour l’imagerie du métabolisme énergétique cellulaire. <https://hal.archives-ouvertes.fr/tel-01698572/>’, Université de Limoges, 2017.
- [190] D. Y. Kim *et al.*, ‘Lissajous Scanning Two-photon Endomicroscope for In vivo Tissue Imaging’, *Sci Rep*, vol. 9, no. 1, p. 3560, Dec. 2019, doi: 10.1038/s41598-019-38762-w.
- [191] D. Do, H. Yoo, and D.-G. Gweon, ‘Fiber-optic raster scanning two-photon endomicroscope using a tubular piezoelectric actuator’, *J. Biomed. Opt.*, vol. 19, no. 6, p. 066010, Jun. 2014, doi: 10.1117/1.JBO.19.6.066010.
- [192] L. Ye, G. Zhang, and Z. You, ‘5 V Compatible Two-Axis PZT Driven MEMS Scanning Mirror with Mechanical Leverage Structure for Miniature LiDAR Application’, *Sensors (Basel)*, vol. 17, no. 3, Mar. 2017, doi: 10.3390/s17030521.
- [193] H.-Y. Lin and W. Fang, ‘A rib-reinforced micro torsional mirror driven by electrostatic torque generators’, *Sensors and Actuators A: Physical*, vol. 105, no. 1, pp. 1–9, Jun. 2003, doi: 10.1016/S0924-4247(03)00056-6.
- [194] P. M. Hagelin and O. Solgaard, ‘Optical raster-scanning displays based on surface-micromachined polysilicon mirrors’, *IEEE J. Select. Topics Quantum Electron.*, vol. 5, no. 1, pp. 67–74, Feb. 1999, doi: 10.1109/2944.748107.
- [195] W. Lang, H. Pavliček, Th. Marx, H. Scheithauer, and B. Schmidt, ‘Electrostatically actuated micromirror devices in silicon technology’, *Sensors and Actuators A: Physical*, vol. 74, no. 1–3, pp. 216–218, Apr. 1999, doi: 10.1016/S0924-4247(98)00321-5.
- [196] H. Schenk *et al.*, ‘Large deflection micromechanical scanning mirrors for linear scans and pattern generation’, *IEEE J. Select. Topics Quantum Electron.*, vol. 6, no. 5, pp. 715–722, Sep. 2000, doi: 10.1109/2944.892609.
- [197] J. Sun *et al.*, ‘3D In Vivo optical coherence tomography based on a low-voltage, large-scan-range 2D MEMS mirror’, *Opt. Express*, vol. 18, no. 12, p. 12065, Jun. 2010, doi: 10.1364/OE.18.012065.
- [198] D. Hah, S. T.-Y. Huang, J.-C. Tsai, H. Toshiyoshi, and M. C. Wu, ‘Low-Voltage, Large-Scan Angle MEMS Analog Micromirror Arrays With Hidden Vertical Comb-Drive Actuators’, *J. Microelectromech. Syst.*, vol. 13, no. 2, pp. 279–289, Apr. 2004, doi: 10.1109/JMEMS.2004.825314.
- [199] L. Lin and E. Keeler, ‘Progress of MEMS Scanning Micromirrors for Optical Bio-Imaging’, *Micromachines*, vol. 6, no. 11, pp. 1675–1689, Nov. 2015, doi: 10.3390/mi6111450.
- [200] S. R. Samuelson, Lei Wu, Jingjing Sun, Se-woon Choe, B. S. Sorg, and Huikai Xie, ‘A 2.8-mm Imaging Probe Based On a High-Fill-Factor MEMS Mirror and Wire-Bonding-Free Packaging for Endoscopic Optical Coherence Tomography’, *J. Microelectromech. Syst.*, vol. 21, no. 6, pp. 1291–1302, Dec. 2012, doi: 10.1109/JMEMS.2012.2209404.
- [201] W. Piyawattanametha *et al.*, ‘Fast-scanning two-photon fluorescence imaging based on a microelectromechanical systems two-dimensional scanning mirror’, *Opt. Lett.*, vol. 31, no. 13, p. 2018, Jul. 2006, doi: 10.1364/OL.31.002018.
- [202] C. L. Hoy *et al.*, ‘Miniaturized probe for femtosecond laser microsurgery and two-photon imaging’, *Opt. Express*, vol. 16, no. 13, p. 9996, Jun. 2008, doi: 10.1364/OE.16.009996.

- [203] B. A. Flusberg, E. D. Cocker, W. Piyawattanametha, J. C. Jung, E. L. M. Cheung, and M. J. Schnitzer, ‘Fiber-optic fluorescence imaging’, *Nat. Methods*, vol. 2, no. 12, pp. 941–950, Dec. 2005, doi: 10.1038/nmeth820.
- [204] J. Wang *et al.*, ‘A Confocal Endoscope for Cellular Imaging’, *Engineering*, vol. 1, no. 3, pp. 351–360, Sep. 2015, doi: 10.15302/J-ENG-2015081.
- [205] M. Kyrish *et al.*, ‘Needle-based fluorescence endomicroscopy via structured illumination with a plastic, achromatic objective’, *J. Biomed. Opt.*, vol. 18, no. 9, p. 096003, Sep. 2013, doi: 10.1117/1.JBO.18.9.096003.
- [206] A. R. Rouse, A. Kano, J. A. Udovich, S. M. Kroto, and A. F. Gmitro, ‘Design and demonstration of a miniature catheter for a confocal microendoscope’, *Appl. Opt.*, vol. 43, no. 31, p. 5763, Nov. 2004, doi: 10.1364/AO.43.005763.
- [207] L. Yang, J. Wang, G. Tian, J. Yuan, Q. Liu, and L. Fu, ‘Five-lens, easy-to-implement miniature objective for a fluorescence confocal microendoscope’, *Opt. Express*, vol. 24, no. 1, p. 473, Jan. 2016, doi: 10.1364/OE.24.000473.
- [208] H. Bao, S. Y. Ryu, B. H. Lee, W. Tao, and M. Gu, ‘Nonlinear endomicroscopy using a double-clad fiber coupler’, *Opt Lett*, vol. 35, no. 7, pp. 995–997, Apr. 2010, doi: 10.1364/OL.35.000995.
- [209] M. Gu, H. Bao, and H. Kang, ‘Fibre-optical microendoscopy: FIBRE-OPTICAL MICROENDOSCOPY’, *Journal of Microscopy*, vol. 254, no. 1, pp. 13–18, Apr. 2014, doi: 10.1111/jmi.12119.
- [210] C. M. Brown *et al.*, ‘In vivo imaging of unstained tissues using a compact and flexible multiphoton microendoscope’, *J. Biomed. Opt.*, vol. 17, no. 4, p. 040505, 2012, doi: 10.1117/1.JBO.17.4.040505.
- [211] D. G. Ouzounov *et al.*, ‘Dual modality endomicroscope with optical zoom capability’, *Biomed. Opt. Express*, vol. 4, no. 9, p. 1494, Sep. 2013, doi: 10.1364/BOE.4.001494.
- [212] C. Hage *et al.*, ‘A readily usable two-photon fluorescence lifetime microendoscope’, *J. Biophotonics*, vol. 12, no. 5, May 2019, doi: 10.1002/jbio.201800276.
- [213] K. König, ‘Clinical multiphoton tomography’, *J. Biophoton.*, vol. 1, no. 1, pp. 13–23, Mar. 2008, doi: 10.1002/jbio.200710022.
- [214] F. Poulon *et al.*, ‘Multimodal Analysis of Central Nervous System Tumor Tissue Endogenous Fluorescence With Multiscale Excitation’, *Front. Phys.*, vol. 6, p. 109, Oct. 2018, doi: 10.3389/fphy.2018.00109.
- [215] F. Poulon *et al.*, ‘Optical properties, spectral, and lifetime measurements of central nervous system tumors in humans’, *Sci Rep*, vol. 7, no. 1, p. 13995, Dec. 2017, doi: 10.1038/s41598-017-14381-1.
- [216] M. Zanello *et al.*, ‘Multimodal optical analysis of meningioma and comparison with histopathology’, *J. Biophoton*, vol. 10, no. 2, pp. 253–263, Feb. 2017, doi: 10.1002/jbio.201500251.
- [217] F. Helmchen and W. Denk, ‘Deep tissue two-photon microscopy’, *Nat. Methods*, vol. 2, no. 12, pp. 932–940, Dec. 2005, doi: 10.1038/nmeth818.
- [218] S. Tang, T. B. Krasieva, Z. Chen, G. Tempea, and B. J. Tromberg, ‘Effect of pulse duration on two-photon excited fluorescence and second harmonic generation in nonlinear optical microscopy’, *J. Biomed. Opt.*, vol. 11, no. 2, p. 020501, 2006, doi: 10.1117/1.2177676.
- [219] K. König, T. W. Becker, P. Fischer, I. Riemann, and K.-J. Halbhauer, ‘Pulse-length dependence of cellular response to intense near-infrared laser pulses in multiphoton microscopes’, *Opt. Lett.*, vol. 24, no. 2, p. 113, Jan. 1999, doi: 10.1364/OL.24.000113.

- [220] S. N. Arkhipov, I. Saytashev, and M. Dantus, ‘Intravital Imaging Study on Photodamage Produced by Femtosecond Near-infrared Laser Pulses In Vivo’, *Photochem. Photobiol.*, vol. 92, no. 2, pp. 308–313, 2016, doi: 10.1111/php.12572.
- [221] P. Xi, Y. Andegeko, D. Pestov, V. V. Lozovoy, and M. Dantus, ‘Two-photon imaging using adaptive phase compensated ultrashort laser pulses’, *J Biomed Opt*, vol. 14, no. 1, p. 014002, Feb. 2009, doi: 10.1117/1.3059629.
- [222] I. Saytashev, S. N. Arkhipov, N. Winkler, K. Zuraski, V. V. Lozovoy, and M. Dantus, ‘Pulse duration and energy dependence of photodamage and lethality induced by femtosecond near infrared laser pulses in *Drosophila melanogaster*’, *J. Photochem. Photobiol. B, Biol.*, vol. 115, pp. 42–50, Oct. 2012, doi: 10.1016/j.jphotobiol.2012.06.009.
- [223] D. Pestov, Y. Andegeko, V. V. Lozovoy, and M. Dantus, ‘Photobleaching and photoenhancement of endogenous fluorescence observed in two-photon microscopy with broadband laser sources’, *J. Opt.*, vol. 12, no. 8, p. 084006, Aug. 2010, doi: 10.1088/2040-8978/12/8/084006.
- [224] H. J. Koester, D. Baur, R. Uhl, and S. W. Hell, ‘Ca<sup>2+</sup> fluorescence imaging with pico- and femtosecond two-photon excitation: signal and photodamage’, *Biophys. J.*, vol. 77, no. 4, pp. 2226–2236, Oct. 1999, doi: 10.1016/S0006-3495(99)77063-3.
- [225] R. Stupp *et al.*, ‘Radiotherapy plus concomitant and adjuvant temozolomide for glioblastoma’, *N. Engl. J. Med.*, vol. 352, no. 10, pp. 987–996, Mar. 2005, doi: 10.1056/NEJMoa043330.
- [226] D. A. Hardesty and N. Sanai, ‘The Value of Glioma Extent of Resection in the Modern Neurosurgical Era’, *Front. Neur.*, vol. 3, 2012, doi: 10.3389/fneur.2012.00140.
- [227] M. Lacroix and S. A. Toms, ‘Maximum safe resection of glioblastoma multiforme’, *J. Clin. Oncol.*, vol. 32, no. 8, pp. 727–728, Mar. 2014, doi: 10.1200/JCO.2013.53.2788.
- [228] K. Roessler, A. Becherer, M. Donat, M. Cejna, and I. Zachenhofer, ‘Intraoperative tissue fluorescence using 5-aminolevulinic acid (5-ALA) is more sensitive than contrast MRI or amino acid positron emission tomography ((<sup>18</sup>F)-FET PET) in glioblastoma surgery’, *Neurol. Res.*, vol. 34, no. 3, pp. 314–317, Apr. 2012, doi: 10.1179/1743132811Y.0000000078.
- [229] S. E. L. Craig, J. Wright, A. E. Sloan, and S. M. Brady-Kalnay, ‘Fluorescent-Guided Surgical Resection of Glioma with Targeted Molecular Imaging Agents: A Literature Review’, *World Neurosurg*, vol. 90, pp. 154–163, Jun. 2016, doi: 10.1016/j.wneu.2016.02.060.
- [230] S. A. Boppart *et al.*, ‘Label-free optical imaging technologies for rapid translation and use during intraoperative surgical and tumor margin assessment’, *J Biomed Opt*, vol. 23, no. 2, pp. 1–10, 2017, doi: 10.1117/1.JBO.23.2.021104.
- [231] C. Xu and W. W. Webb, ‘Measurement of two-photon excitation cross sections of molecular fluorophores with data from 690 to 1050 nm’, *J. Opt. Soc. Am. B*, vol. 13, no. 3, p. 481, Mar. 1996, doi: 10.1364/JOSAB.13.000481.
- [232] P. Xi, Y. Andegeko, L. R. Weisel, V. V. Lozovoy, and M. Dantus, ‘Greater signal, increased depth, and less photobleaching in two-photon microscopy with 10fs pulses’, *Optics Communications*, vol. 281, no. 7, pp. 1841–1849, Apr. 2008, doi: 10.1016/j.optcom.2007.09.066.
- [233] B. W. Pogue *et al.*, ‘In Vivo NADH Fluorescence Monitoring as an Assay for Cellular Damage in Photodynamic Therapy’, *Photochemistry and Photobiology*, vol. 74, no. 6, pp. 817–824, Dec. 2001, doi: 10.1562/0031-8655(2001)0740817IVNFMA2.0.CO2.

- [234] A. K. Dunn, V. P. Wallace, M. Coleno, M. W. Berns, and B. J. Tromberg, ‘Influence of optical properties on two-photon fluorescence imaging in turbid samples’, *Appl Opt*, vol. 39, no. 7, pp. 1194–1201, Mar. 2000, doi: 10.1364/ao.39.001194.
- [235] X. F. Wang, A. Periasamy, B. Herman, and D. M. Coleman, ‘Fluorescence Lifetime Imaging Microscopy (FLIM): Instrumentation and Applications’, *Critical Reviews in Analytical Chemistry*, vol. 23, no. 5, pp. 369–395, Jan. 1992, doi: 10.1080/10408349208051651.
- [236] H. Hamzeh, C. Lefort, F. Louradour, G. Latour, F. Pain, and D. A. Haidar, ‘Optimization of Nonlinear Multimodal Microendoscopy Based on DCF and GRIN Lenses for Optical Biopsy’, in *Frontiers in Optics 2013*, Orlando, Florida, 2013, p. FW2B.3, doi: 10.1364/FIO.2013.FW2B.3.
- [237] A. Ibrahim *et al.*, ‘Spectral and lifetime measurements of endogenous fluorescence using endoscopic and benchtop microscope configuration’, in *Frontiers in Optics 2017*, Washington, D.C., 2017, p. FW5D.3, doi: 10.1364/FIO.2017.FW5D.3.
- [238] J. R. Barrio, G. L. Tolman, N. J. Leonard, R. D. Spencer, and G. Weber, ‘Flavin 1, N 6 -ethenoadenine dinucleotide: dynamic and static quenching of fluorescence’, *Proc. Natl. Acad. Sci. U.S.A.*, vol. 70, no. 3, pp. 941–943, Mar. 1973, doi: 10.1073/pnas.70.3.941.
- [239] C. Stringari, A. Cinquin, O. Cinquin, M. A. Digman, P. J. Donovan, and E. Gratton, ‘Phasor approach to fluorescence lifetime microscopy distinguishes different metabolic states of germ cells in a live tissue’, *Proc. Natl. Acad. Sci. U.S.A.*, vol. 108, no. 33, pp. 13582–13587, Aug. 2011, doi: 10.1073/pnas.1108161108.
- [240] A. Pitzschke *et al.*, ‘Optical properties of rabbit brain in the red and near-infrared: changes observed under *in vivo*, postmortem, frozen, and formalin-fixed conditions’, *J. Biomed. Opt.*, vol. 20, no. 2, p. 025006, Feb. 2015, doi: 10.1117/1.JBO.20.2.025006.
- [241] L. Joosen, M. A. Hink, T. W. J. Gadella, and J. Goedhart, ‘Effect of fixation procedures on the fluorescence lifetimes of *Aequorea victoria* derived fluorescent proteins’, *J Microsc.*, vol. 256, no. 3, pp. 166–176, Dec. 2014, doi: 10.1111/jmi.12168.
- [242] H.-W. Wang, Y.-H. Wei, and H.-W. Guo, ‘Reduced Nicotinamide Adenine Dinucleotide (NADH) Fluorescence for the Detection of Cell Death’, *ACAMC*, vol. 9, no. 9, pp. 1012–1017, Nov. 2009, doi: 10.2174/187152009789377718.
- [243] F. Knorr, D. R. Yankelevich, J. Liu, S. Wachsmann-Hogiu, and L. Marcu, ‘Two-photon excited fluorescence lifetime measurements through a double-clad photonic crystal fiber for tissue micro-endoscopy’, *J Biophotonics*, vol. 5, no. 1, pp. 14–19, Jan. 2012, doi: 10.1002/jbio.201100070.
- [244] A. G. Ryder, S. Power, T. J. Glynn, and J. J. Morrison, ‘Time-domain measurement of fluorescence lifetime variation with pH’, San Jose, CA, Jul. 2001, pp. 102–109, doi: 10.1117/12.432487.
- [245] S. R. Kantelhardt *et al.*, ‘Imaging of brain and brain tumor specimens by time-resolved multiphoton excitation microscopy *ex vivo*’, *Neuro-oncology*, vol. 9, no. 2, pp. 103–112, Apr. 2007, doi: 10.1215/15228517-2006-034.
- [246] R. Galli *et al.*, ‘Intrinsic Indicator of Photodamage during Label-Free Multiphoton Microscopy of Cells and Tissues’, *PLoS ONE*, vol. 9, no. 10, p. e110295, Oct. 2014, doi: 10.1371/journal.pone.0110295.
- [247] G. H. Patterson and D. W. Piston, ‘Photobleaching in two-photon excitation microscopy’, *Biophys. J.*, vol. 78, no. 4, pp. 2159–2162, Apr. 2000, doi: 10.1016/S0006-3495(00)76762-2.

- [248] T.-S. Chen, S.-Q. Zeng, Q.-M. Luo, Z.-H. Zhang, and W. Zhou, ‘High-order photobleaching of green fluorescent protein inside live cells in two-photon excitation microscopy’, *Biochem. Biophys. Res. Commun.*, vol. 291, no. 5, pp. 1272–1275, Mar. 2002, doi: 10.1006/bbrc.2002.6587.
- [249] S. Kalies, K. Kuetemeyer, and A. Heisterkamp, ‘Mechanisms of high-order photobleaching and its relationship to intracellular ablation’, *Biomed. Opt. Express*, vol. 2, no. 4, p. 805, Apr. 2011, doi: 10.1364/BOE.2.000805.
- [250] A. Vogel, J. Noack, G. Hüttman, and G. Paltauf, ‘Mechanisms of femtosecond laser nanosurgery of cells and tissues’, *Appl. Phys. B*, vol. 81, no. 8, pp. 1015–1047, Dec. 2005, doi: 10.1007/s00340-005-2036-6.
- [251] K. S. Samkoe *et al.*, ‘Photobleaching kinetics of optically trapped multilamellar vesicles containing verteporfin using two-photon excitation section sign’, *Photochem. Photobiol.*, vol. 82, no. 1, pp. 152–157, Feb. 2006, doi: 10.1562/2005-05-28-RA-549.
- [252] K. S. Samkoe and D. T. Cramb, ‘Application of an ex ovo chicken chorioallantoic membrane model for two-photon excitation photodynamic therapy of age-related macular degeneration’, *J Biomed Opt*, vol. 8, no. 3, pp. 410–417, Jul. 2003, doi: 10.1117/1.1577117.
- [253] R. L. Goyan and D. T. Cramb, ‘Near-infrared two-photon excitation of protoporphyrin IX: photodynamics and photoproduct generation’, *Photochem. Photobiol.*, vol. 72, no. 6, pp. 821–827, Dec. 2000, doi: 10.1562/0031-8655(2000)072<0821:nitpeo>2.0.co;2.
- [254] D. T. Cramb and R. L. Goyan, ‘Dynamic behavior of photosensitizers after multiphoton excitation’, San Jose, CA, Apr. 2001, p. 41, doi: 10.1117/12.424585.
- [255] K. Blinova *et al.*, ‘Mitochondrial NADH fluorescence is enhanced by complex I binding’, *Biochemistry*, vol. 47, no. 36, pp. 9636–9645, Sep. 2008, doi: 10.1021/bi800307y.
- [256] K. König, H. Liang, M. W. Berns, and B. J. Tromberg, ‘Cell damage in near-infrared multimode optical traps as a result of multiphoton absorption’, *Opt Lett*, vol. 21, no. 14, pp. 1090–1092, Jul. 1996, doi: 10.1364/ol.21.001090.
- [257] M. Sibai *et al.*, ‘The Impact of Compressed Femtosecond Laser Pulse Durations on Neuronal Tissue Used for Two-Photon Excitation Through an Endoscope’, *Sci Rep*, vol. 8, no. 1, p. 11124, Dec. 2018, doi: 10.1038/s41598-018-29404-8.
- [258] F. Khodamoradi, M. Ghoncheh, R. Pakzad, H. S. Gandomani, and H. Salehiniya, ‘The incidence and mortality of brain and central nervous system cancer’, p. 5.
- [259] K. K. Farmanfarma, M. Mohammadian, Z. Shahabinia, S. Hassanipour, and H. Salehiniya, ‘Brain cancer in the world: an epidemiological review’, p. 5.
- [260] ‘curebraincancer foundation’, *curebraincancer.org*.  
<https://www.curebraincancer.org.au/page/8/facts-stats>.
- [261] P. D. Brown *et al.*, ‘A Prospective Study of Quality of Life in Adults with Newly Diagnosed High-grade Gliomas: The Impact of the Extent of Resection on Quality of Life and Survival’, *Neurosurgery*, vol. 57, no. 3, pp. 495–504, Sep. 2005, doi: 10.1227/01.NEU.0000170562.25335.C7.
- [262] M. Schulder and P. W. Carmel, ‘Intraoperative Magnetic Resonance Imaging: Impact on Brain Tumor Surgery’, *Cancer Control*, vol. 10, no. 2, pp. 115–124, Mar. 2003, doi: 10.1177/107327480301000203.
- [263] G. Unsgaard *et al.*, ‘Intra-operative 3D ultrasound in neurosurgery’, *Acta Neurochir (Wien)*, vol. 148, no. 3, pp. 235–253, Mar. 2006, doi: 10.1007/s00701-005-0688-y.



- [264] S. Chan, F. Conti, K. Salisbury, and N. H. Blevins, ‘Virtual Reality Simulation in Neurosurgery: Technologies and Evolution’, *Neurosurgery*, vol. 72, pp. A154–A164, Jan. 2013, doi: 10.1227/NEU.0b013e3182750d26.
- [265] N. Lakomkin and C. G. Hadjipanayis, ‘The Use of Spectroscopy Handheld Tools in Brain Tumor Surgery: Current Evidence and Techniques’, *Front. Surg.*, vol. 6, p. 30, May 2019, doi: 10.3389/fsurg.2019.00030.
- [266] J. Popp, B. Dietzek, M. Schmitt, P. Rosch, R. Moller, and C. Krafft, ‘Raman spectroscopy - An essential tool for biophotonics’, in *2011 International Workshop on Biophotonics*, Parma, Italy, Jun. 2011, pp. 1–3, doi: 10.1109/IWBP.2011.5954844.
- [267] J.-C. Tonn, ‘Fluorescence-guided Resection of Malignant Gliomas Using 5-aminolevulinic Acid’, *Clinical Neurosurgery*, vol. 55, p. 7, 2008.
- [268] K. S. Yashin *et al.*, ‘Cross-Polarization Optical Coherence Tomography for Brain Tumor Imaging’, *Front. Oncol.*, vol. 9, p. 201, Apr. 2019, doi: 10.3389/fonc.2019.00201.
- [269] M. Pedrazzani *et al.*, ‘Comparison of line-field confocal optical coherence tomography images with histological sections: Validation of a new method for in vivo and non-invasive quantification of superficial dermis thickness’, *Skin Res Technol*, vol. 26, no. 3, pp. 398–404, May 2020, doi: 10.1111/srt.12815.
- [270] H. Mehidine *et al.*, ‘Optical Signatures Derived From Deep UV to NIR Excitation Discriminates Healthy Samples From Low and High Grades Glioma’, *Sci Rep*, vol. 9, no. 1, p. 8786, Dec. 2019, doi: 10.1038/s41598-019-45181-4.
- [271] A. Ibrahim *et al.*, ‘Spectral and fluorescence lifetime endoscopic system using a double-clad photonic crystal fiber’, *Opt. Lett.*, vol. 41, no. 22, p. 5214, Nov. 2016, doi: 10.1364/OL.41.005214.
- [272] J. Allen, R. Pattie, R. Vance, and M. Gu, ‘Fast handheld two-photon fluorescence microendoscope with a 475  $\mu\text{m}$   $\times$  475  $\mu\text{m}$  field of view for in vivo imaging’, p. 3.
- [273] C. H. Hage *et al.*, ‘Towards two-photon excited endogenous fluorescence lifetime imaging microendoscopy’, *Biomed. Opt. Express*, vol. 9, no. 1, p. 142, Jan. 2018, doi: 10.1364/BOE.9.000142.
- [274] H. Mehidine *et al.*, ‘Multimodal imaging to explore endogenous fluorescence of fresh and fixed human healthy and tumor brain tissues’, *J. Biophotonics*, vol. 12, no. 3, Mar. 2019, doi: 10.1002/jbio.201800178.
- [275] M. Sibai *et al.*, ‘Comparison of optically-derived biomarkers in healthy and brain tumor tissue under one- and two-photon excitation’, *J. Biophotonics*, vol. 12, no. 11, Nov. 2019, doi: 10.1002/jbio.201900111.
- [276] S. Tang *et al.*, ‘Design and implementation of fiber-based multiphoton endoscopy with microelectromechanical systems scanning’, *J. Biomed. Opt.*, vol. 14, no. 3, p. 034005, 2009, doi: 10.1117/1.3127203.
- [277] Q. A. A. Tanguy *et al.*, ‘A 2-axis MEMS scanning micromirror with a 45° auto-positioning mechanism for endoscopic probe’, in *2017 19th International Conference on Solid-State Sensors, Actuators and Microsystems (TRANSDUCERS)*, Kaohsiung, Taiwan, Jun. 2017, pp. 1947–1950, doi: 10.1109/TRANSDUCERS.2017.7994450.
- [278] L. Zhou, X. Zhang, and H. Xie, ‘An Electrothermal Cu/W Bimorph Tip-Tilt-Piston MEMS Mirror with High Reliability’, *Micromachines*, vol. 10, no. 5, p. 323, May 2019, doi: 10.3390/mi10050323.
- [279] H. Kekhia, L. Rigolo, I. Norton, and A. J. Golby, ‘Special Surgical Considerations for Functional Brain Mapping’, *Neurosurgery Clinics of North America*, vol. 22, no. 2, pp. 111–132, Apr. 2011, doi: 10.1016/j.nec.2011.01.004.

- [280] C. Nimsky, O. Ganslandt, M. Buchfelder, and R. Fahlbusch, ‘Intraoperative visualization for resection of gliomas: the role of functional neuronavigation and intraoperative 1.5 T MRI’, p. 6.
- [281] C. Duan *et al.*, ‘A 45°-tilted 2-axis scanning micromirror integrated on a silicon optical bench for 3D endoscopic optical imaging’, in *2015 28th IEEE International Conference on Micro Electro Mechanical Systems (MEMS)*, Estoril, Portugal, Jan. 2015, pp. 948–951, doi: 10.1109/MEMSYS.2015.7051117.
- [282] E. Pengwang, K. Rabenorosa, M. Rakotondrabe, and N. Andreff, ‘Scanning Micromirror Platform Based on MEMS Technology for Medical Application’, *Micromachines*, vol. 7, no. 2, p. 24, Feb. 2016, doi: 10.3390/mi7020024.
- [283] M. Nakada *et al.*, ‘Optical coherence tomography by all-optical MEMS fiber endoscope’, *IEICE Electron. Express*, vol. 7, no. 6, pp. 428–433, 2010, doi: 10.1587/elex.7.428.
- [284] K. Isamoto *et al.*, ‘A high speed MEMS scanner for 140-kHz SS-OCT’, in *16th International Conference on Optical MEMS and Nanophotonics*, Istanbul, Turkey, Aug. 2011, pp. 73–74, doi: 10.1109/OMEMS.2011.6031072.
- [285] K. H. Koh, T. Kobayashi, F.-L. Hsiao, and C. Lee, ‘A 2-D MEMS Scanning Mirror Using Piezoelectric PZT Beam Actuators’, *Procedia Chemistry*, vol. 1, no. 1, pp. 1303–1306, Sep. 2009, doi: 10.1016/j.proche.2009.07.325.
- [286] K. H. Kim *et al.*, ‘Two-axis magnetically-driven MEMS scanning catheter for endoscopic high-speed optical coherence tomography’, *Opt. Express*, vol. 15, no. 26, p. 18130, Dec. 2007, doi: 10.1364/OE.15.018130.
- [287] Potekhina and Wang, ‘Review of Electrothermal Actuators and Applications’, *Actuators*, vol. 8, no. 4, p. 69, Sep. 2019, doi: 10.3390/act8040069.
- [288] M. Li, Q. Chen, Y. Liu, Y. Ding, and H. Xie, ‘Modelling and Experimental Verification of Step Response Overshoot Removal in Electrothermally-Actuated MEMS Mirrors’, *Micromachines*, vol. 8, no. 10, p. 289, Sep. 2017, doi: 10.3390/mi8100289.
- [289] S. Luo *et al.*, ‘A Miniature Endoscopic Optical Coherence Tomography Probe Based on C-Lens’, *IEEE Photonics J.*, vol. 10, no. 5, pp. 1–10, Oct. 2018, doi: 10.1109/JPHOT.2018.2870690.
- [290] J. Chai, H. Jia, D. Wang, H. Liu, Q. Chen, and H. Xie, ‘A MEMS Based Fourier Transform Spectrometer and Its Scan Stability Study’, *ECS J. Solid State Sci. Technol.*, vol. 7, no. 7, pp. Q3025–Q3031, 2018, doi: 10.1149/2.0051807jss.
- [291] X. Zhang, L. Zhou, and H. Xie, ‘A Fast, Large-Stroke Electrothermal MEMS Mirror Based on Cu/W Bimorph’, *Micromachines*, vol. 6, no. 12, pp. 1876–1889, Dec. 2015, doi: 10.3390/mi6121460.
- [292] H. Zhang, D. Xu, X. Zhang, Q. Chen, H. Xie, and S. Li, ‘Model-Based Angular Scan Error Correction of an Electrothermally-Actuated MEMS Mirror’, *Sensors*, vol. 15, no. 12, pp. 30991–31004, Dec. 2015, doi: 10.3390/s151229840.
- [293] S. Anand *et al.*, ‘Effects of formalin fixation on tissue optical properties of in-vitro brain samples’, San Francisco, California, United States, Mar. 2015, p. 93210Z, doi: 10.1117/12.2076961.
- [294] A. Roggan, D. Schaedel, U. Netz, J.-P. Ritz, C.-T. Germer, and G. J. Mueller, ‘Effect of preparation technique on the optical parameters of biological tissue’, Saratov, Russia, May 2001, pp. 186–199, doi: 10.1117/12.431520.
- [295] J. Lin, R. Jandial, A. Nesbit, B. Badie, and M. Chen, ‘Current and emerging treatments for brain metastases’, *Oncology (Williston Park, N.Y.)*, vol. 29, no. 4, pp. 250–257, Apr. 2015.

- [296] T. Hollon, S. L. Hervey-Jumper, O. Sagher, and D. A. Orringer, ‘Advances in the Surgical Management of Low-Grade Glioma’, *Semin Radiat Oncol*, vol. 25, no. 3, pp. 181–188, Jul. 2015, doi: 10.1016/j.semradonc.2015.02.007.
- [297] P. L. Kubben, K. J. ter Meulen, O. E. M. G. Schijns, M. P. ter Laak-Poort, J. J. van Overbeeke, and H. van Santbrink, ‘Intraoperative MRI-guided resection of glioblastoma multiforme: a systematic review’, *Lancet Oncol.*, vol. 12, no. 11, pp. 1062–1070, Oct. 2011, doi: 10.1016/S1470-2045(11)70130-9.
- [298] K. Uluç, G. C. Kujoth, and M. K. Başkaya, ‘Operating microscopes: past, present, and future’, *FOC*, vol. 27, no. 3, p. E4, Sep. 2009, doi: 10.3171/2009.6.FOCUS09120.
- [299] J.-C. Tonn and W. Stummer, ‘Fluorescence-guided resection of malignant gliomas using 5-aminolevulinic acid: practical use, risks, and pitfalls’, *Clin Neurosurg*, vol. 55, pp. 20–26, 2008.
- [300] S. W. Perry, R. M. Burke, and E. B. Brown, ‘Two-photon and second harmonic microscopy in clinical and translational cancer research’, *Ann Biomed Eng*, vol. 40, no. 2, pp. 277–291, Feb. 2012, doi: 10.1007/s10439-012-0512-9.
- [301] V. K. Ramanujan, J. A. Jo, G. Cantu, and B. A. Herman, ‘Spatially resolved fluorescence lifetime mapping of enzyme kinetics in living cells’, *J Microsc*, vol. 230, no. 3, pp. 329–338, Jun. 2008, doi: 10.1111/j.1365-2818.2008.01991.x.
- [302] A. C. Croce *et al.*, ‘Diagnostic potential of autofluorescence for an assisted intraoperative delineation of glioblastoma resection margins’, *Photochem. Photobiol.*, vol. 77, no. 3, pp. 309–318, Mar. 2003, doi: 10.1562/0031-8655(2003)077<0309:dpoafa>2.0.co;2.
- [303] P. P. Provenzano, K. W. Eliceiri, and P. J. Keely, ‘Multiphoton microscopy and fluorescence lifetime imaging microscopy (FLIM) to monitor metastasis and the tumor microenvironment’, *Clin. Exp. Metastasis*, vol. 26, no. 4, pp. 357–370, 2009, doi: 10.1007/s10585-008-9204-0.
- [304] J. Adur, H. F. Carvalho, C. L. Cesar, and V. H. Casco, ‘Nonlinear optical microscopy signal processing strategies in cancer’, *Cancer Inform*, vol. 13, pp. 67–76, 2014, doi: 10.4137/CIN.S12419.
- [305] S. C. Gebhart, W. C. Lin, and A. Mahadevan-Jansen, ‘In vitro determination of normal and neoplastic human brain tissue optical properties using inverse adding-doubling’, *Phys Med Biol*, vol. 51, no. 8, pp. 2011–2027, Apr. 2006, doi: 10.1088/0031-9155/51/8/004.
- [306] F. Bevilacqua, D. Piguet, P. Marquet, J. D. Gross, B. J. Tromberg, and C. Depeursinge, ‘In vivo local determination of tissue optical properties: applications to human brain’, *Appl Opt*, vol. 38, no. 22, pp. 4939–4950, Aug. 1999, doi: 10.1364/ao.38.004939.
- [307] A. N. Yaroslavsky, P. C. Schulze, I. V. Yaroslavsky, R. Schober, F. Ulrich, and H. J. Schwarzmaier, ‘Optical properties of selected native and coagulated human brain tissues in vitro in the visible and near infrared spectral range’, *Phys Med Biol*, vol. 47, no. 12, pp. 2059–2073, Jun. 2002, doi: 10.1088/0031-9155/47/12/305.
- [308] H. R. Eggert and V. Blazek, ‘Optical properties of human brain tissue, meninges, and brain tumors in the spectral range of 200 to 900 nm’, *Neurosurgery*, vol. 21, no. 4, pp. 459–464, Oct. 1987, doi: 10.1227/00006123-198710000-00003.
- [309] P. van der Zee, M. Essenpreis, and D. T. Delpy, ‘Optical properties of brain tissue’, Los Angeles, CA, Sep. 1993, pp. 454–465, doi: 10.1117/12.154665.

- [310] H. Soleimanzad, H. Gurden, and F. Pain, ‘Optical properties of mice skull bone in the 455- to 705-nm range’, *J. Biomed. Opt.*, vol. 22, no. 1, p. 010503, Jan. 2017, doi: 10.1117/1.JBO.22.1.010503.
- [311] ‘Inverse Adding-Doubling Software’. <https://omlc.org/software/iad/> (accessed Jul. 26, 2020).
- [312] N. Sanai and M. S. Berger, ‘Surgical oncology for gliomas: the state of the art’, *Nat Rev Clin Oncol*, vol. 15, no. 2, pp. 112–125, Feb. 2018, doi: 10.1038/nrclinonc.2017.171.
- [313] U. Testa, G. Castelli, and E. Pelosi, ‘Genetic Abnormalities, Clonal Evolution, and Cancer Stem Cells of Brain Tumors’, *Med Sci (Basel)*, vol. 6, no. 4, Oct. 2018, doi: 10.3390/medsci6040085.
- [314] S. J. Smith, M. Diksin, S. Chhaya, S. Sairam, M. A. Estevez-Cebrero, and R. Rahman, ‘The Invasive Region of Glioblastoma Defined by 5ALA Guided Surgery Has an Altered Cancer Stem Cell Marker Profile Compared to Central Tumour’, *Int J Mol Sci*, vol. 18, no. 11, Nov. 2017, doi: 10.3390/ijms18112452.
- [315] D. Jain, M. C. Sharma, C. Sarkar, D. Gupta, M. Singh, and A. K. Mahapatra, ‘Comparative analysis of diagnostic accuracy of different brain biopsy procedures’, *Neurol India*, vol. 54, no. 4, pp. 394–398, Dec. 2006, doi: 10.4103/0028-3886.28113.
- [316] F. Vasefi, N. MacKinnon, D. L. Farkas, and B. Kateb, ‘Review of the potential of optical technologies for cancer diagnosis in neurosurgery: a step toward intraoperative neurophotonics’, *Neurophoton*, vol. 4, no. 1, p. 011010, Dec. 2016, doi: 10.1117/1.NPh.4.1.011010.
- [317] E. Belykh *et al.*, ‘Utilization of intraoperative confocal laser endomicroscopy in brain tumor surgery’, *J Neurosurg Sci*, vol. 62, no. 6, pp. 704–717, Dec. 2018, doi: 10.23736/S0390-5616.18.04553-8.
- [318] C. Pohling *et al.*, ‘Multiplex coherent anti-Stokes Raman scattering microspectroscopy of brain tissue with higher ranking data classification for biomedical imaging’, *J. Biomed. Opt.*, vol. 22, no. 6, p. 066005, Jun. 2017, doi: 10.1117/1.JBO.22.6.066005.
- [319] S. Dochow *et al.*, ‘Combined fiber probe for fluorescence lifetime and Raman spectroscopy’, *Anal Bioanal Chem*, vol. 407, no. 27, pp. 8291–8301, Nov. 2015, doi: 10.1007/s00216-015-8800-5.
- [320] M. Skala and N. Ramanujam, ‘Multiphoton redox ratio imaging for metabolic monitoring in vivo’, *Methods Mol. Biol.*, vol. 594, pp. 155–162, 2010, doi: 10.1007/978-1-60761-411-1\_11.
- [321] D. R. Rivera *et al.*, ‘Compact and flexible raster scanning multiphoton endoscope capable of imaging unstained tissue’, *Proc. Natl. Acad. Sci. U.S.A.*, vol. 108, no. 43, pp. 17598–17603, Oct. 2011, doi: 10.1073/pnas.1114746108.
- [322] L. Jiang *et al.*, ‘Label-free imaging of brain and brain tumor specimens with combined two-photon excited fluorescence and second harmonic generation microscopy’, *Laser Phys. Lett.*, vol. 14, no. 10, p. 105401, Oct. 2017, doi: 10.1088/1612-202X/aa7c9a.
- [323] P. A. Valdés *et al.*, ‘Combined fluorescence and reflectance spectroscopy for in vivo quantification of cancer biomarkers in low- and high-grade glioma surgery’, *J Biomed Opt*, vol. 16, no. 11, p. 116007, Nov. 2011, doi: 10.1117/1.3646916.
- [324] S. Bahar, M. Suh, M. Zhao, and T. H. Schwartz, ‘Intrinsic optical signal imaging of neocortical seizures: the “epileptic dip”’, *Neuroreport*, vol. 17, no. 5, pp. 499–503, Apr. 2006, doi: 10.1097/01.wnr.0000209010.78599.f5.

- [325] J. R. Mourant, A. H. Hielscher, A. A. Eick, T. M. Johnson, and J. P. Freyer, ‘Evidence of intrinsic differences in the light scattering properties of tumorigenic and nontumorigenic cells’, *Cancer*, vol. 84, no. 6, pp. 366–374, Dec. 1998.
- [326] N. Honda, K. Ishii, Y. Kajimoto, T. Kuroiwa, and K. Awazu, ‘Determination of optical properties of human brain tumor tissues from 350 to 1000 nm to investigate the cause of false negatives in fluorescence-guided resection with 5-aminolevulinic acid’, *J Biomed Opt*, vol. 23, no. 7, pp. 1–10, 2018, doi: 10.1117/1.JBO.23.7.075006.
- [327] M. Mesradi *et al.*, ‘Experimental and analytical comparative study of optical coefficient of fresh and frozen rat tissues’, *J. Biomed. Opt*, vol. 18, no. 11, p. 117010, Nov. 2013, doi: 10.1117/1.JBO.18.11.117010.
- [328] Z. Hong *et al.*, ‘Optical diagnosis of gallbladder cancers via two-photon excited fluorescence imaging of unstained histological sections’, *Lasers Med Sci*, vol. 30, no. 1, pp. 225–233, Jan. 2015, doi: 10.1007/s10103-014-1652-y.
- [329] X. Wu *et al.*, ‘Label-free detection of breast masses using multiphoton microscopy’, *PLoS ONE*, vol. 8, no. 6, p. e65933, 2013, doi: 10.1371/journal.pone.0065933.
- [330] J. Yan *et al.*, ‘Preclinical study of using multiphoton microscopy to diagnose liver cancer and differentiate benign and malignant liver lesions’, *J Biomed Opt*, vol. 17, no. 2, p. 026004, Feb. 2012, doi: 10.1117/1.JBO.17.2.026004.
- [331] S. S. Nazeer, A. Saraswathy, A. K. Gupta, and R. S. Jayasree, ‘Fluorescence spectroscopy to discriminate neoplastic human brain lesions: a study using the spectral intensity ratio and multivariate linear discriminant analysis’, *Laser Phys.*, vol. 24, no. 2, p. 025602, Feb. 2014, doi: 10.1088/1054-660X/24/2/025602.
- [332] F. Bestvater *et al.*, ‘Two-photon fluorescence absorption and emission spectra of dyes relevant for cell imaging’, *J Microsc*, vol. 208, no. Pt 2, pp. 108–115, Nov. 2002, doi: 10.1046/j.1365-2818.2002.01074.x.
- [333] R. Cicchi and F. S. Pavone, ‘Multimodal nonlinear microscopy: A powerful label-free method for supporting standard diagnostics on biological tissues’, *J. Innov. Opt. Health Sci.*, vol. 07, no. 05, p. 1330008, Sep. 2014, doi: 10.1142/S1793545813300085.
- [334] J. H. Ostrander *et al.*, ‘Optical Redox Ratio Differentiates Breast Cancer Cell Lines Based on Estrogen Receptor Status’, *Cancer Res*, vol. 70, no. 11, pp. 4759–4766, Jun. 2010, doi: 10.1158/0008-5472.CAN-09-2572.
- [335] Y. Sun *et al.*, ‘Endoscopic fluorescence lifetime imaging for in vivo intraoperative diagnosis of oral carcinoma’, *Microsc. Microanal.*, vol. 19, no. 4, pp. 791–798, Aug. 2013, doi: 10.1017/S1431927613001530.
- [336] W. C. Lin, S. A. Toms, M. Johnson, E. D. Jansen, and A. Mahadevan-Jansen, ‘In vivo brain tumor demarcation using optical spectroscopy’, *Photochem. Photobiol.*, vol. 73, no. 4, pp. 396–402, Apr. 2001, doi: 10.1562/0031-8655(2001)073<0396:ivbtdu>2.0.co;2.
- [337] A. Pradhan *et al.*, ‘Steady state and time-resolved fluorescence properties of metastatic and non-metastatic malignant cells from different species’, *Journal of Photochemistry and Photobiology B: Biology*, vol. 31, no. 3, pp. 101–112, Dec. 1995, doi: 10.1016/1011-1344(95)07178-4.
- [338] F. Jamme *et al.*, ‘Deep UV autofluorescence microscopy for cell biology and tissue histology: Deep UV autofluorescence microscopy’, *Biol. Cell*, vol. 105, no. 7, pp. 277–288, Jul. 2013, doi: 10.1111/boc.201200075.
- [339] F. Fereidouni, A. N. Bader, and H. C. Gerritsen, ‘Spectral phasor analysis allows rapid and reliable unmixing of fluorescence microscopy spectral images’, *Opt. Express*, vol. 20, no. 12, p. 12729, Jun. 2012, doi: 10.1364/OE.20.012729.

- [340] F. Fereidouni, A. N. Bader, A. Colonna, and H. C. Gerritsen, 'Phasor analysis of multiphoton spectral images distinguishes autofluorescence components of *in vivo* human skin: Phasor analysis of skin images', *J. Biophoton.*, vol. 7, no. 8, pp. 589–596, Aug. 2014, doi: 10.1002/jbio.201200244.
- [341] G. Bourg-Heckly *et al.*, 'Endoscopic ultraviolet-induced autofluorescence spectroscopy of the esophagus: tissue characterization and potential for early cancer diagnosis', *Endoscopy*, vol. 32, no. 10, pp. 756–765, Oct. 2000, doi: 10.1055/s-2000-7704.
- [342] S. Villette, S. Pigaglio-Deshayes, C. Vever-Bizet, P. Validire, and G. Bourg-Heckly, 'Ultraviolet-induced autofluorescence characterization of normal and tumoral esophageal epithelium cells with quantitation of NAD(P)H', *Photochem. Photobiol. Sci.*, vol. 5, no. 5, p. 483, 2006, doi: 10.1039/b514801d.
- [343] Y. Pu *et al.*, 'Native fluorescence spectroscopy reveals spectral differences among prostate cancer cell lines with different risk levels', *J Biomed Opt*, vol. 18, no. 8, p. 87002, Aug. 2013, doi: 10.1117/1.JBO.18.8.087002.
- [344] H.-W. Wang *et al.*, 'Differentiation of apoptosis from necrosis by dynamic changes of reduced nicotinamide adenine dinucleotide fluorescence lifetime in live cells', *J Biomed Opt*, vol. 13, no. 5, p. 054011, Oct. 2008, doi: 10.1117/1.2975831.
- [345] J. M. Levitt *et al.*, 'Intrinsic fluorescence and redox changes associated with apoptosis of primary human epithelial cells', *J Biomed Opt*, vol. 11, no. 6, p. 064012, Dec. 2006, doi: 10.1117/1.2401149.
- [346] J. M. Levitt, M. E. McLaughlin-Drubin, K. Münger, and I. Georgakoudi, 'Automated Biochemical, Morphological, and Organizational Assessment of Precancerous Changes from Endogenous Two-Photon Fluorescence Images', *PLoS ONE*, vol. 6, no. 9, p. e24765, Sep. 2011, doi: 10.1371/journal.pone.0024765.
- [347] M. V. Liberti and J. W. Locasale, 'The Warburg Effect: How Does it Benefit Cancer Cells?', *Trends Biochem. Sci.*, vol. 41, no. 3, pp. 211–218, Mar. 2016, doi: 10.1016/j.tibs.2015.12.001.
- [348] M. R. Kasimova *et al.*, 'The free NADH concentration is kept constant in plant mitochondria under different metabolic conditions', *Plant Cell*, vol. 18, no. 3, pp. 688–698, Mar. 2006, doi: 10.1105/tpc.105.039354.
- [349] N. J. Gogtay, 'Principles of sample size calculation', *Indian J Ophthalmol*, vol. 58, no. 6, pp. 517–518, Dec. 2010, doi: 10.4103/0301-4738.71692.
- [350] J. C. Buckner, P. D. Brown, B. P. O'Neill, F. B. Meyer, C. J. Wetmore, and J. H. Uhm, 'Central Nervous System Tumors', *Mayo Clinic Proceedings*, vol. 82, no. 10, pp. 1271–1286, Oct. 2007, doi: 10.4065/82.10.1271.
- [351] G. Barkhoudarian and J. P. Whitelegge, 'Proteomics Analysis of Brain Meningiomas in Pursuit of Novel Biomarkers of the Aggressive Behavior', *J Proteomics Bioinform*, vol. 09, no. 02, 2016, doi: 10.4172/jpb.1000389.
- [352] S. Q. Sun, A. H. Hawasli, J. Huang, M. R. Chicoine, and A. H. Kim, 'An evidence-based treatment algorithm for the management of WHO Grade II and III meningiomas', *FOC*, vol. 38, no. 3, p. E3, Mar. 2015, doi: 10.3171/2015.1.FOCUS14757.
- [353] D. Simpson, 'THE RECURRENCE OF INTRACRANIAL MENINGIOMAS AFTER SURGICAL TREATMENT', p. 18.
- [354] L. Pantanowitz, Y. Chen, C.-P. Liang, Y. Liu, A. Fischer, and A. Parwani, 'Review of advanced imaging techniques', *J Pathol Inform*, vol. 3, no. 1, p. 22, 2012, doi: 10.4103/2153-3539.96751.

- [355] A. P. Dhawan, B. D'Alessandro, and X. Fu, 'Optical Imaging Modalities for Biomedical Applications', *IEEE Rev. Biomed. Eng.*, vol. 3, pp. 69–92, 2010, doi: 10.1109/RBME.2010.2081975.
- [356] A. Giuliani *et al.*, 'DISCO: a low-energy multipurpose beamline at synchrotron SOLEIL', *J Synchrotron Rad.*, vol. 16, no. 6, pp. 835–841, Nov. 2009, doi: 10.1107/S0909049509034049.
- [357] Y. Rivenson *et al.*, 'Virtual histological staining of unlabelled tissue-autofluorescence images via deep learning', *Nat Biomed Eng.*, vol. 3, no. 6, pp. 466–477, Jun. 2019, doi: 10.1038/s41551-019-0362-y.
- [358] H. Mehidine, E. Akan, A. Tauziede-Espariat, P. Varlet, B. Devaux, and D. A. Haidar, 'Comparison of brain tissue structures on histological slides and fluorescence microscopy images', in *Biophotonics Congress: Optics in the Life Sciences Congress 2019 (BODA,BRAIN,NTM,OMA,OMP)*, Tucson, Arizona, 2019, p. BW4A.6, doi: 10.1364/BRAIN.2019.BW4A.6.
- [359] I. Gregorio, P. Braghetta, P. Bonaldo, and M. Cescon, 'Collagen VI in healthy and diseased nervous system', *Dis. Model. Mech.*, vol. 11, no. 6, p. dmm032946, Jun. 2018, doi: 10.1242/dmm.032946.
- [360] B. Chance and B. Hess, 'Spectroscopic Evidence of Metabolic Control', *Science, New Series*, vol. 129, no. 3350, pp. 700–708, 1959, [Online]. Available: <http://www.jstor.org/stable/1757449>.